UNIVERSIDAD COMPLUTENSE DE MADRID
FACULTAD DE CIENCIAS FÍSICAS
Departamento de Estructura de la Materia, Física Térmica y Electrónica

TESIS DOCTORAL

Physics of cellular processes: the role of characteristic spatial scales of the cell membrane

Física de procesos celulares: el papel de las escalas espaciales características de la membrana célula

MEMORIA PARA OPTAR AL GRADO DE DOCTOR

PRESENTADA POR

Elena Beltrán de Heredia Rodríguez

Directores

Francisco Javier Cao García
Francisco Monroy Muñoz

Madrid
Ed. electrónica 2019

UNIVERSIDAD COMPLUTENSE DE MADRID

FACULTAD DE CIENCIAS FÍSICAS

Departamento de Estructura de la Materia, Física Térmica y Electrónica

PHD THESIS

Physics of Cellular Processes: The role of characteristic spatial scales of the cell membrane

Física de Procesos Celulares: El papel de las escalas espaciales características de la membrana celular

By

Elena Beltrán de Heredia Rodríguez

Submitted in partial fulfillment of the requirement for the degree of

Philosophiæ Doctor

Thesis advisors:

Dr. Francisco Javier Cao García
Dr. Francisco Monroy Muñoz

Madrid, 2018

To my parents

To Fluffy

Contents

Acknowledgments

Since its inception four years ago, this thesis has come to an end with the kind support and help of many people. I would like to extend my sincere thanks to all of them.

Undoubtedly, I would like to express my gratitude to my supervisors, Francisco J. Cao and Francisco Monroy, for their exceptional guidance and mentorship. They helped and encouraged me at all stages of my thesis work and gave me the confidence to develop my ideas. I have learnt a lot from them.

Funding from the EEA Grant allowed me to stay for a month at the University of Bergen (Norway). I would like to thank Dag L. Aksnes and his research team for hosting me during this period.

Financial support from Ministry of Education (Spain) through research FPU grant is gratefully acknowledged. This grant also allowed me to enjoy a short-term studentship at Institut Curie (Paris). I would like to thank Patricia Bassereau for her valuable input and useful discussions during my stay. I am also grateful to the whole Curie team for their friendly assistance, in particular, to Kodjo for his big help with the experiments. Many thank also to Frederic for providing us material and for his interest in my research.

Especially, Feng's collaboration in the experimental part of my thesis was more than precious. Thank you so much Feng for your altruistic commitment during my work in Paris. I really appreciate your confidence, kind words, and suggestions.

Really sincere thanks to all my siblings in pain: my fellows at the UCM, Colegio de España, IMDEA, FPU members, and other PhD and Post-Doc students over the world, for their constructive advice and their important knowledge about bureaucratic processes and grant applications. I further express my gratitude to Borja, Fer, Lauri, Berta, and Lara, for showing me experimental techniques and also for entertaining talks. Special thanks to the best office partner, Javi Jarillo, for enhancing my days and for teaching me so many things.

I am deeply thankful to my family for their genuine care and helpful intuitions. Many thanks to my parents for their affection, motivation, and example of hard work; and to my sister, M Jesús, for having a comfortable home at the end of the day and for her patience in listening to my cries and complains during these years.

No doubt, this thesis would not have been finished without the continuous support of all my friends and special people around me. They help me remind me who I am and what I really love. Thank you my friends, for spending a lot of fun times with me and for ensuring my survival during some difficult times in these years. Special mention to Lala, for insistently reminding me that there is a wonderful world outside university and for awaiting my thesis defense with desire.

Great thanks to Fluffy, a person who has been by my side ever since we first met at the Physics degree in Badajoz and has supported me in every conceivable way throughout this thesis and my life in general. Without him, this thesis would not have been started or finished. For this and much more, I dedicate the thesis to him.

This research received financial support from FPU grant 13/02826 (Ministerio de Educación, Cultura y Deporte, Spain). A collaboration with Institut Curie (Paris, France) was possible by a short-term fellowship from Ministerio de Educación, Cultura y Deporte (Spain) and a collaboration with University of Bergen (Norway) was possible by the funding from EEA Grant (European Economic Area).

Summary of the Thesis

Introduction

The study of cells helps us understand how organisms function. After all, our bodies are made up of trillions of cells. There are many processes that cells must complete to carry out their life functions and to meet their basic needs. In the present thesis, we will study the physics of some cellular processes in which the effect of cell size and membrane curvature plays a major role.

First, we will investigate the mechanics of constriction during cell division. Cell division is the process of formation of new daughter cells from the pre-existing mother cell. An important phase preceding division is cell constriction, a non-spontaneous process which involves large membrane deformations at the site of fission. In this thesis, we will investigate the mechanical route for symmetric constriction using a model cell composed by a flexible membrane that encloses the cytoplasm.

Next, we will study the cardiolipin segregation induced by membrane curvature. Cardiolipin (CL) is a cone-shaped lipid localized at high concentration in specific membrane sites with high curvature. The proposed mechanism of that accumulation is assumed to be geometry-driven; arguably, CL's conical shape matches the curved regions of the membranes thus relaxing the curvature frustration of these sites. In this thesis, we will measure the CL-sorting in experiments that isolate the effects of the membrane curvature by using lipid-bilayer pulled from cell-sized vesicles.

Finally, we will also study the phytoplankton size scaling with ambient nutrient concentration. Phytoplankton are the autotrophic microorganisms of the plankton community and a key factor in oceanic ecosystems and biogeochemical cycling. To support their activities, these microorganisms incorporate nutrients from the environment across the cell membrane. In this thesis, we will derive scaling relations that determine how phytoplankton traits are expected to vary with organism size and ambient nutrient concentration.

Objectives

In this thesis we will address the study of different cellular processes in which the characteristic spatial scales of the cell membrane play an essential role. The specific objectives will be grouped in the following three parts.

Mechanics of constriction during cell division

1. Develop a theoretical model for the mechanics of cell constriction during division which allows us to determine the optimal cell shapes along the constriction pathway and to find approximate analytical expressions for the main properties of the constricted cell (such as energy, constriction and stabilization forces, volume, and membrane area). Analyze the influence of the cell size, the spontaneous curvature of the membrane, the surface tension, and the external pressure in these properties. Determine the mechanical conditions for symmetric constriction to become spontaneous and stable against lateral displacements of the constriction ring.

Cardiolipin segregation induced by membrane curvature

2. Determine experimentally whether cardiolipin (CL) molecules accumulate in curved regions of the membrane by using membrane nanotubes of controlled radius pulled from giant vesicles. Implement a thermodynamic model to explain our experimental measurements. Predict the CL intrinsic curvature from the fit of the model and compare it with previous estimates.

Phytoplankton size scaling

3. By combining previous theoretical and experimental results, extract empirical relationships that determine how phytoplankton size should scale with ambient nitrate concentration and how the number of porters in the membrane and the handling time depend on the cell size.

Results and Conclusions

Below, the main results and conclusions to the previous objectives are presented. They will be grouped in the same three parts.

Mechanics of constriction during cell division

We have addressed a theoretical study of the mechanics of constriction during cell division by computing the bending energy of symmetrically deformed vesicles. The optimal cell shapes along the constriction pathway were computed. These shapes can have prolate (rod-like), oblate (disk-like), or spherical polar caps depending on the external fields (surface tension and external pressure) and on the constitutive parameters of the cell (size and spontaneous curvature). We have derived general formulas for the more relevant properties involved in the constriction process of the cell (energy, constriction and stabilization forces, volume, and area). For cells of micro size with flexible membranes, the constriction and stabilization forces obtained are in the range of picoNewton, which is the range of forces practicable by bimolecular motors. We have found that stronger forces are required for smaller cells. The more favorable conditions for cell constriction are determined, obtaining that lower forces are required in hypotonic media and with low membrane tensions. We have also studied the stability and spontaneity of symmetric cell constriction. We have seen that stable symmetric constriction requires positive effective spontaneous curvature, while spontaneous constriction requires a spontaneous curvature higher than the characteristic inverse cell size.

Cardiolipin segregation induced by membrane curvature

Our *in vitro* measurements on nanotubes pulled from Giant Unilamellar Vesicles (GUVs) demonstrate that cardiolipin (CL) accumulates in curved membranes based on their shape alone, without the involvement of any cellular protein machinery. Our results show that this accumulation is higher in more highly curved membranes, reaching a maximum at optimal CL concentrations. The experimental data are compatible with a model based on membrane elasticity and van der Waals entropy, which predicts for CL an intrinsic curvature of 1.10 nm^{-1}, in agreement with previous estimates. In addition, a lateral cohesive interaction clustering into small domains of typically 10 CL molecules in equilibrium with the environment is deduced from the experimental data

Phytoplankton size scaling

Based on previously published experimental observations of marine species of phytoplankton, we have determined that phytoplankton dominant size r should scale approximately with $S^{0.85}$ where S represents the ambient nitrate concentration. Furthermore, by combining a trait-based uptake model with previous experimental results, we have derived scaling relations for two phytoplankton traits: the number of porters and the handling time. Our results indicate that handling time decreases approximately with $r^{-0.90}$ while porter number increases approximately with $r^{1.56}$.

Resumen de la tesis

Introducción

El estudio de las células nos ayuda a comprender cómo funcionan los organismos. Al fin y al cabo, nuestros cuerpos están formados por billones de células. Hay muchos procesos que las células deben completar para llevar a cabo sus funciones vitales y satisfacer sus necesidades. En la presente tesis, estudiaremos la física de algunos procesos en los que el efecto del tamaño celular y la curvatura de la membrana es crucial.

Primero, investigaremos la mecánica de la constricción durante la división celular. La división celular es el proceso de formación de células hijas a partir de la célula madre. Una fase importante que precede a la división es la constricción celular, un proceso no espontáneo que involucra grandes deformaciones de membrana en la zona de fisión. En esta tesis estudiaremos el mecanismo de la constricción simétrica usando como célula modelo una membrana flexible que encierra el citoplasma.

A continuación, estudiaremos la segregación de cardiolipina inducida por la curvatura de la membrana. La cardiolipina (CL) es un lípido de forma cónica localizado en zonas específicas de membrana con alta curvatura (polos y zona de división de bacterias y pliegues de la membrana mitocondrial interna). El mecanismo propuesto para explicar esta acumulación se basa en la geometría: la forma cónica de la CL se ajusta a las regiones curvadas de las membranas relajando la frustración causada por la curvatura. En esta tesis, mediremos la segregación de CL en experimentos que aíslan los efectos de la curvatura mediante el uso de nanotubos de membrana extraídos de vesículas de tamaño celular.

Finalmente, estudiaremos el escalado del tamaño del fitoplancton con la concentración de nutrientes en el medio. El fitoplancton es el conjunto de los microorganismos autótrofos de la comunidad planctónica y un factor clave en los ecosistemas oceánicos y en el ciclo biogeoquímico. En esta tesis determinaremos cómo varias características del fitoplancton deben variar con su tamaño y con la disponibilidad de nutrientes en el medio.

Objetivos

En esta tesis abordaremos el estudio de procesos celulares en los que la escala espacial característica de la membrana tiene un papel esencial. Los objetivos específicos se agruparán en las siguientes tres partes.

Mecánica de la constricción durante la división celular

1. Desarrollar un modelo teórico para la mecánica de la constricción celular durante la división que nos permita determinar las formas celulares a lo largo del proceso de constricción y obtener fórmulas analíticas aproximadas de las principales propiedades de la célula (energía, fuerzas de constricción y estabilización, volumen, y área). Analizar la influencia del tamaño de la célula, la curvatura espontánea, la tensión superficial y la presión externa en estas propiedades. Determinar las condiciones mecánicas para que la constricción simétrica se vuelva espontánea y estable frente a desplazamientos laterales del anillo de constricción.

Separación de cardiolipina inducida por la curvatura de la membrana

2. Determinar experimentalmente si las moléculas de cardiolipina (CL) se acumulan en regiones curvadas de la membrana mediante el uso de nanotubos de membrana de radio controlado extraídos de vesículas gigantes. Implementar un modelo termodinámico para explicar nuestras medidas experimentales. Predecir la curvatura intrínseca de la CL a partir del ajuste al modelo y compararla con estimaciones anteriores.

Escalado del tamaño del fitoplancton

3. Combinando resultados teóricos y experimentales previos, determinar cómo el tamaño del fitoplancton debe escalar con la concentración de nitrato ambiental y cómo el número de portadores de membrana y el tiempo de absorción de nutrientes dependen del tamaño de la célula.

Resultados y conclusiones

A continuación, se presentan los principales resultados y conclusiones a los objetivos anteriores. Se agruparán en los mismos tres apartados.

Mecánica de la constricción durante la división celular

Hemos realizado un estudio teórico de la mecánica de la constricción durante la división celular calculando la energía de curvatura en vesículas deformadas simétricamente. Se han obtenido las formas óptimas de las células a lo largo del proceso de constricción. Estas formas pueden tener casquetes polares prolatos (tipo barra), oblatos (tipo disco) o esféricos, dependiendo de las variables externas (tensión superficial y presión) y de los parámetros constitutivos de la célula (tamaño y curvatura espontánea). Hemos derivado expresiones analíticas aproximadas para las magnitudes más relevantes involucradas en el proceso de constricción (energía, fuerzas de constricción y estabilización, volumen y área de la membrana). Células microscópicas con membranas flexibles requieren fuerzas de constricción y estabilización en el rango de los picoNewton, que es el rango de fuerzas ejercidas por motores moleculares. Hemos obtenido que células más pequeñas requieren mayores fuerzas para constreñirse de forma estable. Las condiciones más favorables para la constricción son medios hipotónicos y membranas con tensiones superficiales bajas. También hemos visto que para que la constricción simétrica transcurra de forma estable es necesaria una curvatura espontanea positiva, mientras que para que la constricción simétrica sea espontánea se requiere una curvatura espontánea mayor que el inverso del tamaño característico de la célula.

Segregación de cardiolipina basada en la curvatura de la membrana

Nuestras medidas en nanotubos de membrana extraídos de vesículas gigantes demuestran que la cardiolipina (CL) se acumula en las zonas curvadas de las membranas, con mayor acumulación cuanto más curvadas son. Los datos experimentales son compatibles con un modelo basado en la elasticidad de membranas biológicas y en la entropía de van der Waals, el cual predice una curvatura intrínseca de la CL de 1.10 nm^{-1}, que coincide con estimaciones previas. Además, a partir de los datos experimentales se deduce la existencia de una interacción cohesiva lateral entre las moléculas de CL que las agrupa en pequeños dominios de aproximadamente 10 moléculas.

Escalado del tamaño del fitoplancton

Basándonos en observaciones experimentales previamente publicadas, hemos determinado que el tamaño dominante de la comunidad fitoplanctónica r escala aproximadamente con $S^{0.85}$, donde S representa la concentración de nitrato ambiental. Además, hemos derivado relaciones de escalado para dos características del fitoplancton: el número de portadores de la membrana y el tiempo de absorción de nutrientes. Nuestros resultados indican que el tiempo de absorción decrece aproximadamente con $r^{-0.90}$ mientras que el número de portadores aumenta aproximadamente con $r^{1.56}$.

List of Publications

Included in this thesis:

1. Beltran-Heredia E, Almendro-Vedia VG, Monroy F, & Cao FJ (2017) Modeling the mechanics of cell division: influence of spontaneous membrane curvature, surface tension, and osmotic pressure. *Front Physiol* 8:312. Journal in quartile Q1, with 2016 Impact Factor 4.134. (Source: Thomson and Reuters). Included in Chapter 4.

2. Beltran-Heredia E, Almendro-Vedia VG, Monroy F, & Cao FJ (2018) Mechanical conditions for stable symmetric cell constriction. *Manuscript submitted for publication.* Included in Chapter 5.

3. Beltran-Heredia E*, Tsai FC*, Cao FJ, Bassereau P, & Monroy, F (2018) Membrane curvature induces cardiolipin sorting. *These authors contributed equally. *Manuscript submitted for publication.* Included in Chapter 6.

4. Beltran-Heredia E, Aksnes DL, & Cao FJ (2017) Phytoplankton size scaling with nutrient concentration. *Mar Ecol Prog Ser* 571: 59-64. Journal in quartile Q1, with 2015 Impact Factor 2.361. (Source: Thomson and Reuters). Included in Chapter 7.

5. Beltran-Heredia E (2017) Portraits of cell division. Available at: http://demonstrations.wolfram.com/PortraitsOfCellDivision/ Included in Chapters 4 and 5.

6. Beltran-Heredia E (2015) Model of microbial nutrient uptake. Available at: http://demonstrations.wolfram.com/ModelOfMicrobialNutrientUptake/ Included in Chapter 7.

Other publications:

7. Jarillo J, Morin JA, Beltran-Heredia E, Villaluenga JPG, Ibarra B, & Cao FJ (2017) Mechanics, thermodynamics, and kinetics of ligand binding to biopolymers. *PLoS One* 12(4):e0174830. Journal in quartile Q1, with 2016 Impact Factor 2.806. (Source: Thomson and Reuters).

8. Morin JA*, Cerrón F*, Jarillo J*, Beltran-Heredia E, Ciesielski GL, Arias-González JR, Kaguni LS, Cao FJ, & Ibarra B (2017) DNA synthesis determines the binding mode of the human mitochondrial single-stranded DNA-binding protein. *Nucleic Acids Res* 45(12):7237-7248. *These authors contributed equally. Journal in quartile Q1, with 2016 Impact Factor 10.162. (Source: Thomson and Reuters).

9. Beltran-Heredia E & Santos A (2014) Fourth virial coefficient of additive hard-sphere mixtures in the Percus-Yevick and hypernetted chain approximations. *J Chem Phys* 140:134507. Journal in quartile Q1, with 2014 Impact Factor 2.20. (Source: Thomson and Reuters).

10. Beltran-Heredia J, Carmona C, & Beltran-Heredia E (2014) *Obtención de adsorbentes a partir de Eichhornia crassipes (camalote)*. (Editorial Académica Española, Germany).

11. Beltran-Heredia J & Beltran-Heredia E (2014) Adsorbent Biopolymers from Tannin Extracts for Water Treatment. *Tannins. Biochemistry, Food Sources and Nutritional Properties*, Ed. Combs CA (Nova Science Publishers, New York), pp 1-28.

PART I

Introduction, Objectives, and State of the Art

Introduction and Objectives

This initial chapter summarizes some fundamental aspects about the cell. After a brief historical review, we describe the structure of the two major types of cells: prokaryotes and eukaryotes. The following sections introduce the cellular processes of division, curvature-based lipid sorting, and nutrient uptake, as they are the main topics of the original results of this thesis. Finally, we state the objectives and the structure of the thesis.

The Cell

Cells consist of a crowded water solution called cytoplasm, which contains many biomolecules such as proteins and nucleic acids, enclosed within a cell membrane (known as the plasma membrane). Crowding occurs since these high concentrations of biomolecules occupy a large proportion of the cell volume, providing cells with a densely packed structure and with a gel-like, viscous, appearance. Such large viscosity plays a major role in cell function, e.g. by influencing bimolecular reaction rates and altering the molecular diffusion constants measured in dilute solutions. The cell's interior is further crowded by protein filaments called cytoskeleton, which provides the cells with structure, shape, and internal organization. Organisms can be unicellular (consisting of a single cell, as bacteria) or multicellular (consisting of many cells, as plants and animals). In complex multicellular organisms, cells specialize into different cell types that are adapted to particular functions. In mammals, major cell types include skin cells, muscle cells, neurons, blood cells, fibroblasts, stem cells, and others. Cells emerged on Earth at least 3.5 billion years ago.

The cell was first discovered and named by Hooke [1] in 1665 thanks to the invention of the microscope at the beginning of the seventeenth century. He examined very thin slices of cork and described the pores he viewed, which were actually non-living cell walls. He remarked that the boxy partitions looked strangely similar to cells (small rooms) in a monastery, thus deriving the name. At the time, Leeuwenhoek improved the original microscope designs which led him to be the first to observe living cells in 1674. While he called them “animalcules,” they are now known to us as microorganisms. Several other researchers during the 1600s were also looking at various biological specimens under microscopes and this demand soon made it clear that better instruments were needed. The creation of apochromatic lens in the 1800s allows for important discoveries such as the cell division and the cell nucleus. In view of what was going on in these cells improved, scientists developed many cell theories to understand how the cells functioned. In the decade of 1840, Schleiden, Schwann, and Virchow developed the first cell theory, which contained three fundamental parts of its modern version: (1) All organisms are composed of one or more cells. (2) The cell is the structural and functional unit of all organisms. (3) Cells come from preexisting cells by division (spontaneous generation does not occur).

The current understanding of cellular substructure began with the use of the electron microscope in 1920s. Porter [2] was a pioneer in this field and was the first to identify the endoplasmic reticulum and many elements of the cytoskeleton. With the rapid growth of molecular biology in the mid-twentieth century, cell biology research exploded in the 1950's. Nowadays, it is possible to maintain, grow, and manipulate cells outside of living organisms. This advance of scientific knowledge has led to fascinating improvements in microscopy, biochemistry, and genetics, undreamed of by the earliest cell biologists.

Cell Structure

All living organisms can be classified according to the structure of their cells into two main classes: prokaryotes and eukaryotes. The most fundamental difference is that eukaryotic cells have a nucleus containing their DNA, whereas the genetic material in prokaryotic cells is not membrane-bound. Eukaryotes developed at least 2.7 billion years ago after millions of years in which prokaryotes were the only form of life on Earth.

Prokaryotes

Prokaryotes include two of the three domains of life, Bacteria and Archaea. The name comes from the Greek words *pro* (before) and *karyon* (nucleus), and refers to the organisms without a cell nucleus or any separate membrane-bound compartment. Instead, all their intracellular components (ribosomes, plasmids, and DNA) are free in the cytoplasm (see Figure 1). Their DNA is poorly structured and is condensed in an area called nucleoid. Enclosing the cell is the plasma membrane, covered by a cell wall (some of them may be further covered by a third layer named capsule). Prokaryotic cells often have protrusions (flagella, fimbriae, and pili) projected from the cell surface that allow the cell to stick to surfaces, move around, or communicate with other cells. Most prokaryotes are unicellular, but some types can be also part of multicellular organisms. They can have spherical, rod, or spiral shape, with a diameter ranging from 0.2 to 2.0 μm.

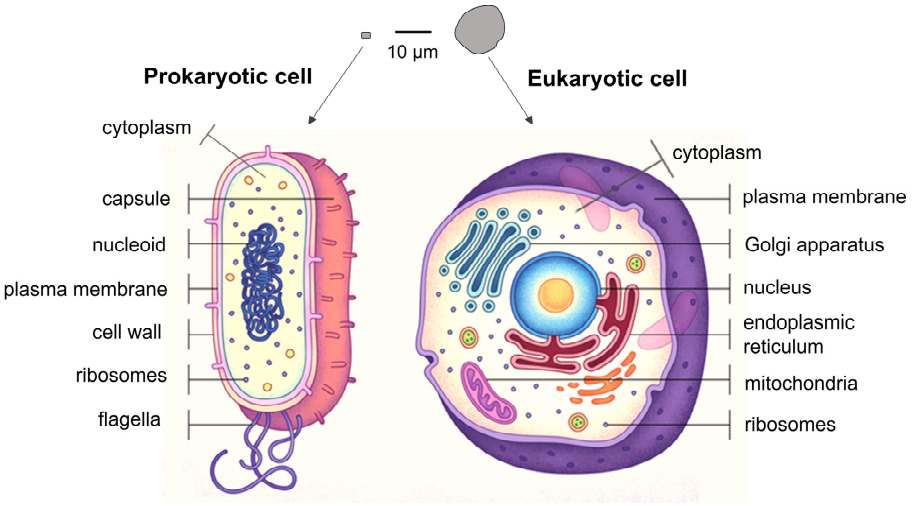

Figure 1. Sketch depiction of a prokaryotic and a eukaryotic cell. Adapted from Ref. [3].

Eukaryotes

Eukaryotes belong to the third domain of life, Eukarya, which includes animals, plants, fungi, and protists. The most fundamental difference with prokaryotes is that eukaryotic cells are

organized into complex membrane-bound compartments called organelles (see Figure 1). Each organelle has a specific role within a cell which is important to the proper functioning of both the cell and the organism. Especially important is the nucleus, which contains the DNA enclosed by the nuclear membrane. This feature gives them their name, which comes from the Greek *eu* (true) and *karyon* (nucleus). Eukaryotic cells also contain other organelles such as mitochondria, endoplasmic reticulum, Golgi apparatus, and others. Plants and some protits also contain chloroplasts. Unlike animal cells, plants, fungi, and some protists are enclosed by a cell wall. Some eukaryotic cells are single-celled entities, but most of them are part of multicellular organisms. They are about fifteen times wider than a typical prokaryote and can be thousand times greater in volume.

Cell Division

Cell division is the essential feature of life by which a mother cell divides into two or more daughter cells. This process leads to procreation in unicellular organisms and to growth in multicellular ones. Prokaryotic cells, such as bacteria, reproduce by binary fission, a process that includes DNA replication, chromosome separation, and cytokinesis (cytoplasmic division), see Figure 2. During this process, a single cell creates two genetically identical cells (except random mutations).

Eukaryotic cell division either involves mitosis or a more complex process called meiosis. Mitosis, like binary fission in prokaryotes, leads to the production of two daughter cells with the same number of chromosomes and DNA as the parental cell (*i.e.,* no genetic diversity is created), see Figure 2. This type of cell division makes up most of tissues and organs and it is fundamental for growth, repair, and maintenance. Eukaryotic cells can also divide by meiosis, a process that creates sex cells (sperm or egg cells). Unlike mitosis, meiosis produces four daughter cells which have half the number of chromosomes as the mother cell and contain a unique set of genetic information (see Figure 2). After meiosis, the sperm and egg cells could join to create a new organism with the normal amount of chromosomes and genetically unique.

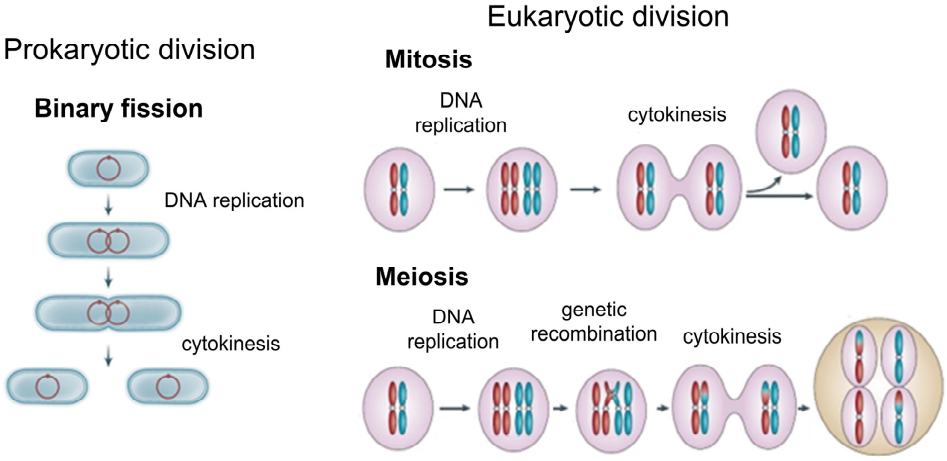

Figure 2. Schematic diagrams of the binary fission in prokaryotes and mitosis and meiosis in eukaryotic cells. Adapted from Refs. [4] and [5].

Both prokaryotic and eukaryotic cells replicated from preexisting cells through cytokinesis, the final process of cell division that divides the cytoplasm in two. Cytokinesis largely resembles the

prokaryotic process of binary fission, but because of differences between prokaryotic and eukaryotic cell structures and functions, the mechanisms differ. In animal cells, cytokinesis occurs when a band of cytoskeletal fibers called the contractile ring contracts inward and pinches the cell in two. The indentation produced as the ring contracts inward is called the cleavage furrow. Animal cells can be pinched in two because they're relatively soft and squishy. Plant cells are much stiffer than animal cells; they're surrounded by a rigid cell wall and have high internal pressure. Because of this, plant cells divide in two by building a new structure down the middle of the cell. This structure, known as the cell plate, is made up of plasma membrane and cell wall components delivered in vesicles.

Lipid Sorting in Cells

The eukaryotic cells are divided into intracellular organelles delimited by membranes, which are composed of a large variety of lipids and proteins. Each one of these membranes have different shape, composition, and function. Their shapes are usually described in terms of curvature, a mathematical property characterizing how the local shape of the membrane deviates from flatness. Presumably, the molecular geometry of membrane components is a determinant factor to the structural stability of the curved sites in biological membranes. The intracellular compartments are not isolated structures. Instead, they constantly communicate and exchange material. To transport material from one organelle to another, a vesicle buds out of the donor compartment and is transported in the cytoplasm along cytoskeleton filaments to its target compartment where it releases its content after fusion. There is quite a few evidence in literature showing that the cell is able to sort lipids during intracellular trafficking [6, 7]. One possible mechanism of this sorting is that these transport intermediates are formed from preexisting lipid domains. Vesicles budding from these domains would have different composition and would be addressed to different destination. Another possible mechanism could be a coupling between lipid composition and membrane curvature, so that membrane composition would change when membrane geometry changes in order to reduce the curvature frustration. Since a strong negative curvature must be generated at the budding site, the cone shape of some lipids makes them ideally suited for fitting in the area of constriction (see Figure 3).

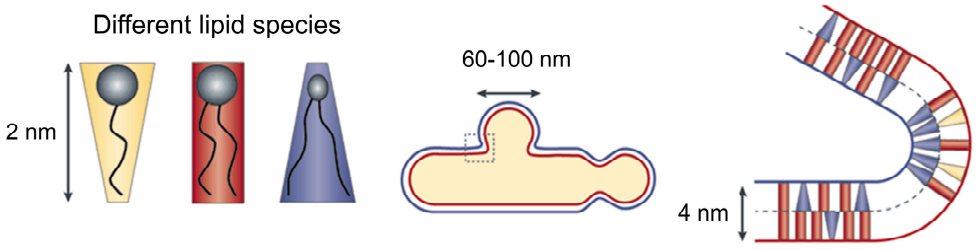

Figure 3. Lipid shapes could be at the origin of curvature-based lipid sorting during vesicle budding. Cone shaped lipids prefer highly curved parts of the membrane. Adapted from Ref. [8].

In order to understand how intracellular trafficking maintains the composition differences between membranes compartments of the cell, curvature-driven partitioning has been extensively explored in recent years in typical lipid systems as well as for embedded proteins. Using *in vitro* approaches, Bassereau and colleagues [9] have shown that membrane curvature is able to induce lipid sorting only for membrane compositions close to demixing (when lipid-lipid interactions become dominant). In ideal lipid mixtures, however, lipid sorting cannot occur

due to the overwhelming cost of mixing entropy. Since there is strong evidence that the plasma membrane is close to phase separation [10], the mechanism of lipid sorting induced by curvature is thought to be physiologically relevant.

Uptake of Nutrients by the Cell

Unicellular organisms are made up of a single cell (although some of them live in colonies). Individually, they can only be seen using a microscope. For this reason, unicellular organisms are often called microorganisms. The main groups of unicellular organisms are bacteria, archaea, protozoa, unicellular algae, and unicellular fungi. They can be either prokaryotes or eukaryotes. Like larger organisms, microorganisms require nutrients for growth, reproduction, and cell maintenance. These nutrients provide raw material and energy for building new cell constituents and power metabolic processes. All microorganisms require a minimum set of macronutrients, *i.e.,* nutrients needed in large quantities. Six macronutrients—carbon, nitrogen, phosphorus, hydrogen, oxygen, and sulfur—make up the carbohydrates, lipids, nucleic acids, and proteins of the cell. Four other macronutrients are cations that serve as cofactors for specific enzymes (Mg^{2+}, Fe^{2+}, and K^{+}) or act as regulatory signaling molecules (Ca^{2+}). All cells also require very small amounts of certain trace elements, called micronutrients. These include cobalt, copper, manganese, molybdenum, nickel, and zinc.

Microorganisms incorporate nutrients from the environment across the cell membrane by two major mechanisms: passive transport and active transport (see Figure 4). The uptake is highly specific as only necessary substances are acquired. Passive transport is the process by which molecules and gases move from a region of higher concentration to one of lower concentration with no energy consumption. This type of transport involves either direct simple diffusion through a membrane or diffusion through facilitator proteins embedded within the cell membrane, which can act as channels or carriers. Since microorganisms live in nutrient poor habitats, they must be also able to transport nutrients into the cell against concentration gradient. In order to do this, the cell utilizes energy (from electrochemical gradient, light, or ATP) in a process known as active transport. All types of active transport utilize carrier proteins.

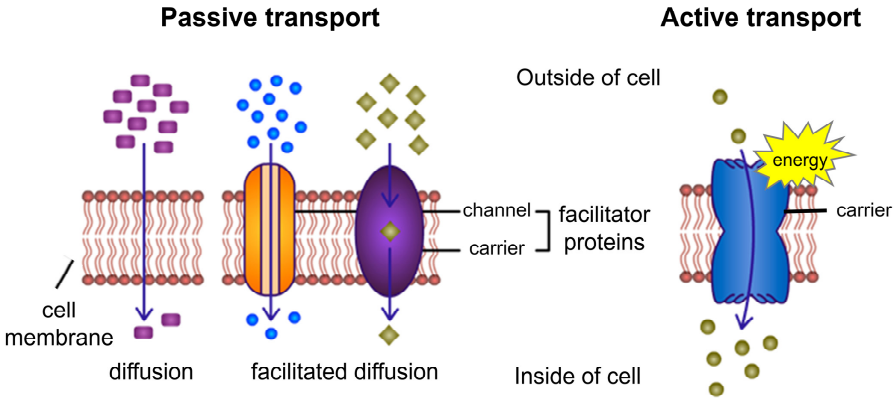

Figure 4. Cartoon illustrating the passive and the active transport uptake mechanisms by microorganisms. Adapted from Ref. [11].

Objectives of the Thesis

In this thesis we address the study of different cellular processes in which the effect of cell size and membrane curvature plays a major role. Below, the main objective are detailed.

The first objective of this thesis is develop a theoretical model for the mechanics of constriction during cell division using a model cell composed by a flexible membrane that encloses the cytoplasm. It aims to determine the optimal cell shapes along the constriction pathway and to derive approximate analytical formulas for the main properties of the constricted cell (such as energy, constriction force, volume, area, and stability of symmetric constriction). These analytical expressions have to be compared with the exact solutions obtained from numerical computations in order to verify the validity of our approximate method. We also intend to determine under which conditions vesicles (or cells) constrict more easily (with lower constriction forces) by analyzing the effects of the cell size, the spontaneous curvature of the membrane, the surface tension, and the external pressure.

The second objective of this thesis is to determine, both analytically and numerically, the mechanical conditions for symmetric constriction to become spontaneous and stable against lateral displacements of the constriction ring. We want this analysis to be done under three paradigmatic cases that resemble different biological scenarios: constriction at constant cell size, at constant membrane area, and at constant volume enclose. Finally, we wish to study how the spontaneity and the stability of symmetric cell division vary as constriction progress.

The third objective of this thesis is to determine the cardiolipin (CL) sorting induced by membrane curvature. CL is a conical lipid localized predominantly in the cellular poles and the division site of bacteria [12–14] and in the highly curved folds of the inner mitochondrial membrane [15]. The cone shape of the CL molecule is thought to be a determinant geometric factor which contribute to the structural stability of these highly curved sites. Indeed, the proposed mechanism of the observed localization has been argued to be geometry-driven as the CL's conical shape matches the curved regions of those membranes thus relaxing the curvature frustration in these sites [16]. Although there is quite a few evidence in the literature suggesting an apparent coupling between CL content and membrane shape [16–19], no definitive evidence of curvature induced CL-sorting is available from controlled experiments performed *in vitro*. In this thesis, we want to measure the CL sorting as a function of membrane curvature by performing a set of fluorescence measurements on membrane nanotubes of controlled radii pulled from Giant Unilamellar Vesicles (GUVs). Additionally, it will be required to implement a mathematical model in order to explain our experimental results. This model will allow us to predict the intrinsic curvature of the CL molecule and to compare it with previous estimates.

The fourth and final objective of this thesis is to study the phytoplankton size scaling with ambient nutrient concentration. Phytoplankton are microscopic, single-celled photosynthetic organisms that live suspended in water. Over much of the ocean, phytoplankton growth is limited by nitrogen uptake (as nitrate). This thesis is aimed to extract novel empirical relationships that determine how phytoplankton traits are expected to vary with organism size and nitrate supply by combining previous theoretical and experimental results. In particular, we want to determine the phytoplankton size scaling with nitrate concentration and the dependence of the number of porters in the membrane and the handling time with the cell size.

Structure of the Thesis

The present thesis has been organized in different thematic parts according to the specific proposed objectives (see Figure 5). Part I contains the introductory chapters that provide the background for the next parts, which are dedicated to the original results. The next parts, Part II, III, and IV, include our original results; some of which are already published in international journals (the remainder are in progress). They provide answers to the objectives of the thesis pointed above. Part II presents our theoretical model for the mechanics of constriction during cell division and a detailed analysis of its implications that responds specifically to the objectives 1 and 2 presented above. The next part, Part III, includes our experimental and theoretical research about the cardiolipin sorting induced by membrane curvature, thereby providing answers to the third objective of this thesis. Part IV addresses the last objective of this thesis and shows novel empirical relations that determine how phytoplankton traits are expected to vary with organism size and ambient nutrient concentration. In addition to the discussion and conclusions in each chapter, we also include in Part V a general discussion, the final conclusions, and possible future work. These different parts are marked with the color codes detailed in Figure 5 which are also displayed in the page heads.

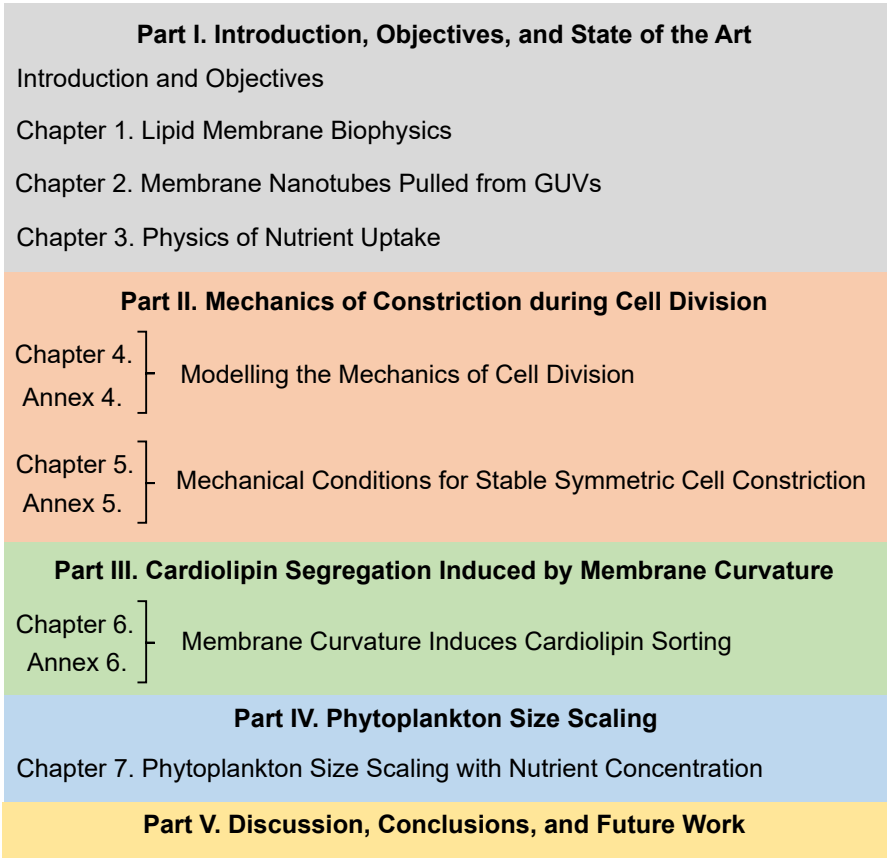

Figure 5. Structure of the present thesis. The different colors represent the different thematic blocks.

Chapter 1

Lipid Membrane Biophysics

The present chapter contains an introduction to the lipid membrane biophysics whose knowledge is necessary to correctly understand the results shown in Parts II and III of this thesis. It starts with a brief description of the nature of biological membranes, which includes their composition, structure, and some important properties (Section 1.1). After, in Section 1.2, we present the model system commonly used to study the physical properties of membranes. Section 1.3 describes the main physical properties of membranes at equilibrium and Section 1.4 provides an overview about lipid sorting mechanisms. The next section deals with the equilibrium shapes of the simplest systems: cells or vesicles without a nucleus or a space filling-cytoskeleton. Finally, in Section 1.6, we summarize previous results about the mechanics of cell constriction during division in a model which depicts the cells as a tensionless, turgor-free and symmetrical lipid bilayer vesicle.

1.1 Membrane Composition and Structure

Before the emergence of electron microscopy in the 1950s, the structure and composition of the biological membranes were unknown. Researches used indirect methods to identify membranes that they could not visualize. Thanks to the advances of Overton [20, 21], Langmuir [22], Gorter and Grendel [23], and Danielli and Davson [24], it was deduced that membranes contain lipids and proteins assembled in a bilayer. The advent of the electron microscope, the proposal of Singer and Nicolson [25], additional work of Unwin and Henderson [26], and the findings of Robertson [27] all contributed to the development of the modern membrane model. According to this model, called *fluid mosaic model*, biological membranes can be considered as two-dimensional lipid bilayers in which proteins are embedded, resulting in a mosaic of components. This arrangement is fluid, not solid, and both individual lipids and proteins can diffuse more or less easily within the membrane.

1.1.1 Membrane Lipids

The primary constituent of any biological membrane, that gives its chemical and physical properties, are lipids. The structure of the lipids consists of two important regions: a polar (hydrophilic) head region, able to form hydrogen bonds with water, and a nonpolar

(hydrophobic) tail region, consisting in general of two fatty acid chains of various length and degree of unsaturations, see Figure 1.1. As they contain both hydrophilic and hydrophobic regions, they are called amphipathic molecules. The polar head determines the lipid type, which can be neutral or negatively charged. The area per lipid is approximately 0.7 nm^2 with a height of around 2 nm.

Most lipids in eukaryotic cells are synthesized in the smooth endoplasmic reticulum. In prokaryotes, which do not have endoplasmic reticulum, all lipid synthesis occurs in the cytosol. Cell membranes contain more than a thousand species of lipids. The amount of each depends upon the type of cell and the organelle, but they can be generally categorized into two major groups: phospholipids and sterols.

Phospholipids

Phospholipids are the most abundant lipids in cell membranes, often contributing for over 50% of all lipids. The structure of phospholipids consists of a hydrophilic head containing a phosphate group and a hydrophobic tail containing an alcohol molecule. The two major classes of phospholipids are glycerophospholipids and sphingolipids:

a) Glycerophopholipids have a diacylglycerol backbone, *i.e.,* two fatty acid chains covalently linked to a glycerol molecule. If the head group consists in the phosphate alone, then the lipid is called phosphatidic acid (PA). However, phosphate may further be attached to additional molecules such as choline, serine, or ethanolamine, giving rise to phosphatidylcholine (PC), phosphatidylserine (PS), or phosphatidylethanolamine (PE), respectively. PC is the most abundant glycerophospholipid in animal cells. Both PC and PE are zwitterionic, *i.e.,* contain both a positive and a negative charge and are therefore net neutral. In contrast, PA and PS are both negatively charged. Other glycerol-based phospholipid, cardiolipin (CL), forms a dimer of two PA joined at the head, resulting in a large molecule with two negative charges. Glycerophospholipids are commonly found in both eukaryotes and prokaryotes.

b) Sphingolipids look very similar to glycerophospholipids but they contain no glycerol. Instead, they have a ceramide backbone (sphingoid base amide-linked to a fatty acid). One of the major sphingolipids in mammalian cells is sphingomyelin (SM), a lipid with a head group made up of a phosphate group linked to a choline. Sphingolipids are rare in prokaryotes but widely present in eukaryotes.

The fatty chains in phospholipids are composed of a string of carbons and hydrogens. They usually contain an even number of carbon atoms, typically between 16 and 20, and may be saturated or unsaturated, with the configuration of the carbon-carbon double bonds nearly always cis. The shape of the tails is determined by the number of these double bonds, which induce kinks in the tails.

Phospholipids can be attached to carbohydrate monosaccharides or oligosaccharides. These lipids are called glycolipids and only account for an amount of about 2% of all lipids.

Sterols

Sterols are drastically different in size and structure from phospholipids. Their hydrophobic part consists of a rigid planar array of rings with an attached hydrocarbon tail. Sterols are major

components of animal and plant membranes but are absent in prokaryotes. Cholesterol is the predominant sterol in eukaryotic cells, which represents around 30-40% of all their lipids.

The chemical structure of the lipids described above is drawn in Figure 1. 1.

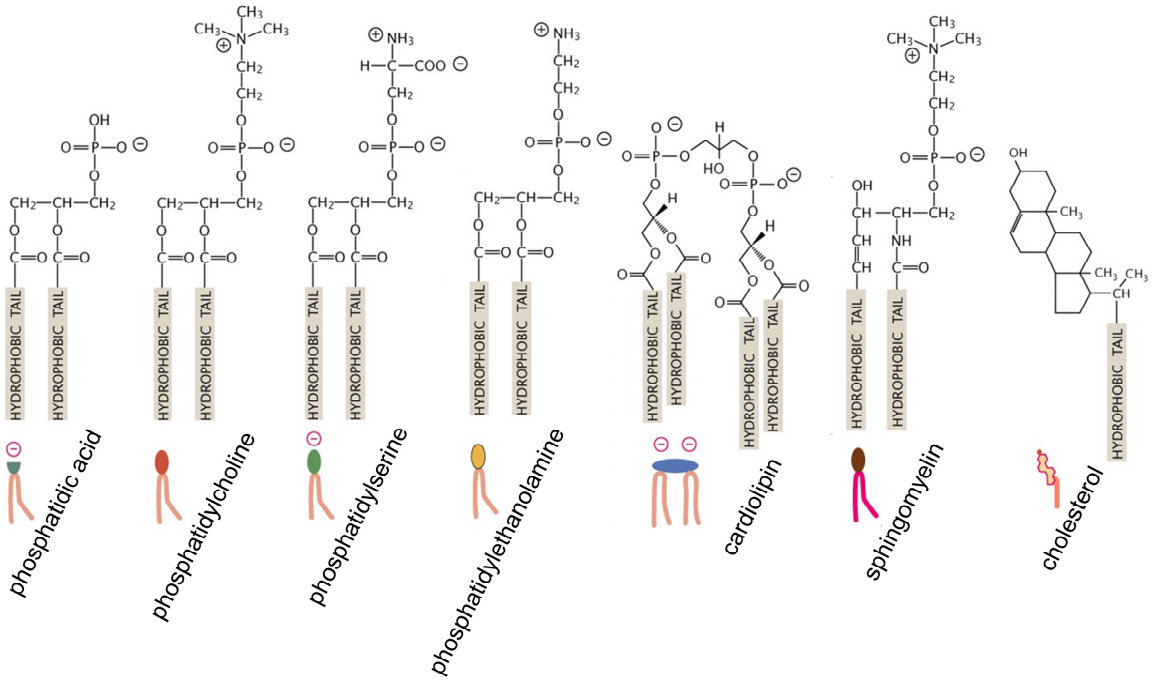

Figure 1.1. Chemical structures of some lipids commonly found in cells. Adapted from Ref. [28].

Geometrical shape of lipids

Lipids have different geometrical shapes depending on the size of the head, the number of tails, and the degree of saturation of the bonds in the tails. Most lipids found in cells, such as PA, PC, PS, and SM, have a nearly cylindrical shape. In other cases, when the cross-section of the lipid head is larger than the cross-section of the lipid tail (as in single-chain lipids like lysophospholipids), the molecule has the overall shape of an inverted cone. On the other hand, if the cross-section of the lipid head is smaller than that of the lipid tail (as in PE, CL, and cholesterol), the resulting shape is a cone. Figure 1.2 shows a schematic representation of these different kinds of geometries. Both inverted-cone and cone lipids can induce curvature on membranes.

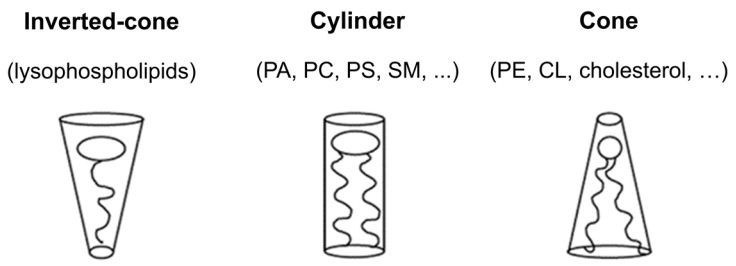

Figure 1.2. Geometrical shape of lipids.

Self-organized lipid structures

When lipids are present in aqueous dispersion at a sufficiently high concentration (approximately above 10^{-12} M [29]), they spontaneously organize into structures where the hydrophilic heads are in contact with the solvent whereas the hydrophobic tails are buried in the core of the structure.

The optimal arrangement of lipids in water results from the competition between two forces: the lipid head repulsion (which tends to separate lipids from each other, increasing the interfacial area) and the hydrophobic attraction (which tends to aggregate the lipids together, decreasing the interfacial area). Consequently, there exists an optimal interfacial area at which these opposite forces are balanced. The hydrophobic attraction is not a real force, but an effective one. It results from the so-called *hydrophobic effect*: tendency of hydrophobic molecules to aggregate in aqueous solution and exclude water molecules. This configuration reduces the entropic cost associated with the rearrangement of water molecules around hydrophobic ones [30].

In vitro studies have shown that the aqueous dispersions of lipids can form different types of assemblies. The architecture of these assemblies depends largely on the shape of individual lipid (see Figure 1.3):

- Lipids with inverted conical shapes are most easily packed in micellar (M_I), hexagonal (H_I), or cubic (C_I) phases in water.
- Conical lipids pack preferentially in inverted micellar (M_{II}), inverted hexagonal (H_{II}), or inverted cubic (C_{II}) phases in water.

The subscripts I and II represent the normal (hydrophobic core) and inverted (hydrophilic core) topologies, respectively.

- Finally, cylindrically shaped lipids (as most lipids found in biological membranes) tend to pack in lamellar (L) phases in water. In order to prevent hydrophobic tails touching water molecules, it is common for flexible lamellae to form vesicles: closed spherical structures containing water inside.

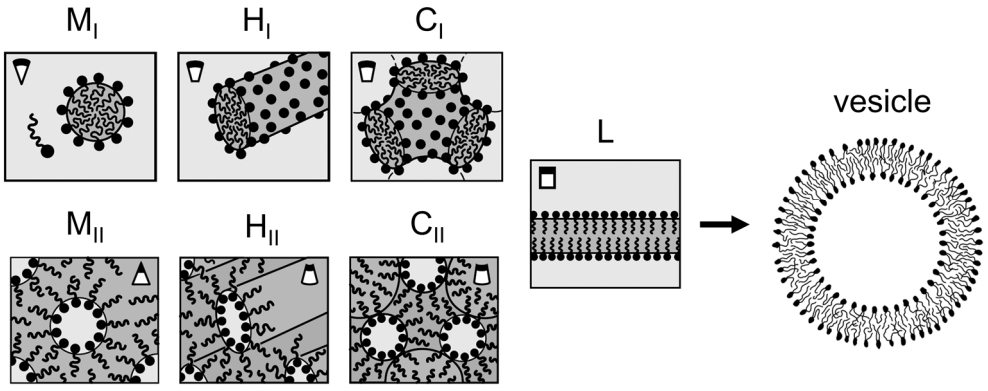

Figure 1.3. The main types of assemblies formed by lipids in aqueous solutions depending on their geometrical shape. M for micellar, H for hexagonal, C for cubic, L for lamellar, and subscripts I and II for normal and inverted (aqueous core) structures. Adapted from Ref. [30].

Within a class of lipids, environmental variables such as temperature, pH, hydration, ionic strength, and interactions with other molecules can influence the lipid assembly. The lipid assemblies shown in Figure 1.3 are then mutually related and can transform into each other driven by these environmental variables.

1.1.2 The Lipid Bilayer

Biological membranes are composed of a double monolayer of lipids called lipid bilayer. Lipid bilayers are spontaneously organized in such a way that the lipid tails are arranged parallel to each other being sandwiched by the lipid heads (see Figure 1.4). As a result, the hydrophobic tails are isolated from water by the polar heads.

A feature of the lipid bilayer is their extremely tiny aspect ratio: they are approximately 4 nm thick with a lateral extend in the order of micrometers. Therefore, it is usually represented as a two-dimensional structure. The lipid bilayer forms the barrier that separates the inside from the outside of the cell. Inside cells, the lipid heterogeneity together with the influence of membrane proteins contribute to form complex intracellular membrane-bound compartments called organelles. The precise membrane composition depends largely on the organelle. It is dynamically adjusted by endocytosis and exocytosis as well as by chemical transformations by enzyme proteins.

Underlying the lipid bilayer there is the cytoskeleton (see Figure 1.4). The cytoskeleton is a complex network of filamentous proteins which fills the space between organelles and provides the cell with structure and shape. It is present in cells of all domains of life and plays a role in a great diversity of cellular processes such as cell motility, cell protection, intracellular transport, cytokinesis, cell division, and the organization of the organelles within the cell. Eukaryotic cells contain three main kinds of cytoskeletal filaments: microfilaments, microtubules, and intermediate filaments.

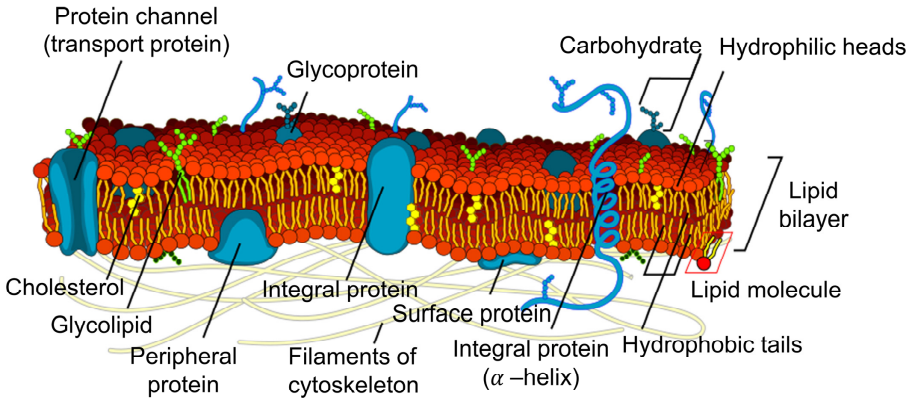

Figure 1.4. Illustration of a biological membrane.

1.1.3 Membrane Proteins

In addition to lipids, the cell membrane also contains a large number of proteins, typically around 50% of membrane composition. Proteins are made from one or more long chains of amino acids. While the lipid bilayer provides the structure for the cell membrane, membrane proteins perform multiple functions vital to the survival of organisms. These include, among

others: transport proteins, which allow particles to move across the membrane; receptor proteins, which allow communication between the cell and the extracellular environment; enzymes, which accelerate chemical reactions; and cell adhesion proteins, which allow cells to identify each other and interact. Membrane proteins divide into three main types based on how they are linked to the bilayer (see Figure 1.4): integral proteins, peripheral proteins, and lipid-bound proteins.

Integral proteins. Integral proteins are permanently attached to the membrane. They are classified as integral monotopic proteins that are attached to only one side of the membrane and transmembrane proteins that span across the membrane. As a result of their structure, transmembrane proteins are the only class of proteins that can carry out functions on both sides of the bilayer. The stretch of the integral proteins within the hydrophobic core of the bilayer is also hydrophobic, made up of nonpolar amino acids. Like the lipid bilayer, the exposed ends of the integral protein are hydrophilic. Transmembrane proteins can have different structural architectures: helix bundle proteins, which are found in all types of biological membranes, and beta barrel proteins, which are only present in some biological membranes. Examples of integral proteins include ion channels and proton pumps.

As lipids, integral proteins can contain carbohydrate monosaccharides or oligosaccharides covalently attached. These last proteins are called glycoproteins.

Peripheral proteins. Peripheral membrane proteins are temporarily attached either to the biological membranes or to integral proteins by electrostatic, hydrophobic, and other non-covalent interactions. Consequently, these proteins have only temporary interactions with the membrane, and once they reacted, the molecule dissociates to perform its function in the cytoplasm. Some enzymes and hormones are examples of peripheral proteins.

Lipid-bound proteins. Lipid-bound proteins are proteins located on the surface of the cell membrane that are covalently bounded to single or multiple lipids embedded within the cell membrane. Therefore, these proteins are not in direct contact with the membrane (e.g., the G-protein).

1.1.4 Properties of Biological Membranes

Some important properties of biological lipid bilayers are:

Asymmetry. Structurally, the lipid bilayer is asymmetrical: the lipid and protein composition in each of the two monolayers is different. The differences can arise by the different ratios or types of lipids, the different positioning of the proteins or the orientation of proteins spanning the membrane. Cell membranes also exhibit lateral heterogeneities.

Selective permeability. An important feature of the biological membranes is their selectively permeable structure. This property allows membranes to control what molecules can or cannot pass through. To do that, the cell employs several transport mechanisms. These mechanisms can be divided into passive mechanisms, like diffusion and osmosis, which do not require energy, and active mechanisms, like endocytosis and exocytosis processes, which require an input of energy to operate.

Fluidity. A further important property is that both lipids and proteins can spontaneously diffuse laterally within each of the two monolayers. Fluidity depends on both the specific structure of the fatty acid chains and temperature (fluidity increases with temperature). The unsaturated double bonds in lipid tails, which induces kinks, disrupts the packing order of the other molecules and contributes to increase the lateral fluidity. Unlike the lateral movement, lipid flipping from one monolayer of the bilayer to the other is a very slow process since it requires hydrophilic lipid heads to cross the hydrophobic region. Consequently, this process requires active mechanisms to occur.

Fluid mosaic model

The description of the biological membrane as a two-dimensional fluid matrix where lipids and embedded proteins can diffuse freely within each monolayer is known as the *fluid mosaic model* of Singer and Nicolson, proposed by them in 1972 [25]. This simple model, although widely accepted, is an oversimplification of the structural heterogeneity within the membranes. Nowadays it is well known that biological membranes contain associations of proteins and lipids assembled into microdomains, called lipid rafts. Lipid rafts are more ordered and tightly packed than the surrounding bilayer and then with lower fluidity. Moreover, in living cells, the membrane does not exist in two-dimensional world but long branched chains of carbohydrates protrude into the third dimension and structural elements such as cytoskeleton interact extensively with the membrane components.

1.2 Model Membranes

The complexity of cell membranes and the difficulty of isolating them and maintaining their native physiological conditions makes it challenging to extract meaningful data from experiments on whole cells. Therefore, it is frequent to use artificial model membranes which have greatly simplified structures and composition to make experiments more tractable. The model used depends on the purpose of the investigation and the parameters of interest like structure and functions of lipids, membrane curvature, membrane asymmetry, interactions between different species, among others.

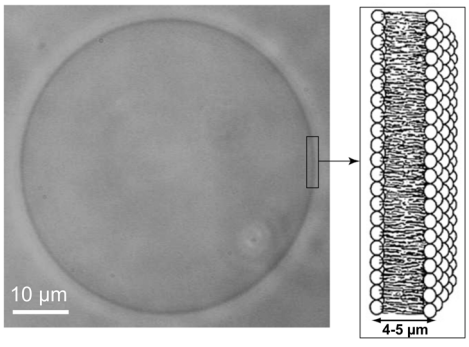

Figure 1.5. Image of a GUV observed under a phase-contrast microscope. The schematic diagram on the right represents the molecular detail of the membrane consisting in a lipid bilayer of around 4 nm thick. From Ref. [31].

In order to study the physical properties of membranes (Section 1.3) and vesicle shapes (Section 1.4), Giant Unilamellar Vesicles (GUVs) are the best system. GUVs consist of a single lipid bilayer enclosing an aqueous solution with a size similar to cell size (dozens of micrometres) (see Figure 1.5). Because of their size, GUVs are well suited for visualization under a light microscope. First

experiments on GUVs started in the 80s. Since then, the methodology has continuously improved, allowing to model highly sophisticated scenarios such as complex lipid compositions, reconstituted membrane proteins within the GUVs, a reconstituted cytoskeleton inside the GUV, or budding and fission mechanisms in order to mimic the endocytosis and exocytosis processes. See Ref. [32] for details and references of GUVs preparation methods and applications.

1.3 Physics of Membranes at Equilibrium

The first step to theoretically describe the properties of biological membranes is to have a good characterization of the simplest systems: lipid membrane vesicles without the presence of proteins, space-filling cytoskeleton, or cell wall.

1.3.1 Lipid Bilayer Mechanics: Energy of Membrane Deformation

Lipid bilayer mechanics is the study of the mechanical properties of lipid bilayers, describing their behavior as a continuous surface shell with stress and strain rather than through the detailed biochemical interactions. The first elasticity theory that describes the energy contribution of the various kinds of membrane deformation was developed in the 70s by Canham and Helfrich [33, 34]. Since the thickness of the membrane, of about 4 nm, is much smaller than its lateral extent, on the order of micrometers, the membrane can be represented approximately by a two-dimensional mathematical surface. This leads to an effective elastic model that is much simpler than its corresponding three-dimensional counterpart. A membrane is deformable in more than one way (see Figure 1.6). The primary types of membrane deformation: stretching, shearing, thickness variation, and bending are briefly described below. The volume deformation of a closed lipid bilayer is also introduced at the end of this section. Translations or rotations of a bilayer do not change its energy at all – unless there exist external position dependent fields affecting the membrane, but it is assumed that this is not the case.

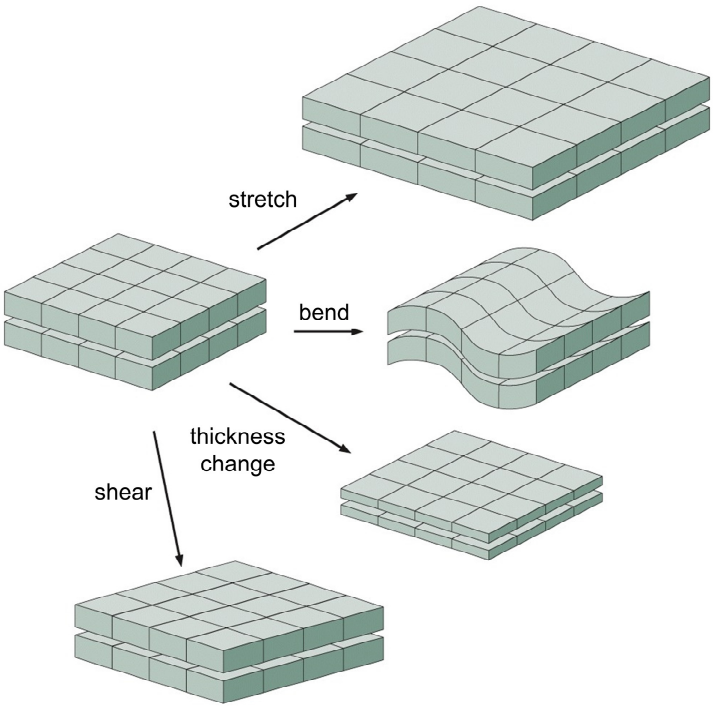

Figure 1.6. Schematic overview of the primary modes of membrane deformation. From Ref. [28].

Membrane stretching

Stretching is the deformation involving a variation in area in the membrane plane as indicated schematically in Figure 1.6. The energetic cost of stretching a membrane from its equilibrium value A_0 is [35]

$$E_s = \frac{\kappa_a}{2} \int \left(\frac{\Delta A}{A_0}\right)^2 \mathrm{d}A \tag{1.1}$$

where κ_a is the stretching modulus with the dimensions of energy per unit area and $\Delta A = A - A_0$ is the change in area. Typical values of κ_a are in the range 55-70 k_BT/nm^2 (230-290 mN/m) [36]. The rupture strain of biological membranes is only a few percent, above this value lysis by pore opening is observed [37].

Surface tension: membrane fluctuations

In general terms, membrane surface tension Σ represents the stress associated to changes in the membrane area. However, its definition is not as simple as in other systems that are under high tension. The difficulty with membranes arises in the definition of its area. Since their thickness is very small (around 4 nm), biological membranes fluctuate around their equilibrium position due to the Brownian motion of the surrounding water molecules. Thus, at a microscopic scale, the surface of a membrane is not flat, but full of spontaneous undulations [38] (see Figure 1.7).

If the applied surface tension is large enough (typically above 10^{-4} N/m) to have ironed out all the wrinkles in the membrane (enthalpic regime), Σ can be obtained as the derivative of the stretching energy E_s [Eq. (1.1)] with respect to area

$$\Sigma = \frac{\partial E_\mathrm{s}}{\partial A} = \kappa_a u \text{ (enthalpic regime)}, \tag{1.2}$$

where the dimensionless strain is $u = A/A_0 - 1$. Note that the Eq. (1.2) corresponds to the Hooke's law for membrane stretching: stress is proportional to strain, and the constant of proportionality is the stretching modulus κ_a.

However, at lower surface tensions (entropic regime), the fluctuations are not completely stretched out of the membrane. Consequently, in this regime, the macroscopic (observed) area of the membrane is smaller than the microscopic (real) area, and the relation between the observed area and the applied stress is not linear. In order to describe accurately this non-linear area elasticity, one approach has been proposed, analogous to the unfolding of a polymer in solution [39]. This approach stablishes that

$$u \approx \frac{k_BT}{8\pi\kappa_b} \ln\left(\frac{A_0\Sigma_{\text{entropic}}}{\pi^2\kappa_b}\right) \text{ (entropic regime)}, \tag{1.3}$$

where the strain, $u = A/A_0 - 1$, corresponds to the difference between the microscopic (real) and the observed area of the membrane in this regime. The parameter κ_b is the bending modulus (briefly described below), which is related with the resistance of the membrane to bending, k_B is the Boltzmann constant, and T is the temperature.

Typical values of the surface tension are on the order of 10^{-5} N/m. Increases of the area in the enthalpic regime is limited. A pure lipid membrane can only stretch by few percent before lysis.

This corresponds to membrane tension of the order of 10^{-3} N/m [37].

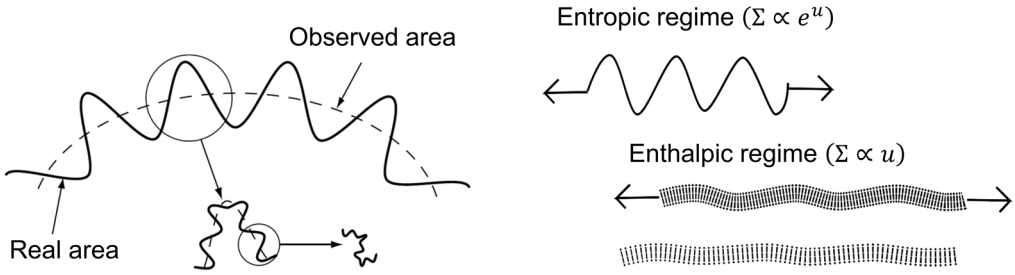

Figure. 1.7. Schematic representation of the membrane fluctuations. To stretch a membrane one has first to pay the entropic cost for unfolding it (entropic regime). When tension is large enough (typically above 10^{-4} N/m), membrane fluctuations are small, and stretching the membrane results in an overall increase of the average distance between lipids (enthalpic regime). Adapted from Ref. [40].

Membrane shearing

Shear is the stress acting in two parallel opposite directions and causing a deformation in the membrane plane without changing its area (see Figure 1.6). This deformation mode does not play an essential role for the membrane elasticity in its fluid state and usually is neglected. It only need to be considered when dealing with non-fluid membranes, like membranes in gel phase or polymerized membranes. Also, for biological membranes where there exists an interaction with the underlying cytoskeleton, an effective shear modulus arises.

Thickness variation

Another type of membrane deformation results from changing the bilayer thickness (see Figure 1.6). The thickness of the membrane in the vicinity of a protein varies continuously, adopting its equilibrium value only sufficiently far from the protein. When the influence of proteins is not considered, this contribution to the total energy can be omitted.

Membrane bending: Canham-Helfrich hamiltonian

Bending is the term which describes the membrane deformations caused by curvature (see Figure 1.6). The corresponding bending energy can be written in terms of the curvature as [35]

$$E_b = \frac{\kappa_b}{2}\int (C_1 + C_2 - C_0)^2 \mathrm{d}A + \kappa_G \int C_1 C_2 \mathrm{d}A\,, \tag{1.4a}$$

a model known as Helfrich-Canham Hamiltonian. The parameters κ_b and κ_G are the bending modulus and Gaussian modulus, respectively; $C_1 = 1/R_1$ and $C_2 = 1/R_2$ are the principal curvatures describing the shape of the membrane at a given point (see Section 1.3.2 for a brief explanation of surface curvature) and C_0 is the spontaneous curvature of the membrane (described below). Equation (1.4a) can be equivalently written in terms of the mean curvature $H = (C_1 + C_2)/2$ (which gives the mean energy contribution E_m) and the Gaussian curvature $K = C_1 C_2$ (which gives the Gaussian energy contribution E_G), as

$$E_b = E_m + E_G = \frac{\kappa_b}{2}\int (2H - C_0)^2 \mathrm{d}A + \kappa_G \int K \mathrm{d}A\,. \tag{1.4b}$$

For a spherical membrane of radius R_0, the principal curvatures are $C_1 = C_2 = 1/R_0$, and the bending energies are $E_m^{(\mathrm{sph})} = 8\pi\kappa_b(1 - R_0C_0/2)^2$ and $E_G^{(\mathrm{sph})} = 4\pi\kappa_G$.

Spontaneous curvature

The parameter C_0 in Eq. (1.4) is the spontaneous curvature of the membrane and represents the spontaneous tendency of the membrane to build up in a concave (as $C_0 < 0$), convex (as $C_0 > 0$), or flat (as $C_0 = 0$) configuration. It permits to describe bilayers that are spontaneously curved in their equilibrium state due to asymmetry factors in the membrane (e.g. due to different chemical environment on both sides of the membrane or different composition of the two monolayers). The spontaneous curvature of the bilayer depends on the spontaneous curvature of their monolayers, which is mainly determined by the geometrical shape of the constituting lipids (see Figure 1.8).

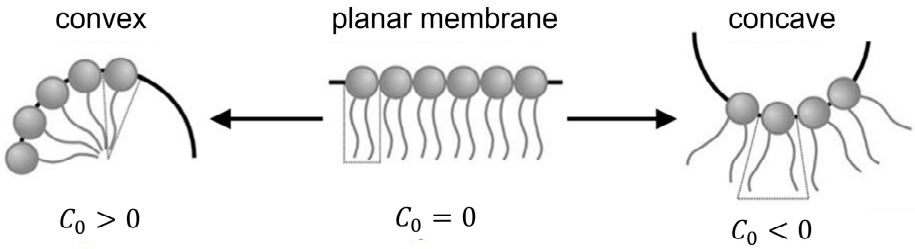

Figure 1.8. The spontaneous curvature of a monolayer is mainly determined by the geometrical shape of the constituting lipids. Cylindrical lipids form planar membranes with a zero spontaneous curvature. In contrast, cone and inverted-cone lipids tend to form curved membranes with, respectively, concave ($C_0 < 0$) and convex ($C_0 > 0$) surfaces.

Bending and Gaussian moduli

The bending modulus κ_b is a constant which quantifies the extend to how much the bending energy is affected from a deviation from the spontaneous curvature and can be thought of as the rigidity of the membrane. In lipid membranes, κ_b ranges typically between 10 and 20 k_BT [41]. The bending modulus κ_b and the stretching modulus κ_a are related through the geometrical properties of the membrane. Thin material mechanics predicts that κ_b should scale as

$$\kappa_b = \kappa_a h^2/\alpha\,, \tag{1.5}$$

where h is the membrane thickness (around 4-5 nm) and α is a normalization constant. This constant is expected to be equal to 12 for a single membrane monolayer, to 24 for a bilayer and to 48 for a bilayer with uncoupled monolayers (free to slide past each other) [35]. This relation derives from the fact that to bend the membrane the inner monolayer must be compressed and the outer monolayer must be stretched. It can indeed be found in the literature quite often, and it is sometimes even used to determine the bending modulus by way of measuring κ_a.

Unlike κ_b, the sign of the Gaussian modulus κ_G is not necessarily positive. In fact, for some kinds or artificial membranes, it is negative and of the order of the bending modulus. Membranes with different signs of κ_G prefer different membranes shapes. A positive κ_G indicates that the Gaussian energy contribution (second term of Eq. (1.4)) minimizes when the principal curvatures have different sign and then, the membrane is most likely to adopt the shape of a saddle point. If κ_G is negative, the Gaussian energy contribution minimizes for surfaces whose

principal curvatures have the same sign, preferring tightly wrapped morphologies such as vesicles. Unfortunately, because the Gaussian energy contribution E_G is topologically invariant (see below), it is difficult to measure the sign and the magnitude of its modulus κ_G in real membranes.

Gauss-Bonnet theorem

The Gauss-Bonnet theorem shows that the integral over the Gaussian curvature, the second term in Eq. (1.4), has the same value for topologically equivalent surfaces (*i.e.,* surfaces which can be related through deformations that do not involve creations of new holes). Indeed, for a closed surface, this theorem establishes that

$$E_G = \kappa_G \int K \mathrm{d}A = 4\pi\kappa_G(1-g), \tag{1.6}$$

where g is a topology concept indicating the surface's genus. In simpler terms, the value of a surface's genus is equal to the number of holes the surface has. Some examples of surfaces with different genus are shown in Figure 1.9.

According to this theorem, for a closed surface (like a vesicle or a cell) no matter what deformations the membrane suffers, the contribution from Gaussian curvature remains fixed and then can be ignored. It is only when the surface changes its topology (like going from a sphere to a donut) when the Gaussian term comes into play. The contribution of the Gaussian curvature might be a significant part of the total energy in complicated morphologies of the endoplasmic reticulum and mitochondria since holes, tubes, and tori are often created and destroyed in these organelles.

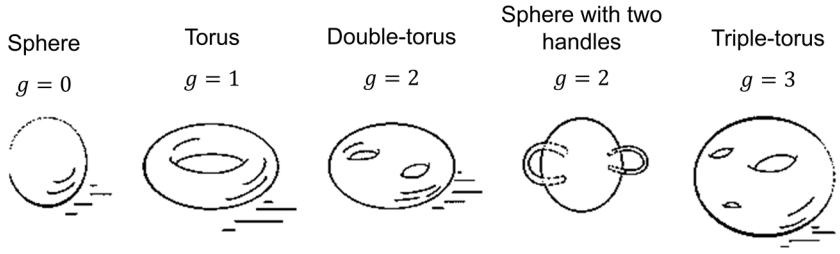

Figure 1.9. Surfaces with different genus g. Adapted from Ref. [42].

Volume deformations induced by pressure differences

In order to prevent hydrophobic tails touching water, it is common for flexible bilayers to spontaneously form vesicles: closed structures containing water inside. For a closed lipid bilayer, $\Delta p \int \mathrm{d}V$ describes the energy contribution associates to volume deformations induced by pressure differences between the membrane's out and inner ($\Delta p = p_{\mathrm{out}} - p_{\mathrm{in}}$; $\Delta p < 0$ for an inflated vesicle).

The semipermeable nature of the bilayer allows water but does not allow ions to diffuse through it. If extracellular solution has different concentration of ions from the interior of cells, a resulting flow of water emerges in an attempt to equilibrate the difference in concentrations. When cells are placed in a hypertonic medium ($\Delta p < 0$), water flows out of the cell, decreasing its volume. In contrast, when cells are placed in a hypotonic solution ($\Delta p > 0$), water rushes into

the membrane increasing its volume. This phenomenon can cause the cells to shrink or to swell and even burst. Typical values for osmotic pressures are on the order of 0.01 Pa.

1.3.2 Mathematics of Curvature

Let us consider a point Q on a surface representing the cell membrane as shown in Figure 1.10. The tangent plane to the surface at Q is defined as the plane that contains all the tangent vectors of curves on the surface that pass through the point. Now, let us consider a normal plane P to the tangent plane at the point Q. The intersection between the surface and this plane P is known as the normal curvature of the surface at Q, which can be a straight line or have a certain curvature C.

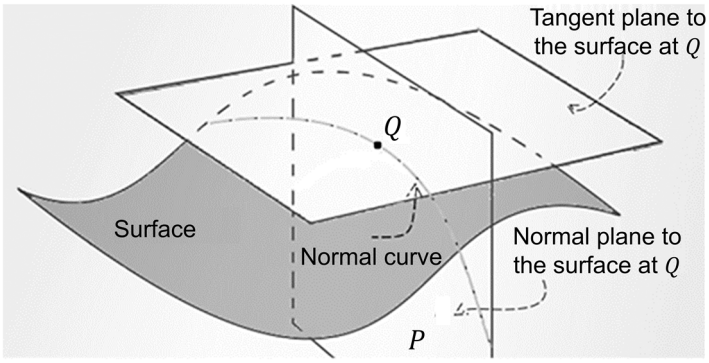

Figure 1.10. Illustration of the normal curve of a surface at Q. Adapted from Ref. [42].

In order to give a value to the normal curvature, note that a straight line (by definition with zero curvature) can be seen as a circumference with an infinite radius. This suggests that the curvature can be defined as the inverse of the curvature radius ($C \equiv 1/R$). This curvature is assigned a sign which allows us to distinguish the two possible orientations of the curve: a positive curvature ($C > 0$) describes a convex curve, and conversely, a negative curvature ($C < 0$) describes a concave curve. The case of zero curvature ($C = 0$) represents a straight line (see Figure 1.11).

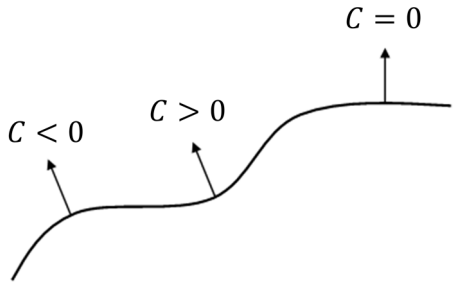

Figure 1.11. Positive curvature ($C > 0$) describes a convex curve, negative curvature ($C < 0$) describes a concave curve, and zero curvature ($C = 0$) describes a straight line.

As we defined the plane P simply as a perpendicular plane to the tangent plane at the point Q, there is an infinite number of possible orientations for P. Depending on the orientation, the different possible normal curves have different curvatures. It can be mathematically proven that, for each point of a surface, there are two characteristic directions, perpendicular with each other, for which the normal curvature is an extreme (maximum in one case and minimum in the other). These directions are called principal directions, and the corresponding curvatures are called

principal curvatures (usually denoted as C_1 and C_2). All other normal curvatures at the same point can be expressed in terms of these two principal curvatures [35].

Mathematically, it is more appropriate to change the variables C_1 and C_2 for two combinations of them, the so-called mean curvature $H = (C_1 + C_2)/2$ and Gaussian curvature $K = C_1C_2$. In general, H and K vary from point to point of a surface (according to the variations of C_1 and C_2), however, there are special surfaces for which their principal curvatures are constant (see Figure 1.12).

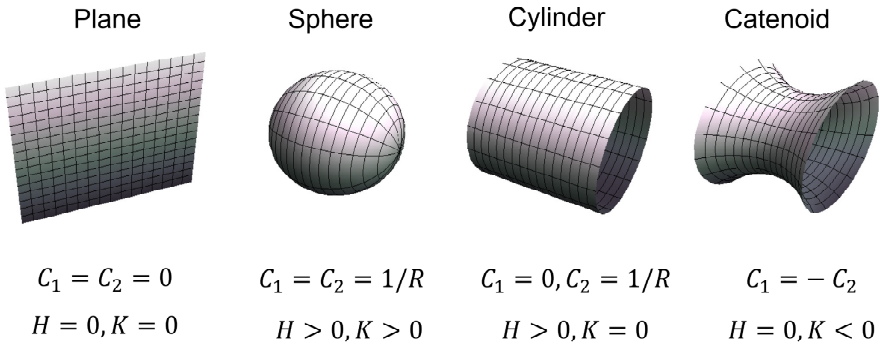

Figure 1.12. Some surfaces with constant principal curvatures.

Monge parameterization is the most straightforward one to describe a membrane surface: the position $\vec{r}$ on a surface has Cartesian coordinates and is defined by giving its height h over some $x - y$ plane (see Figure 1.13)

$$\vec{r} = \big(x, y, h(x,y)\big). \tag{1.7}$$

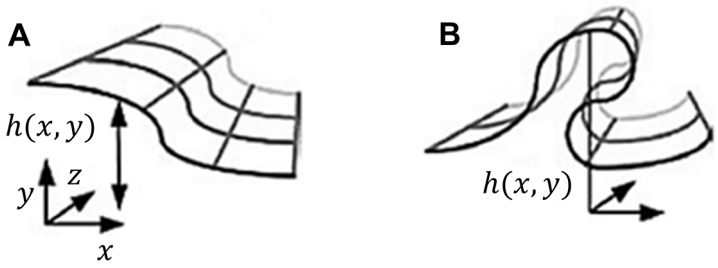

Figure 1.13. Illustration of the Monge parameterization. (A) A surface can be defined by a function $h(x,y)$ of a set of external Cartesian coordinates x, y. (B) The function $h(x,y)$ is constrained to be single-valued; but, in general, there exist overhangs. Adapted from Ref. [35].

One disadvantage of the Monge parameterization is that it is unable to describe overhangs (see Figure 1.13B), *i.e.*, $h(x,y)$ is constrained to be single-valued. The two tangent vectors to $\vec{r}$, $\overrightarrow{e_x}$ and $\overrightarrow{e_y}$, are given by

$$\overrightarrow{e_x} = \frac{\partial \vec{r}}{\partial x} = (1, 0, h_x), \qquad \overrightarrow{e_y} = \frac{\partial \vec{r}}{\partial y} = \big(0, 1, h_y\big), \tag{1.8}$$

where $h_x = \partial h/\partial x$. Note that even though the coordinates in the reference plane are orthogonal, the vectors $\overrightarrow{e_x}$ and $\overrightarrow{e_y}$ are not unit vectors, and are not generally orthogonal. However, they define the plane tangent to the surface at point $\big(x, y, h(x,y)\big)$, and can generate the unit normal vector $\vec{n}$ to the surface via the cross product

$$\vec{n} = \frac{\overrightarrow{e_x} \times \overrightarrow{e_y}}{\left|\overrightarrow{e_x} \times \overrightarrow{e_y}\right|} = \frac{1}{\sqrt{1 + h_x^2 + h_y^2}}\left(-h_x, -h_y, 1\right). \tag{1.9}$$

A segment of length dx along the x-axis corresponds to a vector $\overrightarrow{e_x}$dx along the surface. The cross product of the vectors $\overrightarrow{e_x}$dx and $\overrightarrow{e_y}$dy gives the area element dA on the surface corresponding to dxdy in the coordinate plane:

$$\mathrm{d}A = \left|\overrightarrow{e_x} \times \overrightarrow{e_y}\right|\mathrm{d}x\mathrm{d}y = \sqrt{1 + h_x^2 + h_y^2}\mathrm{d}x\mathrm{d}y. \tag{1.10}$$

The element of volume enclosed by the surface is

$$\mathrm{d}V = h\mathrm{d}x\mathrm{d}y. \tag{1.11}$$

After considering mathematical aspects of differential geometry, it can be shown that the mean curvature $H = (C_1 + C_2)/2$ and Gaussian curvature $K = C_1C_2$ are given in terms of the height functions by [35]

$$H = \frac{C_1 + C_2}{2} = \frac{(1 + h_x^2)h_{yy} + \left(1 + h_y^2\right)h_{xx} - 2h_xh_yh_{xy}}{2\left(1 + h_x^2 + h_y^2\right)^{3/2}}, \tag{1.12}$$

$$K = C_1C_2 = \frac{h_{xx}h_{yy} - h_{xy}^2}{\left(1 + h_x^2 + h_y^2\right)^2}. \tag{1.13}$$

Surfaces of revolution

For the particular case of axisymmetric shapes with the axis of symmetry along the x–axis

$$h(x, y) = \pm\sqrt{R^2(x) - y^2}, \tag{1.14}$$

where $R(x)$ is the functional form describing the membrane profile in the $x - z$ plane (see Figure 1.14). The signs + and – parameterize, respectively, the upper half Ω_+ and the lower half Ω_- of the surface. Using the parameterizations for Ω_+ the mean curvature [Eq. (1.12)] becomes

$$H = \frac{C_1 + C_2}{2} = \frac{1 + R_x^2 - R_{xx}R}{2(1 + R_x^2)^{3/2}R}, \tag{1.15}$$

where $R_x = \partial R/\partial x$ and $R_{xx} = \partial R_x/\partial x$ are, respectively, the first and second derivatives of the membrane profile $R(x)$. The elements of area [Eq. (1.10)] and volume [Eq. (1.11)] are

$$\mathrm{d}A = R\sqrt{\frac{1+R_x^2}{R^2-y^2}}\mathrm{d}x\mathrm{d}y, \quad \mathrm{d}V = \sqrt{R^2(x) - y^2}\mathrm{d}x\mathrm{d}y. \tag{1.16}$$

If the surface is between x_i and x_f , its total area will be

$$A = 2\int_{\Omega_+}\mathrm{d}A = 2\int_{x_i}^{x_f} R\sqrt{1 + R_x^2}\int_{-R(x)}^{R(x)}\frac{1}{\sqrt{R^2 - y^2}}\mathrm{d}y\mathrm{d}x = 2\pi\int_{x_i}^{x_f} R\sqrt{1 + R_x^2}\,\mathrm{d}x, \tag{1.17}$$

where the factor 2 outside the integral comes for the symmetry between $\Omega_+$and Ω_-, and we have integrated the y variable. The total volume enclosed by the surface can be obtained as

$$V = 2\int_{\Omega_+} \mathrm{d}V = 2\int_{\Omega_+} \sqrt{R^2(x) - y^2}\,\mathrm{d}y\mathrm{d}x = \pi\int_{x_i}^{x_f} R^2\,\mathrm{d}x. \tag{1.18}$$

Finally, the mean energy E_m of Eq. (2.4) for a surface of revolution is given by

$$\begin{aligned} E_m &= \kappa_b \int_{x_i}^{x_f} \frac{\left[1 + R_x^2 - R_{xx}R - RC_0(1+R_x^2)^{3/2}\right]^2}{(1+R_x^2)^{5/2}R} \int_{-R(x)}^{R(x)} \frac{1}{\sqrt{R^2 - y^2}}\mathrm{d}y\mathrm{d}x \\ &= \pi\kappa_b \int_{x_i}^{x_f} \frac{\left[1 + R_x^2 - R_{xx}R - RC_0(1+R_x^2)^{3/2}\right]^2}{(1+R_x^2)^{5/2}R}\mathrm{d}x. \end{aligned} \tag{1.19}$$

Note that the results of Eqs. (1.17)–(1.19) are independent of the coordinate y, as expected for surfaces with rotational symmetry around x.

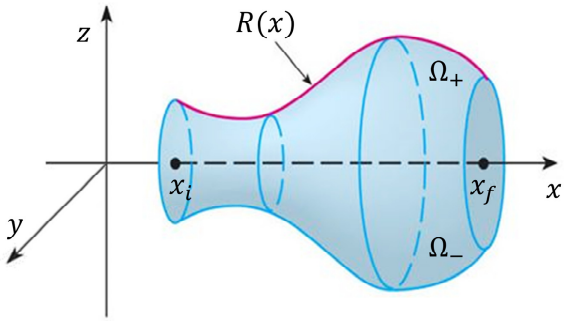

Figure 1.14. Surface of revolution with rotational symmetry around x–axis.

1.3.3 Measuring Mechanical Properties

Many techniques have been designed to measure the mechanical properties introduced in Section 1.3.1. A detailed description of them is out of the scope of this manuscript. We will just briefly present here the most relevant techniques related to the experiments presented in Chapters 2 and 6 of this thesis.

Micropipette aspiration

The micropipette aspiration technique consists in monitoring the evolution of the membrane area of a vesicle as a function of the applied tension. The key features of this experiment are shown in Figure 1.15A: a vesicle is aspirated in a small micropipette, which allows to control membrane tension by varying the aspiration pressure. The surface tension applied to the vesicle is given in terms of the pressure difference between the surrounding medium and the micropipette Δp and the geometrical parameters R_1 (radius of the hemispherical cap of the aspirated membrane) and R_v (radius of the vesicle) as

$$\Sigma = \frac{\Delta p}{2}\frac{R_1}{1 - R_1/R_v}. \tag{1.20}$$

This equation can be easily deduced by applying the Young-Laplace equation at both interfaces between the inside and the outside of the vesicle. By thinking of the deformed vesicle as a large sphere with a small cylinder ending in a hemispherical cap attached to it (pipette), it is also possible to measure the macroscopic change in the membrane area $\Delta A = A - A_0$ as

$$\Delta A = 2\pi R_1 l + 2\pi R_1^2, \tag{1.21}$$

where l is the length of the aspirated vesicle and the reference area is $A_0 = 4\pi R_v^2$. Note that it is assumed that the vesicle radius remains unchanged during the whole experiment. This expression allows for obtaining the area strain $u = \Delta A/A_0$.

By combining Eqs. (1.20) and (1.21) it is possible to distinguish if $\Sigma \propto \kappa_b \, e^{\kappa_b u}$ [Eq. (1.3)] (entropic regime) or if $\Sigma = \kappa_a u$ [Eq. (1.2)] (enthalpic regime) and determine the mechanical moduli κ_a and κ_b as well as the lysis tension of many types of lipid membranes.

Membrane pulling

Another way to characterize membrane mechanical properties consists in measuring the force necessary to extract a membrane tube by applying force on it, as is represented in Figure 1.15B. The energy of the membrane in the tube is deduced from the Helfrich's Hamiltonian [Eq. (1.4)]

$$E_{\text{tube}} = \frac{\pi \kappa_b L}{r} + 2\pi r L \Sigma - fL, \tag{1.22}$$

where r and L are, respectively, the tube radius and the tube length and f is the force necessary to hold the tube. This energy reflects the competition between the bending energy (first term), that tends to increase the tube radius r (decrease the tube curvature $C = 1/r$), and the surface tension Σ (second term) that tends to minimize the area of the deformation favouring small tubes. Note that this expression is neglecting the contribution of the spontaneous curvature. Minimizing this energy with respect to the tube radius and the tube length it is obtained that the equilibrium radius r_0 and the force necessary to maintain the tube f_0 are

$$r_0 = \sqrt{\frac{\kappa_b}{2\Sigma}}, \quad f_0 = 2\pi\sqrt{2\kappa_b \Sigma}, \tag{1.23}$$

The tube radius can hence be controlled by adjusting the tension using the micropipette aspiration technique presented above and then the measure of the force can be used to determine κ_b. Pulling tubes from a GUV aspirated in a micropipette was used to obtain the experimental data shown in Part III of this thesis (for more details about the experimental system see Chapter 2).

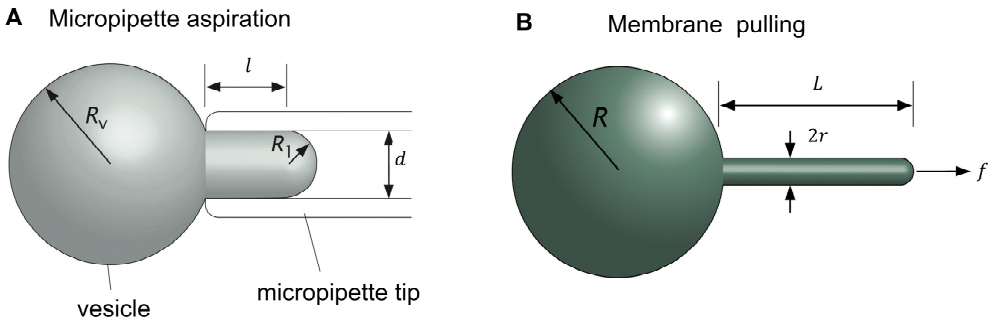

Figure 1.15. Techniques to measure the mechanical properties of membranes. Experimental configurations of the micropipette aspiration (A) and membrane pulling (B) techniques. Adapted from Ref. [28].

1.3.4 Different States of Lipid Bilayers

As any physical system, lipid bilayers exhibit different phases depending on physical parameters such as temperature. At zero to low temperatures, lipid bilayers are in crystalline-solid or gel

phases where the hydrocarbon chains are ordered and with low degree of lateral mobility. Liquid phase appears upon melting of crystalline and gel phases. In the liquid phase, lipids are totally disordered and the bilayer is fluid, which closely resemble the state of biological membranes (see Figure 1.16A).

The temperature at which the transition from the gel to the liquid state occurs is the melting temperature T_m. This temperature depends on external (hydration, pH, ionic strength) and internal (degree and position of unsaturations, type of lipid heads, and length of the lipid tails) parameters and varies from -60 to 80 °C.

It has been observed that the addition of cholesterol affects drastically membrane properties. It tends to disrupt the lateral order of the gel phase and to order the liquid phase, giving rise to an intermediate liquid-ordered phase. This phase has attracted much attention in recent years because of its relevance to mimic the lipid rafts, which are enriched in cholesterol in eukaryotic membranes.

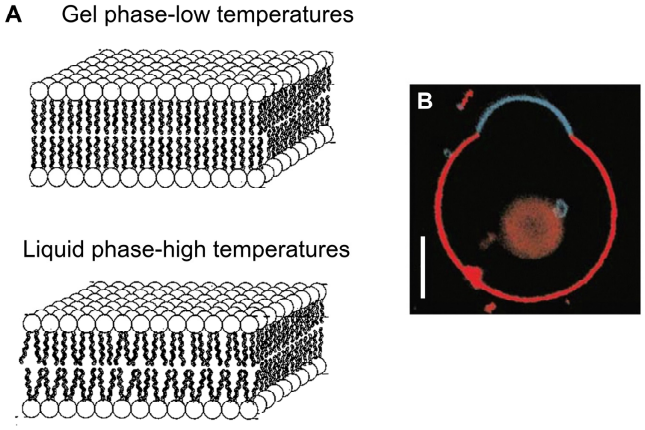

Figure 1.16. Different states of lipid bilayers. (A) Gel and liquid phases in lipid bilayers. (B) GUV displaying liquid disordered (red fluorescent dye) and liquid ordered (blue fluorescent dye) phase separation. Scale bar is 5 μm. From Ref. [43].

Phase coexistence

When two or more lipids with different molecular shapes or different melting temperatures T_m coexist in a single structure, they tend to spontaneously segregate into separate domains (see Figure 1.16B). The edges of these domains are characterized by an edge or line tension. Since the length of the domain boundary decreases if the domain buds, the competition between this edge tension and the bending energy determine the optimal shape of the structure. These effects can lead to domain budding and even to membrane fission. Lipid segregation is opposed, however, by loss of mixing energy. The structure of multicomponent systems depends mainly upon the external variables, especially the temperature, and the relative concentrations of their components. Usually, the bilayer exhibits a homogeneous one-phase region at high temperature (when entropy dominates) and a phase coexistence region at lower temperatures for a certain range of compositions.

1.4 Lipid Sorting

Lipids are not homogeneously distributed throughout the main organelles of the cell. For example, in mammalian cells, the ratio of cholesterol to total phospholipid is approximately 0.15

in the endoplasmic reticulum, 0.2 in the Golgi apparatus and 1 in the plasma membrane. Another example is that sphingomyelin is not found in the endoplasmic reticulum but it is largely present in plasma membrane [44]. It is also worth noticing that lipids are often not synthesized in the organelle they are most present. However, there exists a constant material exchange between cell organelles via intracellular trafficking which should produce, in principle, a homogeneous lipid distribution [45].

The implication of the above observations is that the cell maintains the steady state composition of each organelle (membrane homeostasis) thanks to or despite membrane trafficking. Years ago, it was proposed that lipid sorting occurs when a trafficking vesicle is formed and there are now evidences in the literature showing that the cell is actually able to sort lipids during intracellular trafficking [6, 7]. To transport material from one organelle to another, a vesicle buds out of the donor compartment and is transported in the cytoplasm along cytoskeleton filaments to its target compartment where it releases its content after fusion. Depending on the final destination, some components (lipid or proteins) are enriched in the transport intermediate and some remain in the donor compartment. This is a good explanation from the maintenance of membrane homeostasis in the cell, but the mechanisms required to account for lipid sorting are still not fully understood. Unlike proteins, that can be recognized and targeted thanks to peptidic sequences, lipids do not contain such recognized targeting motifs [46]. Consequently, alternative mechanisms have to be proposed for their targeting and localization. We describe here two possible mechanisms for lipid sorting: based on lipid rafts and based on an interplay between lipid composition and membrane curvature.

Raft-based lipid sorting

According to this mechanism, the trafficking vesicles could be formed from preexisting lipid domains. If a donor membrane is laterally segregated in different domains, transport intermediates budding from these domains will have different composition and will go to different destinations (see Figure 1.17).

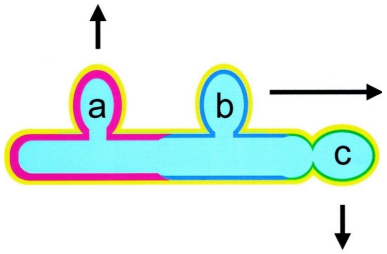

Figure 1.17. Raft-based lipid sorting. Lateral segregation of lipids into microdomains could explain how different lipids could be sorted to different destinations. From Ref. [47].

Curvature-based lipid sorting

This mechanism suggests that membrane curvature might play an important role in the regulation of intracellular processes. Indeed, transport intermediates are highly curved structures (typical radii of 50 nm) compared to the donor membrane. It has been proposed that this difference in curvature could induce a difference in lipid composition between the curved and the flat regions of the membrane. Because the bending energy depends on the membrane properties, such as spontaneous curvature and bending rigidity, and because these properties depend on membrane composition, a coupling between lipid composition and curvature might

minimize the bending energy by reducing the curvature frustration. Unlike the raft based sorting, this mechanism does not require domain formation. One can estimate the energy involved in curvature based lipid sorting by considering the physical properties of the different membrane structures in cells. In its simplest form, the bending energy per unit area of a membrane is given by [Eq. (1.4)] $E_b = \kappa_b/2(C - C_0)^2$, where $C = C_1 + C_2$ is the total curvature of the membrane, C_0 is the spontaneous curvature of the membrane, and κ_b is the bending modulus. Thus, two membrane reorganization mechanisms could lead to a decrease of the energy of the curved membrane (see Figure 1.18):

1. Based on the spontaneous curvature C_0: lipids can reorganize to have the outer monolayer enriched in cylindrical and inverted conical lipids whereas the inner monolayer enriched in conical ones. This creates an asymmetry between the two monolayers and causes a local change of membrane spontaneous curvature. This local spontaneous curvature is closer to the local membrane curvature which implies a reduction of the bending energy.

2. Based on the bending modulus κ_b: lipids softening the membrane should be enriched in the curved part which leads to a local decrease in bending rigidity.

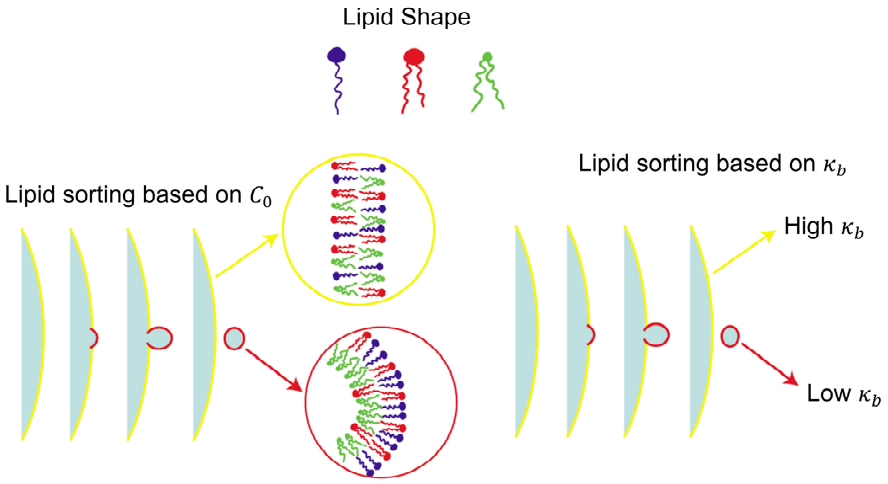

Figure 1.18. Curvature-based lipid sorting. Schematic representation of lipid sorting based on a local change of spontaneous curvature (left) or a local change of bending rigidity (right). Adapted from Ref. [48].

Both effects indicated above can also contribute simultaneously. However, both experiments [9, 49, 50] and theory [51] have shown that these effects are not effective driving mechanisms in lipids. In general, lipid sorting due to bending minimization is a very weak effect and mixing entropy tends to disperse any concentration heterogeneity by homogenizing the lipid distribution. The importance of entropy can be highlighted by a simple order of magnitude calculation as described in Ref. [48]. In the extreme case of a difference of bending moduli between the soft and the stiff phase of $\Delta\kappa_b = 40k_BT$, a tube radius of 20 nm (tube curvature of C =1/20 nm^{-1}) and a lipid area of $A = 0.5$ nm^2, the gain in mechanical energy upon lipid sorting would be

$$\Delta E_b = \frac{1}{2}\Delta\kappa_b C^2 A = \frac{k_BT}{40} \ll k_BT. \tag{1.24}$$

Therefore, the energetic gain of curvature for a single lipid at physiological curvatures is on the order of 1% k_BT, which implies that curvature preference alone is insufficient for significant lipid sorting at the cellular scale. In other words, entropy is expected to be dominant due to the small size of lipids. Conversely, for bigger objects like proteins (a membrane protein area is typically 10 times larger than the area of a lipid head), sorting by curvature becomes significant [52–55].

The above calculation is valid, however, only if we consider the membrane to be an ideal solution of lipids. Membranes consisting of a mixture of lipids are characterized not only by elastic bending but also by the short-range interactions among the different lipid species. Below the melting (miscibility) temperature, these interactions can give rise to large-scale domains (see Figure 1.16). Moreover, interactions with a protein enriched in curved membranes can also enhance lipid sorting [56, 57].

Previous works of Bassereau's group investigated the curvature-based lipid sorting mechanism using an *in vitro* approach that consists in pulling tubes from a GUV aspirated in a micropipette (see Section 1.3.3). This technique allows for reproducing the geometry adopted by the membrane when sorting is supposed to take place during transport intermediate formation: a highly curved part of the membrane is connected to a flat membrane reservoir. On the basis of their work [9, 48], they noticed that it is very unlikely that individual lipids, unassisted by interactions with themselves or with proteins, can be enriched in curved regions simply based on their shape alone. Instead, lipid-lipid interactions or lipid-protein-interactions appear to be essential in making the membrane susceptible to curvature-induced lipid sorting. Indeed, they observed that lipid sorting only occurs if the system is close to a phase-separated point, when lipid-lipid interactions become dominant, and this process is amplified when lipids are clustered upon proteins. Since there is strong evidence that the plasma membrane is close to phase separation [10] the mechanism of lipid sorting induced by curvature is thought to be physiologically relevant.

Coupling between membrane curvature and cardiolipin content

Cardiolipin (CL) is a negatively charged lipid found predominantly in the inner mitochondrial membrane of eukaryotic cells [15] and in the plasma membranes of certain bacteria [58]. In eukaryotes such as yeasts, plants and animals, the CL synthesis processes are believed to happen in mitochondria [59], while in prokaryotic cells (which do not have mitochondria) the synthesis occurs in the cytoplasm. CL is composed of two phosphatidic acids linked together by a short glycerol bridge resulting in a conical shape with a small polar head relative to the four acyl chains (see Figure 1.19A). As expected from the molecular dimensions of CL, the absolute value of its intrinsic curvature should be of the order of 1 nm^{-1} [12] (much higher than that of typical phospholipids), making this lipid prone to localize in highly curved regions of the membrane. Indeed, CL-enriched domains have been observed in the cellular poles and the division site of bacteria [12–14, 60, 61] as well as in mitochondrial *cristae*, tubular-like invaginations of the mitochondrial inner membrane (see Figure 1.19B). Presumably, the cone shape of the CL molecule is a determinant geometric factor which, together other possible molecular traits related to energetic interactions, contribute to the structural stability of these highly curved sites in the lipid membranes. The observed localization has been then argued to be geometry-driven as CL's conical shape matches the curved regions of those membrane regions thus relaxing the curvature frustration of these sites [16]. Despite the biological significance of these stabilization

factors, they have not been so far quantitatively determined in experimental realizations containing CL specifically localized in the membrane site of high curvature. There is quite a few evidence in the literature suggesting a coupling between CL content and membrane shape [16–19], especially in the presence of protons [62–69], but no precise experimental data are available for curvature-based CL sorting *in vitro*. Among these studies, worth noting are the molecular dynamic simulations developed recently by Boyd and colleagues [16]. They show that CL accumulates at high curvature regions of the membrane, while PE, another cone-shaped lipid with only two acyl chains, presents much a weaker propensity to localize in these curved regions (see Figure 1.19C). As pointed by that work, CL appears to possess some unique characteristics that give its special affinity for curved regions of membranes but they cannot be inferred simply from molecular geometry considerations.

One of the objectives of this thesis is to explore the curvature-based CL sorting *in vitro* in experiments that isolate the effects of membrane curvature by pulling membrane nanotubes out of GUVs containing CL. This procedure combines micropipette aspiration and membrane pulling (both techniques were briefly introduced in Section 1.3.2). In particular, we used the experimental set-up in P. Bassereau's lab (Paris, France). These original results can be found in Part III of this thesis.

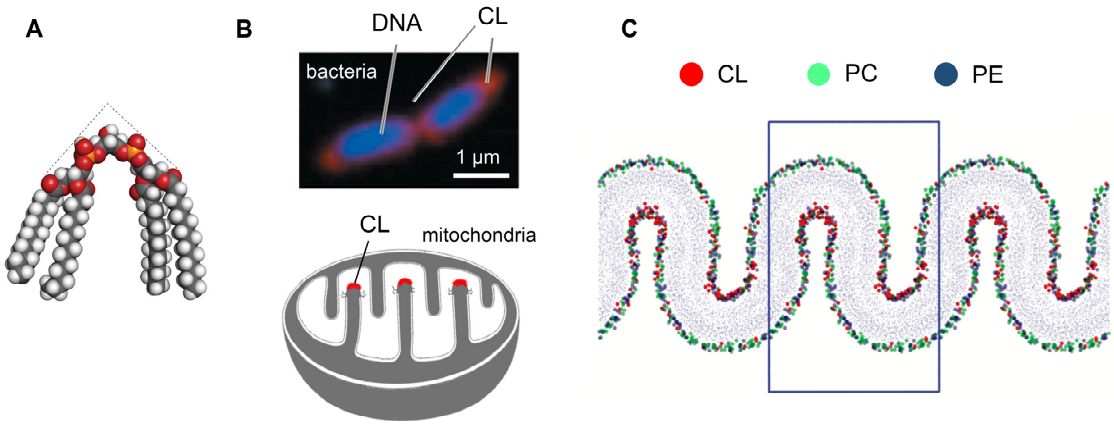

Figure 1.19. Coupling between membrane curvature and cardiolipin content. (A) CL molecule. (B) CL localizes at the cell poles and division sites in bacteria (from Ref. [70]) as well as in folds of the inner mitochondrial membrane. (C) Result of the simulation performed by Boyd et al. 2017 in Ref. [16] showing the CL accumulation (red beads) at highly curved regions of the membrane.

1.5 Vesicle Shapes

One of the first applications of the physical models of membranes is to predict vesicle shapes. The observation of vesicles by optical microscopy showed that they can adopt various shapes (sphere, oblate, prolate, stomatocyte, pearlike, etc...) which can be transformed into one another by changing the osmotic conditions, the lipid composition, or the temperature.

In equilibrium, vesicles acquire the shape at which their total energy is minimal. In modelling such energy, one must be taken into account that vesicles are in general subject to two geometrical constraints:

a) Constant area: biological membranes are hardly stretched from the equilibrium area (the energy scale associated with a macroscopic stretching of the bilayer is several orders of magnitude higher than that involved in bilayer bending). Thus, they can be considered

essentially inextensible/incompressible with a close to zero surface tension. In addition, lipids are practically insoluble in the aqueous medium, which implies no relevant exchange of lipids between the vesicle membrane and the surrounding media. Therefore, in the absence of high enough thermal fluctuations, these two facts provide us a constraint for the surface area of the vesicle, which remains fixed.

b) Constant volume: biological membranes are permeable to water, but not to large molecules such as ions (on experimentally relevant time-scales). This means that any transfer of water through the membrane leads to an osmotic pressure. This pressure is huge on the scale of the bending energy and then cannot be counterbalanced by it. Consequently, the enclosed volume of the vesicle is fixed by the concentration of ions inside and outside the vesicle through the requirement that the osmotic pressure is balanced by the hydrostatic pressure.

These geometrical constrains are usually implemented by introducing the Lagrange multipliers Δp and Σ, coupled, respectively, with the vesicle volume and surface area The Lagrange multiplier Δp must be adjusted in order to ensure this prescribed volume. Likewise, the parameter Σ is the Lagrange multiplier to ensure a fixed surface area. Alternatively, one can fix a surface tension and a pressure and determine the resulting vesicle's area and volume.

1.5.1 Spontaneous-Curvature Model

Based on the Canham-Helfrich model [Eq. (1.4)], the stationary shapes of the vesicle may be determined by minimizing the membrane's curvature elasticity E_b for a given area A and a given volume V. The shape equations are then obtained from

$$\delta E_T = \delta(E_b + \Sigma A + \Delta p V) = 0 \tag{1.25}$$

where δ denotes variation with respect to the shape of the vesicle. This constitutes the spontaneous-curvature (SC) model as introduced by Canham and Helfrich [33, 34].

For topologically equivalent shapes, the Gaussian energy contribution E_G to the bending energy is constant and then can be omitted [Eq. (1.6)]. In these cases, it is enough to minimize the mean curvature energy E_m with the constraints of fixed area and volume

$$\delta E_T = \delta(E_m + \Sigma A + \Delta p V) = \delta\left[\frac{\kappa_b}{2}\int (2H - C_0)^2 \mathrm{d}A + \Sigma A + \Delta p V\right] = 0. \tag{1.26}$$

It can be mathematically proven that the equilibrium condition of Eq. (1.26) gives the following shape equation [35]

$$\Delta p = \kappa_b[\nabla^2 H + (2H - C_0)(2H^2 - 2K + C_0 H)] - 2H\Sigma. \tag{1.27}$$

where ∇^2 is the Laplace–Beltrami operator. This nonlinear partial differential equation is extremely complicated to solve. For the special case of a sphere of radius R, the curvatures are $H = 1/R$ and $K = 1/R^2$, so the shape-equation has the analytical solution

$$\Delta p R^3 + 2\Sigma R^2 + \kappa_b(C_0 R - 2)C_0 R = 0. \tag{1.28}$$

The Eq. (1.26), or equivalently the Eq. (1.27), does not have analytical solution in general, but can be solved numerically and different methods have been developed to solve it, such as numerical procedures [71, 72], perturbation methods [73, 74], or variational approaches [75]. A

significant simplification arises by restricting our research to axisymmetric, single-component vesicles with spherical topology [no holes, $g = 0$ and $E_G = 4\pi\kappa_G = \text{constant}$, see Eq. (1.6)]. This study can be generalized to vesicles with non-spherical topology (which also have been observed), with non-rotational symmetry, as well as for multicomponent lipid vesicles; but these complex systems are not described in this summary (for a review see Ref. [71]).

The stationary shapes in the SC model can be expressed in terms of the reduced volume $v = V/[4/3\pi R_0^3]$, being R_0 the radius of the sphere corresponding to an area $\sqrt{A/(4\pi)}$, and the reduced spontaneous curvature $C_0 R_0$. For a given C_0 there exist several shapes of local minimal energy but one can proof mathematically that the sphere is the absolute minimum.

Stationary shapes for $C_0 = 0$

Let us consider first the simplest model for axisymmetric vesicles consisting of a symmetric bilayer characterized by $C_0 = 0$. In this case, the bending energy is scale invariant, *i.e.,* the energy of a vesicle does not depend on its size (note that $\int H^2 \mathrm{d}A$ is a dimensionless quantity). For example, the bending energy of a spherical vesicle in this case is $E_T = 8\pi\kappa_b + 4\pi\kappa_G$. This means that once we have determined the shape that minimizes the energy, its transformation under an overall dilatation leads to a shape that has the same energy and also minimizes the energy.

When $C_0 = 0$, only the reduced volume v determines the shapes of lowest bending energy (see Figure 1.20A). For $v = 1$, the shape is necessarily a sphere, while for $v < 1$ the solutions predict three main branches: prolate ellipsoids/dumbbells (rod-like), oblate ellipsoids/discocytes (disk-like), and stomatocytes. For $v \lesssim 1$ the prolates have lowest energy, for $v < 0.65$ the energy of the oblates become smaller than the energy of the prolates, and for $v < 0.59$ the stomatocytes are the shapes of minimal energy. The nature of these transitions is abrupt (discontinuous), as can be seen in Figure 1.20B.

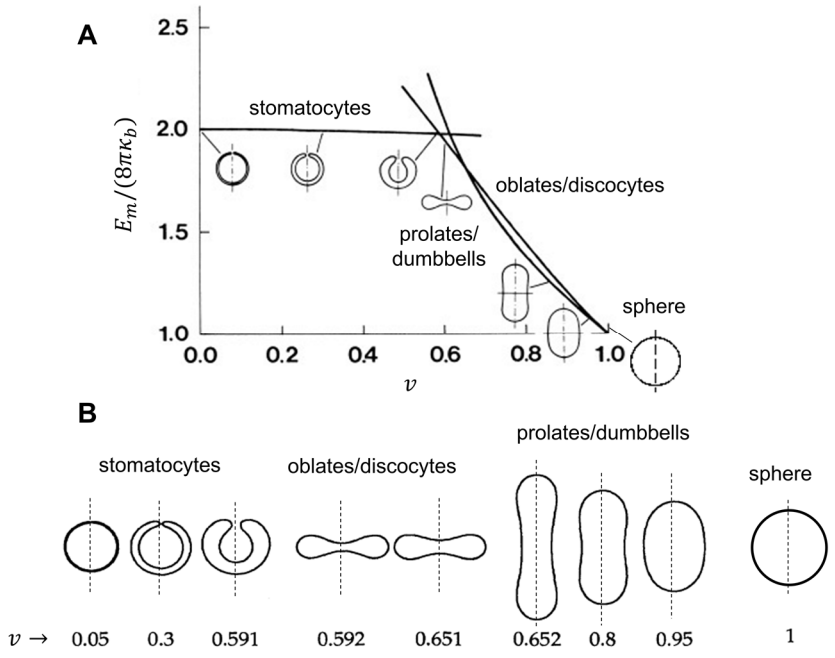

Figure 1.20. Stationary shapes according to the SC model for $C_0 = 0$. (A) Mean curvature energy E_m [Eq. (1.4)] as a function of the reduced volume v. (B) Corresponding stationary shapes for certain values of the reduced volume. All shapes displayed have the same area and are axisymmetric with respect to the dashed lines. Adapted from Ref. [76].

Phase diagram: stationary shapes for $C_0 \neq 0$

Unlike the previous case, the bending energy when $C_0 \neq 0$ depends on the size of the vesicle. For example, the bending energy of a spherical vesicle with radius R is $E_T = 8\pi\kappa_b(1 - R_0C_0/2)^2 + 4\pi\kappa_G$, implying that the shape with the lowest energy has a particular size $R_0 = 2/C_0$. So now, the stationary shapes not only depends on the reduced volume v, but also on the reduced spontaneous curvature C_0R_0. The phase diagram for vesicles at $C_0 \neq 0$ has been partially explored and is shown in Figure 1.21. It contains large regions of stomatocyes, oblates/discocytes, prolates/dumbbells, and pear-shaped vesicles. Stomatocytes and oblates are more favored at $C_0 < 0$, while a positive C_0 leads to prolate and pear-shaped vesicles.

Most transitions predicted by SC model are abrupt (discontinuous). So far, there are no indications that the ground-states of the explored regions of Figure 1.21 are non-axisymmetric; in other words, all minimum energy shapes are, in principle, axisymmetric. Since the solutions of the Eq. (1.26) contain local energy minima as well as unstable saddle points, it would thus be necessary to check the stability of each solution [76]. In obtaining the phase diagram of Figure 1.21 it is assumed that C_0 is uniform over the membrane. However, this is not generally true when the composition of the bilayer is multicomponent. In these cases, the energy minimization becomes more involved.

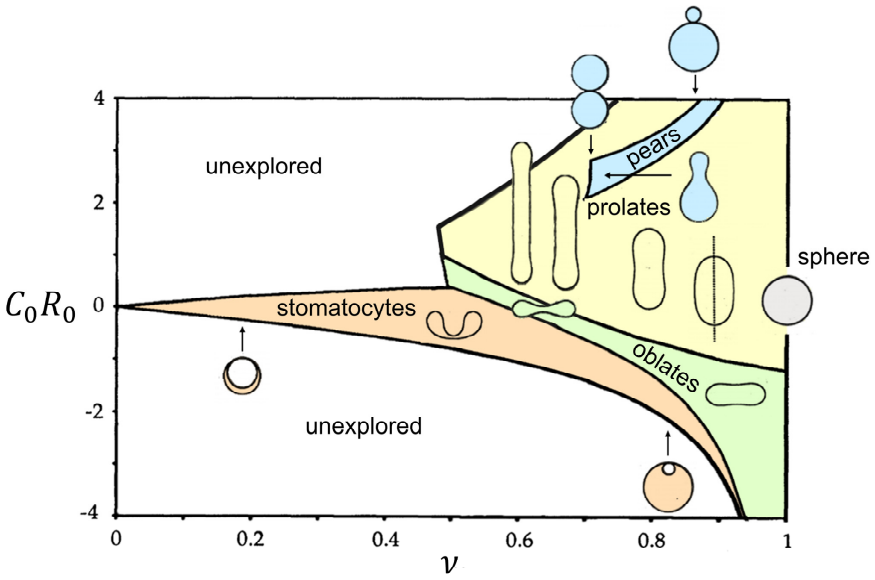

Figure 1.21. Partial phase diagram of the SC model for shapes with spherical topology as a function of the reduced volume v and the scaled spontaneous curvature C_0R_0. Adapted from Ref. [76].

1.5.2 Other Curvature Models

The SC model presented above succeeds in predicting most of observed vesicle shapes. However, it fails in capturing all the features of the shape transitions and complicated non-axisymmetric shapes such as starfish, for instance. In order to circumvent these limitations, two different curvature models have been proposed: the so-called bilayer coupling model (BC) and the subsequent area-difference elasticity (ADE) model.

Bilayer Coupling model

In a more complete description of vesicle shapes, the fact that membranes are composed of two monolayers has to be taken into consideration. The two monolayers of a bilayer can be considered as compositionally independent, because the transbilayer (flip-flop) movement of lipids is slow (one monolayer keeps a constant number of lipids over many hours, or possible days). This fact, together with the assumption that the area per lipid is fixed, leads to consider the difference the area ΔA between the two monolayers constant in short time scales. Under the condition that the two monolayers are separated a distance d over the membrane surface, ΔA is given by

$$\Delta A = h \int_{\Omega} (C_1 + C_2) dA = 2h \int_{\Omega} H dA \,, \tag{1.29}$$

which is correct to first order in h. This constitutes the bilayer coupling model (BC) or ΔA model, originated from the works of Refs. [77–79].

In BC model, the equilibrium shapes are determined by two parameters: ΔA and v. The spontaneous curvature here appears as a Lagrange multiplier which must be adjusted to guarantee the fixed ΔA. Indeed, qualitatively speaking, ΔA takes the role of C_0: large ΔA favors prolate and pearlike vesicles, while smaller values predict stomatocytes and oblates. There exist two important differences to the phase diagram of the SC model: (a) all transitions here are smooth (continuous) and (b) a region of non-axisymmetric shapes emerges between the oblate and prolate shapes. Unlike the SC model, the BC model reproduces very well different sequences of continuous shape transitions observed experimentally. See, for example, the Figure 1.22, where shape changes are induced by heating (which causes a thermal expansion of the area of the two monolayers and then a decrease in the reduced volume of the vesicle).

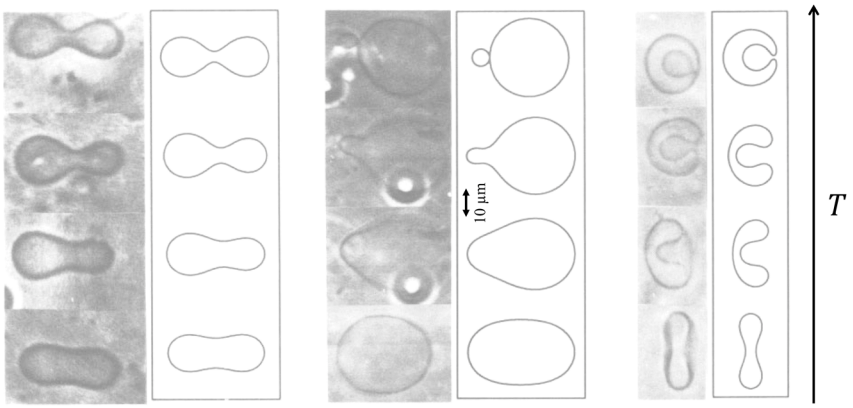

Figure 1.22. Experimentally observed vesicle shapes are well described by minimizing the bending energy of the vesicle membrane according to the BC model. Each column corresponds to a shape transformation process induced by increasing the temperature (upward direction). From Ref. [80].

Area-Difference Elasticity (ADE) model

The constraint of fixed area imposed in the BC model implies a high-stress situation in the membrane. Imagine an initially flat symmetric bilayer membrane with the same number of lipids in both monolayers. Bending this membrane leads to a stretching of the outer monolayer and to a compression of the inner one, with the outer monolayer having only a fraction of the number

of lipids per unit area as the inner one. This situation generates mechanical stress. This stress can be relaxed if the two monolayers are mechanically uncoupled, in the sense that they can slide past one another to redistribute the lipids within each monolayer. In general, this redistribution does not succeed completely and the two monolayers do not fit entirely the shape. As a result, there exist a cost in the elastic energy which can be written as an area-difference-elasticity as

$$E_{ADE} = \frac{\overline{\kappa}\,\pi}{2A_0 h}(\Delta A - \Delta A_0)^2, \tag{1.30}$$

where $\overline{\kappa}$ is a non-local bending rigidity, ΔA_0 is the preferred area difference between the two monolayers, based on both the number of lipids they contain and their interaction with the surroundings, and ΔA [Eq. (1.29)] can be larger or smaller, provided that an appropriate cost in elastic energy is paid. Therefore, this model takes into account that two monolayers are stretched relative to each other and shows that the effect of stretching on the already-small area difference ΔA is important.

The ADE model includes this additional contribution to the total energy $E_{T,ADE} = E_T + E_{ADE}$, with E_T given by Eq. (2.4), and is less restrictive than the previous two models as the shapes are now a function of three parameters $\overline{\kappa}/\kappa_b$, ΔA_0, and v. As in BC model, the spontaneous curvature C_0 also appears as a Lagrange multiplier. Two limiting cases of Eq. (1.30) include the SC model at $\overline{\kappa} = 0$ and the BC model at $\overline{\kappa} \to \infty$, where the elastic energy for the area-difference enforces the hard constraint $\Delta A = \Delta A_0$. As a result, the phase diagram in ADE model interpolates between the SC and BC phase diagrams. This model was proposed in Refs. [81, 82] in order to explain some complex details of the shape transitions between vesicles like the order of the budding transition and complicated vesicles shapes such as starfish, for instance.

1.6 Mechanics of Cell Constriction during Division in the Simplest Model

Many cell division processes have been conserved throughout evolution and are being revealed by studies on model organisms such as bacteria, yeasts, and protozoa. Cellular membrane constriction is one of these processes, observed almost universally during cell division. It happens similarly in all organisms through a mechanical pathway synchronized with the sequence of cytokinetic events in the cell interior. During constriction, cells undergo dynamic changes in shape and large membrane deformations at the site of fission (see Figure 1.23).

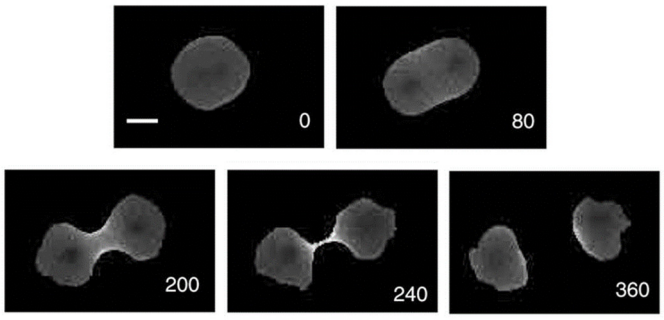

Figure 1.23. A time series images of a dividing animal cell. Scale bar is 5 μm. From Ref. [83].

The mechanics of cell constriction is a crucial problem of biophysics, whose solution should inform us about the forces necessary to duplicate the cell in a stable way.

In the simplest model, the natural cell can be depicted as a homogeneous lipid vesicle where a given constriction force is applied to create a circumferential furrow positioned at the cell equator. Although the network of cytoskeleton structures provides additional physical properties that cannot be recapitulated with the physics of membranes alone, this model can be considered as a good starting point to construct a general minimal model of cell constriction. In this simple model the effect of the cytoplasm and the other cell content can be introduced as effective forces acting on the cell membrane. This model does not consider a cell wall, making it more suitable to describe the division process of animal cells. Prokaryotes and plant cells would require the specific consideration of the mechanical effects of the cell wall where they are encapsulated. Computing the constriction forces requires a knowledge about the minimal energy configuration at each constriction stage. Different approaches have been developed to find the minimum energy shape of a membrane under given constrains and boundary conditions. They are based on calculating the membrane bending energy with the Canham-Helfrich Hamiltonian [Eq. (1.4)] and minimizing it through numerical procedures [71, 72], perturbation methods [73, 74], or variational approaches [75]. Since the constriction process (up to the final fission) does not change the topology, and only involves shapes that are topologically equivalent to a sphere, the Gaussian energy contribution remains constant [Eq. (1.6)] and then can be omitted. Consequently, to analyse the mechanics of constriction we must just deal with the variations of energy due to changes in mean curvature E_m. The mechanics of cell constriction was previously investigated in Ref. [75] by following a variational approach to the minimization problem of the bending energy [Eq. (1.26)] in the case of tensionless ($\Sigma = 0$), turgor-free ($\Delta p = 0$), and symmetrical lipid bilayer ($C_0 = 0$) membrane

$$\delta E_T = \delta E_b = \delta E_m = \delta \left[\frac{\kappa_b}{2} \int (C_1 + C_2)^2 \, \mathrm{d}A \right] = 0. \tag{1.31}$$

Note that for zero spontaneous curvature the bending energy [Eq. (1.31)] becomes independent on the size of the system. This means that the shape that minimizes the energy has the same energy and also minimizes the energy under an overall dilatation. In Ref. [75], they used a linear combination of trigonometric functions as a variational proof of the membrane profile and compared this approach with the exact (numerical) solution of the corresponding Euler-Lagrange equations. They found that the zeroth-order variational solution selected was extremely efficient in approaching the exact solution in a broad range of membrane constrictions from the initial spherical state. Using this solution as an ansatz of the membrane profile, they took advantage of the perturbative method to get approximate analytic expressions for the main descriptors of a symmetrically constricted vesicle (or simplified cell), such as energy, area, volume and constriction and stabilization forces [74]. These works contribute to a better quantitative understanding of the mechanical pathway of cellular division and predict the requirements for successful symmetrical division with negligible effects from spontaneous curvature, surface tension, and pressure difference. This is the case when membrane components generating spontaneous curvature are scarce, membrane trafficking is present with low energetic cost, and the external medium is isotonic. Three main results for the case they considered ($C_0 = 0$, $\Sigma = 0$, and $\Delta p = 0$) must be highlighted:

- Initial (unconstricted) equilibrium configuration is always spherical.
- Constriction is a non-spontaneous process: for cell-sized vesicles with flexible membranes the constriction forces required are in the range of picoNewtons. This is the range of forces practicable by molecular motors.
- Symmetric constriction is unstable against longitudinal asymmetries: additional mechanisms providing a stabilization potential with a constant $\geq 30k_BT$ are required to stabilize symmetrical constriction.

Constriction under more general conditions, which account for the additional effects of non-zero spontaneous curvature, non-zero membrane tension, and non-zero external pressure is part of the original results of this thesis, and can be found in Part II.

Chapter 2

Membrane Nanotubes Pulled from GUVs

This chapter describes the experimental technique used to study the interplay between membrane curvature and cardiolipin (CL) content, whose original results can be found in Part III of this thesis. It consists in pulling membrane nanotubes out of Giant Unilamellar Vesicles (GUVs) containing CL and combines micropipette aspiration and membrane pulling (both techniques were briefly introduced in Section 1.3.2). Specific details of the experimental procedure can be found in Annex 6.

As previously stated in Section 1.2, studying the influence of membrane curvature in living cells is fairly difficult due to the lack of control on size and membrane composition. This complexity has motivated the development of a wide variety of simpler model systems whose size, geometry, and composition can be known with great precision. To be useful for our purpose, such a system should allow to vary membrane curvature in a controlled way and to simultaneously measure the evolution of the CL composition between the curved and non-curved regions of the membrane.

The experimental model system, perfectly suited to fulfil these requirements, has been developed by Bassereau's group. It combines micromanipulation, confocal fluorescence, and optical trapping and allows for manipulating individual GUVs, controlling their surface tension, generating membrane nanotubes, measuring their radius and pulling force, and determining the density of membrane components between the GUV and the tube. The procedure is based on pulling membrane nanotubes from GUVs aspirated in a micropipette as illustrated in Figure 2.1. On one side, a GUV is held by a micropipette exerting a small suction. On the other side, an optically trapped bead is used to apply the force necessary to pull a membrane nanotube. The optical tweezers provide the capability to measure this force. The control of the pipette aspiration sets the tube radius over a biologically relevant range (typically between 10 and 100 nm). During the experiment, the membrane compositions of the tube and the GUV are measured using fluorescence microscopy. This model system allows for a quantitatively validation of the curvature-induced sorting hypothesis [84].

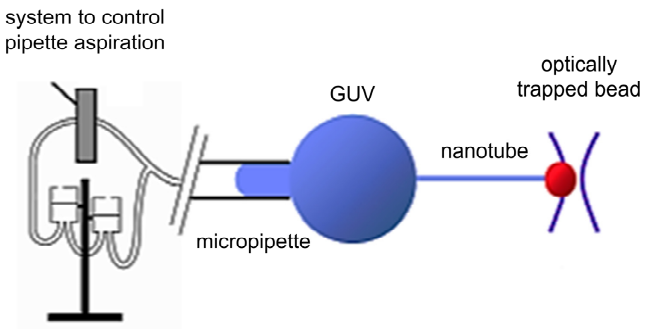

Figure 2.1. Schematic view of the experimental system. Adapted from Ref. [46].

2.1 Experimental Set-Up

The experimental set-up is based on a commercial confocal microscope. It is equipped with three optical channels (see Figure 2.2): for confocal fluorescence, for bright field imaging, and for optical trapping. Since they are not naturally compatible, the light spectrum is split in three separate channels: confocal fluorescence operates in the visible ($400 < \lambda < 750$ nm), bright field microscopy operates in the near infrared channel ($750 < \lambda < 900$ nm), and optical trapping operates in the infrared channel ($\lambda > 900$ nm).

Confocal fluorescence microscopy is achieved by equipping the microscope with a confocal system (port #3 in Figure 2.2) composed of a scanning head with two lasers ($\lambda = 488$ nm, argon, and $\lambda = 543$ nm, HeNe), and detectors (photomultiplier tube). We use a commercial software to control data acquisition.

The system is imaged in parallel with bright field microscopy, which enables us to perform micromanipulations on GUVs in good conditions as well as to detect the bead position by video-tracking (required to deduce the pulling force). To avoid overlap between bright field and confocal data, a visible light absorbing filter (750-900 nm, filter #1 in Figure 2.2) is inserted in front of the lamp. The bright field imaging path is obtained by introducing a dichroic mirror ($\lambda_c = 750$ nm, port #2 in Figure 2.2). This mirror reflects the near infrared light coming from the halogen lamp towards the imaging port, while transmitting visible light used for confocal imaging. A convergent lens is added to the fluorescence excitation path in order to project the image plane onto a video camera. The video signal is then digitized using a Labview based custom software.

Finally, the microscope includes an optional stage rise that creates an extra port which serves to integrate the optical tweezers into the setup. Optical trapping is achieved by focusing the infrared beam on the sample plane (see next section for a brief introduction to the working principle of optical tweezers). The beam is injected into the objective by a second dichroic mirror ($\lambda_c = 900$ nm, port #1 in Figure 2.2). This mirror reflects the infrared light used for optical trapping and transmits the lower wavelength light used for bright field and confocal imaging.

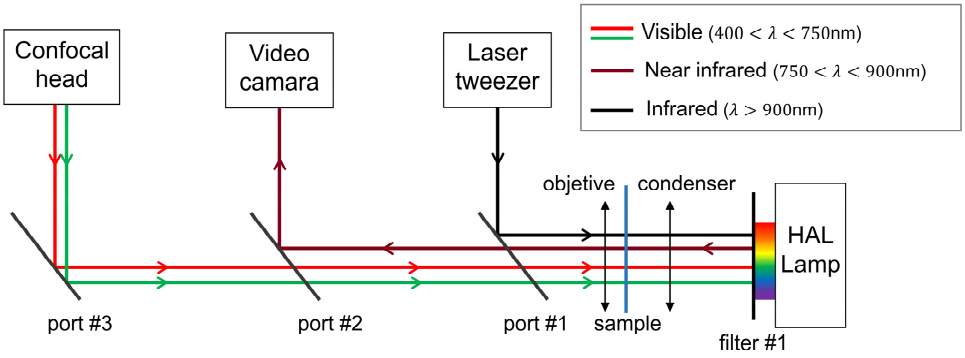

Figure 2.2. Three independent optical channels of the experimental set-up. Confocal microscopy operates in the visible (red and green beams), bright field imaging operates in the near-infrared (dark red beam), and optical trapping operates in the infrared (black beam). Adapted from Ref. [9].

Optical tweezers

Optical tweezers (or optical traps) are devices used to study, manipulate, or trap microscopic objects with nanometer precision and measure femto- and pico-Newton range forces. Ashkin pioneered the development of a three-dimensional stable trap in the 1970s and originally demonstrated that optical forces can manipulate micro-sized dielectric particles in water [85]. Optical traps have become an important tool in a wide range of fields such as biophysics, material science, and bioengineering. This technique has been particularly successful in single-molecule studies of DNA elasticity, mechanical interactions between DNA and proteins, and the behavior of molecular motors. See, for example, Ref. [86], where we investigate the binding mode of the human mitochondrial single-stranded DNA-binding protein using optical tweezers.

The working principle of optical trap depends on the size of the trapped particle relative to the wavelength of light used to trap it. In cases where the diameter of the particle is much larger than the wavelength, trapping can be described using ray optics. This is the regime of our experiments: the beads have diameter of about 3 μm and the optical trapping operates in the infrared, $\lambda \approx 1$ μm. When a laser beam passes through a bead with high index of refraction related to the medium, it refracts and change its direction and its momentum. Due to Newton's third law, there should be an equal and opposite momentum acting on the bead to conserve the total momentum (see Figure 2.3).

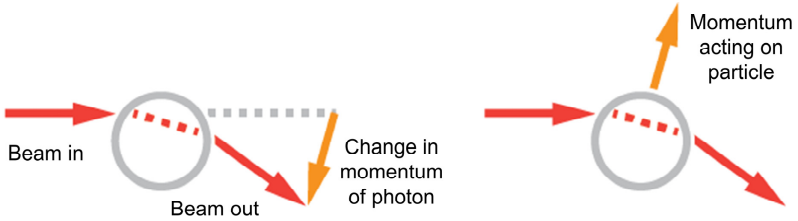

Figure 2.3. Refraction of light. Re-direction of a laser beam and change of its momentum as it passes through a bead with high index of refraction related to the medium (left). Equal and opposite momentum is transferred from the photons to the bead according to Newton's third law of energy conservation (right). Adapted from Ref. [87].

Most optical traps operate with a Gaussian beam profile intensity. In this case, if the bead is displaced from the center of the beam, the rays closer to the center will be more intense and will transfer more momentum to the bead than those rays closer to the edge. This will apply a lateral

gradient force to the bead towards the center of the beam (see Figure 2.4A). Once the bead is located at the center, the rays refracting through the bead will be symmetric, resulting in no net lateral force, and the bead will be laterally trapped. The gradient force in this case is along the axial direction of the trap (the *z*-axis), which will act towards the focus (see Figure 2.4B). As rays are also backscattered at the solvent-bead interface, the light will transfer momentum to the bead, leading to a scattering force in the direction of light propagation (see Figure 2.4C). The cancellation of the axial gradient force with the scattering force makes the bead to be stably trapped slightly above the beam waist (see Figure 2.4D). In order to trap beads in the image plane of a microscope, the laser focus has to be slightly offset to compensate for the scattering force. For an object to be efficiently trapped, the gradient force must exceed the scattering force (optical tweezers were originally called single-beam gradient force traps). This is the reason why the laser beam must be tightly focused. This is also why the beam is usually designed to overfill the back aperture of the objective.

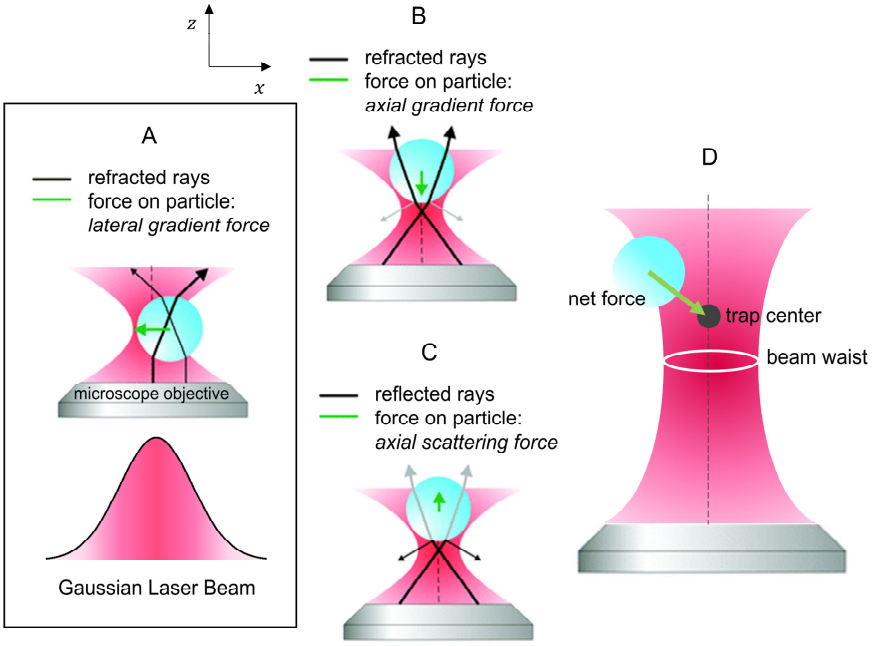

Figure 2.4. This diagram illustrates the principles of optical trapping for a simple gradient force optical tweezers. (A) For beads displaced perpendicularly to the beam center, the larger momentum change of the more intense rays cause a lateral (gradient) force to be applied back toward the center of the laser. (B) The gradient force also acts along the axial direction of the trap (the *z*-axis). (C) Additionally, there is an effect of scattering force which tends to displace the bead in the forward direction of the beam. (D) As a result, beads will stay slightly above the beam waist, where the gradient force counterbalances the scattering force. Adapted from Ref. [88].

When the diameter of the particle is much smaller than the wavelength, the ray theory breaks down but the conditions for Rayleigh scattering are satisfied and the particle can be treated as a point dipole in an inhomogeneous electromagnetic field. In this case, the gradient force arises from the interaction between the inhomogeneous field and the induced dipole while the scattering force results from absorption and re-radiation [89]. For particle sizes comparable to the wavelength, neither the ray optics nor the Rayleigh theory applies and the electromagnetic field analysis becomes more involved. There are several references detailing this theory, such as [90–93]

For a limited range of displacements around the center of the trap, optical tweezers can be compared to a simple spring, which follows Hooke's law, *i.e.,* the restoring force is proportional to the distance from the equilibrium position Δx with a direction opposite to that of the displacement

$$f_0 = -k\Delta x, \tag{2.1}$$

where the stiffness of the trap k is proportional to the laser power.

In our tube-pulling experiments, the optical tweezers serve two purposes: pulling a tube from a GUV using the trapped bead as handle, and measuring the equilibrium pulling force. To measure the force with this technique, one needs to know the bead position and the trap stiffness. The bead position can be measured by video tracking using a Labview based custom software and the trap stiffness is regularly calibrated by using the Stokes drag force method. The principle of this method is to trap a bead and move its surrounding medium at constant velocity. During the movement, the bead experiences a drag force in the direction of the displacement. As the Reynolds number of the flow is very low, the force applied on the bead is given by the Stokes's law $f = 6\pi\eta Rv$, where η is the viscosity of the fluid, R the bead radius and v the velocity of the fluid. Therefore, we can move the sample until the restoring force exerted by the trap equals the viscous force and determine the trap stiffness. Previous calibrations on the group gave values of $k \approx 40$ pN/(μm W) [46].

Micropipette fabrication

In our experiments, the micropipette is used to hold the GUV and to set membrane tension and the tube radius. These pipettes are made of borosilicate glass capillaries (internal radius 0.7 mm, external radius 1 mm). They are fabricated using a pipette puller, which pulls on both ends of the capillary while heating it in the middle with a laser beam. This creates a thin elongated tip closed at its end by the merged glass walls. Subsequently, the pipette opening is set to the appropriate size (≈ 5 μm diameter) using a microforge.

To perform the experiments, the micropipette is connected to a water circuit that ends in a mobile water tank (see Figure 2.5d). The GUV can be aspirated by lowering the height of the water tank since it decreases the pressure inside the micropipette. The micropipette is also attached to a three-axis mechanical micromanipulator, enabling us to move it in the three directions within the chamber (see Figure 2.5b).

The membrane tension of the GUV is proportional to the pressure difference between the chamber and the micropipette [Eq. (I.20)]. This pressure difference corresponds to the hydrostatic difference of pressure imposed by the vertical displacement of the water reservoir (see Figure 2.5d) attached to the pipette $\Delta p = \rho_{H_2O} g \Delta h_{H_2O}$ where ρ_{H_2O} is the density of water at room temperature, g is the gravitational acceleration, and Δh_{H_2O} is the height of the reservoir relative to that of the experiment chamber. Typically, we vary the height of the tank by a total of 1 to 1.5 cm over the course of an experiment, thus imposing tensions ranging from0.01 to 0.2 mN/m.

The experimental chamber

The experimental chamber used in our experiments is limited by two glass coverslips placed on top of each other (bottom: 11x32 mm, top: 9x35 mm) (see Figure 2.5c).

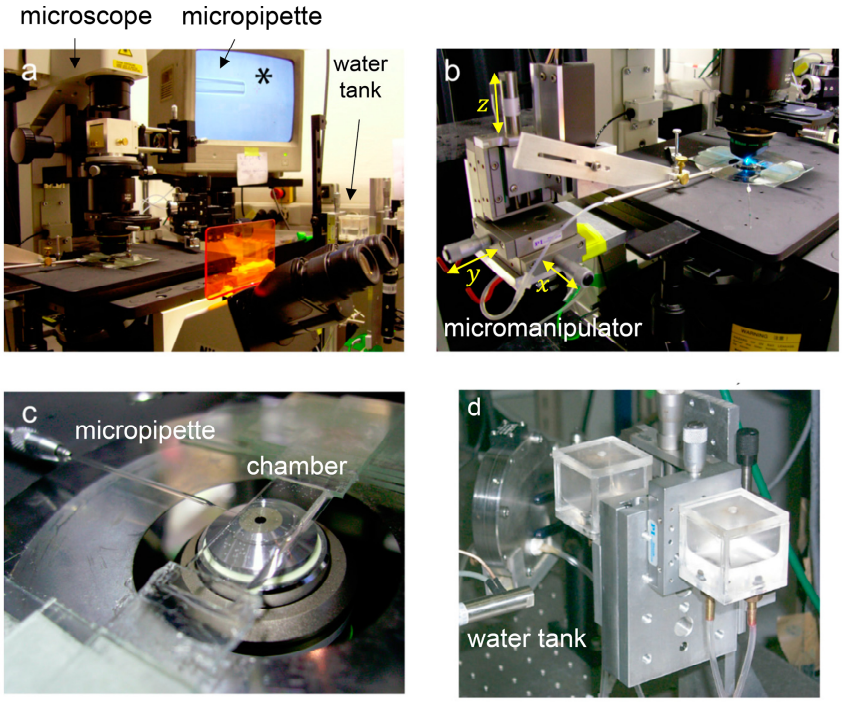

Figure 2.5. A few pictures of the experimental set-up. Images a, b, and c are from Ref. [46] and image d is from Ref. [31].

2.2 GUV Formation: Electroformation Technique

Among different techniques available for Giant Unilamellar Vesicles (GUV) formation, the electroformation technique is one of the easiest and most efficient. This technique allows to form giant vesicles (from 1 to 100 µm) in a few hours with a good yield and few multilamellar ones. The chamber for the vesicle preparation consists of two ITO coated glasses separated by a silicone greaser to prevent leakage (see Figure 2.6A). Briefly, the procedure for preparing GUVs using the electroformation technique is the following. Lipids are first dissolved in chloroform/methanol at a concentration of 1 mg/ml. Two drops of approximately 10 µl are deposited and spread on two ITO coated glasses. The films are then dried under high vacuum for 30–60 min at room temperature and subsequently rehydrated with the inner buffer for the vesicles (typically sucrose). This buffer must contain as few ions as possible to avoid altering the bending rigidity or the spontaneous curvature of the membrane [94]. After that, the electrodes are connected to a function generator and an alternating potential difference (peak-to-peak) of typically 1.1 V, 10 Hz is applied immediately. GUVs of non-uniform size are formed by swelling under the AC field. The time for vesicles to grow is usually a few hours (this time can be optimized according to the chamber thickness and the solution viscosity). Vesicles growth can be monitored through the ITO glass using a phase contrast inverted microscope (see Figure 2.6B). To enhance the contrast between the inner and outer medium, vesicles should be transferred into a solution with a refractive index different from that of the inner buffer, for

example, glucose or KCl. It is essential that the osmolarity of the outer medium matches the osmolarity of the medium inside the GUVs within ~ 10% [94].

In our experiments (see Part III of this thesis), we measure CL sorting as a function of membrane curvature in a homogeneous lipid mixture with egg phosphatidylcholine (EPC) at different CL-contents. GUVs are grown at room temperature, 22 ± 1 °C, in 400 mM sucrose solution. A red fluorescent reference lipid (BODIPY-TR Ceramide) is included in the lipid mixture at 1% by mole to allow membrane visualization. A green fluorescent lipid (Top-Fluor CL) is also included at 1% by mole to allow the quantification of the CL-enrichment as a function of the membrane curvature. To get adhesion between the vesicle membrane and the streptavidin-coated beads holding the tube in the trap, a small amount of biotin is also added to the lipid mixture.

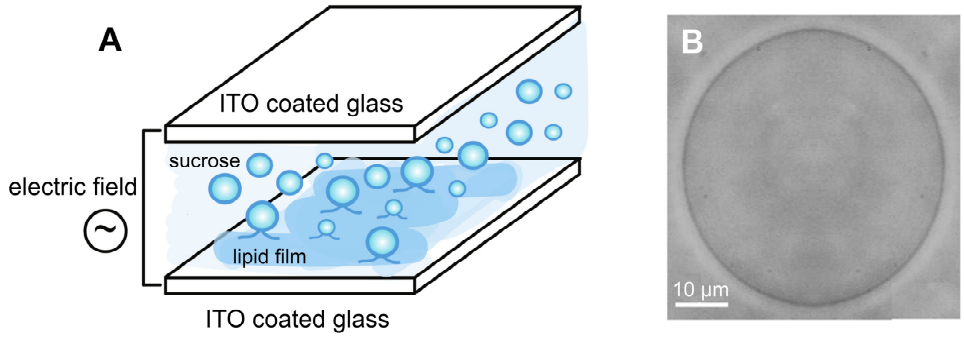

Figure 2.6. GUV formation. (A) Sketch of the electroformation process. GUVs of non-uniform size are formed from a dried lipid film by swelling under application of an electric field between two conductive slides. From Ref. [95]. (B) Image of a GUV made by electroformation in P. Bassereau's lab observed under a phase-contrast microscope.

2.3 Pulling a Nanotube from a GUV

Tube pulling experiments were performed using a set-up developed by Patricia Bassereau's group. The procedure is based on pulling membrane nanotubes from GUVs aspirated in a micropipette (see Section 1.3.2 for a description of the micropipette aspiration and the membrane pulling techniques). Before starting experiments, both the micropipette and the chamber are filled with a solution containing of β-casein in order to prevent the vesicles from sticking to the glass. Then, the chamber is rinsed with the external buffer and filled with a few µl of GUVs and a few µl of streptavidin-coated beads. To be able to impose a tension using the micropipette aspiration technique it is necessary to have GUVs with an initially low tension. This can be achieved by waiting for at least 15 min to slowly increase the osmolarity of the solution in the chamber by evaporation. The solution outside the GUV is thus at higher osmolarity than the inside which leads to a deflation of the vesicles and a decrease of their tension. When the tension is low enough (based on the visual observation of fluctuating vesicles), we close both edges of the chamber with mineral oil in order to stop the evaporation and to maintain a constant pressure inside the chamber. Before each set of experiments on a new vesicle, it is necessary to set the zero reference pressure in the micropipette by detecting the absence of movement of a bead in the pipette. The change in height Δh_{H_2O}, that controls the membrane tension of the vesicle, is measured relative to this reference. Once that is done, a GUV is aspirated in a micropipette applying a high aspiration pressure (checking the GUV "tongue" in the micropipette) and a streptavidin-coated bead is trapped in an optical trap. The vesicle, which contains a very small fraction of biotinylated lipids, is then pushed against this bead so that a

small patch of membrane sticks to the bead due to the binding of the biotinylated lipids contained in the vesicle and the streptavidin molecules at the surface of the bead. Finally, the vesicle is pulled away to create a membrane nanotube of 5-10 μm. This length is kept constant during the whole experiment. We perform successive step-variations of the membrane tension (which varies the tube radius over a biologically relevant range, typically between 10 and 100 nm) by adjusting the pipette aspiration pressure. Between each data point we wait for at least 45 seconds to let the system equilibrate by lipid diffusion and then we acquire one fluorescence image. All experiments were performed at room temperature, 22 ± 1 °C.

2.4 Fluorescence Measurements

Fluorescence is the emission of light by a substance that has absorbed light or other electromagnetic radiation. It is a form of luminescence. In most cases, the emitted light has a longer wavelength, and therefore lower energy, than the absorbed radiation. Fluorescence occurs when an orbital electron of a molecule or atom relaxes to its ground state by emitting a photon from an excited singlet state:

Excitation: $S_0 + h\nu_{ex} \rightarrow S_1$

Fluorescence (emission): $S_1 \rightarrow S_0 + h\nu_{em} + \text{heat}$

where $h\nu = h/\lambda$ is a generic term for photon energy with h the Plank's constant, ν the frequency of light, and λ the wavelength of light. The specific frequencies of exciting and emitted light are dependent on the particular system. S_0 is called the ground state of the fluorescent molecule, and S_1 is its first excited singlet state.

The fluorescence is visible by confocal microscopy. Confocal microscopy is crucial for our purposes because the more basic epi-fluorescence technique does not offer sufficiently high signal-to-noise ratio to enable imaging of thin tubes [46]. To measure the CL-enrichment as a function of the membrane curvature we have to extract information from the confocal images. Our vesicles contain two fluorophores: a red fluorescent reference lipid (BODIPY-TR Ceramide) and a green fluorescence labelled CL (Top-Fluor CL). They were excited, respectively, by a HeNe laser ($\lambda = 543$ nm) and an argon laser ($\lambda = 488$ nm). Red and green channel images are acquired sequentially to avoid any fluorescence bleed between both channels. The illumination and acquisition parameters are selected in order to prevent photobleaching while keeping a high signal-to-noise ratio.

2.4.1 Membrane Fluorescence Quantification

Confocal images are acquired with a comercial software and then analyzed using a custom Matlab program which allows to quantify the intensity values for the two fluorophores in the tube ($I_{\text{tube, BOD-TR}}$, and $I_{\text{tube, Top-CL}}$) and in the vesicle ($I_{\text{GUV, BOD-TR}}$, and $I_{\text{GUV, Top-CL}}$). I_{tube} represents the mean fluorescence along the length of the tube and I_{GUV} represents the mean fluorescence along part of the contour of the GUV. Briefly, the procedure to obtain these intensities is as follows. The program works within a user-defined regions of interest. In our case, two rectangular areas are selected: one around the horizontal tube and the other around a (quasi)horizontal part of the vesicle (see Figure 2.7). Within these boxes, pixel values are averaged along horizontal lines. In this way, both images are transformed into one-dimensional

data sets that correspond to the averaged fluorescence profile of the tube and the vesicle along the vertical axis. After that, the maxima of the fluorescence profiles are reduced by the corresponding noise levels (average values of the background). The same area in the tube and in the vesicle is used for each dye. While I_{tube} is highly dependent on the tube radius, I_{GUV} is almost independent of the radius of the vesicle. Due to the high fluctuations on the number of fluorophores per voxel, the fluorescence intensities are averaged along the entire length of the tubes.

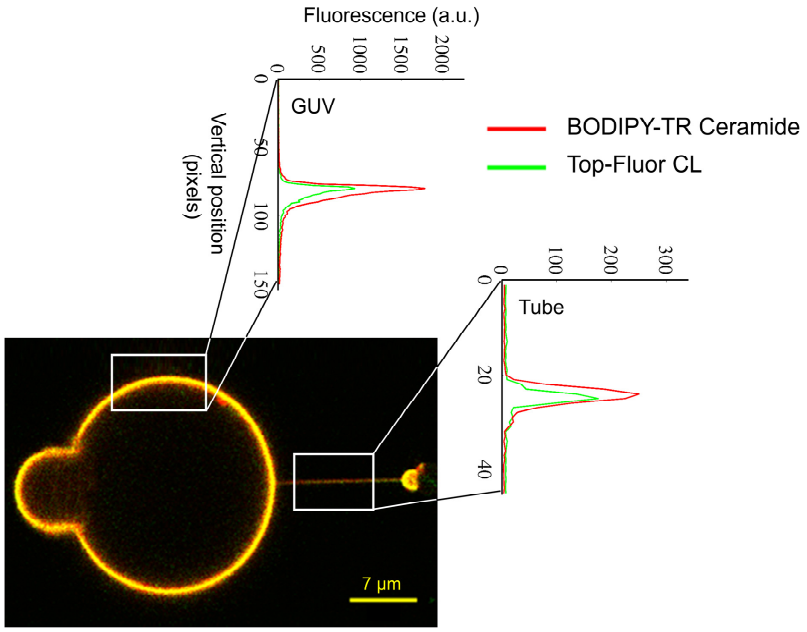

Figure 2.7. **Confocal image analysis.** For each region delimited by the white frames, the program calculates the mean intensity along the horizontal lines to get an averaged fluorescence profile along the vertical axis (plots). Fluorescence intensity is obtained by subtracting the average value of the background to the maximum value. Contrast has been enhanced, and green and red intensities have been scaled to match in the GUV (which is orange-yellowish).

Once we know how to quantify the fluorescence intensities of both dyes, it is recommended to perform the following verifications (see Annex 6 for specific details of the results).

Phase separation

As briefly described in Chapter 1, when two or more lipids with different molecular shapes or different melting temperatures coexist in the same structure, they tend to spontaneously segregate into different domains. It is then important to check whether our EPC/CL GUVs exhibit a homogeneous fluorescence along their contour or, conversely, they are phase separated. Figure A6.1 in Annex 6 shows a confocal image of a GUV with a high concentration of CL (40% by mole). Even at this CL excess, there is no visible evidence of phase separation in EPC/CL bilayers. The absence of such a separation is consistent with the results of Nichols-Smith [17], who observed a complete miscibility for mixed EPC/CL monolayers at all the molar ratios at room temperature. Note that fluorescence microscopy only detects phase separation when the domains are larger than 1 µm. Then, the existence of self-associating CL finite-sized clusters, possibly stabilized by long-range repulsive electrostatic interactions, cannot be excluded from our measurements. This study would require additional experimental observations.

Photobleaching

Photobleaching occurs when a dye or a fluorophore molecule permanently loses the ability to fluoresce due to photon-induced chemical damage and covalent modification. Such irreversible modifications in covalent bonds is caused by transition from a singlet state to the triplet state of the fluorophores. This effect may complicate the observation of fluorescent molecules, since they will eventually be destroyed by the light exposure necessary to stimulate them into fluorescing. The average number of excitation and emission cycles that occur for a particular fluorophore before photobleaching is dependent upon the molecular structure and the local environment. Some fluorophores bleach quickly after emitting only a few photons, while others that are more robust can undergo thousands or millions of cycles before bleaching.

As we noticed that the fluorescence labelled CL (Top-Fluor CL) bleaches quite rapidly, we have to select our imaging conditions and microscope settings so that the photobleaching is as low as possible. In Annex 6 we estimate the amount of photobleaching by fitting the fluorescence decrease with the number of consecutive images. In general, our bleaching is weak, but the bleaching of the tube is larger than the vesicle due to its confined geometry (see Figure A6.3). This bleaching is prevented by acquiring only one image per membrane tension step and no more than 8 images during one experiment on the same vesicle.

Cardiolipin diffusivity

Thought our tube pulling set-up is not designed to determine the CL diffusion coefficient, we can see qualitatively whether CL molecules can exchange between the GUV and the tube. This test is essential since a diffusion impediment would mean that the CL distribution in our experiments would not be at equilibrium. To study this phenomenon, the first step we can do is to completely photobleach the green-labelled CL (Top-Fluor CL) in the tube by imaging it at high laser power. Next, we can monitor the green fluorescence recovery in the tube after photobleaching by imaging at low laser power. A recovery would indicate that CL molecules are able to freely diffuse across the tube, while no recovery would suggest that the neck of the tube acts as a diffusion barrier impeding CL diffusion. Figure A6.2 in Annex 6 shows that CL molecules freely exchange between curved and flat membranes which depicts CL as a mobile molecule.

2.4.2 Procedure for Determining the Cardiolipin Density in GUVs

In general, the fluorescence intensity I is proportional to the concentration of the fluorophore ρ

$$\rho = A \times I, \tag{2.3}$$

where the proportionality constant A depends upon both the confocal parameters (microscope objective, laser power, dwell time, pinhole diameter, etc.) and the fluorophore efficiency.

This property allows us to establish a relation between the fluorescence intensity of the GUV $I_{\mathrm{GUV,\,Top\text{-}CL}}$ and the surface density of labelled CL in the membrane $\rho_{\mathrm{GUV,Top\text{-}CL}}$. For this purpose, we need a calibration standard, *i.e.,* a fluorescent species emitting in the same channel as Top-Fluor CL that we can incorporate in GUVs at known densities. The only other requirement is that the fluorophore must be imaged under identical conditions as the CL. We used the green fluorescent lipid BODIPY-FL HPC, a green lipidated dye. From measurements of the

fluorescence of GUVs containing controlled amounts of BODIPY-FL HPC, we derive the calibration coefficient A. However, this coefficient cannot be used directly for determining the surface density of labelled CL in the membrane. Since Top-Fluor CL has a different efficiency than BODIPY-FL HPC, the calibration has to be corrected to take into account the spectral differences of the two dyes and how these spectra are affected by the microscope optics. Then, to calculate the density of labelled CL molecules the calibration coefficient A has to be normalized by the ratio of fluorescence of the two fluorescent species in bulk solution. Importantly, bulk solutions of BODIPY-FL HPC and Top-Fluor CL have to be imaged under the same confocal conditions as those used to measure A.

See Annex 6 for a detailed explanation of the calibration procedure where we explicitly determine the CL density in GUVs from the measurements of the intensity $I_{\text{GUV, Top-CL}}$.

2.4.3 Tube Radius Calibration

The radius of the membrane nanotubes pulled this way is below optical resolution and therefore is not measurable by optical means. However, it can be calculated if the membrane tension and force necessary to pull the tube are known, which is the case in this set-up (see Section 1.3.3). For an ideal, elastic membrane at equilibrium, the tube force f_0, the membrane tension Σ, and the tube radius r_0 are related as [Eq. (1.23)]

$$r_0 = \frac{f_0}{4\pi\Sigma}. \tag{2.4}$$

and f_0 and Σ are measured quantities in our system.

We are going to see now that the tube radius can be more easily determined from the reference lipid fluorescence intensities ($I_{\text{tube, BOD-TR}}$ and $I_{\text{GUV, BOD-TR}}$) by a calibration. In our experiments, the tube diameter is smaller than the thickness of the confocal volume, and then, the red fluorescence signal coming from the tube is proportional to the number of fluorophores per unit length. It is thus proportional to the area of the tube divided by its length

$$I_{\text{tube, BOD-TR}} \propto \frac{A_{\text{tube}}}{L_{\text{tube}}} = \frac{2\pi r_0 L_{\text{tube}}}{L_{\text{tube}}} = 2\pi r_0. \tag{2.5}$$

However, the value $I_{\text{tube, BOD-TR}}$ depends on the dye used, and more crucially on the ratio of labelled to unlabelled lipids (recall that we are using 1% by mol of BODIPY-TR Ceramide and much larger quantities of EPC). Therefore, it is likely to vary from one experiment to another and even from one GUV to another if the dye is not incorporated homogeneously between the GUVs. For this reason, we normalize $I_{\text{tube, BOD-TR}}$ by the red fluorescence of the vesicle $I_{\text{GUV, BOD-TR}}$. The ratio $(I_{\text{tube}}/I_{\text{GUV}})_{\text{BOD-TR}}$ should be independent on the ratio of labelled to unlabelled lipids and even of the dye used (as long as it does not display any florescence anisotropy effect). Then, it is more appropriate to write the Eq. (2.5) as

$$r_0 = R_c \times \left(\frac{I_{\text{tube}}}{I_{\text{GUV}}}\right)_{\text{BOD-TR}}. \tag{2.6}$$

The constant of proportionally R_c can be determined by linear fit of the radii values obtained from tube force and tension measurements [Eq. (2.4)]. Previous results in the group using the same set up for GUVs containing PC lipids gave the following values:

- $R_c = (200 \pm 50)$ nm for DOPC with 6 independents GUVs [53].
- $R_c = (229 \pm 30)$ nm for EPC:EPA 9:1 with 4 independents GUVs [55].
- $R_c = (203 \pm 16)$ nm for 57% EPC, 8% PIP2, 15% cholesterol, 10% DOPS and 10% DOPE with 11 independents GUVs [96].

As can be seen, all their measurements are consistent within their standard deviation errors even with different lipid compositions. For our analysis with EPC/CL vesicles we have used a constant of 200 nm.

From the force and tension measurements one can also obtain the membrane bending modulus [Eq. (1.23)]. Previous results in the group for pure EPC membranes yielded a value of $\kappa_b = (10 \pm 1)\ k_B T$ [46], in agreement with values measured in literature using different techniques . This is the value we will use in Chapter 6 for mathematical sorting modelling.

2.4.4 Sorting Ratio

The CL-enrichment relative to the reference lipid (Bodipy-TR-Ceramide) is quantified by the sorting ratio S. We calculate it as the ratio of fluorescence of green and red channels in the tube normalized by the same ratio in the vesicle

$$S = \frac{(I_{\mathrm{CL}}/I_{\mathrm{BOD\text{-}TR}})_{\mathrm{tube}}}{(I_{\mathrm{CL}}/I_{\mathrm{BOD\text{-}TR}})_{\mathrm{GUV}}}. \tag{2.2}$$

The normalization by the red fluorescence intensities is required to correct for the difference in membrane areas considered in both measurements (the tube and the GUV). According to this definition, $S > 1$ implies that CL is enriched in the tube as compared to the GUV, while a value in the range $0 \leq S < 1$ means that CL is depleted from the tube. In the absence of driving mechanisms for sorting, the CL molecules must be homogeneously distributed throughout the membrane both in the tube and in the GUV, resulting in a sorting ratio equals to unity, $S = 1$. Sorting ratio is expected to be equal to unity at large tube radii, when the effect of membrane curvature ($C \equiv 1/r_0$) is negligible and CL molecules must be homogeneously distributed throughout the whole membrane.

Additional control experiments were also performed in order to discard possible systematic differences between the red and green lasers of the set-up. In these experiments, vesicles contain no CL but a green fluorescent lipid (BODIPY-FL HPC) which was previously shown [55] to have equal affinity for the membrane tube that the lipid dye emitting in the red channel, Bodipy-TR Ceramide. In this control experiments, the sorting ratio is expected to be equal to one even for curved membranes.

Our fluorescence labelled lipids are not sensitive to membrane polarization and then we have not to correct for the polarization effects. If the fluorescence emissions were sensitive to the excitation laser polarization, it would be necessary to include a factor in Eq. (2.2) in order to normalize the sorting ratio.

2.5 Modelling the Curvature-Dependence Sorting

As previously introduced in Chapter 1, any membrane deformation caused by curvature, such as the creation of nanotubes, implies an increase of membrane bending energy. Lipid bilayer membranes are usually modelled as two-dimensional fluid-like bilayers where lipids (and proteins) can move freely. Since the bending energy of the GUV is virtually zero (the vesicle is essentially flat compared to the nanotube), the energy required to bend the membrane into a cylindrical tube of curvature C is given by the Helfrich energy [Eq. (1.4)] as $1/2\,\kappa_b(C-C_0)^2$, where κ_b is the membrane bending modulus and C_0 is the spontaneous curvature of the membrane, both dependent on tube composition. According to this expression, molecules softening and/or bending the membrane in the direction of the imposed curvature (C and C_0 with the same sign) are expected to be enriched in the tube. In contrast, molecules stiffening or bending the membrane in against the imposed curvature (C and C_0 with different sign) should be depleted from the tube (see Figure 1.18 in Chapter 1 for an illustration of these curvature-based lipid sorting mechanisms). In the absence of driving mechanisms for sorting, the molecules must be homogeneously distributed throughout the membrane both in the tube and in the GUV, resulting in a sorting ratio equals to unity, $S = 1$. At equilibrium, the reduction of the bending energy is counterbalanced with the entropic cost of distributing molecules non-uniformly. Additionally, any non-ideal interactions between molecules could modify sorting. These interactions should not be important when the concentration of the interacting molecules is small. However, at higher densities, repulsive self-interactions should reduce sorting, while attractive self-interactions should increase it.

There exist numerous theoretical works studying the coupling between membrane shape and composition [51, 55, 97–101]. For our experiments with CL, we will implement the thermodynamic model proposed in Ref. [55]. According to this model, the mixing entropy can be approximated by the van der Waals equation of state and the possible interaction between CL molecules can be incorporated as an interaction parameter a, which can take positive or negative values depending on whether the interactions are repulsive or attractive, respectively. When ideal mixing is assumed (in the absence of binary interactions), then $a = 0$. CL sorting between the tube and the vesicle is then theoretically determined by the tradeoff between the bending, the entropic, and the interaction contributions to free energy. It can be obtained numerically by computing the tube composition that minimizes the total free energy of the system. For a full description of this model see the original paper where it was proposed, Ref. [55], and for a detailed analysis in our particular case with CL see Annex 6. The resulting equations require a self-consistent solution and there is not a simple, general, analytic expression. In Ref. [55], however, several approximate analytical expressions are proposed for different limiting cases.

Chapter 3

Physics of Nutrient Uptake

This chapter introduces the physics of microbial nutrient uptake as required to correctly understand the results shown in Part IV of this thesis. Firstly, we present the Michaelis-Menten (MM) model, originally proposed for enzyme kinetics, but adapted to characterize the nutrient uptake in microorganisms. After that, we show the trait-based model of Asknes and Cao, where inherent microbial traits are explicitly distinguished from environmental variables. Since our original results focus on phytoplankton nutrient uptake, we finish the chapter with an overview about phytoplankton, the microscopic plant-like organisms that live in the ocean.

3.1 Microbial Nutrient Uptake

In order to support their activities, microorganisms incorporate nutrients from the environment across the cell membrane through different transport mechanisms. Different criteria are used to classify these mechanisms, but the most commonly used classification is on the basis of energy requirements. On one side, energy-independent transport is the process in which molecules move from a region of higher concentration to one of lower concentration. It includes passive and facilitated diffusion through facilitator proteins embedded within the cell membrane. Together, these mechanisms are termed as passive transport. On the other side, energy-dependent transport is the process in which molecules moves to higher concentration regions, or against concentration gradient, with the use of external energy. It includes primary and secondary active transport and group translocation. Together, these mechanisms are termed as active transport. Figure 1 in the introductory chapter illustrates both types of transport.

Usually, very small molecules like water and certain gases such as O_2, CO_2, NH_3, weak acids, bases, and some hydrophobic molecules can pass through the membrane by simple diffusion. If uptake occurred solely by passive diffusion the uptake rate would be directly proportional to the external concentration (see Figure 3.1). Larger molecules, polar substances, and some ions require the presence of facilitator proteins. Facilitator proteins can act as channels or carriers. Channels are proteins which facilitate the transport of substances by creating an aqueous channel. They do not bind the solute being transported (their specificity is only function of the size and charge) and are not saturable. In contrast, carrier proteins bind the substrate with high

specificity and are saturable at high substrate concentrations. Both types of proteins increase greatly the rate of simple diffusion (see Figure 3.1).

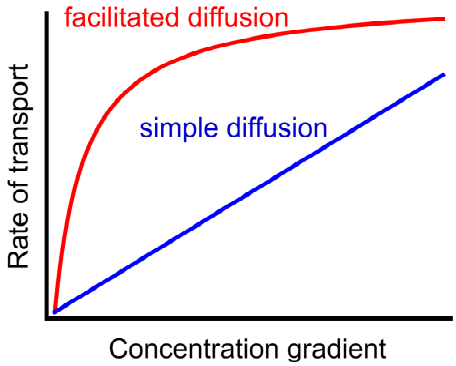

Figure 3.1. A comparison of nutrient transport rates by simple (blue) and facilitated (red) diffusion. Transport by facilitator proteins is much more rapid than transport by simple diffusion but becomes saturated at high solute concentrations.

Since most microorganisms live in environments with low nutrient availability, it is difficult for them to acquire all necessary nutrients by passive transport. Rather, they require energy and proteins to incorporate them within the cell. In order to do this, the cell utilizes energy (from electrochemical gradient, light, or ATP) in a process known as active transport. Cells use this mechanism to transport ions, sugars, amino acids, and peptides. All types of active transport utilize carrier proteins. Many of these proteins are selective, *i.e.,* their structure admits only certain types of nutrients through.

3.2 Nutrient Uptake Models

Models for nutrient uptake in phytoplankton represent them as spherical organisms with a finite number of uptake porters on the cell membrane (representing proteins) where encountered nutrient molecules can be handled (see Figure 3.2). The uptake kinetics in microbial shows features that are very similar to those of enzymes: most of their proteins bind the substrate with high specificity and the uptake rate across the cell membrane exhibits saturation at high substrate concentrations (see Figure 3.1). For this reason, the kinetics of many transport processes is often described by using the Michaelis-Menten equation for enzyme kinetics [102].

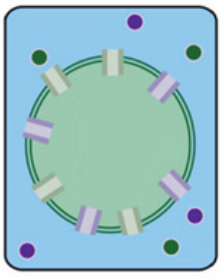

Figure 3.2. Schematic representation of a microbial model cell assuming spherical shape and two types of uptake porters (coloured, respectively, in green and purple). Adapted from Ref. [103].

3.2.1 Michaelis–Menten Model

The formalism of microbial nutrient uptake is commonly represented as an analogy of enzymatic kinetic, proposed by Michaelis and Menten in 1913 [102], where the role of the enzymes is played

by the uptake porters. The uptake process can be then described by the reaction [104]

$$S + n_f \underset{\kappa_{-1}}{\overset{\kappa_1}{\rightleftarrows}} nS \xrightarrow{\kappa_2} S_i + n_f, \tag{3.1}$$

where S represents the ambient nutrient concentration, n_f is an unoccupied (free) uptake porter, nS is the uptake porter-nutrient complex, S_i represents the nutrient concentration incorporated by uptake porters into the cell and κ_1, κ_{-1} and κ_2 are the rate constants. The reaction scheme of Eq. (3.1) describes a process in which nutrients hit an uptake porter at a constant encounter rate κ_1 and form the uptake porter-nutrient complex nS. The porter remains occupied until the complex is completely dissociated inside the cytoplasm, which occurs at a constant rate κ_2. The complex can be dissociated outside the cell at a rate κ_{-1} (rebound process), although this process is assumed to occurs at a frequency too small to be taken into account.

By applying the Law of Mass Action, which states that the rate of a reaction is proportional to the product of the concentrations of the reactants, it is possible to deduce an equation for the nutrient uptake

$$V = \frac{\kappa_2 nS}{\kappa_2/\kappa_1 + S} = \frac{V_{\max} S}{K + S}. \tag{3.2}$$

This is the Michaelis-Menten (MM) functional form with $n = n_f + nS$ the number of porters. The maximum uptake rate $V_{\max} = \kappa_2 n$ and the half-saturation constant (corresponding to the nutrient concentration at which the uptake rate is $V_{\max}/2$) $K = \kappa_2/\kappa_1$, are known as the MM kinetic parameters (see Figure 3.3). At low nutrient concentration $S \to 0$ (oligotrophic regime) uptake rate approaches αS where $\alpha \equiv V_{\max}/K$ is the affinity of the cell, which indicates the uptake ability of an organism at low nutrient concentrations. At high nutrient concentration $S \to \infty$ (eutrophic regime) uptake rate saturates in $V_{\max}$. This maximum rate is reached when all porters are bound to nutrients.

Determination of the kinetic parameters

The typical method for determining the kinetic parameters $V_{\max}$ and K involves multiple flask incubation where different nutrient concentrations are added to each flask [105]. Nutrient uptake is generally determined by measuring the decreasing concentration of the limiting nutrient in the culture medium or by measuring the incorporation of isotopes such as ^{15}N, ^{32}P, or ^{30}Si to determine nutrient incorporation into the cell. Uptake rates V are calculated as the difference between the concentration added and that remaining at the end of the experiment after a relative short incubation time. A linear transform of the Michaelis-Menten equation $S = V_{\max}(S/V) - K$ can be used to easily calculate the kinetic constants. In this equation S is either the initial or the mean nutrient concentration in the flasks [105], the maximum uptake rate $V_{\max}$ is given as the slope of the linear regression equation S vs. S/V and the half saturation constant K as the Y-intercept. As long as S is saturating, the constant $V_{\max}$ is independent of the incubation time.

Many measurements of phytoplankton nutrient uptake show close conformity to the predicted MM behaviour of Eq. (3.2), and hence to the generalized plot showed in Figure 3.3. In ecological modelling, K often appears as an invariant trait of a microbial species or of a functional group

while $V_{\max}$ is often assumed to be temperature dependent [106].

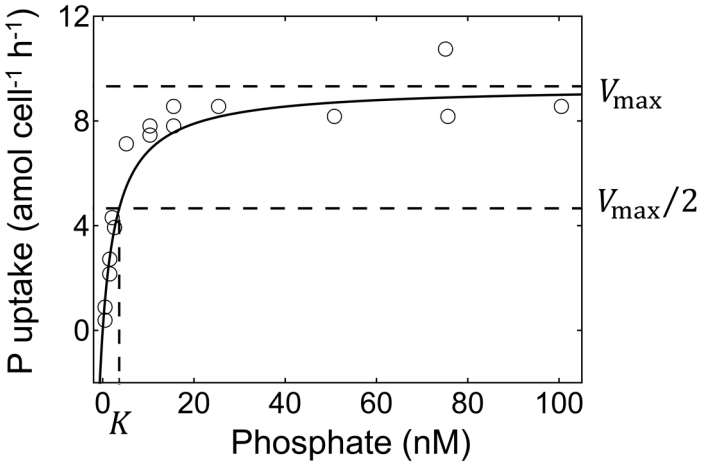

Figure 3.3. MM behavior of phytoplankton nutrient uptake. Phosphate uptake rate as a function of concentration for one species of cyanobacteria measured in October 2011 in the western North Atlantic Ocean. The line represents their fit to the MM model of Eq. (3.2). Data extracted from Figure 1E of Ref. [107].

Diffusion-limitation correction

The necessary diffusion-limitation correction to MM model is deduced from considering the more realistic situation in which microorganisms, due to their small size, are in general surrounded by a boundary layer with decreasing nutrient concentration towards the cell. As a result, the local nutrient concentration is smaller than the ambient concentration caused by the difference in the fluxes owing to nutrient consumption by the microorganism and the diffusive transport of nutrients in the medium towards the cell. By assuming stationary conditions and a spherical cell, we can write the net flux of nutrient molecules toward the cell as $4\pi Dr(S - S_0)$, where D is the diffusion constant of the nutrient, r is the cell radius, S is the nutrient concentration outside the boundary layer (which in practice corresponds to the ambient concentration measured in experiments) and S_0 is the nutrient concentration at the cell surface. The relative difference between S_0 and S determines whether uptake is limited due to physical constraints imposed by nutrient diffusion (uptake rate faster than diffusion rate and then $S_0 < S$) or due to the cellular machinery (uptake site limitation and then $S_0 \approx S$) [104].

By equating the MM uptake rate [Eq. (3.2)] with the net flux of nutrients, it is obtained a quadratic expression that connects S_0 and S

$$\left(\frac{V_{\max}}{4\pi Dr} + K_0 - S\right) S_0 - K_0 S + S_0^2 = 0. \tag{3.3}$$

This relation was first derived by Pasciak and Gavis in 1974 [108] and leads to a quadratic (non-MM) model for uptake. This approach was revisited by Armstrong in 2008 [109], who derived the following MM approximation of the quadratic solution

$$V \approx \frac{V_{\max} S}{K_0(1 + V_{\max}/4\pi DrK_0) + S}. \tag{3.4}$$

This expression has the MM functional form with an effective half-saturation constant $K = K_0(1 + V_{\max}/4\pi DrK_0)$ and takes into account how the possible presence of a boundary layer

formed around the cell modifies the microbial uptake rate. This model explicitly differentiates between both half-saturation coefficients, K and K_0, which are defined according to the corresponding reference nutrient concentration (S and S_0) [110]. When the diffusion rate D or the ambient concentration S are small, the Eq. (3.3) predicts an uptake rate given by $4\pi DrS$. This corresponds to the diffusive flow of nutrients to the cell when it depletes completely the surrounding layer ($S_0 = 0$) and all nutrients encountering the cell surface are immediately absorbed. As D or S increases, Eq. (3.3) approaches to Eq. (3.2), and uptake rate is gradually limited by the transport through the membrane, reaching eventually the limit $V = V_{\max}$ [104].

3.2.2 Trait-Based Models

The MM is simple and measurements of the kinetic parameters $V_{\max}$ and K are widely available in the literature. However, a limitation of the MM model is that it provides no theoretical expectations on how the kinetic parameters $V_{\max}$ and K scale with microbial traits such as cell size, number of uptake porters, and uptake porter size. Consequently, the kinetic parameters do not fully describe an organism's response to a nutrient concentration and more parameters are needed. Such uncertainty can be reduced in trait-based models where these properties are embedded.

One of the first theoretical trait-based models for nutrient uptake was proposed by Aksnes and Egge in 1991 [111]. Their approach is based on Holling's "disk" equation or functional response II, used to model predation in animals. The parameters they incorporated in their model are: the number of uptake porters n, each with a nutrient catchment area at the cell surface A, the nutrient handling time h , which corresponds to the time interval an uptake porter is blocked due to the handling of a nutrient molecule from the outside to the inside of the cell, the number of encountered molecules m, and the mass transfer coefficient v, interpreted as the velocity between molecules and uptake porters. Following their steps, the number of molecules encountered by one uptake porter during a time interval T_1 must be $m = T_1 AvS$, and the time required for processing m encounters is $T_2 = mh$. Then, the total time necessary for processing m encounters is $T_1 + T_2$ and the uptake rate for one site becomes $m/(T_1 + T_2)$. Since the cell has n uptake porters, the uptake rate for the cell results

$$V = \frac{nAvS}{1 + hAvS}. \tag{3.5}$$

Rearrangement of this equation into a MM form yields $V_{\max} = n/h$, $K = 1/(Ah)$ and $\alpha = nAv$ Note that this equation does not explicitly address the boundary layer of the cell. The maximum nutrient uptake $V_{\max}$ is limited by number of uptake porters and handling time, which can be interpreted as an exclusively biological limitation. At low nutrient concentrations, the uptake rate approaches $V_{S\to 0} = nAvS$, which represents the encounter limitation, and depends on both biological characteristics (such as the number of porters and porter area) and on the mobility (through the parameters v and S). Note also that neither handling time nor affinity are part of uptake rate at low nutrient concentration. This is because these parameters reflect the response when the encounter is the rate-limiting step, not handling [111].

However, later theoretical works [112–114] showed that the chance of capturing a nutrient molecule in the oligotrophic regime (at low nutrient concentrations) is a non-linear function of the porter number but can be expressed as

$$V_{S\to 0} = 4\pi DrS\frac{ns}{ns+\pi r(1-p)}, \quad p = \frac{n\pi s^2}{4\pi r^2} \tag{3.6}$$

where n is the number of porters, D is the molecular diffusion coefficient, r is the radius of the cell, s is the porter radius, and p is the fraction of the surface area covered with uptake porters.

This expression assumes that uptake porters are always receptive for uptake and then predicts no saturation in uptake rate with increasing S. This is a reasonable assumption in oligotrophic regimes, where the time interval between nutrient encounters at a porter is much longer than the time it takes to absorb the nutrient molecule [106]. When S increases, the uptake rate is gradually limited by the uptake apparatus rather than by diffusion-mediated transport, and Eq. (3.6) becomes increasingly inaccurate. As earlier proposed Aksnes and Egge in 1991 [111], when all uptake porters are blocked, the uptake rate becomes independent of S, but cannot exceed the biological limitation

$$V_{S\to\infty} = \frac{n}{h}, \tag{3.7}$$

and this limit is not considered in Eq. (3.6).

Aksnes and Cao model

In order to consider this upper limit on the uptake rate as the nutrient concentration increases, Aksnes and Cao [106] combined the results of Eqs. (3.6) and (3.7) and derived the following analytical expression for uptake rate of a spherical cell

$$V = \frac{b}{2a}\left(1-\sqrt{1-\frac{4a}{b^2}}\right), \tag{3.8}$$

with

$$a = \frac{h}{4\pi DrSn}\left(1-\frac{\pi rp}{ns}\right), \quad b = \frac{1}{\alpha S}+\frac{h}{n}, \quad \alpha = 4\pi Dr\frac{ns}{ns+\pi r(1-p)},$$

where the uptake affinity α corresponds to the initial slope of the relation V vs S ($V_{S\to 0} = \alpha S$).

At low nutrient concentrations this uptake rate approaches Eq. (3.6) whereas at high nutrient concentrations approaches the upper limit n/h. Therefore, this model is consistent with both oligotrophic and eutrophic regimes. The effect of temperature is not explicitly expressed in this model, but temperature affects molecular diffusion (and thus affinity) as well as the cellular machinery through $V_{\max}$, or equivalently through h.

The trait-based model of Aksnes and Cao is not of MM type but they proposed two alternative MM approximations. In the first approximation, they defined the MM half-saturation constant as the ratio $V_{\max}/\alpha$, as commonly assumed within a MM framework. This provides

$$K = \frac{\pi r(1-p)+ns}{4h\pi Drs}. \tag{3.9a}$$

In the second approximation, they used the use the analytical expression for the half-saturation constant of the uptake model, obtained as the nutrient concentration where uptake equals 50% of the maximum uptake rate (*i.e.*, $n/2h$)

$$K = \frac{\pi r(2-p) + ns}{8h\pi Drs}. \tag{3.9b}$$

By inserting these coefficients into the equation $V = V_{\max} S/(K+S)$ with $V_{\max} = n/h$, we obtain two approximations to the MM model. The error of both approximations diminish for low porter densities, *i.e.,* when $ns^2 \ll 4r^2$, and particularly when the stronger condition $ns \ll 4r$ holds [106].

The model of Aksnes and Cao provides novel expectations on how nutrient uptake is affected by cell size, porter density, temperature, and nutrient regimes. Variations of the nutrient uptake as a function of these parameters can be found in their original paper [106], as well as in the interactive program that I created, which anyone can play with Wolfram's free player software [115].

Thought most microbial traits have still not measured experimentally (such as number of porters, handling time, or porter size), they can be estimated by combining the MM approximations [Eq.(3.9)] with the measurements of $V_{\max}$ and K. This estimation constitutes one of the objectives of this thesis whose original results can be found in Part IV. There, we use previous phytoplankton data compilation to extract several empirical relationships that predict how phytoplankton number of porters and handling time are expected to vary with organism size and nutrient supply. But before showing these results, let's take some time to get more familiar with phytoplankton.

3.3 Phytoplankton: Microbes in the Ocean

The suspended matter in the watery environments, both salty and fresh, consists of living organisms called plankton and dead particles commonly referred to as detritus. Plankton was defined by Hensen in 1887 as all organisms passively 'drifting' along with water movements. The name comes from the Greek word *plankton* (made to wander or drift). Phytoplankton, from the Greek prefix *phyto* (plant), are the plant-like components of plankton and represent a key factor in oceanic ecosystems as well as in biogeochemical cycling. Phytoplankton is made up of unicellular (exceptionally multicellular) prokaryotic or eukaryotic microorganisms (less than 1 mm in diameter) which are either solitary or colonial. They are extremely diverse: some phytoplankton are bacteria, some are protists, and most are single-celled plants. The most common kinds are cyanobacteria, diatoms, dinoflagellates, green algae, and coccolithophores. Figure 3.4 shows a few common types of phytoplankton.

Figure 3.4. Drawings of common types of phytoplankton, not to scale. Adapted from Ref. [116].

3.3.1 Phytoplankton Growth and Distribution

Phytoplankton requires carbon dioxide, water, sunlight, and nutrients for growth. Like land plants, phytoplankton are autotrophs: they use the solar energy through the process of photosynthesis to convert water molecules and carbon dioxide into carbohydrates. To do that, phytoplankton contains photosynthetic pigments such as chlorophylls. Since sunlight is most abundant at sea surface, phytoplankton often remain close to the surface. As plants on land, phytoplankton growth varies seasonally according to the sunlight.

The survival of phytoplankton is crucially dependent on mineral nutrients, such as nitrate, phosphate, silicate, calcium, and trace amounts of iron. Consequently, phytoplankton thrive at high latitudes, near coastlines and continental shelves, where nutrients are abundant, but scarce in remote oceans, where nutrient levels are low.

Other factors influence phytoplankton growth are water temperature and salinity, water depth, wind, and the graze by predators.

Bloom

Because of their small size, most phytoplankton cannot be individually seen with the unaided human eye. However, under good growing conditions, phytoplankton populations reproduce explosively, a phenomenon known as bloom. Blooms are often visible events in which the water appear greenish, reddish, or brownish depending upon the pigments found in the species and the density of phytoplankton population (see Figure 3.5).

Blooms in the ocean can cover hundreds of square kilometres and are often used by scientifics to estimate the chlorophyll concentration in the water and the biomass of phytoplankton in the ocean. A bloom may last several weeks, but an individual phytoplankton only lives for about a day or two.

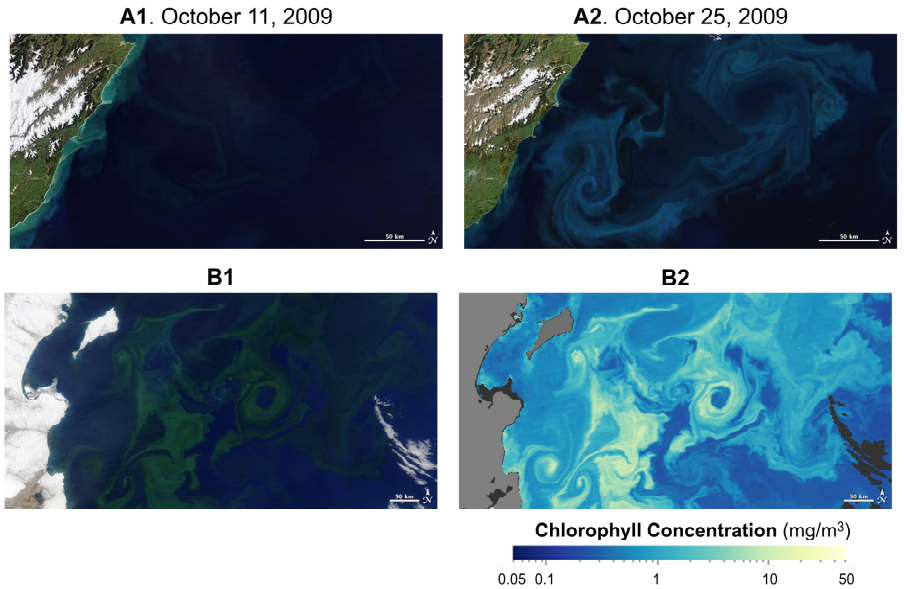

Figure 3.5. Phytoplankton blooms. (A) Phytoplankton can grow explosively over a few days or weeks. This pair of images shows the emergence of a bloom east of New Zealand between October 11 and October 25, 2009. (B) Example of the estimation of the chlorophyll concentration in the water from the colour of the water. Image of a bloom near Kamchatka on June, 2010. From Ref. [116].

Upwelling

Upwelling is a determining factor in phytoplankton growth and distribution. This phenomenon involves a wind-driven motion of the cooler and nutrient-rich water from lower depths towards the surface (where the phytoplankton can use them), replacing the warmer and nutrient-depleted surface water. This leads to an abundant concentration of phytoplankton in equatorial areas where Trade winds produce upwelling (see Figure 3.6).

The effect of seasonal variations in upwelling is especially important in the Arabian Sea and the waters around Indonesia. In these zones, seasonal blooms are often linked to monsoon-related changes in winds. Climate cycles have also an impact on phytoplankton growth. One of them, El Niño, in the tropical Pacific, with an approximately five-years cycle, causes reduced upwelling, with warmer water and less phytoplankton; its opposite phase, La Niña, gives rise to more phytoplankton than normal.

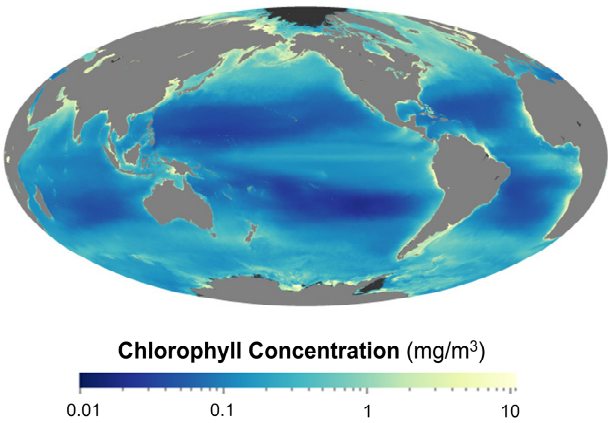

Figure 3.6. Phytoplankton distribution. This map shows the average chlorophyll concentration in the global oceans from July 2002–May 2010. Phytoplankton are most abundant in high latitudes, near coastlines, and in upwelling zones along the equator. They are scarce in remote oceans. From Ref. [116].

3.3.2 Importance of Phytoplankton

The food web

Phytoplankton form the basis of life in the ocean as they are the foundation of the aquatic food web. Zooplankton feed on phytoplankton, which in turn are consumed by larger animals such as fish, whales, birds, and so on. Consequently, if phytoplankton disappear, the food web breaks, and all animals suffer. While most phytoplankton are harmless, there are some species that produce powerful toxins, making them responsible for so-called harmful algal blooms. These toxic blooms can damage and kill aquatic life and people who eat contaminated animals.

Carbon cycle

As previously stated, phytoplankton absorb carbon dioxide and produce organic carbon through photosynthesis. Some of this carbon is transported down into the deep ocean when phytoplankton die, and some is transferred to different layers of the ocean as phytoplankton are eaten by other organisms. This phenomenon is known as biological carbon pump, which is part of the oceanic carbon cycle and responsible for the cycling of organic matter. Worldwide, this pump transfers about 10 gigatonnes of carbon from the atmosphere to the deep ocean each year.

Climate change

Phytoplankton affect climate change, and vice versa. On one side, the larger phytoplankton population along the world, the more carbon dioxide is taken from the atmosphere and then, the lower the average temperature because of the reduction of this greenhouse gas. On the other side, phytoplankton growth responds very rapidly to variations in their environment, especially in sunlight, water, wind, and nutrient concentrations. Then, by comparing phytoplankton trends, such as its density, areal distribution, and growth rate, to other measurements, such as temperature, scientists try to deduce how phytoplankton contribute to, and is affected by, climate and environmental change.

3.3.3 Kinetic Parameters of Phytoplankton

As described in the beginning of this chapter, Michaelis-Menten model [Eq. (3.2)], originally derived for enzyme kinetics, has been adapted to characterize microbial nutrient uptake (including phytoplankton). This model is expressed in terms of the kinetic parameters, half-saturation constant K and maximum uptake rate V_{max}, both quantities easily measured and widely available in literature. Previous phytoplankton data compilation [117] has shown that these parameters increase with organism volume (see Figure 3.7A-B). Independent studies [118–120] have also reported that K increases with nitrate concentration S (see Figure 3.7C). This increase can be thought to be due to an increase in the dominant organism size in the phytoplankton community with increasing nutrient concentration. Previous studies support this assumption, showing that nitrate abundance is the main factor determining dominant organism size [121–127]. Based on this assumption and on the published experimental observations for K, we have obtained how phytoplankton dominant size r is predicted to scale with nitrate concentration. This increase in dominant size can also entail size-related changes in traits (such as the number of porters and handling time) that impact both V_{max} and K. Furthermore, by combining the trait-based uptake model of Aksnes and Cao [Eq. (3.8)] with the experimental results of V_{max} and K, we have derived scaling relations for the number of porters and the handling time in terms of r. These estimations remain hypothetical today since they are still untested experimentally but may be useful in characterizing size dependent nutrient uptake in marine ecosystems and biogeochemical cycling models. Details on these results can be found in Part IV of this thesis

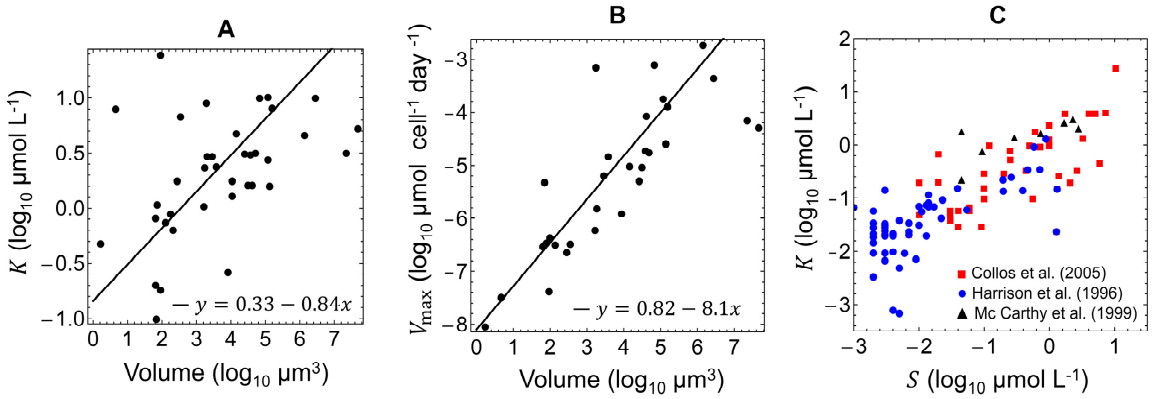

Figure 3.7. Kinetic parameters of marine species of phytoplankton. (A-B) Scaling relations between the kinetic parameters V_{max} and K for nitrate versus cell volume. Data extracted from Figure 1 of Ref. [117]. (C) Compilation of half-saturation values K as a function of nitrate concentration S.

PART II

Mechanics of Constriction during Cell Division

Chapter 4

Modelling the Mechanics of Cell Division

Chapter based on Beltrán-Heredia E, Almendro-Vedia VG, Monroy F, & Cao FJ (2017) Modeling the mechanics of cell division: influence of spontaneous membrane curvature, surface tension, and osmotic pressure. Front Physiol 8:312.

Many cell division processes have been conserved throughout evolution and are being revealed by studies on model organisms such as bacteria, yeasts, and protozoa. Cellular membrane constriction is one of these processes, observed almost universally during cell division. It happens similarly in all organisms through a mechanical pathway synchronized with the sequence of cytokinetic events in the cell interior. Arguably, such a mechanical process is mastered by the coordinated action of a constriction machinery fueled by biochemical energy in conjunction with the passive mechanics of the cellular membrane. Independently of the details of the constriction engine, the membrane component responds against deformation by minimizing the elastic energy at every constriction state following a pathway still unknown. In this chapter, we address a theoretical study of the mechanics of membrane constriction in a simplified model that describes a homogeneous membrane vesicle in the regime where mechanical work due to external pressure, membrane tension, and bending energy are comparable. We develop a general method to find approximate analytical expressions for the main descriptors of a symmetrically constricted vesicle. Analytical solutions are obtained by combining a perturbative expansion for small deformations with a variational approach that was previously demonstrated valid at the reference state of an initially spherical vesicle at isotonic conditions. The analytic approximate results are compared with the exact solution obtained from numerical computations, getting a good agreement for all the computed quantities (energy, area, volume, constriction force). We analyze the effects of the spontaneous curvature, the membrane tension and the external pressure in these quantities, focusing especially on the constriction force. The more favorable conditions for vesicle constriction are determined, obtaining that smaller constriction forces are required for positive spontaneous curvatures, low or negative membrane tension and hypotonic media. Conditions for spontaneous constriction at a given constriction force are also determined. The implications of these results for biological cell division are discussed. This work contributes to a better quantitative understanding of the mechanical pathway of cellular division, and could assist the design of artificial divisomes in vesicle-based self-actuated microsystems obtained from synthetic biology approaches.

4.1 Introduction

The cell division cycle is a central process in biology, the essential mechanism whereby cells grow and duplicate [128]. The mechanics of cell division is an essential part of the epigenetic program that supports cellular reproduction in all living organisms [35]. The division program of any cellular organism involves changes in cell shape that are directly determined by the intrinsic deformability of the cellular plasma membrane. Far from being a passive element, the mechanics of the cellular plasma membrane is known to be physically, as well as biochemically, influenced by different transport processes, particularly, membrane biogenesis shuttled by lipid trafficking from the sites of metabolic synthesis to the cellular membranes [129], and stress-induced membrane remodeling occurred under the action of the cytokinetic machinery which, together with other passive skeletal structures, form the cellular divisome. Cytokinetic machinery is different in prokaryotes [130–133] and eukaryotes [128, 134–138], but both provide mechanisms to generate constriction forces. Cytokinetic membrane remodeling is assumed to arise from a mechanical interplay between membrane tension, osmotic stresses and constriction forces exerted by the divisome. These membrane stresses underlie subcellular force effectors, which are structurally and functionally coupled to dynamically adaptable plasma membrane, the extracellular medium and the cytoskeleton [134]. In prokaryote division, the constricted cellular membrane is maintained under tension by the resistance of an outer peptidoglycan layer, which is dynamically linked to the inner lipid membrane [139–141]. In eukaryotes, however, cortical tensions generated under actomyosin contraction are assumed to be the main source of membrane tension during cytokinesis [142, 143]. Secondarily, membrane trafficking may have the effect of buffering membrane tension by varying cell membrane surface [144]. A quantitative insight on the membrane configurations that minimize the mechanical energy during cytokinesis is an important topic in cell biophysics [35, 145]. Such membrane-focused rationale should allow us to compute the forces needed to divide the cell, thus providing a better understanding about the different routes of cell division in different organisms [146, 147]. Cell growth and further division requires indeed de novo synthesis of plasma membrane [137]. All cells can synthesize lipid molecules that are dynamically incorporated into their membranes [148, 149]. Biosynthetic lipid transport ensures that each cellular membrane have dynamically regulated an adequate lipid composition, which supports the functions of the associated proteins [137]. Cells have developed several, often redundant, mechanisms to transport lipids during the different stages of the cell cycle [150–152], which synchronize with the membrane growth occurred during cytokinetic progression [153–155]. In this chapter, we provide a minimal physical model for membrane constriction that considers either, impeded growth of membrane area characterized by positive membrane tension, which requests mechanical work to be exerted by the cytokinetic machinery [130, 134], or facilitated membrane growth characterized by negative membrane tension. Figure 4.1 depicts the possible modes of deformation of a model (lipid bilayer) membrane under stresses induced by constriction forces, and external fields with different orientations. A great amount of energy, which ultimately depends on cell size and membrane rigidity, is needed to distort the unconstricted initial configuration of the deformable membrane. The knowledge of these energies is especially interesting to know how the cell performs the large curvature deformations required for membrane constriction at the site of division.

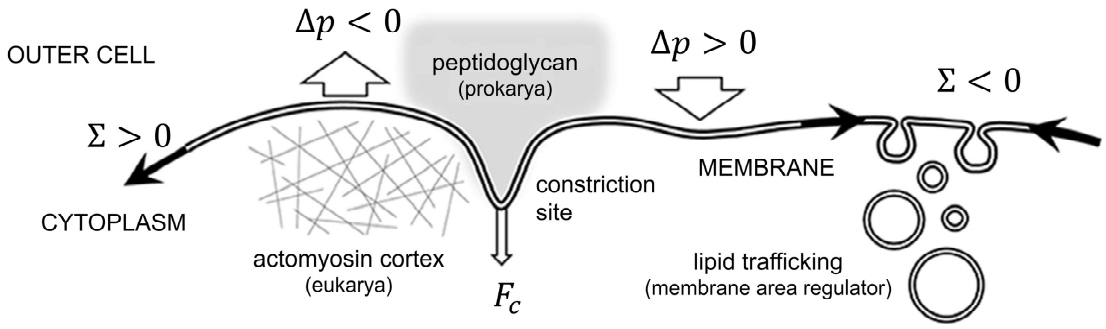

Figure 4.1. Sketch depiction of the different modes of deformation possible in a flexible membrane under the action of a constriction force (F_c) (representative of the constriction deformations in cellular plasma membranes at the site of cell division), and of external stress fields applied either transversally, as a external pressure (Δp), or longitudinally, as a lateral membrane tension (Σ). Negative external pressure ($\Delta p < 0$), represents a cell at the inflated state of turgor, whereas positive external pressure ($\Delta p > 0$) is identified with a flaccid cellular membrane in a hypertonic medium. Regarding lateral membrane tensions, positive surface tension ($\Sigma > 0$) represents biological situations of membrane tension underlateral extensional stresses induced by cortical tensions induced by either the eukaryote cytoskeleton, or the peptidoglycan layer in bacteria; negative surface tension ($\Sigma < 0$) represents situations of regulated creation of membrane area under in situ membrane biogenesis, or membrane uptake from membrane shuttles coming from the metabolic route of lipid synthesis (lipid trafficking).

In a simple model the natural cell is depicted as a vesicle compartment enclosed by a lipid bilayer membrane in which a given constriction force is applied to create a circumferential furrow positioned at the cell equator. Different methods are available to obtain the minimum energy shape of a membrane under given constrains and boundary conditions. They are based on calculating the membrane bending energy with the Canham-Helfrich Hamiltonian [33, 34] and minimizing it through numerical procedures [71, 72], perturbation methods [73, 74], or variational approaches [75]. In a previous work [74], we combined a perturbation expansion for small deformations with a variational approach to compute the minimum energy shapes during the symmetrical constriction of a tensionless vesicle. Here, using a similar framework, we derive analytical formulas during constriction under more general conditions, which account of the additional effects of non-zero spontaneous curvature, membrane tension, and external pressure. Additionally, exact results are computed numerically by solving the corresponding Euler-Lagrange equations (see Section A4.1 in Annex A4). This let us determine the accuracy of the approximate analytical results. By expanding the quantities up to sixth-order of perturbation in the deformations around the non-constricted shape, a good agreement between analytic and exact results is reached for low and intermediate constriction stages. Once the shape that minimizes the energy was calculated, other relevant properties of the system were obtained. Therefore, the proposed method should be sufficiently powerful to map the energy landscape of several mechanical pathways required for optimal cell division in a wide variety of biological situations.

This chapter is organized as follows: in Section 4.2, we present the model used to compute the mechanical energy of an axisymmetric vesicle. In Section 4.3.1, we derive the analytical approximate formulas for the main properties of the constricted vesicle up to sixth-order of perturbation. In the next subsections, these formulas are compared with the (exact) solution of the Euler-Lagrange equations computed numerically following the procedure explained in

Section A4.1 (Annex A4). In Section 4.3.2, we show the effects of the membrane tension and external pressure in the case of zero spontaneous curvature, in Section 4.3.3 we analyze the effects of the spontaneous curvature, focusing on its impact on the constriction force, especially at the onset of spontaneous constriction and, in Section 4.3.4, we show how to extend the model for constant area and constant volume conditions. In Section 4.4 we discuss the main results in the context of the relevant biological situations and finally, in Section 4.5, we expose the conclusions of this work.

4.2 Methods

4.2.1 Simplified Mechanical Model for Cells and Vesicles

As previously stated, the natural cell is depicted as a vesicle compartment enclosed by a lipid bilayer membrane in which a given constriction force is applied to create a circumferential furrow positioned at the cell equator. The cellular membrane is characterized by bending rigidity, spontaneous curvature and surface tension. The turgor of the vesicle is maintained under a positive difference of osmotic pressure between the inside cell and the outside extracellular milieu, which represents hypotonic conditions. Flaccid configurations are defined, in general by iso-, hypertonic conditions characterized by zero, or positive, external pressure. Whereas positive membrane tension represents tensioned membrane vesicles forced to create area at the expenses of delivering work of dilation, negative membrane tension will be allowed to consider flaccid vesicles under continuous membrane biogenesis. The problem will be considered in the regime where mechanical work due to external pressure, membrane tension, and bending energy are comparable. We extend here the technique presented in Ref. [74] and introduced in Section 1.6 of Chapter 1, which combines a perturbation expansion for small deformations with a variational approach to compute the minimum energy shapes during the symmetrical constriction of a tensionless vesicle. In such reference problem, a flaccid vesicle was assumed to be constricted at isotonic conditions, and to have a homogeneous membrane with zero spontaneous curvature and negligible tension. In that case, the initial configuration was a spherical vesicle.

The constriction region was described with approximate solutions based on trigonometric functions, whose local curvature is allowed to change depending on the constriction stage. We found previously in Ref. [75] that such ansatz accurately reproduced the results of numerical computations in a broad range of constriction stages. When the spontaneous curvature, membrane tension, and external pressure are non-zero, the initial equilibrium configuration of the vesicle (or the cell) is, in general, non-spherical, but can be approximately represented by an ellipsoid, which can be oblate, prolate or spherical in function of the specific values of these parameters. This represents a more general physical scenario and lets us analyze the effect of the spontaneous curvature, the membrane tension and the external pressure on vesicle constriction and explain in more detail the biological and physical meaning of these quantities. Spontaneous curvature C_0, describes membranes with possible asymmetries in the two lipid monolayers resulting in a convex ($C_0 > 0$), flat ($C_0 = 0$), or concave ($C_0 < 0$) membrane at mechanical equilibrium (see Figure 4.2). The symmetrical case results in a flat membrane at mechanical equilibrium ($C_0 = 0$), which was the case discussed in Ref. [74]. Membrane tension Σ, is defined as the mechanical work per unit area required to increase the membrane area ($\Sigma >$

0), see Section 1.3.1 in Chapter 1. It allows to describe different extensional states of biological membranes as the key regulator of cell surface mechanics [134, 156]. The differential pressure between outside and inside the vesicle Δp, which accounts for either possible osmotic imbalances, a turgor pressure, or simply a Laplace pressure due to local curvature, gives the work per unit volume to increase the vesicle volume and allows describing different turgor states of the constricted vesicles, or cells, either turgid ($\Delta p < 0$), or flaccid ($\Delta p \geq 0$). Specifically, we consider analytic solutions to the general problem of a constricted vesicle constrained by non-zero values of spontaneous curvature, non-zero external pressure, and non-zero membrane tension, in the regime where these effects and bending energy are comparable, this is when $C_0 R_m \approx 1$, and $\Delta p R_m^2 \approx \Sigma R_m^2 \approx \kappa_b (1 - C_0 R_m)^2$ (R_m being the vesicle radius, and κ_b the bending modulus).

4.2.2 Elastic Energy of a Membrane Vesicle

As described in Chapter 1, the membrane of a vesicle, or of a living cell, is composed of a lipid bilayer with a thickness that is much smaller than the dimensions of the vesicle. Therefore, the lipid bilayer can be represented approximately by a two-dimensional mathematical surface in the context of the mechanics of the whole cell. In 1973, Helfrich [34], proposed a simple expression for the bending energy of a membrane in terms of the contributions from mean curvature H (first term, E_m) and Gaussian curvature K (second term, E_G), which are the two geometrical invariants that define the local curvature of the membrane [35]

$$E_b = E_m + E_G = \frac{\kappa_b}{2} \int_\Omega (2H - C_0)^2 \, \mathrm{d}A + \kappa_G \int_\Omega K \mathrm{d}A \,. \tag{4.1}$$

Here, Ω is the closed surface that defines the membrane vesicle, and $\mathrm{d}A$ its element of area. The parameters κ_b and κ_G are the bending modulus and the Gaussian bending rigidity, respectively. The spontaneous curvature, C_0, permits to describe bilayers that are spontaneously curved in their equilibrium state due to the compositional inhomogeneity between the inner and the outer monolayers. This term represents the spontaneous tendency of the membrane to build up in a concave (as $C_0 < 0$), convex (as $C_0 > 0$), or flat (as $C_0 = 0$) surface (see Figure 4.2). In this chapter, we assume that C_0 is uniform over the vesicle.

In terms of the local principal curvatures of the membrane surface, C_1 and C_2, we have $H = (C_1 + C_2)/2$ and $K = C_1 C_2$, and the bending energy of the vesicle takes the form

$$E_b = \frac{\kappa_b}{2} \int_\Omega (C_1 + C_2 - C_0)^2 \, \mathrm{d}A + \kappa_G \int_\Omega C_1 C_2 \mathrm{d}A \,. \tag{4.2}$$

For a spherical shell of radius R_0, $C_1 = C_2 = 1/R_0$, the bending energies are $E_m^{(\mathrm{sph})} = 8\pi\kappa_b (1 - R C_0/2)^2$ and $E_G^{(\mathrm{sph})} = 4\pi\kappa_G$ for the mean and Gaussian contributions, respectively. A non-zero value for the spontaneous curvature has strong effects on the configuration of the spherical shell. First, it introduces a characteristic length scale $l_c \approx C_0^{-1}$, differently to the case of zero spontaneous curvature for which the deformation energy is a size invariant, this is $E_b(C_0 = 0) = 8\pi\kappa_b + 4\pi\kappa_G$. Since the bending energy of a spherical shell with $C_0 \neq 0$ is dependent on R_0 as $E_b(R_0; C_0) = 8\pi\kappa_b (1 - R_0 C_0/2)^2 + 4\pi\kappa_G$, it minimizes at a radius $R_0 = R_{\min} = 2C_0^{-1}$, with the evident consequence that the spherical shell with the lowest bending

energy $E_b^{(\min)}(R_{\min}) = 4\pi\kappa_G$ corresponds to the particular size $R_{\min} = 2C_0^{-1}$ at $C_0 \neq 0$. This conclusion is true for arbitrary shapes [35], meaning that the bending energy is a function not only of cell shape but also of cell size at $C_0 \neq 0$. In addition, the sign of C_0 influences the favored shape of the deformed vesicle [35]; predominantly convex pear-like shapes are preferred if $C_0 > 0$, and predominantly concave shapes are favored if $C_0 < 0$ (see Figure 4.2).

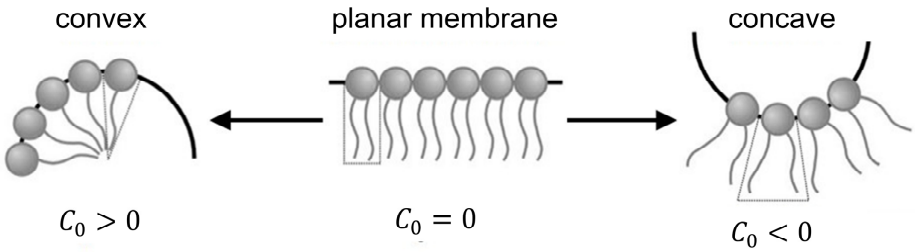

Figure 4.2. Cartoon illustrating how local membrane curvature is determined by the molecular structure of the constituting lipids. Usual phospholipids with a cylindrical molecular aspect assemble as planar membrane aggregates (only a monolayer is shown). In this case (central panel), the equilibrium configuration essentially corresponds to flat bilayer with a zero spontaneous curvature. Charged phospholipids, or lysed species with only one acyl chain present, which show an inverted-cone molecular aspect, cause the membrane to spontaneously bend in a convex configuration (left panel). Inclusion of these membrane molecular formers with a bigger polar head than the thin hydrophobic counterpart leads to situations with positive values of local spontaneous curvature ($C_0 > 0$). Conversely, cone-like phospholipids (right panel), with a big hydrophobic counterpart thicker than the polar head, leads to membrane aggregates with a concave configuration, which represents an equilibrium bending characterized by a negative spontaneous curvature ($C_0 < 0$).

Under the external pressure Δp (the outer minus the inner pressure; $\Delta p < 0$ for an inflated vesicle) and under the action of the membrane tension Σ , the total energy of a vesicle is given by

$$E_T = E_b + \int_\Omega \Sigma \mathrm{d}A + \Delta p \int_V \mathrm{d}V\,, \tag{4.3}$$

where $\mathrm{d}V$ is the element of volume enclosed by the vesicle. Here, we assume that Σ is uniform along the membrane surface and Δp isotropic. Consequently, we can express the Eq. (4.3) as

$$E_T = E_b + \Sigma\, \mathrm{A} + \Delta p V. \tag{4.4}$$

Obviously, changing the membrane shape from its equilibrium configuration changes the total energy [Eq. (4.4)]. However, the Gauss-Bonnet theorem (see Section 1.3.1 in Chapter 1), shows that the integral over the Gaussian curvature, the second term in Eqs. (4.1) and (4.2), is constant for surfaces with the same topology. Since the constriction process in a vesicle does not change its topology, and only involves shapes that are topologically equivalent to a sphere (no holes), the contribution of E_G can be ignored because it remains constant, with $E_G = E_G^{(\mathrm{sph})} = 4\pi\kappa_G$, independently of the size and shape of the vesicle. For the final state, in which the vesicle splits into two separated daughters, it is required to consider the Gaussian contribution since the topological change to two spheres requires an increase of curvature energy by $\Delta E_G = 4\pi\kappa_G$. Therefore, during the constriction process (before the final fission), we only analyze the variations of energy due to the mean curvature E_m and the effects of external pressure and membrane tension.

We consider the particular case of axisymmetric shapes with the axis of symmetry along the x–axis (see Section 1.3.2 in Chapter 1). When these shapes are represented in Cartesian coordinates as $\vec{r} = (x, y, h(x, y))$ with $h(x, y)$, the surface profile can be given as a height on the $x - y$ plane,

$$h(x, y) = \pm\sqrt{R^2(x) - y^2}, \tag{4.5}$$

where $R(x)$ is the functional form describing the membrane profile in the $x - z$ plane (see Figure 4.3A). If the membrane surface is located between x_i and x_f, its bending energy is given by [35]

$$E_m = \pi\kappa_b \int_{x_i}^{x_f} K_m(x)\mathrm{d}x\,, \tag{4.6}$$

with the kernel

$$K_m(x) = \frac{\left[1 + R_x^2 - R_{xx}R - RC_0(1 + R_x^2)^{3/2}\right]^2}{R(1 + R_x^2)^{5/2}}, \tag{4.7}$$

where $R_x = \partial R/\partial x$ and $R_{xx} = \partial R_x/\partial x$ are, respectively, the first and second derivatives of the membrane profile $R(x)$. Furthermore, other relevant vesicle properties can also be computed, particularly the membrane area and the volume enclosed. For a given profile shape $R(x)$, the area of the corresponding revolution surface around the x–axis is

$$A = 2\pi \int_{x_i}^{x_f} R\sqrt{1 + R_x^2}\mathrm{d}x\,, \tag{4.8}$$

and the volume enclosed by this surface is

$$V = \pi \int_{x_i}^{x_f} R^2\mathrm{d}x\,. \tag{4.9}$$

Note that Eqs. (4.7)-(4.9) are independent of the coordinate y, as expected for surfaces with rotational symmetry around x. Along the constriction pathway, the vesicle will take the shapes that minimize the total energy E_T (up to thermal effects). In particular, E_T must be stationary under an infinitesimal scale transformation $\vec{r} \to \lambda\vec{r}$ with small $\lambda - 1$. This leads to the following transformations [71], $\kappa_b \to \kappa_b$, $C_0 \to C_0/\lambda$, $C_1 \to C_1/\lambda$, $C_2 \to C_2/\lambda$, $A \to \lambda^2 A$, $V \to \lambda^3 V$, $\Sigma \to \Sigma/\lambda^2$, and $\Delta p \to \Delta p/\lambda^3$. This means that the shape that minimizes the energy with C_0, Σ, and Δp, has the same energy (and also minimize the energy) under an overall dilatation $\vec{r} \to \lambda\vec{r}$ with $C_0 \to C_0/\lambda$, $\Sigma \to \Sigma/\lambda^2$, and $\Delta p \to \Delta p/\lambda^3$. Note that when $C_0 = \Sigma = \Delta p = 0$, the total energy of the vesicle, which is equal to the bending energy, becomes size invariant. This particular case was previously studied by us in Refs. [74, 75]. Here, we consider the more general case, where C_0, Σ, and Δp are non-zero, and analyze the effects of these parameters for the more relevant properties of the system.

4.2.3 Perturbation Method

We consider the constriction process of a membrane vesicle with rotational symmetry around the longitudinal axis and with central symmetry. The break of the central symmetry can be treated as a stability problem against a linear perturbation from the symmetric case [74, 75]. The initial vesicle deforms by the action of a radial tension exerted as a constriction ring at its equator, which decreases the equator radius till formation of a saddled neck that becomes thinner and thinner under the action of the constriction force (see Figure 4.3). These processes will be followed by the vesicle splitting into two separated daughter vesicles. In previous works [74, 75], we restricted the study to the case of zero spontaneous curvature $C_0 = 0$, negligible tension $\Sigma = 0$, and no pressure difference between internal and external media $\Delta p = 0$, in which the total energy of the vesicle corresponds exclusively to the bending energy (up to thermal effects). In that particular case, the unconstricted initial configuration is a sphere of radius R_m and the constriction process is assumed to proceed by keeping this maximum radius R_m constant, which is equivalent to consider that the two polar caps are hemispheres of radius R_m during the whole process. In the present case, as the parameters C_0, Σ, and Δp are non-zero, the initial configuration is not, in general, a sphere of radius R_m, but a spheroid with polar radius R_m (distance from the center to the upper pole of the spheroid) . This spheroid can be an oblate spheroid (when the polar distance L_p, see Figure 4.3A, is smaller than R_m), a prolate spheroid (when the polar distance L_p is greater than R_m) or a sphere (when the polar distance L_p is equal to R_m). The value of the dimensionless ratio L_p/R_m will depend on the particular values of the dilatation invariant products $C_0 R_m$, ΣR_m^2, and $\Delta p R_m^3$. As in Refs. [74, 75], the constriction is assumed to proceed by keeping the polar radius R_m constant, which implies that, by fixing constant C_0, Σ, and Δp, the shape of the polar caps remains equal to the initial configuration at all stages of constriction. Consequently, the total energy of the polar caps does not change during constriction, making all energy variations arise from central constriction region that goes from $R_c = R_m$ to $R_c = 0$ (see Figure 4.3). The case of constant R_m may describe cells whose structure or contents (cytoskeleton, peptidoglycan wall, nucleoid exclusion) exert an effective line tension at the maximum radius sites towards the exterior, σ_m. Similarly, the force needed to constrain up to a radius R_c is delivered by an effective line tension σ_c around all the constriction ring and directed towards the cell interior (see Figure 4.3A).

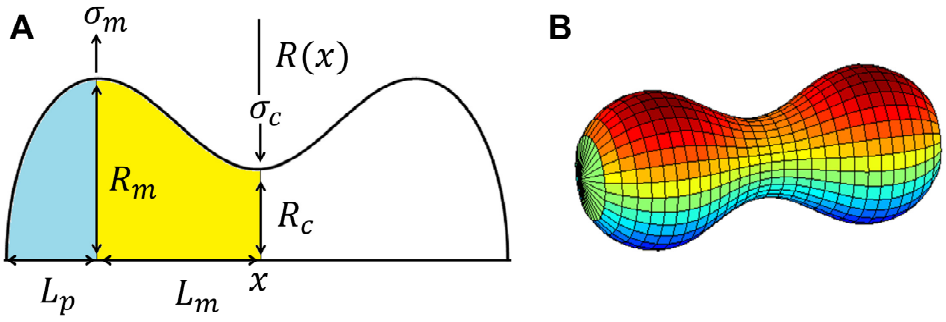

Figure 4.3. (A) Profile $R(x)$ of a symmetrically constricted vesicle with the axis of symmetry along the x–axis and its characteristic parameters. Left polar cap is shaded in yellow and the left half of the constriction zone is shaded in blue. (B) Surface obtained from the revolution around the x–axis of the previous profile $R(x)$.

Each constriction state can be characterized by a constriction parameter s, which is defined in terms of the ratio between the constriction radius R_c and the polar radius R_m in the form

$$s = 1 - R_c/R_m\,. \tag{4.10}$$

This parameter increases from $s = 0$ when there is no constriction and $R_c = R_m$ to $s = 1$ when the constriction is maximal and $R_c = 0$ (see Figure 4.4).

Once the origin of the x coordinate is established in the middle point of the vesicle (see Figure 4.3), the constriction profile is given by

$$R(x;s) = \begin{cases} R_{\text{left polar cap}}(x) & \text{if} \quad x \in \left[-L_p - L_m, -L_m\right] \\ R_{\text{cz}}(x;s) & \text{if} \quad x \in \left[-L_m, L_m\right] \\ R_{\text{right polar cap}}(x) & \text{if} \quad x \in \left[L_m, L_m + L_p\right] \end{cases}, \tag{4.11}$$

where L_m and L_p represent the half of the length of the constriction zone and the polar distance, respectively (see Figure 4.3A). Note that the constriction profile must be continuous in the boundaries of the zones. In addition, since the shape has central symmetry we have the relation $R_{\text{left pole cap}}(x) = R_{\text{right pole cap}}(-x)$.

The perturbative method allows us to easily obtain approximate analytical formulas in terms of C_0, Σ, Δp and the scaling parameter R_m. We need to determine the shapes that minimize the total energy of the vesicle along the constriction pathway, *i.e.*, for each constriction stage s between 0 and 1. In order to determine the approximate shape, we assume an appropriate ansatz for $R(x)$ in each of the existence intervals. These ansatzs will be expressed in terms of the characteristic length rates of each zone: L_p/R_m for the polar caps and L_m/R_m and s for the constriction zone (recall that the polar caps remain constant independently of s). The constriction profile $R(x)$, together with its first and second derivatives, $R_x = \partial R/\partial x$ and $R_{xx} = \partial R_x/\partial x$, allow us computing the integrand K_m [Eq. (4.7)] in each zone. Recall that we are assuming that C_0 and Σ are uniform along the whole surface. In order to apply the perturbative method it is convenient to define a small deformation function and expand K_m in power series of it and of its first- and second-order derivatives. Then, introducing this simplified integrand in the total energy [Eq. (4.6)], we can perform the integration between the two boundaries that define the corresponding surface interval [Eq. (4.11)]. Finally, the total energy minimization with respect to the characteristic length of each zone provides their optimal values

$$\frac{\partial E_{T,\,\text{polar caps}}\left(L_p, R_m, C_0, \Sigma, \Delta p, \kappa_b\right)}{\partial L_p} = 0 \xrightarrow{\text{yields}} L_p = L_p^{\text{opt}}, \tag{4.12a}$$

$$\left.\frac{\partial E_{T,\,\text{cz}}(s, L_m, R_m, C_0, \Sigma, \Delta p, \kappa_b)}{\partial L_m}\right|_s = 0 \xrightarrow{\text{yields}} L_m(s) = L_m^{\text{opt}}(s). \tag{4.12b}$$

As the polar caps do not change their shape during the whole constriction process, the polar distance L_p [Eq. (4.12a)] is independent of the constriction parameter s, (and therefore, the other properties of the system calculated on the polar caps zone are independent of s too). However, the length of the constriction zone changes with the constriction parameter s. Once the optimal total length $L_p^{\text{opt}} + L_m^{\text{opt}}(s)$ is obtained, it is possible to determinate approximate analytical expressions for the more relevant properties of the system as are the total energy, the membrane

area, the volume enclosed and the constriction force at any stage of constriction. These quantities will have the form of a series expansion in powers of the constriction parameter, s. In general, we found that, as expected, that the higher the order included, the better the predictions obtained.

4.2.4 Shape of the Polar Caps Zone: Area and Volume

The polar caps of a tensionless vesicle ($\Sigma = 0$), without pressure difference ($\Delta p = 0$) and for zero spontaneous curvature ($C_0 = 0$) with maximum radius R_m fixed constant, remain as hemispheres of radius R_m during the whole constriction process [74, 75]. However, if these parameters (Σ, Δp, and C_0) are not zero, we have to consider a more general profile for the polar caps. We consider here an ellipsoid with semi-axis R_m (polar radius) and L_p (polar distance) centered in $x = L_m$ (see Figure 4.3A) with rotational symmetry around x-axis given by

$$R_{\text{right polar cap}}(x) = \pm R_m \sqrt{1 - \left(\frac{x - L_m}{L_p}\right)^2}, \quad x \in [L_m, L_m + L_p\,]. \tag{4.13}$$

Now, in order to apply the perturbative method, we define the small deformation function in the polar caps zone as (see Figure 4.3)

$$\epsilon = \frac{L_p - R_m}{R_m}, \tag{4.14}$$

which leads to

$$L_p = R_m(1 + \epsilon). \tag{4.15}$$

The global sign of ϵ determines the shape of the polar caps. When ϵ is negative, positive, or zero, the polar caps are oblate, prolate, or spherical, respectively.

Once we have calculated the length L_p, other relevant magnitudes can be obtained, particularly the membrane area of the polar caps and the volume enclosed on them. Using the expressions for a surface of revolution [Eqs. (4.8) and (4.9)] with the profile of the Eq. (4.13), and integrating between the limits $x_i = L_m$ and $x_f = L_m + L_p$ (see Figure 4.3A) we obtain for the membrane area

$$A_{\text{polar caps}}/A_{\text{sph}} = 1 + \frac{2}{3}\epsilon + \frac{1}{15}\epsilon^2 + \cdots, \tag{4.16}$$

where $A_{\text{sph}} = 4\pi R_m^2$, and for the volume enclosed

$$V_{\text{polar caps}}/V_{\text{sph}} = 1 + \epsilon = L_p/R_m\,, \tag{4.17}$$

where $V_{\text{sph}} = 4/3\pi R_m^3$. Note that the Eq. (4.16) can be also obtained by expanding the surface area of the spheroid around $\epsilon = 0$, $A_{\text{spheroid}} = 2\pi R_m^2[1 + L_p/(R_m e)\text{ArcSin}(e)]$ with $e^2 = 1 - \left(R_m/L_p\right)^2 = \epsilon(\epsilon + 2)/(1 + \epsilon)^2$; and the Eq. (4.17) is exact and corresponds to the volume of the spheroid, $V_{\text{spheroid}} = 4/3\,\pi R_m^2 L_p$.

4.2.5 Shape of the Constriction Zone: Area and Volume

In Ref. [74], we used the variational approach to find the shape that minimize the energy for different constriction stages in the case of $C_0 = 0$, $\Sigma = 0$ and $\Delta p = 0$. There, we considered a family of solutions of the form

$$R(x;s) = R_0(x) + \sum_{i=1}^{\infty} a_i R_i(x) \tag{4.18}$$

in order to describe the constriction region, where the assumed zeroth-order function family was

$$R_0(x;s) = R_m\left\{1 - \frac{s}{2}\left[1 + \cos\left(\frac{\pi x}{L_m}\right)\right]\right\}. \tag{4.19}$$

This simple zeroth-order provided good approximations for low and intermediate constriction regimes, as we previously saw in Ref. [75]. Consequently, we use here this term as the profile of the constriction region in order to apply the perturbative method to the general case. We define the small deformation function in the constriction region as

$$u(x;s) = R_m - R_{\mathrm{cz}}(x;s) = (R_m/2)s[1 + \cos(\pi x/L_m)]. \tag{4.20}$$

Introducing $R_{\mathrm{cz}}(x;s)$ in terms of $u(x;s)$ in the kernel of the total energy [Eq. (4.7)] and expanding it up to the fourth-order of perturbation in u (a higher-order expression can be found in Section A4.2 of Annex A4) we obtain

$$\begin{aligned} K_{T,\mathrm{cz}} = {} & \frac{1}{R_m} - 2C_0 + C_0^2 R_m + \Delta\tilde{p}R_m^2 + 2R_m\tilde{\Sigma} \\ & + \frac{1}{R_m^2}u - C_0^2 u - 2\Delta\tilde{p}R_m u - 2\tilde{\Sigma}u + 2uu_{xx} - 2C_0 R_m u_x \\ & + \frac{1}{R_m^3}u^2 + \Delta\tilde{p}u^2 + 2C_0 uu_{xx} + R_m u_{xx}^2 - \frac{1}{2R_m}u_x^2 + \tilde{\Sigma}R_m u_x^2 \\ & + \frac{1}{R_m^4}u^3 - 3u_x^2 u_{xx} + 2C_0 R_m u_x^2 u_{xx} - uu_{xx}^2 - \frac{C_0^2}{2}uu_x^2 - \frac{1}{2R_m^2}uu_x^2 - \tilde{\Sigma}uu_x^2 \\ & + \frac{1}{R_m^5}u^4 - 2C_0 uu_x^2 u_{xx} - \frac{5R_m}{2}u_x^2 u_{xx}^2 + \frac{3}{8R_m}u_x^4 - \frac{1}{2R_m^3}u^2 u_x^2 - \frac{C_0^2 R_m}{8}u_x^4 + \cdots. \end{aligned} \tag{4.21}$$

As in the polar caps zone, once we know the dimensionless ratio L_m/R_m, we can determine other relevant vesicle properties, as are the membrane area of the constriction zone and the volume enclosed on it. Introducing the functional form $R(x)$ in terms of the small-$u(x)$ variable [Eq. (4.20)] in the formula of the membrane area [Eq. (4.8)] and expanding the integrand in a Taylor series up to fourth order in u, we obtain

$$A_{\mathrm{cz}} = 2\pi\int_{x_i}^{x_f} R\sqrt{1 + R_x^2}\,\mathrm{d}x = 2\pi\int_{x_i}^{x_f}\left[R_m - u + \frac{R_m}{2}u_x^2 - \frac{1}{2}uu_x^2 - \frac{R_m}{8}u_x^4 + \cdots\right]\mathrm{d}x. \tag{4.22}$$

Similarly, expressing the integrand of the formula of the volume enclosed [Eq. (4.9)] in terms of the small variable $u(x)$ [Eq. (4.20)] we obtain the exact result

$$V_{\mathrm{cz}} = \pi \int_{x_i}^{x_f} R^2 \mathrm{d}x = \pi \int_{x_i}^{x_f} (R_m - u)^2 \mathrm{d}x = \pi \int_{x_i}^{x_f} (u^2 - 2R_m u + R_m^2)\, \mathrm{d}x\,. \tag{4.23}$$

4.2.6 Exact Numerical Method: Euler-Lagrange Equations

Analytical formulas derived with the perturbative method are compared with the (exact) solution of the Euler-Lagrange equations computed numerically. The Euler-Lagrange equations do not have an analytical solution in general, but can be solved numerically and different methods have been developed to solve them. As we previously made when we studied the case with $C_0 = \Sigma = \Delta p = 0$ in Ref. [74], we use the methodology proposed in Refs. [71, 72], and apply it to axisymmetric shapes subject to equatorial constriction stress with polar radius R_m maintained constant (see Section A4.1 in Annex A4 for a brief explanation of the numerical procedure followed).

4.2.7 Experimental Values of Bending and Gaussian Moduli

Experimental measurements of the bending modulus κ_b of lipid bilayers in the fluid state give values in the order of 10^{-19} J, or $10 - 20\ k_B T$ at ambient temperatures [35, 41, 157, 158]. They are obtained mostly either from analysis of thermally induced bending fluctuations, or more recently from pipette-aspiration techniques [41]. Observations of the phase behavior of lipid bilayers suggests that $\kappa_G \approx -0.8\kappa_b$ [41, 159], which yields a Gaussian energy contribution to the energy of membrane fusion $4\pi\kappa_G$ in the order of 10^{-18} J, or $100\ k_B T$ at ambient temperatures [160]. Recall that the Gaussian curvature energy is constant for surfaces with the same topology, independently of the size and shape of the surface. Only when fusion process happen, will the Gaussian energy contribution be considered.

4.3 Results

The fundamental scales of the physical problem are determined both by the polar radius R_m, which defines the spatial scale, and the bending modulus κ_b, which defines the energy scale. In a scaling description, given a set of constitutive parameters (κ_b, C_0, R_m), the perturbation problem can be analytically solved for different values of the external fields $(\Sigma, \Delta p)$. The geometrical descriptors (volume, area, length, ...) and the mechanical ones (energy, force, ...) will be defined in terms of power series of two form parameters, the small parameter ϵ, which defines the shape aspect of the polar caps [see Eq. (4.14)], and the constriction parameter s, which defines the shape of the constriction region [see Eq. (4.19)]. Furthermore, the two conditions for energy minimization [see Eqs. (4.12)] establish additional constraints in the equilibrium problem, which are described by two independent linear relationships between constitutive properties and external fields; these are:

$$\Lambda = (1 - C_0 R_m)^2 + 2\tilde{\Sigma} R_m^2 + \Delta\tilde{p} R_m^3, \tag{4.24}$$

$$\Gamma = (2 - C_0 R_m)^2 + 2\tilde{\Sigma} R_m^2 - 1, \tag{4.25}$$

with

$$\tilde{\Sigma} = \frac{\Sigma}{\kappa_b}, \quad \Delta\tilde{p} = \frac{\Delta p}{\kappa_b}. \tag{4.26}$$

where Λ and Γ represent functional forms for the variations of the elastic Hamiltonian that minimize the energy of the vesicle for generalized geometry. In the particular case of constant Λ and Γ, these functional forms are linked to geometrical conditions that minimize the energy and constitute generalized Young-Laplace equations [76, 161], which establish the equilibrium condition between the surface tension and the differential pressure for the different spheroidal geometries defined by the specific values of Λ and Γ. In particular, values of $\Lambda \neq 1$ correspond to spheroids while $\Lambda = 1$ stands for the sphere. The meaning of Γ is more cumbersome, however since $\Gamma = \Lambda + 2(1 - C_0 R_m) - \Delta\tilde{p} R_m^3$, it essentially refers to the inflation status of a given spheroidal shape. The exact numerical method depicted in Section 4.2.6, and further described in Section A4.1 of Annex A4, allows for an accurate description of the constriction pathways of the different spheroids, whose initial surface area and volume are mutually linked for given values of the constitutive parameters $\{C_0, \Sigma, \Delta p\}$ through Eqs. (4.24)-(4.26). A graphical summary of the main results is shown in Figure 4.4, which shows the constriction shapes of representative spheroids along the minimal energy pathway defined at constant Λ. In the following, the approximate solutions provided by perturbation method proposed in Sections 4.2.1-4.2.5 are compared with the exact solutions provided by the numerical analysis of the Euler-Lagrange equations (see Section 4.2.6).

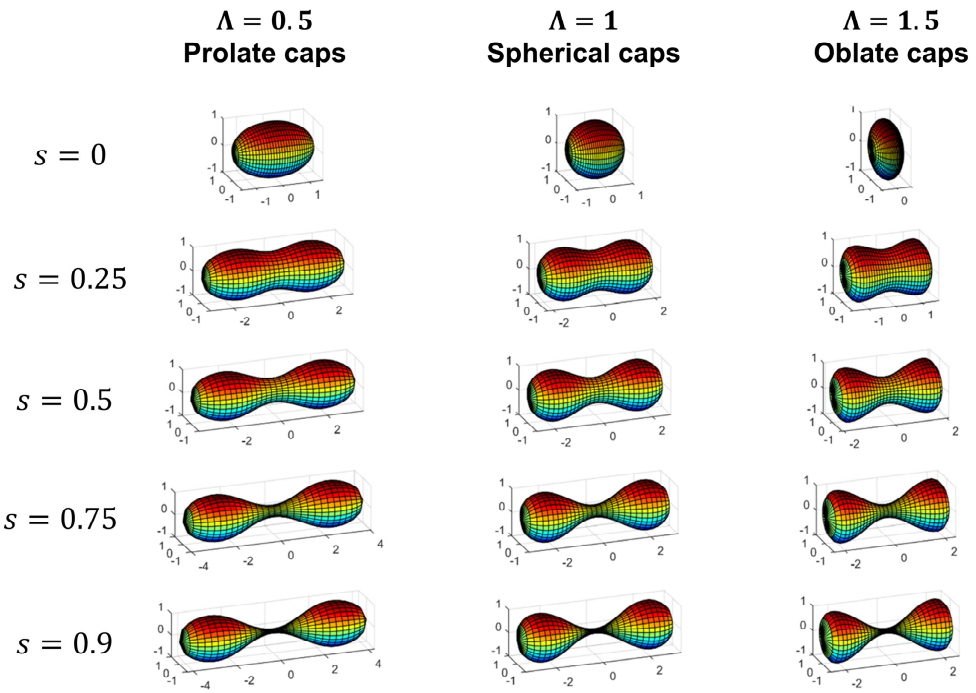

Figure 4.4. Shapes at various constriction stages characterized by the constriction parameter s [Eq. (4.10)] ($s = 0$; $s = 0.25$; $s = 0.5$; $s = 0.75$; and $s = 0.9$) for initially unconstricted prolate, spherical, and oblate vesicles. Prolate case ($L_p = 1.5R_m$) with $\Lambda = 0.5$, spherical case ($L_p = R_m$) with $\Lambda = 1$, and oblate case ($L_p = 0.5R_m$) with $\Lambda = 1.5$, and $\Gamma = -24$ for the three cases represented [see Eq. (4.24) and (4.25) for the definitions of Λ and Γ in terms of $C_0 R_m$, $\tilde{\Sigma} R_m^2$ and $\Delta\tilde{p} R_m^2$]. When $\Gamma > -29$: $\Lambda < 1$ gives prolate polar caps (*i.e.*, $L_p > R_m$), $\Lambda = 1$ gives spherical polar caps (*i.e.*, $L_p = R_m$), and $\Lambda > 1$ gives oblate polar caps (*i.e.*, $L_p < R_m$); while when $\Gamma < -29$ the opposite relation between the values of Λ and the shape of the polar holds.

4.3.1 Approximate Analytical Expressions

In this section we show the approximate analytical expressions obtained for both polar caps and constriction zone in the regime where mechanical work due to osmotic pressure, surface tension, and bending energy are comparable, *i.e.*, $\Delta p R_m^3 \approx \Sigma R_m^2 \approx \kappa_b (1 - C_0 R_m)^2$. A similar condition applies for the spontaneous curvature, which is restricted to the interval $-1 \leq C_0 R_m \leq 1$. We have derived the expressions of the characteristic length, the total energy, the membrane area, and the volume enclosed in both zones. These expressions are given in terms of the spontaneous curvature C_0, the membrane tension Σ, the external pressure Δp, and the polar radius R_m. In the constriction zone these expressions also depend on the constriction parameter s (recall that the polar caps remain constant independently of s). Finally, we have obtained the constriction force from the variations in the total energy during the constriction stage.

Polar caps zone

Introducing the expression of L_p [Eq. (4.15)] in Eq. (4.13) and this, in turn, in Eq. (4.7), we can integrate the resulting kernel between the limits $x_i = L_m$ and $x_f = L_m + L_p$ (see Figure 4.3A) and obtain an approximate analytical expression for the total energy of the right polar cap. As the left and the right polar caps are identical (due to the central symmetry assumed) it is enough to consider one of them and then multiply the expression by a factor 2. Up to second order of perturbation in ϵ, the total energy of the caps is

$$E_{T,\text{polar caps}} = E_{\text{sph}} + \frac{4\pi\kappa_b}{3}(\Lambda - 1)\epsilon + \frac{2\pi\kappa_b}{15}(\Gamma + 29)\epsilon^2 + \cdots, \tag{4.27}$$

where

$$\begin{aligned} E_{\text{sph}} &= 2\pi\kappa_b/3\,(2\Lambda + \Gamma + 7 - 4C_0 R_m) \\ &= \pi\kappa_b[8 + 2R_m^2 C_0^2 - 8C_0 R_m + 4R_m^2\tilde{\Sigma} + 4/3\,R_m^3\Delta\tilde{p}]. \end{aligned} \tag{4.28}$$

Our analytical approximation is valid for small departure from the spherical shape of the polar caps, *i.e.*, as long as $|\epsilon| \ll 1$. This implies that the quantities calculated in the polar caps zone are a slight modification of those corresponding to a sphere of radius R_m. After integration, the total energy of the polar caps is minimized with respect to L_p [Eq. (4.12a)], obtaining the analytical expression for the optimal polar distance L_p of the caps. This length defines the shape of minimal energy and determines if the initial vesicle was an oblate spheroid ($\epsilon < 0$), a prolate spheroid ($\epsilon > 0$), or a sphere ($\epsilon = 0$). The optimal value of L_p resulting from the minimization is determined by the Eq. (4.15) with

$$\epsilon = -\frac{5(\Lambda - 1)}{\Gamma + 29}, \tag{4.29}$$

which states the linear dependence between the function ϵ that defines the changes in the shape of the polar caps and the shape parameter Λ, which is determined by the initial shape of the vesicle. For the case of an initially spherical vesicle $\Lambda = 1$, Eq. (4.29) establishes that the caps remain spherical under an arbitrary small deformation, this is $\epsilon = 0$ (see Figure 4.4).

Note that Γ is greater than -29 when $\tilde{\Sigma}R_m^2 > -28 - (2 - C_0 R_m)^2$. This means that a wide range of values of the dilatation invariant products $C_0 R_m$ and $\tilde{\Sigma}R_m^2$ give a positive denominator in the

Eq. (4.29) and, in this case, the shape of the polar caps will be determined by the value of Λ (see Figure 4.4): $\Lambda = 1$ (or equivalently $\Delta\tilde{p}R_m^3 = 2C_0R_m - C_0^2R_m^2 - 2\tilde{\Sigma}R_m^2$) would correspond to invariably spherical polar caps, but $\Lambda < 1$ (or equivalently $\Delta\tilde{p}R_m^3 < 2C_0R_m - C_0^2R_m^2 - 2\tilde{\Sigma}R_m^2$) would correspond to prolate polar caps, and $\Lambda > 1$ (or equivalently $\Delta\tilde{p}R_m^3 > 2C_0R_m - C_0^2R_m^2 - 2\tilde{\Sigma}R_m^2$) would correspond to oblate polar caps. If Γ is less than -29, which corresponds to strongly negative surface tension $2\tilde{\Sigma}R_m^2 < -28 - (2 - C_0R_m)^2$, then the denominator of Eq. (4.29) takes negative values, and the correlation between the sign of $\Lambda - 1$ and the shape of the polar caps is inverted. If $\Gamma = -29$, the perturbative approach is not valid since gives $\epsilon = -\infty$.

Substituting the perturbative parameter ϵ [Eq. (4.29)] in Eqs. (4.27), (4.16) and (4.17) we obtain the approximate analytical expressions for the energy of the polar caps, their membrane area, and the volume enclosed on them, respectively. For any combination of values of C_0R_m, $\tilde{\Sigma}R_m^2$, and $\Delta\tilde{p}R_m^3$ giving $|\epsilon| \ll 1$ [Eq. (4.29)], the errors between the numerical and the analytical calculations for the polar caps are lower than 5% in all the properties determined. These errors are lower in the cases in which the ratio L_p/R_m is closer than 1, since in these cases the perturbative parameter ϵ becomes smaller in modulus (see Figures 4.5F and 4.6F).

Constriction zone

Integrating Eq. (4.21) between the limits $x_i = -L_m$ and $x_f = L_m$ (see Figure 3A), we obtain an approximate analytical expression for the total energy of the constriction zone. Minimizing this energy with respect to L_m [Eq. (4.12b)] allows deriving the perturbative expansion for the optimal value of the constriction length

$$L_m/R_m \approx \frac{\pi}{2}\left(\frac{6}{\Lambda}\right)^{1/4} s^{1/2}\left\{1 + \frac{1}{288\Lambda}\left[72(\Lambda - \Gamma) + (\Gamma - 4)6^{3/2}\Lambda^{1/2} - 256^{1/2}\Lambda^{3/2}\right]s + \cdots\right\}. \quad (4.30)$$

This formula determines the aspect ratio of the shape of minimal energy for each constriction stage, characterized by the constriction parameter s, up to fourth-order in the perturbative expansion (see Section A4.2 in Annex A4 for a higher-order formula).

Substituting the optimal constriction length in the equation for the total energy [Eq. (4.6)], we obtain the approximate analytical expression for the increase in the total energy due to constriction

$$\Delta E_T/\kappa_b = E_{T,\,cz}/\kappa_b \approx \frac{4}{3}\pi^2 6^{1/4}\Lambda^{3/4}s^{1/2}\left\{1 - \frac{3}{576\Lambda}\left[56^{1/2}\Lambda^{3/2} + 168\Lambda - (\Gamma - 4)6^{3/2}\Lambda^{1/2} - 72\Gamma\right]s + \cdots\right\}. \quad (4.31)$$

This expression is written up to fourth order in the perturbative expansion and a higher-order formula is shown in Section A4.2 of Annex A4.

Once we have calculated the dimensionless ratio L_m/R_m [Eq. (4.30)], we can determine the membrane area of the constriction zone and the volume enclosed on it. Integrating the Eq. (4.22) between the constriction zone limits $x_i = -L_m$ and $x_f = L_m$ (see Figure 4.3A) with L_m given by the Eq. (4.30), we obtain the increase of area during constriction

$$\Delta A/R_m^2 = A_{cz}/R_m^2 \approx 2\pi^2\left(\frac{6}{\Lambda}\right)^{1/4} s^{1/2}\left\{1 + + \frac{1}{576\Lambda}\left[(\Gamma-4)6^{3/2}\Lambda^{1/2} - 72\Gamma - 216\Lambda - 6^{1/2}\Lambda^{3/2}\right]s + \cdots\right\}. \quad (4.32)$$

As for other quantities, this is a fourth-order perturbation expression but a higher-order formula can be found in Section A4.2 of Annex A4. At the initial stages of constriction (when $s \to 0$) the increase of area is given by the leading term of the Eq. (4.32), *i.e.*, $2\pi^2 R_m^2 (6/\Lambda)^{1/4} s^{1/2}$, which is equal to $2\pi R_m \times 2L_m$ with L_m given by the leading term of the Eq. (4.30). Since $2\pi R_m \times 2L_m$ corresponds to the increase of area of a cylinder of length $2L_m$ and polar radius R_m, this means that that a near-cylindrical neck with length $2L_m$ is formed at the initial stages of constriction (see Figure 4.4).

Similarly, integrating the Eq. (4.23) between the constriction zone limits $x_i = -L_m$ and $x_f = L_m$ (see Figure 4.3A) with L_m given by the Eq. (4.30), we obtain the approximate analytical expression for the increase of volume during constriction up to fourth-order in the perturbative expansion of the energy integrand (see Section A4.2 in Annex A4 for higher-order expression)

$$\Delta V/R_m^3 = V_{cz}/R_m^3 \approx \pi^2\left(\frac{6}{\Lambda}\right)^{1/4} s^{1/2}\left\{1 + \frac{1}{576\Lambda}\left[(\Gamma-4)6^{3/2}\Lambda^{1/2} - 72\Gamma - 504\Lambda - 256^{1/2}\Lambda^{3/2}\right]s + \cdots\right\}. \quad (4.33)$$

Analogously to variations of area, we find that the increase of volume at the beginning of constriction ($s \to 0$) is given by the leading term of the Eq. (4.33), *i.e.*, $\pi^2 R_m^3 (6/\Lambda)^{1/4} s^{1/2}$, which is equal to $\pi R_m^2 \times 2L_m$ with L_m given by the leading term of the Eq. (4.30). This product corresponds to the increase of volume of a cylinder of length $2L_m$ and polar radius R_m, which again corresponds with having a near-cylindrical neck with length $2L_m$ at the initial stages of constriction (see Figure 4.4). Once we have calculated the properties for the polar caps and constriction zone, we sum both contributions to obtain the total values.

Finally, we determine the constriction force from the derivative of the total energy with respect to constriction radius

$$F_c \equiv -\frac{dE_T}{dR_c} = -\frac{dE_T}{ds}\frac{ds}{dR_c} = \frac{1}{R_m}\frac{dE_T}{ds}, \quad (4.34)$$

which gives

$$F_c R_m/\kappa_b \approx \frac{2\pi^2 6^{1/4}\Lambda^{3/4}}{3s^{1/2}}\left\{1 - \frac{1}{192\Lambda}\left[56^{1/2}\Lambda^{3/2} + 168\Lambda - (\Gamma-4)6^{3/2}\Lambda^{1/2} - 72\Gamma\right]s + \cdots\right\}. \quad (4.35)$$

The constriction force scales inversely proportional to R_m, *i.e.*, the smaller is the vesicle, the greater is the constriction force required. In other words, smaller cells are harder to constrict. In contrast, the force required to constriction scales proportional to the bending modulus κ_b. This implies stronger constriction forces for less flexible membranes. In the general case, in which the parameters C_0, Σ, and Δp are non-zero, the analytical expressions obtained are divided by powers of $\Lambda^{1/4}$ [see Eqs. (4.30)-(4.33) and (4.35)], which implies a divergence in the results when $\Lambda \to 0$. Therefore, our analytical approach is valid as far as the values of the dilatation invariant products $C_0 R_m$, $\tilde{\Sigma} R_m^2$ and $\Delta\tilde{p} R_m^3$ do not give a Λ close to zero [Eq. (4.24)], and the deformation functions used in the perturbative expansion (ϵ for polar caps and u for constriction zone) are

much lower than 1 in modulus. Conditions giving $\Lambda < 0$ [Eq. (4.24)] (or equivalently $\Delta\tilde{p}R_m^3 < 2C_0R_m - C_0^2R_m^2 - 2\tilde{\Sigma}R_m^2 - 1$) provide complex analytical results (impossible constriction). As we approach to the limit $\Lambda \to 0$, our model predicts very elongated prolate cells for which the symmetric mode of equatorial constriction is no longer possible since these cells cannot create a circumferential furrow at their equator.

There is a good agreement between the exact results and the approximate analytical expressions for low and intermediate constriction regimes, (approximately up to $s \approx 0.65$), (see Figures 4.5 and 4.6). This indicates that the ansatz used to parameterize the constriction zone [Eq. (4.19)] is extremely efficient in describing the exact result in these stages (as it was in Refs. [74, 75] for a more particular case). For higher constrictions, the errors are bigger, as a consequence of the zeroth-order function family assumed for the ansatz [Eqs. (4.18) and (4.19)]. Results that were more accurate would require a constriction profile more precise than Eq. (4.19), including more terms of the family of solutions in order to better accounts for the strong changes of curvature occurring in the constriction zone. The analytical result for the case with $\tilde{\Sigma}R_m^2 = -0.3$ and $C_0 = \Delta p = 0$ (empty blue triangles of Figure 4.5) differs from the exact numerical values more than the other cases. The reason is that this combination of parameters gives the closer-to-zero value of Λ and the analytical formulas diverge as Λ goes to zero.

4.3.2 External Pressure and Membrane Tension Effects

In this section, we analyze the effects of external pressure Δp and membrane tension Σ in the more relevant properties of a membrane vesicle with zero spontaneous curvature. The lower values of membrane tension and the pressure difference, the lower the energies of the vesicle and the smaller constriction forces required (see Figures 4.5A and 4.5B, respectively). This means that membranes with small or negative tension ($\Sigma \leq 0$) and immersed in an isotonic or hypotonic medium ($\Delta p \leq 0$) have less energy and constrict more easily than tensioned membranes ($\Sigma > 0$), immersed in hypertonic medium ($\Delta p > 0$). As we noted in Refs. [74, 75], a kick-off force is required to initiate constriction from the initial configuration. However, once the symmetry is initially broken, smaller forces are sufficient to advance cell constriction. At the high constriction regime, the constriction force increases in order to overcome the curvature barrier involved in the pre-fissioned state (see Figure 4.5B). The total energy of the system (see Figure 4.5A) increases along the constriction pathway up to double at maximal constriction (when $s \to 1$). In the final two-spheres fission state we have to consider the additional Gaussian curvature energy contribution of $4\pi\kappa_G \approx -100\, k_BT$, since $\kappa_G \approx -0.8\kappa_b$ [41, 159], in order to account for the topological change occurred. Inflated vesicles immersed in a hypotonic medium ($\Delta p < 0$) have more volume than vesicles immersed in an isotonic medium ($\Delta p = 0$), and these last have more volume than shrunk vesicles immersed in hypertonic medium ($\Delta p > 0$), (see Figure 4.5D). This inflation-shrinking process is explained by the osmotic turgor of the living cells. When vesicles (or cells) are placed in a hypotonic medium, water rushes into the membrane increasing the volume of the vesicle. In contrast, when vesicles are placed in a hypertonic solution, water flows out of the vesicle into the surrounding solution, decreasing its volume. When the membrane tension is positive, the increase in membrane area is lower under constriction, and vice versa (see Figure 4.5C). This is explained since positive membrane tension implies a tensioned status of the membrane vesicle, which describes biological situations of positive cortical tension with high energetic cost for membrane area extension [134]. Conversely,

negative membrane tension implies a floppy status, which describes biological situations with a low energetic cost for membrane area extension [162]. Negative surface tension is equivalent to a net production of membrane, which actually request a negative mechanical work for membrane dilation [163]. Finally, the lower values of Σ and Δp, the larger the reduced constriction length L_m/R_m (see Figure 4.5E). Moreover, when Δp and Σ are positive, $L_p/R_m < 1$, and the polar caps are oblate (see Figure 4.5F), which corresponds to a deflated vesicle with a tensioned membrane. In contrast, when Δp and Σ are negative, $L_p/R_m > 1$, and the polar caps are prolate, which corresponds to an inflated vesicle with a tensionless membrane. If $\Sigma = \Delta p = 0$, $L_p/R_m = 1$, then $\Lambda = 1$, and the polar caps are spherical. This result let us relate the shape of the polar caps with the properties of the system. Vesicles with oblate polar caps require more constriction force and contain more energy, less membrane area, and less volume enclosed than vesicles with prolate polar caps. The values $\tilde{\Sigma}R_m^2 = \pm 0.3$ and $\Delta\tilde{p}R_m^3 = \pm 0.3$ used in Figure 4.5 correspond to $\Sigma = \pm 1.2 \times 10^{-8}$ N/m and $\Delta p = \pm 1.2 \times 10^{-2}$ N/m², respectively, a realistic set of values reasonably compatible with a cell-sized artificial vesicle ($R_m \approx 1$ μm) [164, 165] with a relatively flexible lipid bilayer membrane ($\kappa_b \approx 10 - 20\, k_B T$) [35, 41, 157, 158] [Eq. (4.26)]. Specifically, Giant Unilamellar Vesicles (GUVs) with sizes ranging a few microns, subjected to osmotic stresses of the order of 10 mOsM as much ($\Delta p < -0.01$ Pa), normally exhibit a lateral tension of the order of $10^{-9} - 10^{-8}$ N/m [158, 166].

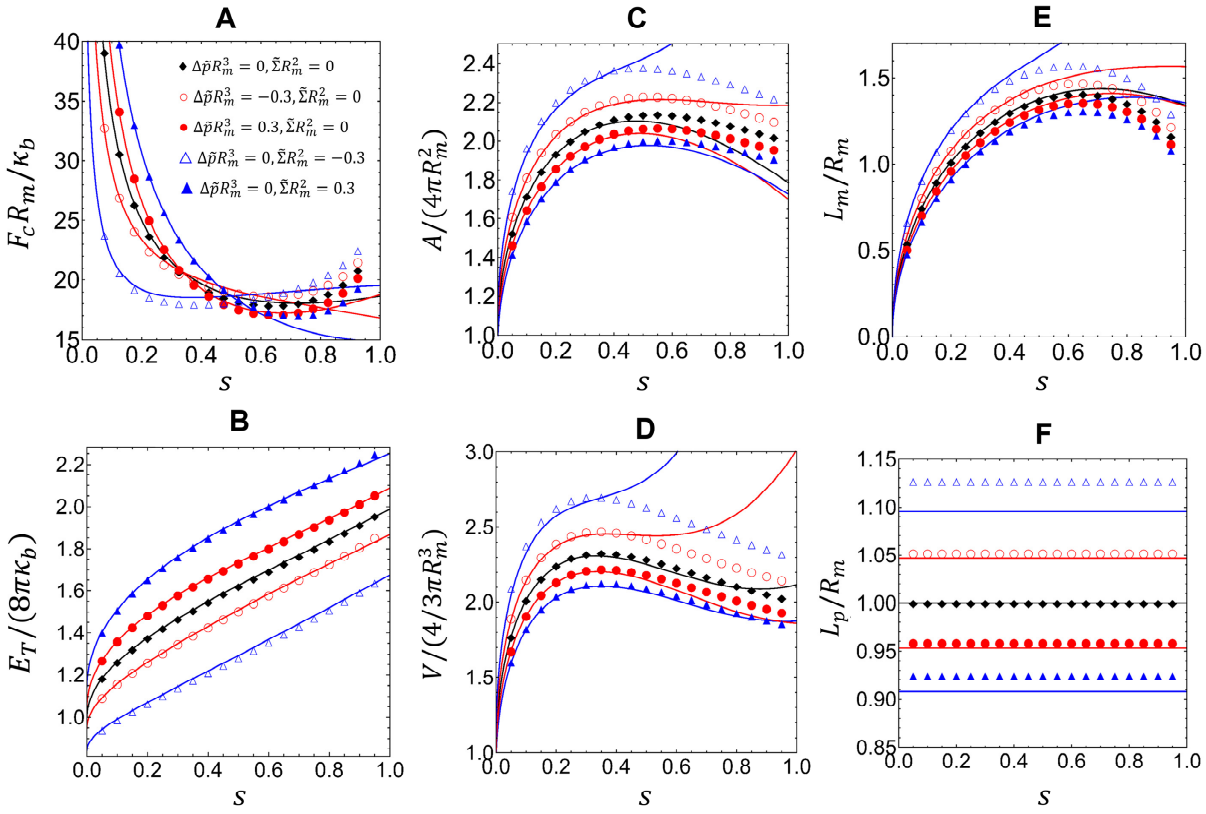

Figure 4.5. More relevant properties of a constricted vesicle with zero spontaneous curvature $C_0 = 0$ at all stages of constriction for different values of the dilatation invariant products $\tilde{\Sigma}R_m^2$ and $\Delta\tilde{p}R_m^2$ m, which are associated with surface tension and pressure, respectively. Total energy E_T in units of $8\pi\kappa_b$ (A), constriction force F_c in units of R_m/κ_b (B), total area A in units of $4\pi R_m^2$(C), total volume V in units of $4/3\pi R_m^3$ (D), constriction length L_m in units of R_m (E) and polar distance L_p in units of R_m (F). Comparison between the exact numerical results (points) with the approximate analytical expressions obtained up to sixth order of perturbation (lines).

4.3.3 Spontaneous Curvature Effects

In this section, we present the results for the constriction process of a membrane vesicle with negligible membrane tension ($\Sigma = 0$) and no pressure difference ($\Delta p = 0$) for two values of the product $C_0 R_m$, corresponding a positive and a negative spontaneous curvature, respectively. In this way, we can analyze the effects of having a convex ($C_0 > 0$) or a concave ($C_0 < 0$) membrane with respect to the flat configuration ($C_0 = 0$), see Figure 4.2. Although here we are considering constant spontaneous curvature, recall that, in general, C_0 is not uniform over the membrane of a real cell [12, 167]. The spontaneous curvature has an important effect on the constriction force (see Figure 4.6B), and a concerted inhomogeneous distribution may play a crucial role in coordinating the contractile rearrangement with the membrane remodeling curvatures are more easily constricted (require smaller constriction forces) than flat membranes. In contrast, membranes with global negative spontaneous curvature need higher constriction forces. As in Section 4.3.2, we can relate the constriction force required with the shape of the polar caps (see Figure 4.6F). Vesicles with oblate polar caps (when $L_p/R_m < 1$) require more constriction forces than vesicles with prolate polar caps (when $L_p/R_m > 1$). The total energy of the vesicle increases as a function of the stage of constriction up to near double its value at the final stage (see Figure 4.6A). The energy of the vesicles whose membranes have global negative spontaneous curvature is greater than the energy in the flat configuration, while for membranes with global positive spontaneous curvature the energy is lower. As $\Sigma = \Delta p = 0$, the total energy of the vesicle in Figure 4.6A is exclusively the bending energy. As in Section 4.3.2, in the final fissioned state we have to consider the additional Gaussian curvature energy contribution of $4\pi\kappa_G \approx -100\ k_B T$ [41, 159], in order to account for the topological change. The increase of the membrane area, vesicle's enclosed volume and constriction length along the constriction pathway is shown in Figures 4.6C, 4.6D and 4.6E, respectively. Vesicles with $C_0 < 0$, which have oblate polar caps (see Figure 4.6F), have less area, less volume, and less constriction length than vesicles with $C_0 > 0$, which have prolate caps. The values $C_0 R_m = \pm 0.3$ used in Figure 4.6 correspond to $C_0 = \pm 0.3\ \mu\text{m}^{-1}$ for a cell-sized vesicle ($R_m \approx 1\ \mu\text{m}$).

Finally, we address the analysis of the constriction force when $C_0 R_m$, $\tilde{\Sigma} R_m^2$, and $\Delta\tilde{p} R_m^3$ are different from zero simultaneously. Figure 4.7 shows three plots with the different regimes of spontaneous curvature: 4.7A with $C_0 R_m = -0.3$, 4.7B with $C_0 R_m = 0$, and 4.7C with $C_0 R_m = 0.3$, varying $\tilde{\Sigma} R_m^2$ between -0.6 and 0.6 (y-axis) and $\Delta\tilde{p} R_m^3$ between -0.3 and 0.3 (x-axis). We have calculated the constriction force at the beginning of constriction ($s = 0.2$) and compare it with the reference constriction force $F_{c,0}$, defined as the constriction force at this stage in the case of $C_0 = \Sigma = \Delta p = 0$. For given values of Σ and Δp, the larger the positive spontaneous curvature, the smaller is the constriction force required (see Figure 4.7B). This means that elongated shapes whose membranes have an uniform $C_0 > 0$ are more easily constricted, *i.e.*, those cells that tend globally to build up in a convex configuration. Membranes with positive spontaneous curvature tend to form vesicles of smaller radius $2/C_0$, which favors the formation of two separated vesicles. Thus, introducing a positive spontaneous curvature extends the region of negative constriction force, *i.e.*, the region where constrictions is an energetically favorable process (see Figure 4.7).

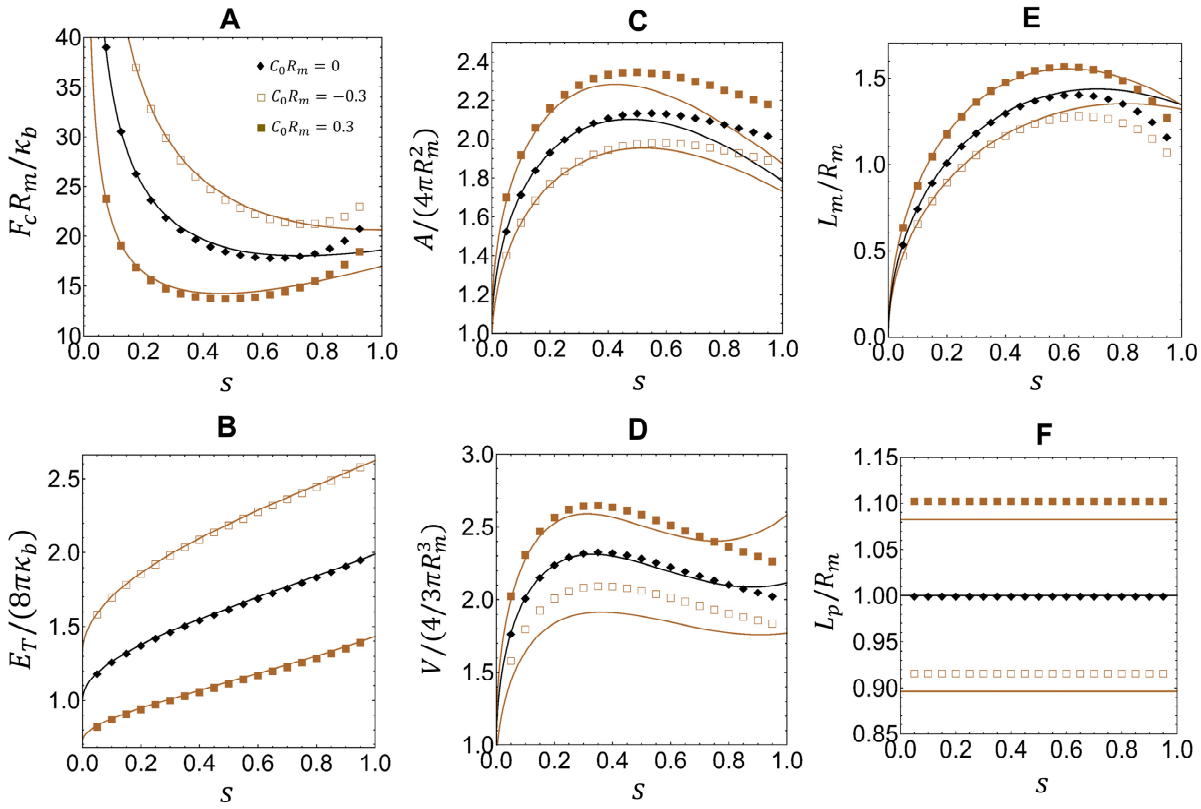

Figure 4.6. More relevant properties of a constricted vesicle at all stages of constriction for $\Sigma = \Delta p = 0$ and three values of the product C_0R_m, corresponding to have negative, zero, and positive spontaneous curvature. Total energy E_T in units of $8\pi\kappa_b$ (A), constriction force F_c in units of R_m/κ_b (B), total area A in units of $4\pi R_m^2$(C), total volume V in units of $4/3\pi R_m^3$ (D), constriction length L_m in units of R_m (E) and polar distance L_p in units of R_m (F). Comparison between the exact numerical results (points) with the approximate analytical expressions obtained up to sixth order of perturbation (lines).

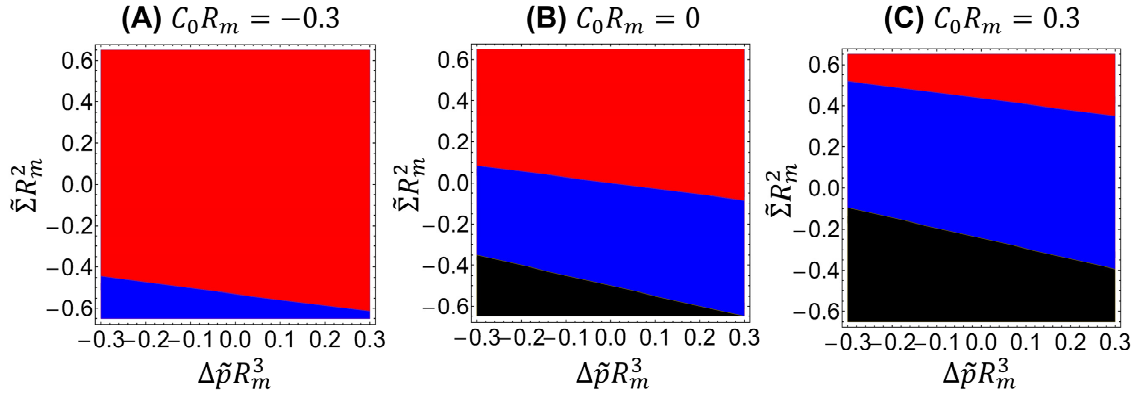

Figure 4.7. Constriction force F_c compared with the reference constriction force $F_{c,0}$ (defined as the constriction force in the case with $C_0 = \Sigma = \Delta p = 0$), both forces are computed at the beginning of constriction ($s = 0.2$). (■ $F_c > F_{c,0}$, ■ $F_c < F_{c,0}$, ■ F_c Imaginary: impossible constriction). Constriction force is shown as a function of $\tilde{\Sigma}R_m^2$ (y-axis) and $\Delta\tilde{p}R_m^3$ (x-axis) with $C_0R_m = -0.3$ (A), $C_0R_m = 0$ (B), and $C_0R_m = 0.3$ (C). Regions shaded in blue (red) correspond to conditions giving constriction forces lower (larger) than $F_{c,0}$ and regions shaded in black correspond to conditions under which constriction is impossible (imaginary analytical results, $\Lambda < 0$, and no numerical solution).

When the product C_0R_m is greater than 1 (this is, when membranes tend to form vesicles with radius smaller than $2R_m$, or cylinder sections with radius smaller than R_m), it is possible to get spontaneous constriction for a certain range of the products $\tilde{\Sigma}R_m^2$ and $\Delta\tilde{p}R_m^3$ (see Figure 4.8B, shaded in orange). This means that spontaneous constriction can be induced with appropriate low values of surface tension and osmotic pressure. If the product C_0R_m is smaller than 1 (this is, if membranes tend to form vesicles with radius bigger than $2R_m$, or cylinder sections with radius larger than R_m), there is no combination of surface tension and osmotic pressure leading to spontaneous constriction (see Figure 4.8A).

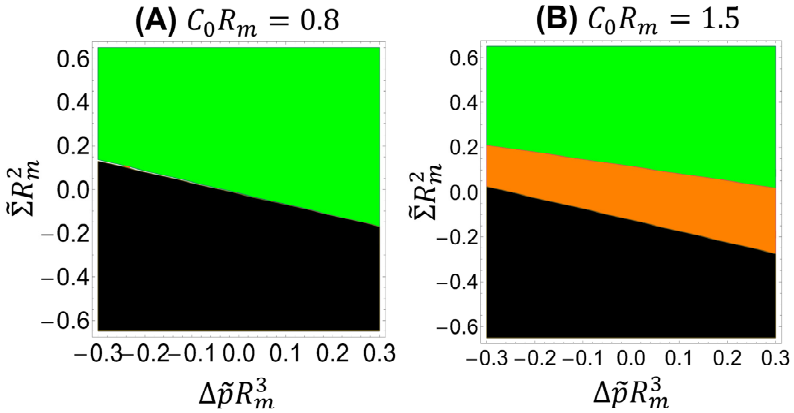

Figure 4.8. Constriction force at the beginning of constriction ($s = 0.2$) as a function of $\tilde{\Sigma}R_m^2$ (y-axis) and $\Delta\tilde{p}R_m^3$ (x-axis) with $C_0R_m = 0.8$ (A) and with $C_0R_m = 1.5$ (B). (■ $F_c > 0$: Non-spontaneous constriction, ■ $F_c < 0$: Spontaneous constriction, ■ F_c Imaginary: impossible constriction). The regions shaded in green correspond to the cases in which an external force is required for constriction. The region shaded in orange corresponds to conditions leading to spontaneous constriction (negative constriction forces). Finally, the regions shaded in black correspond to conditions under which constriction is impossible (imaginary analytical results, $\Lambda < 0$, and no numerical solution. If $C_0R_m > 1$, it is possible to get spontaneous constriction for a certain range of the products $\tilde{\Sigma}R_m^2$ and $\Delta\tilde{p}R_m^3$, but if $C_0R_m < 1$ there is no combination of surface tension and osmotic pressure leading to spontaneous constriction.

4.3.4 Constant Area and Volume Constrictions

Instead of considering the polar radius R_m constant, other conditions as constant area or constant volume could be additionally addressed. In these cases, a re-dimensioning strategy can be used, as described in the previous works [74, 75] defining a rescaling parameter λ with the following scaling transformations $\kappa_b \to \kappa_b, E_T \to E_T,\ C_0 \to C_0/\lambda,\ C_1 \to C_1/\lambda,\ C_2 \to C_2/\lambda,\ A \to \lambda^2 A, V \to \lambda^3 V, \Sigma \to \Sigma/\lambda^2$, and $\Delta p \to \Delta p/\lambda^3$. This parameter corresponds to

$$\lambda(\text{constant } A) = \sqrt{\frac{A(s=0)}{A(s)}}, \tag{4.36}$$

for constant area condition and to

$$\lambda(\text{constant } V) = \sqrt[3]{\frac{V(s=0)}{V(s)}}, \tag{4.37}$$

for constant volume condition. $A(s=0)$ and $V(s=0)$ are, respectively, the membrane area and the volume enclosed by the initial spheroid.

4.4 Discussion

4.4.1 Lipid Bilayer Membrane Vesicles

As introduced in Chapter 1, lipid molecules dispersed in water have the property to self-assemble spontaneously into a bilayer membrane. The lipid bilayer constitutes the main structural ingredient of cell membranes, which endows them with a functional mechanics chiefly determined by its intrinsic elasticity and the curvature properties encoded in the topology of the molecular components [168]. The resistance of bilayers to area compression and area expansion is much larger than their resistance to bending deformations, while, in the fluid state, there is no resistance to shear deformations. The bending moduli of usual lipid bilayers in the fluid state take values about $10 - 20\ k_B T$ [35, 41, 157, 158]. The combination of the minimization concepts discussed in this chapter has allowed the systematic exploration of vesicle energetics under constriction geometry. From our analysis of equatorial constriction (Figure 4.5B), micron-sized vesicles with a flexible lipid bilayer and a zero spontaneous curvature have constriction forces in the range $F_c R_m/\kappa_b \approx 15 - 20$. This corresponds to effective forces of the order of pico-newtons, or even lower, as for $\kappa_b \approx 10\ k_B T$ and $R_m \geq 1$ μm, one has $F_c \leq 1$ pN. Inclusion of non-zero values of spontaneous curvature, osmotic pressure and lateral tension leads to significant changes in the specific quantitative conditions necessary for equatorial constriction (see Figures 4.6-4.8). However, no essential change is imposed by these constraints in the qualitative picture, which is almost governed by a monotonic increase of the total energies upon increasing constriction, as in the reference case of no constraints ($\Sigma = \Delta p = C_0 = 0$).

4.4.2 Global Spontaneous Curvature

Among the more important biophysical consequences of lipid asymmetries, the subsequent spontaneous curvature of the whole membrane has a crucial impact on the shape transformations of artificial lipid bilayer vesicles [35], which exhibit an extreme sensitivity to induced changes in bilayer asymmetry [80]. The simplest description incorporating asymmetry between the two monolayers is given by a non-zero spontaneous curvature C_0, in which case the bending energy becomes dependent of size scale C_0^{-1}, thus being minimal for initially curved configurations. As a result, the bending energy loses size invariance and becomes depending on vesicle shape and vesicle size. As a consequence, different axisymmetric shapes of minimal bending energy can be obtained by breaking various symmetries of the sphere. Allowing for asymmetry as well as reflection symmetry, one can obtain prolate and oblate ellipsoids, which are defined by rotating an ellipse about its major and its minor axes, respectively. Negative spontaneous curvature ($C_0 < 0$) determines polar caps with a predominant oblate shape ($\Lambda > 1$); conversely, positive spontaneous curvature ($C_0 > 0$) favors prolate shapes elongated along the x axis ($\Lambda < 1$). Because of the lower energy changes of the prolate shape when subjected to equatorial constriction (see Figures 4.5B and 4.6B), the radial forces needed to constrict are significantly smaller in the case of prolate shapes ($\Lambda < 1$) than in oblates ($\Lambda > 1$) ones. According to Eq. (4.2), the energies of vesicle shapes depend on the value of the spontaneous curvature in addition to membrane tension and pressure difference, thus, we need to expand our parameter space to three dimensions. The results of minimal energy calculations performed on the basis of Eq. (4.2) subjected to the three parameters ($C_0, \Delta p, \Sigma$) are summarized in Figures 4.5 and 4.6. Total energies increase with increasing constriction from a value compatible with a

single vesicle to a 2-fold value compatible with vesicle fission. The sharper energy changes under initial constriction (s < 0.2) are observed for inflated oblates ($\Delta p < 0, \Sigma \geq 0, C_0 < 0$ thus $\Lambda > 1$), which demand on higher positive constriction forces than in the reference case of a floppy spherical vesicle ($\Lambda = 1$). For prolates shapes ($\Lambda < 1$), the required constriction forces are, in general, smaller than for oblates. Obviously, prolates shapes are easier contractible and stretchable than oblates, which explains the calculated decrease of the constriction force with increasingly positive spontaneous curvature. At large constriction ($s \to 1$), however, total energies vary almost linearly in all cases, which implies a very similar constriction force range $F_c R_m/\kappa_b \approx 20$, in the whole space of parameters. For a vesicle (or cell) of micrometer size with a flexible membrane with $\kappa_b \approx 10 - 20\ k_B T$ [35, 41, 157, 158], in case of favoring constriction under positive global curvature preferring convex prolates shapes, the constriction forces fall in the range of picoNewton, below the value for zero spontaneous curvature (see Figure 4.7B).

4.4.3 Lipid Asymmetry and Local Spontaneous Curvature

A non-zero local spontaneous curvature arises primarily from asymmetry factors in the membrane, particularly differences in the shape and aspect of the component lipids between the two sides of the bilayer. Figure 4.2 depicts the geometry exhibited by some lipid molecules as the driving force that causes spontaneous membrane curvature [30, 35, 169]. Most frequent membrane-formers are cylinder-shaped lipid molecules, which are prone to self-assemble as flat bilayers with a zero spontaneous curvature. Lipids with a polar head group area larger than the cross-sectional area measured at the level of the acyl chains show an inverted-cone shape and tend to curve the membrane positively; in other words, they exhibit positive spontaneous curvature and make the membrane prone to convexity. Prototypical of positive-curvature are lysophospholipids, which are intermediates in phospholipidic metabolism, resulted from partial hydrolysis and removing one of the acyl chains of the phospholipids. Due to their inverted-cone molecular aspect, these lysophospholipids cannot self-assemble as planar bilayers but form inverse hexagonal phase (see Figure 1.3 in Chapter 1). When incorporated into bilayers, such non-bilayer forming lipids introduce packing stresses, which, in turn, can affect membrane integrity. Although found only in small amounts in biological cell membranes, lysophospholipids have a functional role usually related to cell activation and apoptosis [170]. Conversely, cone-shaped lipids with a small head cross-section as compared to hydrophobic tails, such as polyunsaturated lipids, diacyl glycerol (DAG), phosphatidylethanolamines (PE) and cardiolipin (CL) exhibit a negative spontaneous curvature [171], which make the membrane prone to concavity. During cell division, the process of membrane constriction ends up with a separation of the lipid bilayer of the two daughter cells followed by a fusion of the opposite membranes in a region of high concavity that requires dynamic changes of the lateral distribution and the local composition of membrane lipids. Accumulated experimental evidence points out to the possible mechanical role of negative-curvature lipids during late constriction [12, 15, 167, 172–174]. Those findings demonstrate that the localized production of negative-curvature lipids is required for the proper completion of membrane dynamical process in highly negative-curvature sites, where the local accretion of asymmetric lipids may play a crucial role. Therefore, any extended theoretical model of cell division might consider local negative curvature concentrated in the constriction site of the cell membrane. Localized non-zero spontaneous curvature makes the membrane to be locally prone to a specific curvature, convex ($C_0 > 0$) or concave ($C_0 < 0$), depending of the sign of the spontaneous curvature (see Figure

4.2). Since the constriction site is saddle-shaped, local negative values of the spontaneous curvature may contribute to minimize the local bending energy of the membrane, thus making more realistic further models of cell division, specifically, those accounting for the local accretion of negative curvature lipids in the constriction region.

4.4.4 Budding and Spontaneous Fission

Binary fission and budding are two scission mechanisms exploited by cells in asexual reproduction pathways. Major difference between binary fission and budding is that in budding there is an asymmetric outgrowth from the parent individual vesicle, or cell, producing a bud, but in binary fission the parent symmetrically splits into two more or less identical offspring. In biological cells, budding is a rather frequent event, because it represents the first step in the production of transport vesicles which shuttle between different compartments of the cell. The simplest approach to understand budding involves a consideration of the lateral and transverse organization of lipids within a membrane, which induces spontaneous curvature followed by morphological change. In an early hypothesis to bud formation, Sheetz and Singer suggested that a local change in the surface area of the two monolayers could lead to negative membrane curvature, inducing the formation of a membrane neck [77]. However, advanced models for bud formation in biological cells emphasize a chief role for membrane coating proteins [175]. In biological constriction processes, the membrane undergoes large mechanical deformations. Although lipids may serve to define the site of bud emergence [176], or determine the onset of divisional constriction [12, 167], there is almost certainly through the direct action of force exerting proteins [131, 136], or curvature-inducing protein coats [175, 177, 178], that the membrane is able to undergo the large mechanical deformations involved. However, in model vesicles, weak external perturbations suffice to lift the equilibrium constraints of constant area and volume, rendering lipid membranes susceptible of spontaneous budding and fission [145, 179]. For instance, vesicles made of lipids with a weakly negative spontaneous curvature are known to undergo the budding transition at increasing temperature [80, 166, 180], which is equivalent to expanding membrane area. In this budding transition an initially spherical vesicle transforms, via prolate- and pear-shaped intermediates, into two asymmetric spheres, one with a daughter bud, which remains connected to the reduced mother vesicle by a narrow neck [80, 166, 180]. In general, osmotic gradients are known to induce bio-reminiscent morphological transformations in Giant Unillamelar Vesicles (GUVs) ([165], and Refs. therein). In particular, to realize budding in protein-free vesicles made of (zero-curvature) single lipids requires large excess area in a flaccid configuration (*i.e.*, hypertonic conditions and/or negative membrane tension), which induces a spontaneous constriction process that initiates with the formation of a neck and terminates in the scission of the bud. From our calculation, budding and fission are events that could occur spontaneously under sufficiently low (or negative) surface tension (see Figure 4.8). Obviously, initially prolates shapes and hypertonic conditions decrease the onset for negative constriction force, thus favoring spontaneous constriction in a homogenous vesicle. In experiments with giant vesicles asymmetric budding is observed largely more frequent than much rarer events of symmetric fission [80, 166, 180], a reasonable fact since symmetry breaking tends to minimize the bending energy of the constricted vesicle [74]. A further complexity that makes lipid vesicles prone to budding involves the consideration of the lateral and transverse organization of mixtures of lipids within the membrane. Changes in the amount of membrane surface giving rise to excess area, or spontaneous curvature, could occur by transbilayer flip-flop

movement of phospholipids, or by lipid phase separation leading to a change in the lipid packing density (the case of heterogeneous membranes will be addressed in the next section). Asymmetric budding and symmetric fission in vesicles made by a mixture of lipids has already attracted much theoretical interest [100, 181, 182]. The models are all based on the minimization of the bilayer energy, but also vary depending on the interactions among the lipids in multicomponent systems, which make them to separate into phases or not. For monophasic, homogeneous vesicles, the membrane neck involved in the budding transition is produced by the lipid molecules whose local negative curvature is different from the main lipids of the membrane. If the molecules prefer a negatively curved bilayer, they will favor the formation of a bud. For biphasic, heterogeneous vesicles, a line tension exists between the two phases, trying to reduce the interface length, and favoring asymmetric budding and symmetric constriction, eventually leading to spontaneous fission [176]. This heterogeneous scenario will be further discussed the next section. Our results point out the easy practical availability of the onset of spontaneity for the budding/fission transition. Indeed, negative constriction forces are required for relatively low values of membrane tension, even for inflated vesicles under moderately negative external pressure (see Figure 4.8). Obviously, the possibility for spontaneous budding/fission enhances in prolates shapes defined by high positive values of the global spontaneous curvature (see Figures 4.7 and 4.8), a fact already recognized in the early studies of the morphological transitions of membrane vesicles [71, 80, 145]. The current study allows for quantitatively determining the specific conditions for spontaneous budding/fission from very accurate analytic formulas, which provide an interesting predictive framework for the design of smart vesicle microsystems endowing the division functionality [183].

4.4.5 Heterogeneous Lipid Bilayer Membranes

Especially interesting is the case of constriction events driven by the lateral organization of lipid domains in heterogeneous, phase-separated, lipid bilayer membranes (see the sketch in Figure 4.9). This interest is supported on the ample experimental evidence that supports a role for lipid domains in the protein sorting and budding events in biological cells [184]. For instance, lipids attached directly to protein cargo may determine the lateral segregation of this class of molecules into the transport vesicles produced in the Golgi apparatus [174, 185]. In polarized epithelial cells the cargo vesicles that bud from the trans Golgi complex are enriched in glycolipid (GPI)-anchored proteins, which are destined to reside on the apical plasma membrane [186]. The GPI-anchors are believed to partition into a sphingo-glycolipid lipid domain (raft) that may dictate protein sorting into apically directed vesicle buds [187]. These lipidic domain-formers are argued to influence the processes of protein sorting and budding in vivo [175], through forming buds in a well-defined range of sizes, which are able to sort proteins by curvature at a high selectivity [49]. Consequently, the natural process of budding might involve the selection of a certain length scale, corresponding to the sizes of the budding vesicles. The question of what is the physical mechanism underlying this selection has been previously posed in a theoretical context [188]. Whereas the characteristic size of the buds is determined by the area and volume constraints in the case of model homogenous vesicles (see results above), in contrast, domain-induced asymmetric budding represents a local mechanism to specifically determine the bud sizes from the competition between the bending energy of the membrane and the line tension of the domain [188]. Laterally segregated domains experience a lipid boundary tension that is relieved by constriction of the boundary interface, resulting in the

asymmetric budding (β:α) [188]. Such a hypothetical scenario opens further the problem of the mechanics of constriction to the case of a vesicle (or a cell) with several lipid components that represent regions with different bending moduli and spontaneous curvature. In asymmetric phase-separated systems (β:α), the two macroscopic domains usually formed so that each domain contains different kinds of lipid molecules, which result in an additional break of symmetry with a asymmetric dipolar distribution of the spontaneous curvature in the two domains $\left(C_0^{(\alpha)}: C_0^{(\beta)}\right)$. Because non-zero spontaneous curvature imposes a finite characteristic length scale in the curved membrane, specific bud sizes found in biology could arise from adequate combinations of lipid composition and localized spontaneous curvature giving rise to asymmetric phase separation into buds with a specific composition and a characteristic size, as sketched by Figure 4.9 (left scenario). The morphology of axisymmetric vesicles with multi-domains has been already theoretically investigated [72], which constitutes an adequate theoretical framework that a future model of curvature-inducing lipids should consider. In the experimental side, giant bilayer vesicles with a great variety of lipid domains and boundary shapes are usually observed in experiments [43]. The presence of asymmetric lipid domains is well known to facilitate the budding of giant vesicles [189], a process that is reminiscent of the ring-mediated constriction in a dipolar (α:β:α) configuration (see Figure 4.9; left). More recently, Baumgart and cols. [49, 190] have demonstrated that the different spontaneous curvatures and the relative bending moduli of the domains, in concert with the osmotic pressure and the line tension, have significant effects on the constriction configuration, and thereby on the global morphology, of a dipolar vesicle with two macroscopically separated domains chemically dissimilar. There is not in the previous literature an analytic solution of the constriction mechanics on asymmetric vesicles with domains directly from the above equations for the spontaneous curvature model. Only, Wang and Du discussed numerically the morphology of asymmetric vesicles with domains through the phase-field model [191]. The symmetric case of three-domain vesicles (α:β:α) sketched in Figure 4.9 (right scenario) is reminiscent of the accretion of negative-curvature lipids in the constriction furrow, which is experimentally observed both in eukaryotes [167], and in bacteria [12]. The presence of negative-curvature lipids in the equatorial domain β of a constricted vesicle should contribute to create locally concave curvature, so contributing to reduce the constriction forces (see Figure 4.9; right). To our better knowledge, the quantitative study of the mechanics of constriction on the (α:β:α) tri-domain configuration has been not addressed yet, which enlightens us to further investigate, both experimentally and theoretically, the shape equation of each domain and the boundary conditions between domains. The lateral lipid asymmetry observed in vivo should be incorporated in a more accurate model of membrane constriction under inhomogeneous spontaneous curvature that framed on the theoretical elastostatics bases [72], integrates a curvature-mediated mechanism for localization of lipids to specific membrane sites relevant to the divisional cycle, similarly to the curvature-induced phase separation models [192]. The experimental findings suggest that the localized production of negative-curvature lipids is required for the proper completion of cell constriction and that the possible formation of a unique lipid domain in the division site may play a crucial role in coordinating the contractile rearrangement with the membrane remodeling during late cytokinesis. Although our present theoretical model does not account for these membrane heterogeneities, framed on previous approaches [72, 192], those necessary ingredients of biological realm could be easily implemented using a similar mathematical kernel.

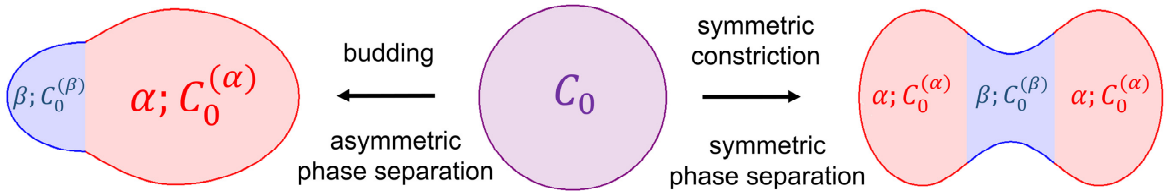

Figure 4.9. Schematic representation of a vesicle (or cell) with several lipid components giving rise to: (left) asymmetric two-domain phase separation (β:α), and (right) symmetric three-domain phase separation (α:β:α). Whereas the asymmetric scenario (β:α) describes budding events where the mother vesicle segregates a differentiated bud, the symmetric scenario (α:β:α) recapitulates the essential ingredients of the membrane constriction and remodeling events occurred during symmetric cell division. The accretion of negative-curvature lipids in the constriction furrow and positive-curvature lipids in the lateral lobes contribute to locally create concave curvature in the equatorial constriction domain β and convex curvature in the lobed domains α,and then to reduce the constriction force necessary for cell division.

4.4.6 Biological Membranes

Any cellular membrane, even in the simplest organisms like bacteria, actually consists of a complex mixture of structural lipids, proteins, and a small amount of functional glycolipids and glycoproteins involved in membrane signaling and trafficking. In the simplest mechanical depiction, a realistic cellular membrane might be modeled as a composite shell [193], composed by a heterogeneous lipid bilayer and adjoined cortical protein, or glycoprotein structures, such as the inner cell cortex in eukaryotes, or the outer peptidoglycan cell wall in bacteria. Such cortical structures can be described as a rigid cover somewhat connected to the fluid bilayer. From the mechanical standpoint, those rigid structures not only strengthen the lipid bilayer against the bending deformation but also bears in-plane shear, which is not supported by the fluid lipids. If the membrane skeleton, or the bacterial wall, are roughly considered to be structurally continuous, the composite cellular shell can still be regarded as a 2D continuum medium, mechanically described by the current material constitutive modelling, eventually accounting for lateral heterogeneity, plus an additional elasticity modulus describing in-plane shear rigidity. In addition, subcellular localization of the cytokinetic apparatus and related proteins is a universal feature of any prokaryote or eukaryote cell. However, although some targeting anchors are known in some organisms, the origin of polar and division-site localization remains mysterious for a large fraction of cytokinetic proteins. Ultimately, the molecular components responsible for such symmetry breaking must employ a high degree of self-organization, which could contribute with additional ingredients to the mechanics of division. For instance, curvature-induced stabilization mechanisms, based on the spontaneous curvature of localized membrane components, have been proposed to account for spontaneous lipid targeting to the poles and division site of rod-shaped bacterial cells [192]. In that model, if one of the membrane components has a large intrinsic curvature, the geometrical constraint of the inner lipid membrane by the more rigid bacterial cell wall naturally leads to lipid phase separation, and the resulting clusters of high-curvature lipids are large enough to spontaneously localize at cell poles and division site [192], in agreement with the experimental evidence of localization of the phospholipid cardiolipin to the negatively curved regions of *E coli* membranes [12], and polar targeting of some cytokinetic proteins during bacterial division [192]. In general, aggregates of lipids, proteins, or lipid-protein complexes may localize in response to cell

geometry, introducing additional ingredients of membrane mechanics that might be accounted for. Although all this complexity might be included on an extended, more realistic, model of cell division, the physical problem exceeds the limits of the present work, which can be however considered as a good starting point to obtain approximate solutions that offer a general depiction of the minimal energy mechanical pathway of divisional constriction in different organisms under different geometrical and constitutive conditions of their cellular membranes.

4.4.7 Towards an Integrated Mechanical Model of Cell Division

The big question, which remains still to be addressed in a comprehensive way, is to know how much of the division of real cells can be understood in terms of a simplified physical model integrating the passive mechanics of the membrane with the active actuation of a cytokinetic engine. In a minimalistic perspective, the division machinery should have evolved to fulfill, at least, the work requirements of reorganizing the cellular plasma membrane along the cell cycle, especially during cytokinesis. Certainly, the membrane deformations involved along the constriction stage of cell division in biological cells request of an expenditure of mechanical work exerted by a cytokinetic engine, which could however be working under conditions of minimal energy consumption, or perhaps nearing the onset for spontaneous constriction.

Evidence of cell division without the action of a cytokinetic machinery is already accepted to exist in complete kingdoms of archea, and in some species of bacteria including *Chlamydia* and *Planctomycetes* among others [183]. The bacterial cytokinetic protein FtsZ is not present in all those organisms, usually called *Dftsz* (devoid FtsZ), which cells are able however to undergo membrane constriction and develop two daughters till mature division without FtsZ. Although *Dftsz* cells spend longer times in division, the constriction slowing-down does not affect their overall growth rate [183]. All *Dftsz* bacteria that divide without FtsZ apparently use their motile apparatus to pull the two daughters apart. Under division the constriction neck appears very elongated, with the pair of daughters connected by a thin extension, similarly to the predictions of our current model at low external pressures $\Delta p < 0$, implying $\Lambda < 1$ [Eq. (4.24)] (see Figure 4.4, first column). Longitudinal traction-mediated cytofission appears to be a competent mechanism for cell division in bacterial cells lacking FtsZ. In those cases, the mechanics of the bending deformations coupled with the osmotic conditions should be essential for the correct understanding of this minimal work-demanding divisional mechanism. Spontaneous constriction via excess membrane area (see Sections 4.3.3 and 4.4.4) seems to be a mechanism for nearly-spontaneous binary fission in some mutant strains of *B. subtilis*, especially L-forms that grow without a cell wall and divides without FtsZ [194]. Detailed observation of the division process of L-forms of *E. coli, Listeria* and *B. subtilis* reveals a two-step mechanism that exploits the large excess area of those *Dftsz* cells, initiating the process by a membrane extrusion phase that leads to a long protrusion, which resolves by cleaving into smaller round progenies [183, 194]. A similar nearly-spontaneous division mechanism was discovered in the eukaryote *Dictyostelium* when its myosin II gen was knocked out [195, 196]. When those myosin lacking cells (thus no cytokinetic motor is working out) are allowed to adhere to a substrate, adhesion forces restore many features of normal furrow constriction and the cells become able to undergo “illegitimate division” by following the same mechanism of traction-mediated cytofission observed in *Dftsz* bacteria.

Constant maximum radius condition may give a simplified description of cytokinesis of rod-shaped cells, like *E. coli* and *Bacillus subtilis*, in which the constant maximum radius is maintained by an external tension (due to a peptidoglycan wall) and represented in our model by the line tension σ_m. Under this condition, our model predicts unchanged poles during all the constriction process, which is consistent with the approximately constant shape of the poles in the rod-shaped cells [197–199]. In addition, our model can be extended to other cases, as constant volume and constant area conditions (see Section 4.3.4). Constriction at constant volume requires a nearly 30% increase in area [75], and may describe divided cells with intense membrane trafficking [148, 149], which is known to play an important role in cytokinesis [154, 155]. On the other hand, if constriction takes place at constant area, the volume must be reduced in approximately 30% [75], which may describe divided cells with low or inhibited membrane trafficking. Thus, in constant area constriction, a greater initial area is required to have the same final volume. Heat shock has been shown to increase the area before division [200, 201] and to affect membrane trafficking molecules genes expression, but also other genes as those of signaling molecules [202].

Normal cell division in evolved cells involves a mature cytokinetic engine able to exert the constriction forces that cleave the cell in the division site. This is an up-hill process that requires the expenditure of an important amount of mechanical work by a constriction machinery. However, other concomitant, perhaps redundant, constriction mechanisms could be working to favor the membrane constriction phase of cell division. Redundant systems are often exploited indeed by living cells [203]. As refers the constriction process during cell division, local creation of negative spontaneous curvature ($C_0 < 0$) might contribute to favor constriction; both, hypotonic stresses ($\Delta p < 0$) and biogenic processes of membrane creation ($\Sigma < 0$) mediated by lipid trafficking also favor constriction. In addition, biological cells undergoing divisional constriction there used to be subjected to area and volume restrictions during the cytokinetic phase of the cell cycle. Despite of his inherent simplicity, all these ingredients are already accounted for by our physical model, which could be used to determine the energy landscape for whole configurational space of geometrical characteristics and constitutive properties captured for different classes of cells, from bacteria to eukaryotes. The optimal pathways for the mainstream mechanism of membrane constriction can be identified on this mechanical landscape, and predictions about changing external field parameters (osmotic stress, membrane tension, etc.) could be realized and checked in view of the experimental observations. Further complexities arising from heterogeneous membrane composition and additional shear rigidity introduced by skeletal structures might contribute to complete the picture.

4.5 Conclusions

We have derived general formulas for the more relevant properties involved in the constriction process of a vesicle in terms of the spontaneous curvature of the membrane, the membrane tension and the pressure difference between external and internal environments. These approximate solutions to the constricted shape are valid in the limit where bending, pressure and tension works are comparable, *i.e.*, in the regime where $\Delta p R_m^3 \approx \Sigma R_m^2 \approx \kappa_b (1 - C_0 R_m)^2$. Combining a perturbative expansion for small deformations with a variational approach, analytical expressions are obtained and compared with the exact results from numerical computations, getting a good agreement for all the properties calculated in a broad range of

constriction stages. The spontaneous curvature of the membrane allows describing vesicles (or simplified cells) with compositional inhomogeneities in its two monolayers, which result in a convex (as $C_0 > 0$), concave (as $C_0 < 0$), or flat (as $C_0 = 0$) membrane in the minimal energy configuration. The surface tension allows describing cellular membranes whose membrane trafficking is present without (as $\Sigma \leq 0$) or with (as $\Sigma > 0$) energetic cost [134, 162], whereas the osmotic pressure difference represents conditions for an external milieu considered hypotonic ($\Delta p < 0$), isotonic ($\Delta p = 0$), or hypertonic ($\Delta p > 0$) with respect to cytoplasm, which allows describing different turgor states [204]. In order to analyze the effects of these parameters (C_0, Σ, and Δp), we have computed the properties of the constricted vesicle for different combinations of values in the regime where these effects and bending energy are comparable. The more interesting results are those corresponding to the force required for constriction, since they show under which conditions vesicles (or cells) constrict more easily (with smaller constriction forces). This analysis is very useful either to understand the physical paths of divisional constriction in living cells or to guide the design of artificial divisomes in self-actuated microsystems. In all cases, if the vesicles (or cells) are of micro size with a flexible membrane with $\kappa_b \approx 10 - 20\ k_B T$ [35, 41, 157, 158], the constriction forces obtained are in the range of picoNewton. This is the range of forces practicable not only by natural divisomes, based on FtsZ rings in bacteria and in actomyosin furrows in eukaryotes, but also by other biomolecular motors. As expected, stronger constriction forces are required for higher values of membrane tension and external pressure, conditions usually present in tensioned membranes of deflated cells, or vesicles. Contrarily, cells, or vesicles, with negative membrane tension, constrict more easily than tensioned membranes with lipid trafficking inhibited. Similarly, turgid cells, or inflated vesicles, immersed in a hypotonic medium constrict easier than shrunk vesicles deflated by a hypertonic medium. Furthermore, our analysis demonstrates that C_0 has an important effect on the force required for constriction and vesicles whose membranes have $C_0 > 0$ (*i.e.,* whose membranes tend to build up in a convex prolate configuration, e.g. cylinder-like bacteria) are the most easily constricted. However, negative values of the local spontaneous curvature, due for instance to local concentrations of lipids with a negatively curvature, make the membranes prone to bend in a neck-like shape with a saddle curvature, so favoring spontaneous budding and asymmetric fission. This result gives an idea about the mechanical constraints of the evolution pathway of the biological cell division mechanisms. The method can serve to get insight on other biological processes involving membrane bending, such as exocytosis and endocytosis, and opens a new avenue of material design in the field of bioinspired microsystems with the potential capability to perform the constriction performances intrinsic to the divisional event necessary for self-replication. The proposed method is sufficiently general, and powerful, to accommodate easily further complexities accounting for different membrane asymmetries/heterogeneities present in real cells. This is being the object of ongoing work.

Acknowledgments

M.A. de Pedro and P. Natale are acknowledged for fruitful discussions on bacterial division. EB acknowledges financial support from FPU grant 13/02826 (Ministerio de Educación, Cultura y Deporte, Spain). Authors acknowledge financial support from Gobierno de España, through Ministerio de Economía y Competitividad (MINECO) and Ministerio de Educación, Cultura y Deporte (MECD), and from Comunidad de Madrid.

Annex A4

Modelling the Mechanics of Cell Division

This chapter contains additional information related to the previous chapter, Chapter 4. In Section A4.1 we briefly explain the numerical procedure followed to obtain the exact solution. In Section A4.2 we present the approximate analytical expressions of the constriction zone written up to sixth order in the perturbative expansion. Finally, in Section A4.3, we analyze the relation between forces exerted at maximum radius and constriction sites.

A4.1 Algorithm Used to Compute the Exact Solution

Any shape of minimal energy under certain boundary conditions can be obtained by solving the corresponding set of Euler-Lagrange equations. We use as independent coordinates to express the surface shape the arc length S along the contour of the shape, and the azimuthal angle ϕ (see Figure A4.1). The shape can also be given in terms of the tilt angle as a function of the arc length $\psi(S)$. Using geometrical relations, the coordinates X and Z, which are the parallel and the perpendicular distance to the axis of symmetry, respectively, are

$$\dot{X} = -\sin\psi, \tag{A4.1}$$

$$\dot{Z} = \cos\psi. \tag{A4.2}$$

The total energy can be expressed as

$$E_T = \pi\kappa \int_0^{S_4} L\left(\psi, \dot{\psi}, Z, \dot{Z}, \gamma\right) \mathrm{d}S, \tag{A4.3}$$

with the Lagrange function

$$L \equiv \frac{X}{2}\left[\dot{\psi}, + \frac{\sin\psi}{Z} - C_0\right]^2 + \tilde{\Sigma} Z + \frac{\Delta\tilde{p}}{2} Z^2 \sin\psi + \gamma\left(\dot{Z} - \cos\psi\right). \tag{A4.4}$$

The first term reflects the mean curvature contribution to the bending energy and the second and third term reflects the contributions to the energy due to the effects of the surface tension and the osmotic pressure, respectively. The last term in Eq. (A4.4), which involves the Lagrange parameter function $\gamma = \gamma(S)$, must be introduced since the variables ψ and Z are related by Eq. (A4.2). The corresponding Euler-Lagrange equations for the minimization of the total energy E_T are

$$\dot{\psi} = U, \tag{A4.5a}$$

$$\dot{U} = -\frac{U}{Z}\cos\psi + \frac{\cos\psi\sin\psi}{Z^2} + \frac{\gamma}{Z}\sin\psi + \frac{\Delta\tilde{p}Z}{2}\cos\psi, \tag{A4.5b}$$

$$\dot{\gamma} = (U - C_0)^2/2 - \frac{\sin^2\psi}{2Z^2} + \Delta\tilde{p}Z\sin\psi + \tilde{\Sigma}, \tag{A4.5c}$$

$$\dot{Z} = \cos\psi. \tag{A4.5d}$$

$$\dot{X} = -\sin\psi. \tag{A4.5d}$$

Applying the appropriate boundary conditions, the system of ordinary differential equations can be solved and the equilibrium shapes can be obtained. The set of conditions which must be satisfied are: at the beginning, $Z(0) = 0$, $X(0) = 0$, $\psi(0) = 0$ and $\gamma(0) = 0$; at the end of the left pole, $Z(S_1) = R_m$ and $\psi(S_1) = \pi/2$; at the constriction ring, $Z(S_2) = R_c$ and $\psi(S_2) = \pi/2$; at the end of the right pole, $Z(S_3) = R_m$ and $\psi(S_3) = \pi/2$ and finally, at the end of the shape, $Z(S_4) = 0$ and $\psi(S_4) = \pi$ (see Figure A4.1). Since the initial condition $Z = 0$ is a singular point of the Eqs. (A4.5), we use the Taylor expansion of the variables around $S = 0$. Introducing these power series in the Eqs. (A4.5), and taking into account that $\psi(0) = Z(0) = \gamma(0) = 0$ and $\lim_{S\to 0} \sin\psi/Z = \dot{\psi}(0) = U(0)$, we can obtain for the initial conditions the approximate solution

$$\psi(S \to 0) = U(0)S + O(S^3), \tag{A4.6a}$$

$$U(S \to 0) = U(0) + \frac{1}{4}\left[\Delta\tilde{p} + 4\tilde{\Sigma} + U(0)\left(U(0)^2 + {C_0}^2 + 4U(0)C_0\right)\right]S^2 + O(S^4), \tag{A4.6b}$$

$$\gamma(S \to 0) = [(U(0) - C_0)^2/2 + \tilde{\Sigma}]S + O(S^3), \tag{A4.6c}$$

$$Z(S \to 0) = S + O(S^3). \tag{A4.6d}$$

$$X(S \to 0) = -\frac{1}{2}S^2 + O(S^3). \tag{A4.6d}$$

Similarly, considering the Taylor expansion in order to apply the final condition $Z(S_4) = 0$, we can solve the set of Euler-Lagrange equations. Maintaining the boundary conditions of fixed radius R_m at S_1 and S_3 and R_c at S_2 requires line tensions σ_m and σ_c, respectively. They act in opposite directions: increasing σ_c forces R_c to decrease, thus increasing constriction. This requires an increase of σ_m to maintain constant R_m during the constriction process [74, 75]. If the left and right poles had different polar radius, the line tensions at S_1 and S_3 would be different too. The boundary matching conditions at these points S_1, S_2 and S_3 are given by [72]

$$\sigma_m = \gamma^+(S_1) - \gamma^-(S_1) = \gamma^+(S_3) - \gamma^-(S_3), \tag{A4.7a}$$

$$\sigma_c = \gamma^+(S_2) - \gamma^-(S_2), \tag{A4.7b},$$

where the plus and minus superscripts refer to the value at the right and at the left of the boundary, respectively. The numerical method is found by determining the unknown values $U(0)$, S_1, $\gamma^+(S_1)$, S_2, $\gamma^+(S_2)$, S_3, $\gamma^+(S_3)$ and S_4 to make the solution verify the boundary conditions. In the case of symmetric constriction γ verifies the symmetric conditions $\gamma^{\pm}(S_3) = -\gamma^{\mp}(S_1)$ and $\gamma^+(S_2) = -\gamma^-(S_2)$. Once the shape equation [Eq. (A4.5)] is solved for a constriction stage $s = 1 - R_c/R_m$, the main properties of the system can be calculated. The total energy is

obtained computing the expressions in Eqs. (A4.3) and (A4.4), and the length of the shape from the Eq. (A4.2). From Eqs. (A4.8) and (A4.9) and using the relations in Eqs. (A4.1) and (A4.2), it is obtained that the membrane area can be calculated as

$$A = 2\pi \int_0^{S_4} Z \mathrm{d}S, \tag{A4.8}$$

and the vesicle volume as

$$V = \pi \int_0^{S_4} Z^2 \sin\psi \mathrm{d}S. \tag{A4.9}$$

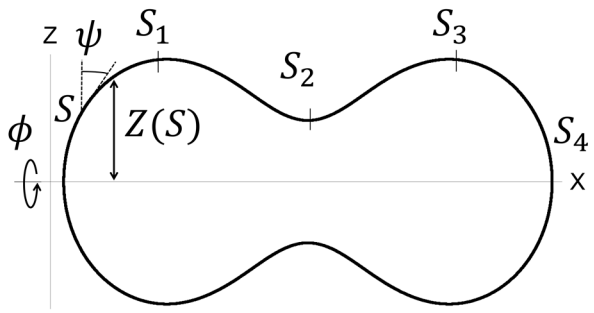

Figure A4.1. Scheme of the parameterization used for numerical solution.

A4.2 Analytical Expressions for Constriction Zone up to Sixth-Order Perturbative Expansions

The quantities of the constriction zone written up to sixth-order of perturbation are

$$\begin{aligned}
K_{T,\mathrm{cz}} = {} & \frac{1}{R_m} - 2C_0 + C_0^2 R_m + \Delta\tilde{p} R_m^2 + 2R_m\tilde{\Sigma} \\
& + \frac{1}{R_m^2}u - C_0^2 u - 2\Delta\tilde{p} R_m u - 2\tilde{\Sigma}u + 2uu_{xx} - 2C_0 R_m u_x \\
& + \frac{1}{R_m^3}u^2 + \Delta\tilde{p}u^2 + 2C_0 u u_{xx} + R_m u_{xx}^2 - \frac{1}{2R_m}u_x^2 + \tilde{\Sigma}R_m u_x^2 \\
& + \frac{1}{R_m^4}u^3 - 3u_x^2 u_{xx} + 2C_0 R_m u_x^2 u_{xx} - u u_{xx}^2 - \frac{C_0^2}{2}u u_x^2 - \frac{1}{2R_m^2}u u_x^2 - \tilde{\Sigma}u u_x^2 \\
& + \frac{1}{R_m^5}u^4 - 2C_0 u u_x^2 u_{xx} - \frac{5R_m}{2}u_x^2 u_{xx}^2 + \frac{3}{8R_m}u_x^4 - \frac{1}{2R_m^3}u^2 u_x^2 - \frac{C_0^2 R_m}{8}u_x^4 \\
& + \frac{1}{R_m^6}u^5 + \frac{15}{4}u_x^4 u_{xx} - 2C_0 R_m u_x^4 u_{xx} + \frac{C_0^2}{8}u_x^4 u + \frac{3}{8R_m^2}u_x^4 u + \frac{\tilde{\Sigma}}{4}u_x^4 u - \frac{1}{2R_m^4}u_x^2 u^3 \\
& + \frac{1}{R_m^7}u^6 + 2C_0 u u_x^4 u_{xx} + \frac{35}{8}R_m u_x^4 u_{xx}^2 + \frac{3}{8R_m^3}u_x^4 u^2 - \frac{5}{16R_m}u_x^6 + \frac{C_0^2 R_m}{16}u_x^6 + \frac{R_m\tilde{\Sigma}}{8}u_x^6 \\
& - \frac{1}{2R_m^5}u_x^2 u^4 + O(u_i^7).
\end{aligned} \tag{A4.10}$$

$$L_m/R_m \approx \frac{\pi}{2}\left(\frac{6}{\Lambda}\right)^{1/4} s^{1/2} + \frac{\pi 6^{1/4} s^{3/2}}{1152\Lambda^{5/4}}\left[72(\Lambda-\Gamma) + (\Gamma-4)6^{3/2}\Lambda^{1/2} - 256^{1/2}\Lambda^{3/2}\right] + \frac{\pi 6^{1/4} R_m s^{5/2}}{221184\Lambda^{9/4}}\left[1505\Lambda^3 + 6006^{1/2}\Lambda^{5/2} + 36(7\Gamma + 24C_0R_m + 32)\Lambda^2 - (7\Gamma + 96C_0R_m + 120)246^{1/2}\Lambda^{3/2} + (\Gamma^2 - 152\Gamma + 576\, C_0R_m - 848)36\Lambda - 4326^{1/2}\Lambda^{1/2}\Gamma(\Gamma-4) + 4320\Gamma^2\right] + \cdots. \tag{A4.11}$$

$$E_{T,\,\mathrm{cz}}/\kappa_b \approx \frac{4}{3}\pi^2 6^{1/4}\Lambda^{3/4}s^{1/2} - \frac{\pi^2 6^{1/4} s^{3/2}}{144\Lambda^{3/4}}\left[56^{1/2}\Lambda^2 + 168\Lambda^{3/2} - (\Gamma-4)6^{3/2}\Lambda - 72\Gamma\Lambda^{1/2}\right] + \frac{\pi^2 6^{1/4} s^{5/2}}{27648\Lambda^{7/4}}\left[215\Lambda^{7/2} + 10806^{1/2}\Lambda^3 + (7\Gamma + 24C_0R_m + 800)12\Lambda^{5/2} - (55\Gamma + 96C_0R_m - 72)246^{1/2}\Lambda^2 + (848 - 576C_0R_m - 232\Gamma - \Gamma^2)36\Lambda^{3/2} + (\Gamma-4)1446^{1/2}\Gamma\Lambda - 864\Gamma^2\Lambda^{1/2}\right] + \cdots. \tag{A4.12}$$

$$A_{\mathrm{cz}} = 2\pi\int_{x_i}^{x_f} R\sqrt{1+R_x^2}\,\mathrm{d}x = 2\pi\int_{x_i}^{x_f}\left[R_m - u + \frac{R_m}{2}u_x^2 - \frac{1}{2}uu_x^2 - \frac{R_m}{8}u_x^4 + \frac{1}{8}uu_x^4 + \frac{R_m}{16}u_x^6 + \cdots\right]\mathrm{d}x. \tag{A4.13}$$

$$A_{\mathrm{cz}}/R_m^2 \approx 2\pi^2\left(\frac{6}{\Lambda}\right)^{1/4} \mathrm{s}^{1/2} + \frac{\pi^2 6^{1/4}\mathrm{s}^{3/2}}{288\Lambda^{5/4}}\left[(\Gamma-4)6^{3/2}\Lambda^{1/2} - 72\Gamma - 216\Lambda - 6^{1/2}\Lambda^{3/2}\right] + \frac{\pi^2 6^{1/4}\mathrm{s}^{5/2}}{55296\Lambda^{9/4}}\left[1841\Lambda^3 + 12006^{1/2}\Lambda^{5/2} - 36(\Gamma - 24C_0R_m + 128)\Lambda^2 - (7\Gamma + 96C_0R_m + 24)246^{1/2}\Lambda^{3/2} + (\Gamma^2 + 40\Gamma + 576\, C_0R_m - 848)36\Lambda - 4326^{1/2}\Lambda^{1/2}\Gamma(\Gamma-4) + 4320\Gamma^2\right] + \cdots. \tag{A4.14}$$

$$V_{\mathrm{cz}}/R_m^3 \approx \pi^2\left(\frac{6}{\Lambda}\right)^{1/4} \mathrm{s}^{1/2} + \frac{\pi^2 6^{1/4}\mathrm{s}^{3/2}}{576\Lambda^{5/4}}\left[(\Gamma-4)6^{3/2}\Lambda^{1/2} - 72\Gamma - 504\Lambda - 256^{1/2}\Lambda^{3/2}\right] + \frac{\pi^2 6^{1/4}\mathrm{s}^{5/2}}{110592\Lambda^{9/4}}\left[1505\Lambda^3 + 54006^{1/2}\Lambda^{5/2} + 36(7\Gamma + 24C_0R_m + 800)\Lambda^2 - (55\Gamma + 96C_0R_m - 72)246^{1/2}\Lambda^{3/2} + (\Gamma^2 + 232\Gamma + 576\, C_0R_m - 848)36\Lambda - 4326^{1/2}\Lambda^{1/2}\Gamma(\Gamma-4) + 4320\Gamma^2\right] + \cdots. \tag{A4.15}$$

$$F_{\mathrm{cz}}R_m/\kappa_b \approx \frac{2\pi^2 6^{1/4}\Lambda^{3/4}}{3s^{1/2}} - \frac{\pi^2 6^{1/4}\mathrm{s}^{1/2}}{96\Lambda^{3/4}}\left[56^{1/2}\Lambda^2 + 168\Lambda^{3/2} - (\Gamma-4)6^{3/2}\Lambda - 72\Gamma\Lambda^{1/2}\right] + \frac{5\pi^2 6^{1/4}\mathrm{s}^{3/2}}{55296\Lambda^{7/4}}\left[215\Lambda^{7/2} + 10806^{1/2}\Lambda^3 + (7\Gamma - 24C_0R_m + 800)12\Lambda^{5/2} - (55\Gamma + 96C_0R_m - 72)246^{1/2}\Lambda^2 + (848 - 576C_0R_m - 232\Gamma - \Gamma^2)36\Lambda^{3/2} + (\Gamma-4)1446^{1/2}\Gamma\Lambda - 864\Gamma^2\Lambda^{1/2}\right] + \cdots. \tag{A4.16}$$

A4.3 Relation between Forces Exerted at Maximum Radius and Constriction Sites

The Canham-Helfrich Hamiltonian gives the energy of a membrane vesicle with non-zero spontaneous curvature under the actions of membrane tension and pressure difference between external and internal environments. However, the constriction process of a vesicle considered here requires additional contributions to the total energy of the vesicle. Keeping fixed R_m and R_c along the constriction pathway mean new constraints, which can be incorporated into the total energy of Eq. (4.4) via Lagrange multipliers $\lambda_m = -4\pi\sigma_m$ and $\lambda_c = 2\pi\sigma_c$, respectively

$$E_{T,\sigma} = E_T + 4\pi\sigma_m R_m + 2\pi\sigma_c R_c. \tag{A4.17}$$

This equation leads to a new stable shape obtained from

$$\delta E_{T,\sigma} = \delta(E_T + 4\pi\sigma_m R_m + 2\pi\sigma_c R_c) = 0, \tag{A4.18}$$

which leads to

$$\frac{\partial E_{T,\sigma}}{\partial R_c} = 0 \rightarrow F_c \equiv -\frac{\partial E_T}{\partial R_c} = 2\pi\sigma_c, \tag{A4.19a}$$

$$\frac{\partial E_{T,\sigma}}{\partial R_m} = 0 \rightarrow F_m \equiv -\frac{\partial E_T}{\partial R_m} = 4\pi\sigma_m\,, \tag{A4.19b}$$

where F_c is the force exerted at the constriction site toward the interior, and F_m is the force exerted at the maximum radius sites toward the exterior. In general, $E_T = E_T(s, C_0 R_m, \Sigma R_m^2, \Delta p R_m^3)$, but in the case of zero spontaneous curvature ($C_0 = 0$), negligible surface tension ($\Sigma = 0$), and isotonic medium ($\Delta p = 0$) this energy, which corresponds to the bending energy of a membrane vesicle with $C_0 = 0$, only depends on the constriction parameter s. For this particular case, the Eq. (A4.19) gives

$$F_c = \frac{1}{R_m}\frac{\partial E_T}{\partial s} = 2\pi\sigma_{c,}, \tag{A4.20a}$$

$$F_m \equiv -\frac{(1-s)}{R_m}\frac{\partial E_T}{\partial s} = 4\pi\sigma_m\,. \tag{A4.20b}$$

From the Eq. (A4.20) we can extract the following relation between F_c and F_m during the constriction process for the case with $C_0 = \Sigma = \Delta p = 0$

$$F_c = -\frac{F_m}{(1-s)} = -\frac{4\pi\sigma_m}{1-s}, \tag{A4.21}$$

or equivalently, the following relation between σ_m and σ_c

$$\sigma_c = -\frac{2\sigma_m}{1-s}. \tag{A4.22}$$

In the general case, when these parameters are non-zero, there is a similar relation between F_c and F_m, but it is more involved due to the presence of the partial derivatives of E_T with respect to $C_0 R_m$, ΣR_m^2, and $\Delta p R_m^3$ in Eq. (A4.20b).

The constriction force computed from the line tensions σ_c and σ_m [Eqs. (A4.20a) and (A4.21)] and from the variations of E_T with respect to constriction radius $\partial E_T/\partial R_c$ as a function of the constriction ratio s for the case with $C_0 = \Sigma = \Delta p = 0$ is shown in Figure A4.2. We obtain an excellent agreement between the three possible ways of computing it. The constriction force computed from $-\partial E_T/\partial R_c$ has been calculated using the mean value theorem; this is the reason why these points are between those arising from the Eqs. (A4.20a) and (A4.21).

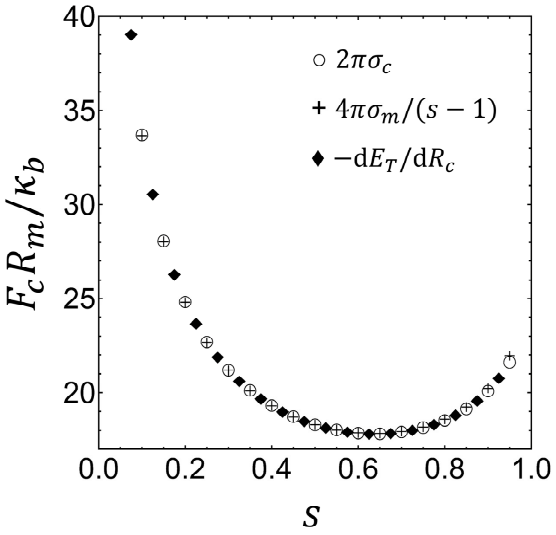

Figure A4.2. Constriction force (in units of R_m/κ_b) numerically computed for $C_0 = \Sigma = \Delta p = 0$. Plotted are $2\pi\sigma_c$ [Eq. (A4.20a)], where σ_c is the line tension at the constriction site (computed numerically), $4\pi\sigma_m/(1-s)$ [Eq. (A4.21)], where σ_m is the line tension at the maximum polar radius site (computed numerically) and $-\partial E_T/\partial R_c$, calculated numerically from variations of the total energy along the constriction pathway. We obtain an excellent agreement between the three possible ways of computing the constriction force.

Chapter 5

Mechanical Conditions for Stable Symmetric Cell Constriction

Chapter based on Beltrán-Heredia E, Almendro-Vedia VG, Monroy F, & Cao FJ (2018) Mechanical conditions for stable symmetric cell constriction. *Manuscript submitted for publication.*

Cell constriction is a decisive step for division in many cells. However, its physical pathway remains poorly understood, calling for a quantitative analysis of the forces required on different cytokinetic scenarios. Using a model cell composed by a flexible membrane that encloses the cytoplasm, we study the mechanical conditions necessary for stable symmetric constriction under radial equatorial forces using analytical and numerical methods. We deduce that stable symmetric constriction requires positive effective spontaneous curvature, while spontaneous constriction requires a spontaneous curvature higher than the characteristic inverse cell size. Surface tension reduction (for example by membrane trafficking) increases the stability and spontaneity of cellular constriction. A reduction on external pressure also increases stability and spontaneity. Cells with prolate lobes (elongated cells) require lower stabilization forces than oblate shaped cells (discocytes). We also evidence that the stability and spontaneity of symmetric constriction increases as constriction progresses. Our quantitative results settle the physical requirements for stable cytokinesis, defining a quantitative framework to analyze the mechanical role of the different constriction machineries and cytokinetic pathways found in real cells, so contributing to a deeper quantitative understanding of the physical mechanism of the cell division process.

5.1 Introduction

As mentioned in many places of this manuscript, cell division under symmetric constriction is an essential feature of life as stems the capacity of any living organism for self-replication [128]. No matter what the cell is, either prokaryote or eukaryote, every cell is replicated from pre-existing cells through cytokinesis, the terminal process of cell cycle thereby the mother cell is cleaved into two daughters [205]. The key cytokinetic features are conserved in the different kingdoms of life, standing out by their reproducibility and regularity in every organism [205–

207]. Such a set of universal characteristics suggests a general mechanical pathway with a tight physical control mediated by specific biomolecular players [208–210]. Specific mechanistic details differ between organisms due to biochemical evolution [211], which made possible to confront different constriction forces with mutable cells of dissimilar sizes and variable mechanical characteristics [207]. In animal cytokinesis, cell constriction has evolved to occur at an equatorial site specifically named a cleavage furrow (see Figure 5.1A; upper panel), which is driven by a contractile engine based on ATP-consuming actomyosin filaments [212]. In plant cells, some structural aspects deviate from the animal cytokinetic scenario; specifically, due to the rigidity of cell walls necessary to support physiological turgor, they form a dividing septum on the equatorial plane of cell division. Cell septation, which is the synthesis of the cell wall that separate the daughter cells, is also exploited by prokaryotes [213]. In bacteria, septation is conducted from the outer peptidoglycan (PG) layer in a sequence of events that is coordinated both spatially and temporally with the invagination of the cytosol membrane [214, 215]. Prokaryote cell constriction force was thought to be leaded by the polymerization of the filamentous protein FtsZ [183, 216]. However, recent experiments suggest the synthesis activity of the PG layer around the furrow of the division site can be the leading constriction mechanism [141, 217].

5.2 The Model Cell

Although important advances have been made in understanding the origin of the constrictive force, with emphasis on the driving proteins involved, gaping holes in physical knowledge prevent the formulation of detailed mechanistic models. At the current state of knowledge, a biomolecular standpoint is unlikely to describe coordinated ring assembly, force generation, furrow constriction, and cell remodeling in a generalized approach to the physical cytokinetic pathway. In order to get a quantitative insight on the stability of symmetric constriction along the cytokinetic pathway, instead of the usual approach to consider where the constriction force come from, we address the question of what mechanical requirements are necessary for. Here, we focus on the case of animal eukaryotic cells, as prokaryotes and plant cells require the specific consideration of the mechanical effects of the cell wall where they are encapsulated.

As we previously made in Chapter 4, the natural eukaryotic cell is modeled as a deformable vesicle with the cellular contents enclosed by a flexible shell, which represents the elasticity properties of the cellular membrane and cortex. The bending energy of the flexible shell is given in terms of its mean curvature H by the Canham-Helfrich (CH) form [33, 34] as

$$E_b = \frac{\kappa_b}{2}\int_\Omega \mathrm{d}A(2H - C_0)^2\,. \tag{5.1}$$

This CH-model membrane is characterized by an effective spontaneous curvature C_0, and an effective bending rigidity κ_b to give an effective theory of cell mechanics [218, 219]. The spontaneous curvature C_0 represents the tendency of the membrane to bend in the equilibrium state [35], usually due to the compositional asymmetry between the inner and the outer sides [220]. In our minimal model, C_0 is assumed to be homogenous along the whole membrane, thus determining the global shape of the vesicle [221] This model membrane, of actual surface area A, is assumed laterally undeformable (inextensible), and subjected to effective cortical tension Σ. The cell interior, including cytoplasm, organelles and other cellular structures, are described

as a hydrostatic fluid enclosed in a vesicle of volume V (and surface area A) subjected to a pressure difference Δp between the outer medium and the cell interior ($\Delta p = p_{\text{out}} - p_{\text{in}}$). This pressure difference accounts for either possible osmotic imbalances, a turgor pressure, or simply a Laplace pressure due to local curvature. The shape of the cell is determined by the minimum of its total energy $E_T = E_b + W$, which is leaded by the bending energy of the effective membrane E_b, and is subjected to geometric constraints of constant membrane area and/or constant cell volume that require a work $W(A,V) = \Sigma A + \Delta p V$; consequently, the total cell energy to be globally minimized in an energetically optimized cytokinetic pathway reads as

$$E_T = E_b + \Sigma A + \Delta p V. \tag{5.2}$$

Additionally, the cell contents are also assumed to exert three types of forces on the cell membrane: one keeping a certain size of each of the lobes of the cell F_m, another force exerting constriction in the middle of the cell F_c, and finally an effective force stabilizing the symmetric constriction F_s (see Figure 5.1B). We explore the stability of the symmetric constriction, which will allow us to compute the required stabilization forces. These results are compared with previous results of required constriction forces. All these results have been derived for leading bending conditions with comparatively similar spontaneous curvature, pressure, tension, and for shapes close to sphericity, using a combination of perturbative and variational approaches, and verified by numerical computations (for details see Annex A4 and Refs. [74, 75, 222]).

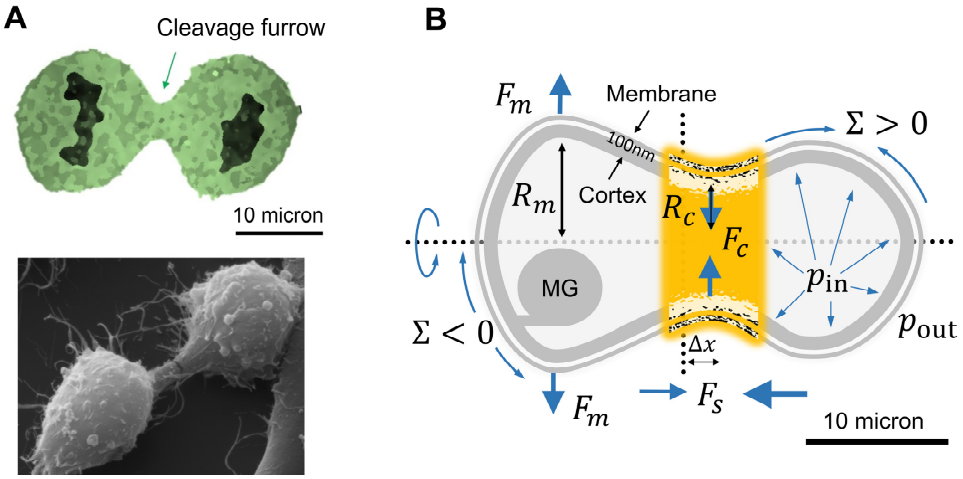

Figure 5.1. Real cells and minimal model cell during cytokinesis. (A) HeLa cell undergoing cell constriction (cytokinesis). Upper panel) Formation of the cleavage furrow (optical microscopy image, courtesy of Alan Siegel and Harold C. Smith, SUNY at Buffalo, Department of Biology). Lower panel) Scanning electron micrograph during final stage of constriction (courtesy of Andrew Wilde, University of Toronto). (B) Profile of a constricted cell and its characteristic parameters. The force F_m at the polar radius R_m keeps the size of the lobes; the constriction force F_c directed toward the cell interior causes constriction to constriction radius R_c; and the stabilization force F_s directed to the middle of the cell ($\Delta x = 0$) symmetrizes the division. External stress fields applied either transversally, as a pressure Δp, or longitudinally, as a lateral membrane tension Σ complete the main systemic factors defining the shape of the cell; whose intrinsic mechanical properties are represented by an effective bending modulus κ_b and an effective spontaneous curvature C_0.

In Chapter 4, initial cell shape (before constriction) was shown to be determined by spontaneous curvature, surface tension, and external pressure through the quantity

$$\Lambda = (1 - C_0 R_m)^2 + 2\Sigma R_m^2/\kappa_b + \Delta p R_m^3/\kappa_b \,. \tag{5.3}$$

$\Lambda = 1$ stands for the sphere, while $0 < \Lambda < 1$ gives prolate (rod-like) and $\Lambda > 1$ oblate (disk-like) spheroids; for $\Lambda < 0$ there are no solutions [222]. The parameter Λ also determines the shape of the cell lobes during division (see Figure 4.4 in Chapter 4 and Figure 5.2). Particularly, during constriction prolate-shaped cells (cylinders) elongate along their axis, and constriction becomes favored by lowering the external pressure, or the surface tension (e.g. by enhancing membrane traffic towards the cell membrane). In contrast, oblate cells (discocytes) have flatter shapes, which are favored by high values of external pressure or surface tension (see Figure 5.3) (for details see Chapter 4). In general, discocytes require much stronger constriction forces giving rise to less stable configurations (see Figure 5.3).

As we in Chapter 4, the degree of constriction is indicated by the constriction parameter $s = 1 - R_c/R_m$, which is defined in terms of the constriction radius R_c and the initial cell size measured as a polar radius R_m (see Figure 5.1B). This parameter increases from $s = 0$, when there is no constriction and $R_c = R_m$, to $s = 1$, when the constriction is maximal and $R_c = 0$.

5.2.1 Constraints to the Constriction Pathway

Constant polar radius constriction

In Chapter 4, we explored the case of symmetric cell division with constant polar radius R_m (*i.e.*, constant maximum transversal radius, see Figure 5.1B). In this case, the shape of the lobes remains equal to the initial prolate, spherical, or oblate configuration at all stages of constriction while the cell area and volume are doubled upon division (see Figure 5.2, black shadowed shapes and bar charts).

Constant volume and area constriction

In this chapter, instead of considering constant polar radius R_m constriction, we also address constant volume or constant area constriction. Constriction at constant volume may describe dividing cells with intense membrane trafficking [148, 149], which is known to play an important role in cytokinesis [154, 155]. Constriction at constant area may describe dividing cells with low or inhibited membrane trafficking. In constant area constriction, a greater initial area is required to have the same final volume [74, 75, 222]. Heat shock has been shown to increase the area before division [200, 201] and to affect membrane trafficking molecules genes expression, but also other genes as those of signaling molecules [202].

There are several possibilities to define these constant area or constant volume constriction paths. In Chapter 4, we proposed a re-dimensioning strategy that rescales the shape in a factor $\lambda(s)$ as: $\kappa_b \to \kappa_b, R_m \to \lambda R_m, C_0 \to C_0/\lambda\,, A \to \lambda^2 A, V \to \lambda^3 V, \Sigma \to \Sigma/\lambda^2$, and $\Delta p \to \Delta p/\lambda^3$ [with $\lambda_A(s)$ at constant area constriction and with $\lambda_V(s)$ at constant volume constriction]. Note that this rescaling constriction path also keeps constant the dimensionless products $C_0 R_m$, ΣR_m^2, and $\Delta p R_m^3$ (and thus Λ) during constriction. Although this simplifies the computations, it could be not very realistic. We explore here a more lifelike constriction path, where the parameters C_0, Σ, and Δp remain constant along the constriction pathway (instead of the products $C_0 R_m$, ΣR_m^2, and

$\Delta p R_m^3$). To do that, we have first to determine the variation of the polar radius during constriction, $R_{m,A}(s)$ or $R_{m,V}(s)$, which also keeps constant either the cell membrane area A or the volume enclosed by cell V, respectively. Therefore, we solve, respectively, the algebraic equations $A(R_m, s) = A(R_0, 0)$ or $V(R_m, s) = V(R_0, 0)$, with R_0 the polar radius of the initial (unconstricted) cell [222]. Thus, the quantity Λ of Eq. (5.3), which determines the shape of the cell lobes, mildly varies along the constriction process due to the variations of $R_{m,AV}(s)$. The model predicts in general shape conservation, thus, oblate, spherical, or prolate mother cells divide, respectively, into two oblate, two spherical, or two prolate daughter cells (see Figure 5.2). At constant volume constriction, each of two daughter parts reduces its polar radius in a 21% and its membrane area in a 37%. This only requires an increase in the total area of a 26%. Instead, if the constriction process occurs keeping the membrane area constant, each of two daughter parts reduces its polar radius in a 29% and its volume in a 64% upon constriction. This requires a reduction in the total volume of 29%. These results are summarized in Figure 5.2 (for details see Figures A5.2 and A5.3 of Annex A5).

5.2.2 Constriction and Stabilization Forces

Constriction force

The constriction force, exerted as a constriction ring at the equator of the cell, is obtained from the variation of the total energy with respect to the constriction radius R_c. Under the constant polar radius R_m condition, the constriction F_{c,R_m} is obtained as

$$F_{c,R_m} \equiv -\frac{\mathrm{d}E_T}{\mathrm{d}R_c} = -\frac{\partial E_T}{\partial s}\frac{\partial s}{\partial R_c} = \frac{1}{R_m}\frac{\partial E_T}{\partial s}, \tag{5.4}$$

where we have used $s = 1 - R_c/R_m$. The constriction force scales inversely proportional to R_m, *i.e.*, smaller cells are harder to constrict. This quantity was previously derived by us (both analytically and numerically) in Chapter 4. Under the new constraints considered in this chapter, the constriction forces at constant volume $F_{c,V}$ or at constant area $F_{c,A}$ are determined as

$$F_{c,VA} = \frac{1}{R_m}\frac{\partial E_T}{\partial s} + \frac{\partial R_m}{\partial s}\left[\frac{C_0}{R_m}\frac{\partial E_T}{\partial (C_0 R_m)} + 2\Sigma\frac{\partial E_T}{\partial (\Sigma R_m^2)} + 3\Delta p R_m \frac{\partial E_T}{\partial (\Delta p R_m^3)}\right], \tag{5.5}$$

where $R_m = R_{m,V}(s)$ or $R_m = R_{m,A}(s)$ is a function of the constriction state s given by the assumed constraint of constant volume or constant area constriction, respectively. The constriction process will be spontaneous when $F_c \leq 0$, since this condition implies a decrease in the total energy of the vesicle as the constriction progresses.

Stabilization force

The stability of the symmetric constriction against longitudinal asymmetries can be addressed by comparing the energy of the symmetrical cell with equal right and left lobes with an asymmetrical cell in which the constriction ring is displaced a small distance Δx from the middle point (see Figure 5.1B). In the asymmetrical case, the polar radius R_m (and consequently the constriction parameter s) is slightly different in each one of the lobes. At constant area (volume) constriction, the transition between the symmetric and the asymmetric shape is assumed to occur by keeping the area (volume) constant. For small displacements Δx, we can write

$$E_{\text{asym},VA} = E_{\text{sym},VA} + k_{VA}\left(\frac{\Delta x}{R_{m,VA}}\right)^2, \tag{5.6}$$

where k_{VA} is the stability coefficients with units of energy (k_V for constant volume and k_A for constant area). Symmetric constriction is stable when the stability coefficients are positive, because in this case the energy of the symmetric configuration is smaller than the asymmetric one. In contrast, negative stability coefficients predict unstable symmetric shapes against longitudinal deformations. The stabilization forces at constant volume $F_{s,V}$ or constant area$F_{s,A}$ constriction are obtained from Eq. (5.6) as

$$F_{s,VA} = -\frac{\partial E_{\text{asym}}}{\partial \Delta x}\bigg|_{AV} = -2k_{AV}\frac{\Delta x}{R_{m,VA}^2}. \tag{5.7}$$

This definition implies that symmetric constriction is stable when $F_s \leq 0$. The stabilization force scales inversely proportional to R_m^2, *i.e.*, smaller cells are more unstable against lateral displacements of the constriction ring. The deduction of the stability coefficients together with their analytical approximate solutions can be found in Annex A5. Recall that $R_{m,VA}$ in Eqs. (5.6)-(5.7) is a function of the constriction state s given by the assumed constraint of constant volume or constant area constriction.

5.2.3 Range of Systemic Parameters

Biological cells are mechanically more complex than vesicle models [35]; they have a stiffer membrane often reinforced by an underlying cell cortex, even a rigid cell wall is present in some cases. The cytoplasm may exhibit some viscoelasticity, which eventually modify the cytokinetic forces involved in cell remodeling leading to division. The cellular nucleus, and other organelle structures, are viscoelastic objects that do not remain indifferent to cytokinetic remodeling; quite the opposite, they participate actively as functional scaffolds to drive cytokinesis [218]. Particularly, in dividing animal cells, the disentangled nuclear material associates to a complex mitotic apparatus based on microtubule spindles, which deeply modify cell elasticity during the cell division process [207]. However, despite this complexity, the minimal theory above depicted recapitulates the mechanical behavior of real cells under effective values of the elasticity parameters. Specifically, global cell flexibility is described by an effective bending rigidity, which takes extremal values that depend either on leading membrane rigidity governed by the lipid bilayer [35], $\kappa_{b,\text{lipid}} \approx 50 - 200\ k_BT$, or dominant cell cortex [134], with a much higher effective value of the bending rigidity [223], $\kappa_{b,\text{cortex}} \approx Eh^3 \gtrsim 10^3\ k_BT$, which is determined by its bulk modulus ($E_{\text{cortex}} \approx 10$ kPa) developed over a larger thickness ($h_{\text{cortex}} \gtrsim 100$ nm) than the lipid membrane ($h_{\text{lipid}} \approx 6$ nm). Regarding membrane tensions, lipid trafficking and cortical flows are englobed under an effective value of the isotropic lateral tension; for tensioned cells, typically [224] $\Sigma_{\text{eff}} \approx 10 - 100$ pN/μm, whereas $\Sigma_{\text{eff}} < 0$ describes floppy conditions of membrane uptake driven by lipid trafficking [144], and/or cortical flows favoring furrow constriction [225]. In addition, hydrostatic stresses present in the cell are described by an effective pressure Δp_{eff}, which is assumed to be essentially regulated under osmotic homeostasis [143]. Therefore, and despite the intrinsic simplicity of our minimal model, the current analytic approach is sufficient to depict the physics of the cytokinetic pathway, provided we restrict our conclusions to the range of validity of the perturbative approximation [74, 75], within the regime where mechanical works due to pressure, membrane tension, and bending energy are comparable, *i.e.,* if $\Delta p_{\text{eff}} R^3 \approx$

$\Sigma_{\text{eff}}R^2 \approx \kappa_{b,\text{eff}}(1 - C_0R)^2$. Moreover, the functional importance of the cellular shape for the success of cell division is recognized in the view of our physical model.

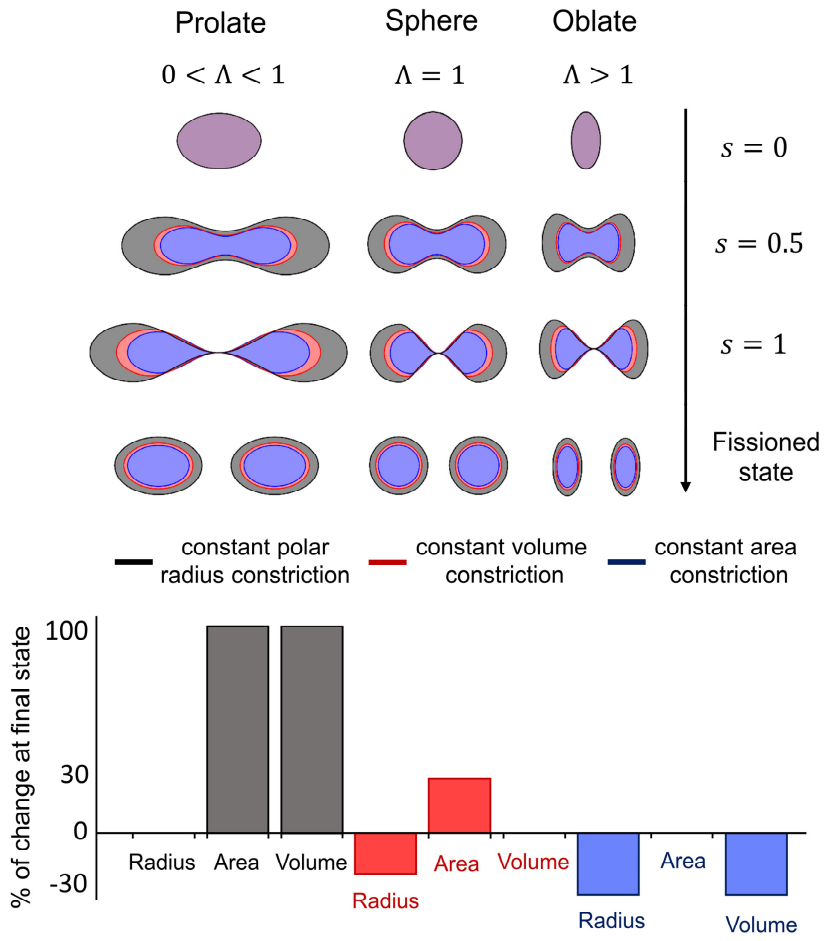

Figure 5.2. Constraints to the constriction pathway. Upper panel) Model shapes for prolate, spherical, and oblate cells at different constriction stages [at $s = 0$: initially unconstricted vesicle at $s = 0.5$: midpoint in the constriction process; at $s = 1$: maximum constriction, and at the finally fissioned state]. Three different constraints to the constriction pathway are considered: constant polar radius (black shadow); constant volume constriction (red shadow); and constant area constriction (blue shadow). Lower panel) Constriction at constant polar radius requires an increase of 100% in membrane area and volume (black columns); constriction at constant volume requires a decrease in polar radius of around 20% and an increase in membrane area of around 26% (red columns); and constriction at constant area requires a decrease in both polar radius and volume of around 30% (blue columns).

5.3 Results

The minimal model of cell constriction includes the essential ingredients involved in cytokinesis, and allows to analyze the mechanical requirements for stable symmetric constriction in different conditions. In particular, it allows to compute the constriction forces required to have constriction, and the stabilization forces required to keep the constriction symmetric. For cells of size $R_0 \approx 10$ μm and effective bending modulus of $\kappa_{b,\text{eff}} \approx 100\ k_BT$, constriction forces are predicted in the range of picoNewtons, $F_c \approx \kappa_b/R \approx 0.1$ pN, which is the range of forces practicable by molecular motors. Stabilization forces are also found to be on the same range. For vesicles of the same size formed with flexible membranes ($\kappa_b \approx 10 - 20\ k_BT$), constriction and stabilization forces are also reduced by a factor ten.

5.3.1 Stable Symmetric Constriction Requires Positive Spontaneous Curvature

The behavior of the symmetric constriction can be separated into three regions divided by the values 0 and 1 of the product $C_0 R_m$ (see Figure 5.3):

1) *Negative spontaneous curvature, $C_0 < 0$: Unstable constriction.* For negative spontaneous curvature, the constriction is non-spontaneous and unstable irrespective of surface tension Σ and external pressure Δp (see A and B panels of Figure 5.3). Negative spontaneous curvature membranes tend to build up in a concave configuration. In cells, although the shape of the constriction zone is concave, the global shape of the constricted cell is convex. Consequently, cells with membranes preferring concave shapes require additional mechanisms generating and stabilizing the symmetric constriction.

2) *Moderately positive spontaneous curvature, $0 \leq C_0 < 1/R_m$: Stable constriction is possible.* Constriction is always non-spontaneous in this case, *i.e.*, when the spontaneous curvature is smaller than the inverse of the characteristic radius of the cell. However, symmetric constriction may be stable for a certain range of surface tension and external pressure, within this range cells do not need symmetrisation mechanism, only constriction mechanisms. (This range is shaded in yellow in the C and D panels of Figure 5.3.)

3) *Considerably positive spontaneous curvature, $C_0 \geq 1/R_m$: Spontaneous and stable constriction is possible*. In this case, (*i.e.,* when the spontaneous curvature of the membrane is higher than the inverse of the cell size) there exist a broad range of values of surface tension Σ and external pressure Δp giving rise to spontaneous and stable symmetric constriction, as discussed below.

5.3.2 Spontaneous Symmetric Constriction Requires that the Spontaneous Curvature is Higher than the Characteristic Cell Radius

In the latest case introduced previously, $C_0 \geq 1/R_m$, or equivalently $C_0 R_m \geq 1$, the symmetric constriction is both spontaneous and stable in a broad range of surface tensions and external pressures. This parameter region is shaded in green in Figure 5.3E-F and represents the optimal conditions for cells to divide since they do not require additional forces generating and stabilizing the symmetric constriction. Symmetric constriction occurring outside of this optimal range may be stable but non-spontaneous (yellow region); becoming also unstable for higher membrane tensions and external pressures (red region in Figure 5.3E).

Spontaneous symmetric constriction is always stable

Other conclusions extracted from our results is that stable symmetric constriction (yellow and green regions in Figure 5.3) is found in a wider range of parameters than spontaneous symmetric constriction (green regions in Figure 5.3). In addition, we have found that spontaneous symmetric constriction is always stable, as can be seen from the region configurations described in Figure 5.3.

Reducing either the surface tension or the external pressure increases the stability and spontaneity of constriction

To symmetrically constrict in a stable and spontaneous way, cells subjected to high external pressures ($\Delta p > 0$) require negative surface tensions, much higher in absolute value than cells

immersed in a iso- or hypotonic media ($\Delta p \leq 0$) (see panels C-F of Figure 5.3). This means that negative surface tensions Σ may counterbalance high positive pressures Δp. Likewise, negative pressures may counterbalance high positive membrane tensions.

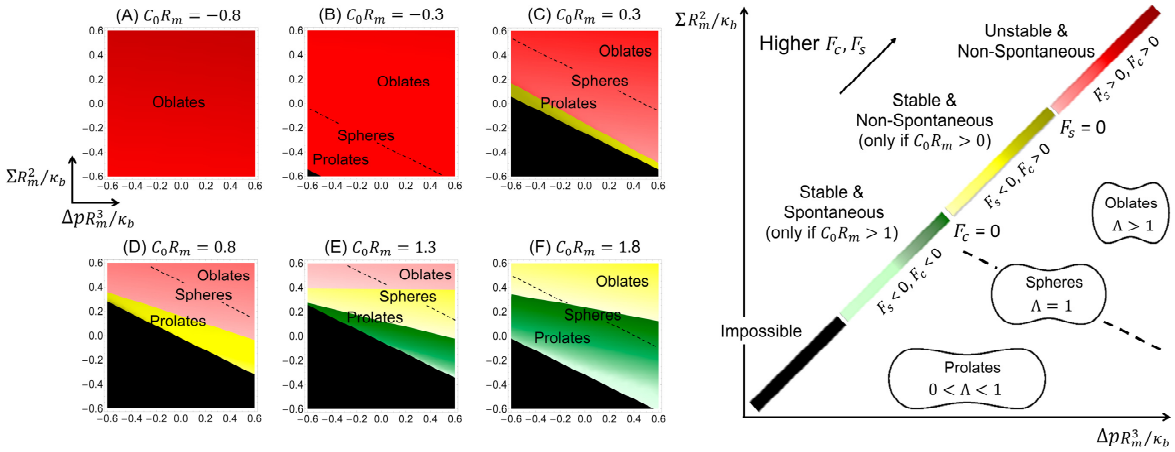

Figure 5.3. Stabilization and constriction forces for different scenarios. Stabilization and constriction forces, F_s and F_c, at the beginning of constriction ($s = 0.2$) as a function of the adimensionalized tension $\Sigma R_m^2/\kappa_b$ (y-axis) and the adimensionalized pressure $\Delta p R_m^3/\kappa_b$ (x-axis) for different values of the adimensionalized spontaneous curvature $C_0R_m = -0.8$ (A), $C_0R_m = -0.3$ (B), $C_0R_m = 0.3$ (C), $C_0R_m = 0.8$ (D), $C_0R_m = 1.3$ (E), and $C_0R_m = 1.8$ (F). Conditions predicting unstable and non-spontaneous constrictions are shaded in red; conditions predicting stable but non-spontaneous constrictions are shaded in yellow; conditions predicting stable and spontaneous constrictions are shaded in green; and conditions under which equatorial constriction is impossible (imaginary analytical results and no numerical solution) are shaded in black. Stable symmetric constriction requires positive spontaneous curvature (C-F) while spontaneous symmetric constriction requires that the spontaneous curvature is higher than the characteristic radius of the cell (E-F). High surface tensions Σ and high external pressures Δp give rise to oblate vesicles, which require large constriction and stabilization forces. In contrast, if Σ and Δp are low, our model predicts prolate shapes requiring smaller forces. Dashed lines correspond to spherical vesicles [curves with $\Lambda = 1$, Eq. (5.3)], case that separates prolates ($0 < \Lambda < 1$) and oblates ($\Lambda > 1$) shapes (note that the curve with $\Lambda = 1$ for $C_0R_m = -0.8$ is not in the region shown).The stabilization force F_s and the constriction force F_c were determined assuming constant volume constriction, but the same conclusions apply for constant area constriction.

Prolate (rod-like) cells require lower stabilization and constriction forces than oblate (disk-like) cells

Lower values of surface tension and external pressure tend to give prolate (rod-like) cell shapes, which are found to require lower stabilization and constriction forces. Conversely, higher values of surface tension and external pressure give rise to oblate (disk-like) cells, which require strong constriction and stabilization forces to divide symmetrically (see Figure 5.3).

Symmetric constriction is no longer possible below a critical threshold

Symmetric constriction is impossible to occur for conditions giving $\Lambda \leq 0$ [Eq. (5.3)], which corresponds to strong negatives values of both Σ and Δp (regions shaded in black in Figure 5.3). As we approach to the limit $\Lambda \to 0$, our model predicts very elongated prolate (rod-like) cells for which the symmetric mode of equatorial constriction is no longer possible since these cells cannot create a single circumferential furrow at their equator.

5.3.3 Stability and Spontaneity of Symmetric Constriction Increase as Constriction Progresses

Non-spontaneous constrictions are uphill processes, characterized by an increase of energy as the constriction advances, and therefore require a constriction force to occur. See in Figure 5.4 the increase of energy in the direction of the constriction stage s-axis for the non-spontaneous regions (red and yellow regions). Note also that progress in constriction implies a decrease in the slope (related to constriction force), which in some cases even becomes negative, implying a transition from non-spontaneous to spontaneous constriction. The slope of the energy in the direction of the constriction stage is related to the constriction force through Eq. (5.3). Stable symmetric constriction entails that symmetric constriction is an energy minimum, and therefore energy increases when the asymmetry Δx goes out of its zero value, giving a concave profile in the Δx direction for the stable cases (yellow and green regions of Figure 5.4). Unstable symmetric constriction corresponds to maxima, and convex profiles appear in the Δx direction (red regions of Figure 5.4). As symmetric constriction progresses it becomes more stable and spontaneous (see Figure 5.4).

Membranes characterized with negatives values of C_0 present unstable and non-spontaneous constriction during the whole process (Figure 5.4A). On the other hand, if C_0 is positive but lower than the characteristic inverse cell size, the constriction is non-spontaneous but reaches the stability at some point of the division (Figure 5.4B). Finally, when C_0 is higher than the characteristic inverse cell size, constriction starts as a non-spontaneous and unstable process but becomes stable and spontaneous at final stages (Figure 5.4C). The points where the transitions between the regions occur depends on the values of the membrane surface tension and external pressure. Note also that the energy of the system decreases as the spontaneous curvature increases.

We could also note that for constant volume or constant area constriction, R_m decreases as constriction advances (see Figures A5.2 and A5.3 in Annex A5). This implies that the product $C_0 R_m$ also decreases during constriction, and therefore it could change from one region of behaviour to another. In practice, this only happens to values very close to the limits of the region (as for example $C_0 R_0 = 1.3$). In particular, it is not the case for the values represented in Figure 5.4.

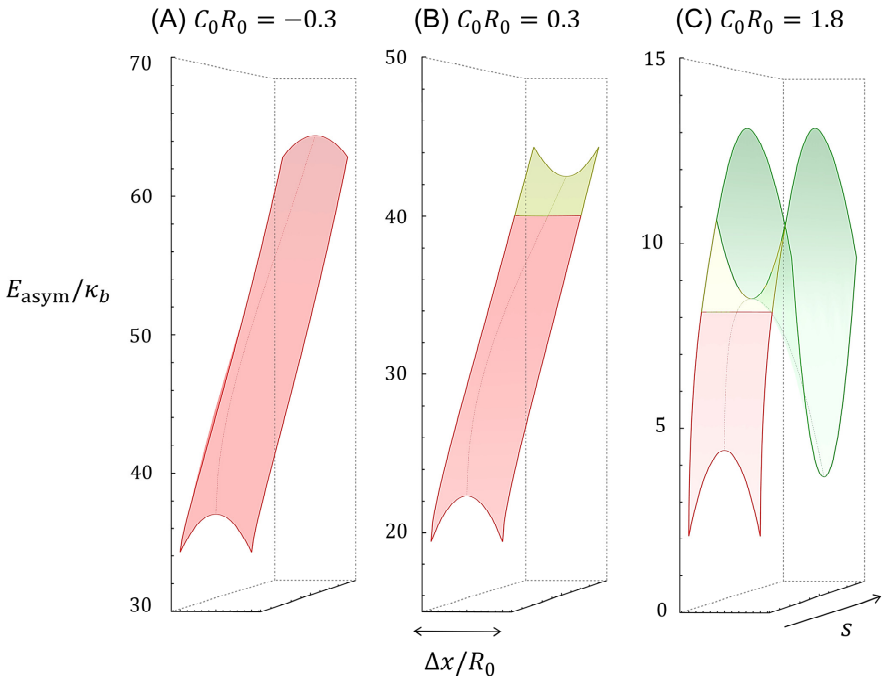

Figure 5.4. Energy landscape during cell constriction for different scenarios. Energy of the asymmetric configuration as a function of the constriction stage s and the displacement of the constriction ring from the middle point $\Delta x/R_0$ for $\Sigma R_0^2/\kappa_b = \Delta p R_0^3/\kappa_b = 0.25$ and for $C_0R_0 = -0.3$ (A), 0.3 (B) and 1.8 (C), with R_0 the initial maximum radius. Unstable, stable, and spontaneous regions are shaded, respectively, in red, yellow, and green. Membranes characterized with negatives values of C_0 (A) present unstable (convex profile) and non-spontaneous constriction (uphill energy) during the whole process. If, instead, C_0 is positive but lower than the characteristic inverse cell size (B), the constriction is non-spontaneous (uphill energy) but reaches the stability at some point of the division (concave profile). Finally, when C_0 is higher than the characteristic inverse cell size (C), constriction starts as a non-spontaneous and unstable process but becomes stable (concave profile) and spontaneous (downhill energy) at final stages. These results were determined assuming constant volume constriction, but the same conclusions apply for constant area constriction.

5.4 Discussion

Our results show that cell constriction is, in general, a non-spontaneous process that requires to be initiated by a constriction apparatus that stresses a radial force at the site of division. For cells of size $R_0 \approx 10$ μm and effective bending modulus of $\kappa_{b,\text{eff}} \approx 100\, k_BT$, constriction forces are predicted in the range of picoNewtons, $F_c \approx \kappa_b/R_0 \approx 0.1$ pN, which is the range of forces practicable by molecular motors. This constriction force could increase up to 10 pN in more rigid scenarios ($\kappa_{b,\text{eff}} \approx 10^4\, k_BT$), which is compatible with the forces exerted by the actomyosin furrow in unicellular eukaryotes with a cell wall [226, 227]. Once constriction is initiated, above a certain spontaneity onset, we show that constriction can progress till final division.

We also found that mechanical stability of symmetric constriction necessarily requires cellular shapes defined by positive spontaneous curvature (prolate-like), a situation typical in elongated eukaryote cells; otherwise, additional stabilization mechanisms might be incorporated to the constriction system. The stabilization forces required are also in the range of the picoNewton. Amazingly, symmetric constriction is shown to occur spontaneously for spontaneous curvatures above a threshold determined by the cell size, a circumstance that could have been exploited by primitive protocells to undergo spontaneous division without a specific cytokinetic machinery.

Furthermore, our results show that a lowering in membrane tension, due to membrane-targeted lipid biogenesis or directed cortical flows, for instance, leads to an increase of stability and spontaneity of cellular constriction. A reduction on the external pressure also gives rise to a similar consequence. This implies that prolate-shaped cells (cylinders) favoured by low pressure and surface tension, in general, require lower constriction and stabilization forces to undergo division.

In the simplest case of cell-sized vesicles ($R_0 \approx 10$ μm), with a single lipid bilayer as flexible membrane ($\kappa_b \approx 10 - 20\, k_B T$), constriction forces are smaller $F_c \approx \kappa_b / R_0 \approx 0.01$ pN. Under adequate conditions of excess area, or reduced volume, regulated by osmotic stresses, asymmetric budding occurs spontaneously in cell-size vesicles without a constriction machinery [166], indicating the chief role of membrane tension, and external pressure, in spontaneous constriction mechanisms leading to facilitated cell scission. Well know is also the mechanical link that exists between the spontaneous curvature of the lipid bilayer and the phenomenon of spontaneous fission observed in model vesicles [43]. Those phenomena observed in artificial models have attracted much theoretical interest [76, 144, 181]. Our minimal model enables to predict conditions for stability and spontaneity of the constriction process, and its general results are consistent with the experimental observations [228–231].

It is well-known that the cell is certainly not in an equilibrium state, rather a large amount of biochemical processes is continuously taking place. We recognize that a description of the cell division using equilibrium arguments has its limitations but still is a very useful approximation. The picture emerged from our model allows to describe the mechanical conditions necessary for stable cell division in different organisms and to obtain approximate analytic expressions for the more relevant magnitudes involved.

Besides that, the detailed biophysics of cell division in evolved cells involves a mature cytokinetic engine strongly influenced by the active role of cortical fluxes [225] and the mitotic spines of tubulin (producing elongation force). Our model is minimal and as such must be taken into account: as a predictor of essential prerequisites, not as a descriptor of real complex processes. Thus, it is expected to represent the simple mechanism of cell division in the early stages of evolution, before the cells developed complex strategies (the wall and the septum in prokaryotes, or the active cortex of actomyosin in nucleated cells). Related to this issue, our model has shown that even a minimum cell can divide spontaneously in a stable way under certain systemic (rigidity, spontaneous curvature) and environmental (pressure, tension) conditions. This result has an unquestionable predictive value in a minimal scenario as it should have been the primal life. Future improvements of this minimal model must include the active flows in the cell cortex, which has been identified as the main source of constriction forces. These flows, generated by concentration gradients of motor proteins (myosin), have been associated with the formation of the contractile ring, furrow constriction, and symmetry breaking during asymmetric cell division. In 2014, Turlier and colleagues developed a nonlinear membrane model for the acto-myosin cortex in which the resulting cortex deformation is calculated numerically [225]. Starting from a quite fundamental physical model of the cortex: a thin viscous layer producing active contraction and subjected to a uniform cytoplasmic pressure, they succeed in reproducing the features of cytokinesis such as cell shape and cortical flows toward the equator. In their model, they assume the cell volume is nearly conserved throughout cytokinesis. However, their model

neglects the bending energy contributions, and do not consider the effects of the bending modulus and the spontaneous curvature of the cell membrane. A detailed comparison between this model and the model presented in this thesis is still lacking. This comparison could lead to a more general and accurate model combining the best ingredients of the two models. In our model, the cell contents are assumed to exert three types of forces on the cell membrane: one determining the radius of the lobes of the cell, another force exerting constriction in the middle of the cell, and finally an effective force stabilizing the symmetric constriction. Each of these effective forces accounts for the different sources of this effect in the different cells. For example, the force determining the radius of the cell lobes are influenced by nucleoid exclusion and cortex activity, constriction force can be due to constriction ring but can also have other sources, and the effective force stabilizing the symmetric constriction is effectively generated by the different positioning mechanism of the constriction region. In our model, the constriction path is described as a succession of equilibrium shapes obtained under the constraints given by the three types of effective forces, described above. This assumes the arrival to equilibrium at each set of constraints given by the forces is faster than the changes of forces. In this way our model can effectively account for a wide variety of forces in a simple way, as it only takes into account the resulting effective force for each type of force. Moreover, our model allows us to address different biological approximate realizations: intense membrane trafficking (modeled by constant volume constriction), inhibited membrane trafficking (modeled by constant area constriction), and constriction at constant radius. In a simplified form, our model can incorporate the effect of cell cortex through an effective membrane bending rigidity and the effect of cortical flows can be englobed under an effective value of the lateral tension. Even with this approximation, we can determine the mechanical conditions for symmetric constriction to become spontaneous (*i.e.*, when constriction occurs without the need of constriction forces), and also the conditions to have stable symmetric constriction. Additional improvements of our model could include a more detailed implementation of the force fields acting on the membrane, and also the viscoelasticity of the cytoplasm, cell nucleus, and the organelle structures, which also participate to drive cytokinesis [218]. Another improvement will entail the inclusion of the cell wall dynamics in prokaryotes and plant cells in order to construct a general minimal model of cell constriction.

Acknowledgments

All authors acknowledge Alan Siegel, Harold C. Smith, and Andrew Wilde for providing permission to use their images in Figure 5.1A. EBH acknowledges financial support from Ministerio de Educación, Cultura y Deporte (MECD, Spain) under FPU grant 13/02826. FM acknowledges financial support from Ministerio de Economía y Competitividad (MINECO, Spain) and European Regional Development Fund (ERDF) under grant FIS201570339-C2-1-R, and from Comunidad de Madrid (CAM, Spain) under grant S2013/MIT-2807. FJC acknowledges financial support from Ministerio de Economía y Competitividad (MINECO, Spain) and from European Regional Development Fund (ERDF) under grant FIS2015-67745-R (MINECO/FEDER).

Annex 5

Mechanical Conditions for Stable Symmetric Cell Constriction

This chapter contains further information related to the previous chapter, Chapter 5. In Section A5.1 we present the generalized Young-Laplace equation, derived from the results obtained in Chapter 4. Section A5.2 contains some useful mathematical expressions about the differential geometry of spheroidal cells and Section A5.3 explains the parameterization of the constricted cell profile. In Section A5.4 we analyze the cell constriction at constant area and constant volume and finally, in Section A5.5, we describe the stability problem of symmetric constriction where we deduce analytical expressions for the stability coefficients.

A5.1 Equilibrium Condition: Generalized Young-Laplace Equation

In our minimal model of deformable cell depicted as a closed vesicle of membrane area A and enclosed volume V, under the net pressure difference $\Delta p = p_{\text{out}} - p_{\text{in}}$ between the outer medium and the cell interior, and the tensional action of the surface tension Σ, the total elastic energy writes in the canonical Canham-Helfrich form as [35]

$$E_T = \int_\Omega \left[\frac{\kappa_b}{2}(2H - C_0)^2 + \kappa_G K + \Sigma\right] \mathrm{d}A + \int_\Omega \Delta p \mathrm{d}V\,, \tag{A5.1}$$

where Ω is the closed surface that delimits the membrane vesicle, H is the mean curvature, K the Gaussian curvature, dA denotes the element of area, and dV the volume counterpart. The parameters κ_b and κ_G are the bending modulus and the Gaussian bending rigidity, which represent the strength of the membrane modes of curvature associated to H and K, respectively; C_0 is the spontaneous curvature of the membrane, which represents the tendency of the membrane to curve in the equilibrium state [35], usually due to the compositional asymmetry between the inner and the outer sides [220]. Note that the Gaussian term $\int_\Omega \kappa_G K \mathrm{d}A$ is omitted in Eq. (5.1) of the main text. This is because this integral is constant for surfaces with the same topology (Gauss-Bonnet theorem [35]). Since the constriction process in a vesicle does not change its topology, and only involves shapes that are topologically equivalent to a sphere (no holes), the contribution of the Gaussian curvature can be ignored because it remains constant independently of the size and shape of the vesicle. For the final fissioned state, in which the vesicle splits into two separated daughters, the Gaussian contribution should be considered.

To determine what generic shape has the lower energy for given values of the mechanical constraints, the first-variation of the energy is calculated from Eq. (A5.1). For a closed membrane vesicle, the equilibrium cell-shape equation is obtained as [232, 233][35]

$$\Delta p + 2\Sigma H - \kappa_b(2H - C_0)(2H^2 - 2K + C_0 H) - 2\kappa_b \nabla^2 H = 0, \tag{A5.2}$$

where ∇^2 is the Laplace–Beltrami operator. This nonlinear partial differential equation is extremely complicated to solve. It represents the local force balance at the vesicle membrane, and apart from the pressure difference and the membrane tension, it accounts for the local stress of curvature.

For the special case of a sphere of constant radius R, the curvatures are $H = 1/R$ and $K = 1/R^2$, so the shape-equation has the analytical solution

$$\Delta p R^3 + 2\Sigma R^2 + \kappa_b(C_0 R - 2)C_0 R = 0\,, \tag{A5.3}$$

which is fulfilled under the geometrical condition $\nabla^2 H = 0$, which describes the constant curvature of the sphere. Amazingly, if no bending rigidity is considered ($\kappa_b = 0$), the relationship in Eq. (A5.3) reduces to the well-known Young-Laplace equation of a soap bubble, $\Delta p = -2\Sigma/R$, which relates the radius of the bubble with the Laplace pressure through the surface tension. Thus, positive membrane tension leads to a negative value of the Laplace pressure, as defined as by the setting in Eq. (A5.1).

In Chapter 4 we derived the following generalized Young-Laplace relationship for ellipsoidal spheroids with revolution symmetry

$$\Delta p R_m^3 + 2\Sigma R_m^2 + \kappa_b(C_0 R_m - 2)C_0 R_m + \kappa_b(1 - \Lambda) = 0\,, \tag{A5.4}$$

where R_m is the polar radius of the spheroid and Λ is the shape parameter. The shape parameter takes values $0 < \Lambda < 1$ for prolate spheroidal shapes, $\Lambda > 1$ for oblate ones, and reduces to $\Lambda = 1$ for the sphere (see Figure 5.2). This expression (A5.4) leads to the definition of Λ shown in Eq. (5.3) of the Chapter 5. For small departures from the spherical shape, the curvatures of spheroids may be approached by those of the sphere, $H \approx 1/R$ and $K \approx 1/R^2$. Thus, comparing Eqs. (A5.2) and (A5.4), the Laplacian–Beltrami term in Eq. (A5.2) for spheroids can be estimated by $\nabla^2 H \approx (\Lambda - 1)/2R_m^3$. The Laplacian of a scalar field measures the convexity, or stress of the field, as indicates how much the value of the field differs from its average value taken over the surrounding points. Oblate shapes ($\Lambda > 1$) give positive values of $\nabla^2 H$, which indicates locally concave scalar curvature fields. Conversely, prolate shapes ($0 < \Lambda < 1$) give $\nabla^2 H < 0$, corresponding to locally convex scalar curvature fields.

A5.2 Differential Geometry of Spheroidal Cells

To describe the membrane surface of the vesicle we use the Monge parameterization [35]: the position $\vec{r}$ on the surface has Cartesian coordinates and is defined by giving its height h over some $x - y$ plane as

$$\vec{r} = \big(x, y, h(x, y)\big). \tag{A5.5}$$

After considering mathematical aspects of differential geometry, the mean curvature $H = (C_1 + C_2)/2$ is found to be given in terms of the height function by [35]

$$H = \frac{C_1 + C_2}{2} = \frac{(1 + h_x^2)h_{yy} + (1 + h_y^2)h_{xx} - 2h_x h_y h_{xy}}{2(1 + h_x^2 + h_y^2)^{3/2}}, \tag{A5.6}$$

where the x and y subscripts represent partial derivatives with respect to this variable. The element of area on the surface and the element of volume enclosed by the surface are [35]

$$\mathrm{d}A = \sqrt{1 + h_x^2 + h_y^2}\mathrm{d}x\mathrm{d}y, \;\; \mathrm{d}V = h\mathrm{d}x\mathrm{d}y. \tag{A5.7}$$

For the particular case of axisymmetric shapes with the axis of symmetry along the x–axis,

$$h(x, y) = \pm\sqrt{R^2(x) - y^2}, \tag{A5.8}$$

where $R(x)$ is the functional form describing the membrane profile in the $x - z$ plane (see Figure A5.1A). The signs + and – parameterize, respectively, the upper half Ω_+ and the lower half Ω_- of the surface. Using the parameterizations for Ω_+ the mean curvature of Eq. (A5.6) becomes

$$H = \frac{C_1 + C_2}{2} = \frac{1 + R_x^2 - R_{xx}R}{2(1 + R_x^2)^{3/2}R}. \tag{A5.9}$$

The elements of area and volume [Eq. (A5.7)] are

$$\mathrm{d}A = \sqrt{\frac{1+R_x^2}{R^2-y^2}}\mathrm{d}x\mathrm{d}y, \;\; \mathrm{d}V = \sqrt{R^2(x) - y^2}\mathrm{d}x\mathrm{d}y. \tag{A5.10}$$

If the surface is between x_i and x_i , its total area would be

$$A = 2\int_{\Omega_+} \mathrm{d}A = 2\int_{x_i}^{x_f} R\sqrt{1 + R_x^2}\int_{-R(x)}^{R(x)} \frac{1}{\sqrt{R^2 - y^2}}\mathrm{d}y\mathrm{d}x = 2\pi\int_{x_i}^{x_f} R\sqrt{1 + R_x^2}\,\mathrm{d}x. \tag{A5.11}$$

For the total volume enclosed by the surface we have

$$V = 2\int_{\Omega_+} h(x, y)\mathrm{d}x\mathrm{d}y = 2\int_{\Omega_+} \sqrt{R^2(x) - y^2}\mathrm{d}y\mathrm{d}x = \pi\int_{x_i}^{x_f} R^2\,\mathrm{d}x, \tag{A5.12}$$

where the factor 2 outside the integrals of Eqs. (A5.10)-(A5.11) comes for the symmetry between $\Omega_+$and Ω_-, and we have integrated the y variable.

Finally, the bending energy E_b (ignoring the Gaussian term) for a surface of revolution is given by

$$\begin{aligned} E_b &= \frac{\kappa_b}{2}\int_{\Omega} (2H - C_0)^2\mathrm{d}A \\ &= \kappa_b\int_{x_i}^{x_f} \frac{\left[1 + R_x^2 - R_{xx}R - RC_0(1 + R_x^2)^{3/2}\right]^2}{(1 + R_x^2)^{5/2}R}\int_{-R(x)}^{R(x)} \frac{1}{\sqrt{R^2 - y^2}}\mathrm{d}y\mathrm{d}x \\ &= \pi\kappa_b\int_{x_i}^{x_f} \frac{\left[1 + R_x^2 - R_{xx}R - RC_0(1 + R_x^2)^{3/2}\right]^2}{(1 + R_x^2)^{5/2}R}\mathrm{d}x. \end{aligned} \tag{A5.13}$$

Note that the results of Eqs. (A5.11)-(A5.13) are independent of the coordinate y, as expected for surfaces with rotational symmetry around x.

A5.3 Parameterization of the Constricted Cell Profile

As we previously made in Chapter 4, the axisymmetric profile of a symmetrically constricted cell is divided into two different regions: polar caps (left polar cap shaded in blue in Figure A5.1A) and constriction zone (left half of the constriction zone shaded in yellow in Figure A5.1A). Establishing the origin of the x coordinate in the middle point of the vesicle, the constriction profile can be expressed as

$$R(x;s) = \begin{cases} R_{\text{left polar cap}}(x) & \text{if} \quad x \in [-L_p - L_m, -L_m] \\ R_{cz}(x;s) & \text{if} \quad x \in [-L_m, L_m] \\ R_{\text{right polar cap}}(x) & \text{if} \quad x \in [L_m, L_m + L_p] \end{cases} \tag{A5.14}$$

where L_m and L_p represent the half of the length of the constriction zone and the polar distance, respectively (see Figure A5.1A). Note that the constriction profile must be continuous in the boundaries of the zones. In addition, since the shape has central symmetry, we have the relation $R_{\text{left pole cap}}(x) = R_{\text{right pole cap}}(-x)$.

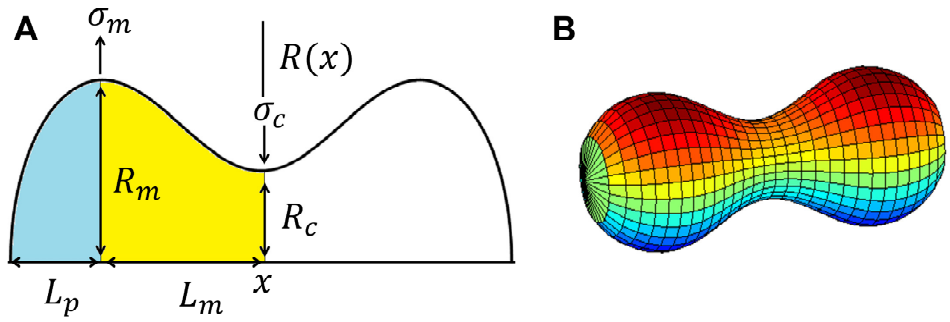

Figure A5.1. Symmetrically constricted vesicle. (A) Profile $R(x)$ of a symmetrically constricted vesicle with the axis of symmetry along the x–axis and its characteristic parameters. Left polar cap is shaded in blue and the left half of the constriction zone is shaded in yellow. (B) Surface obtained from the revolution around the x–axis.

The profile describing the right polar cap with semi-axis R_m (polar radius) and L_p (polar distance) centered in $x = L_m$ (see Figure A5.1A) is

$$R_{\text{right polar cap}}(x) = \pm R_m \sqrt{1 - \left(\frac{x - L_m}{L_p}\right)^2}, \quad x \in [L_m, L_m + L_p]. \tag{A5.15}$$

In previous works [74, 75, 222], we have seen that the constriction zone can be approximately described with a trigonometric function whose local curvature changes along the constriction process as

$$R_{cz}(x;s) = R_m \left\{1 - \frac{s}{2}\left[1 + \cos\left(\frac{\pi x}{L_m}\right)\right]\right\}, \tag{A5.16}$$

where the constriction parameter s is defined in terms of the ratio between the constriction radius R_c and the polar radius R_m in the form $s = 1 - R_c/R_m$. The constriction profile of the vesicle $R(x;s)$ [Eq. (A5.14)], together with its first and second derivatives ($R_x = \partial R/\partial x$ and $R_{xx} = \partial R_x/\partial x$), allow us to determine the minimum energy shapes along the constriction

pathway by minimizing the total energy [Eq. (A5.13)] with respect to the characteristic length of each zone (L_p for the polar caps and L_m for the constriction zone):

$$\frac{\partial E_{T,\,\text{polar caps}}\left(L_p, R_m, C_0, \Sigma, \Delta p, \kappa_b\right)}{\partial L_p} = 0 \xrightarrow{\text{yields}} L_p = L_p^{\text{opt}}, \tag{A5.17a}$$

$$\left.\frac{\partial E_{T,\,\text{cz}}(s, L_m, R_m, C_0, \Sigma, \Delta p, \kappa_b)}{\partial L_m}\right|_s = 0 \xrightarrow{\text{yields}} L_m(s) = L_m^{\text{opt}}(s). \tag{A5.17b}$$

Once optimal total length $L_p^{\text{opt}} + L_m^{\text{opt}}(s)$ has been obtained, other quantities of the system can be calculated, as are the total energy, the membrane area, the volume enclosed and the constriction forces. These expressions are given in terms of the spontaneous curvature C_0, the surface tension Σ, the osmotic pressure Δp, the polar radius R_m, and the constriction parameter s (analytical formulas can be found in Chapter 4). The fourth-order expressions describe with 95% agreement the numerical solution up to constrictions as large as $s \approx 0.65$ (see Figures 4.5 and 4.6 in Chapter 4). Higher constriction stages require a constriction profile more accurate than Eq. (A5.16) to describe the strong changes of curvature.

When the constriction process is assumed to proceed by keeping the polar radius R_m constant, the polar distance L_p [Eq. (A5.17a)] becomes independent of the constriction parameter s (and therefore, other properties of the system calculated on the polar caps zone are also independent of s). Conversely, under constant area or constant volume conditions (see below), these quantities are not constant but vary along the constriction pathway.

Exact numerical method

Analytical formulas derived with the perturbative method are compared with the (exact) solution of the Euler-Lagrange equations computed numerically. The Euler-Lagrange equations do not have an analytical solution in general, but can be solved numerically and different methods have been developed to solve them. As we made in Chapter 4, we use here the methodology proposed in Refs. [71, 72], and apply it to axisymmetric shapes subject to equatorial constriction stress with either polar radius R_m, enclosed volume V, or membrane area A maintained constant.

A5.4 Constriction at Constant Volume and at Constant Area

Instead of considering the polar radius R_m constant, constrictions at constant volume or at constant area can be additionally addressed. There are several possibilities to define these constant volume or constant area constriction paths. In Chapter 4 we proposed a re-dimensioning strategy that rescales the shape in a factor $\lambda(s)$ as: $R_m \to \lambda R_m$, $\kappa_b \to \kappa_b$, $E_T \to E_T$, $C_0 \to C_0/\lambda$, $C_1 \to C_1/\lambda$, $C_2 \to C_2/\lambda$, $A \to \lambda^2 A$, $V \to \lambda^3 V$, $\Sigma \to \Sigma/\lambda^2$, and $\Delta p \to \Delta p/\lambda^3$. This parameter corresponds to

$$\lambda_V = \sqrt[3]{\frac{V(s=0)}{V(s)}}, \tag{A5.18}$$

for constant volume condition and to

$$\lambda_A = \sqrt{\frac{A(s=0)}{A(s)}}, \tag{A5.19}$$

for constant area condition. $A(s=0)$ and $V(s=0)$ are, respectively, the membrane area and the volume enclosed by the initial spheroid. This rescaling method imposes shape-invariance since it maintains the dimensionless products $C_0 R_m$, ΣR_m^2, and $\Delta p R_m^3$ constant upon constriction [and then maintain Λ invariant, see Eq. (5.3) in Chapter 5]. Although this simplifies the computations, it could be not very realistic.

We explore here a more lifelike constriction path, where the parameters C_0, Σ, and Δp remain constant along the constriction pathway (instead of products $C_0 R_m$, ΣR_m^2, and $\Delta p R_m^3$). To do that, we compute the variation of the polar radius during constriction that keeps constant either the volume enclosed by the cell V, or the cell membrane area A, $R_{m,VA}(s)$, then allowing Λ to vary in both cases along the constriction pathway. Therefore, we solve the respective algebraic equations, either $V(R_m, s) = V_0(R_0, s=0)$ at variable $A(R_m, s)$ or $A(R_m, s) = A_0(R_0, s=0)$ at variable $V(R_m, s)$, with R_0 being the polar radius of the mother cell (unconstricted configuration). The expressions of the cell volume $V(R_m, s)$ and the membrane area $A(R_m, s)$ along the constriction pathway were previously derived for us (both analytically and numerically) in Chapter 4. Except in the simple case when $C_0 = \Sigma = \Delta p = 0$, there is not analytical solution of these equations, but they can be solved numerically. Equivalently, $R_{m,VA}(s)$ can be obtained by evaluating the following differential equations with the initial condition $R_{m,VA}(0) = R_0$

$$\frac{\mathrm{d}R_{m,V}}{\mathrm{d}s} = -\frac{\partial V/\partial s}{\partial V/\partial R_m}, \qquad \frac{\mathrm{d}R_{m,A}}{\mathrm{d}s} = -\frac{\partial A/\partial s}{\partial A/\partial R_m} \tag{A5.20}$$

Consequently, the quantity Λ of Eq. (5.3), which determines the shape of the cell lobes, mildly varies along the constriction process due to the variations of $R_{m,VA}$. The model predicts in general shape conservation, thus, oblate, spherical, or prolate mother cells divide, respectively, into two oblate, two spherical, or two prolate daughter cells (see Figure 5.2 in Chapter 5).

A5.4.1 Increase of Area at Constant Volume

Constriction at constant volume requires a decrease in polar radius $R_{m,V}$ and an increase of the membrane area A_V (see Figure A5.2). There is a close agreement between the analytical and the numerical results for both quantities at low and intermediate regimes. At large constrictions, the analytical formulas do not describe the exact solution properly but underestimate significantly the increase of area. At final constriction, when $s \to 1$, the decrease in polar radius is

$$\lim_{s\to 1} \frac{R_{m,V}}{R_0} = 2^{-1/3} \approx 0.79, \tag{A5.21}$$

while the increase in membrane area is

$$\lim_{s\to 1} \frac{A_V}{A_0} = 2^{1/3} \approx 1.26. \tag{A5.22}$$

Consequently, the constriction process at constant volume requires a final decrease in polar radius of around 20% and a final increase in the membrane area of around 26% independently of C_0, Σ, and Δp, which is in agreement with the numerical limits (see Figure A5.2).

Constriction at constant volume may describe divided cells with intense membrane trafficking [148, 149], which is known to play an important role in cytokinesis [154, 155].

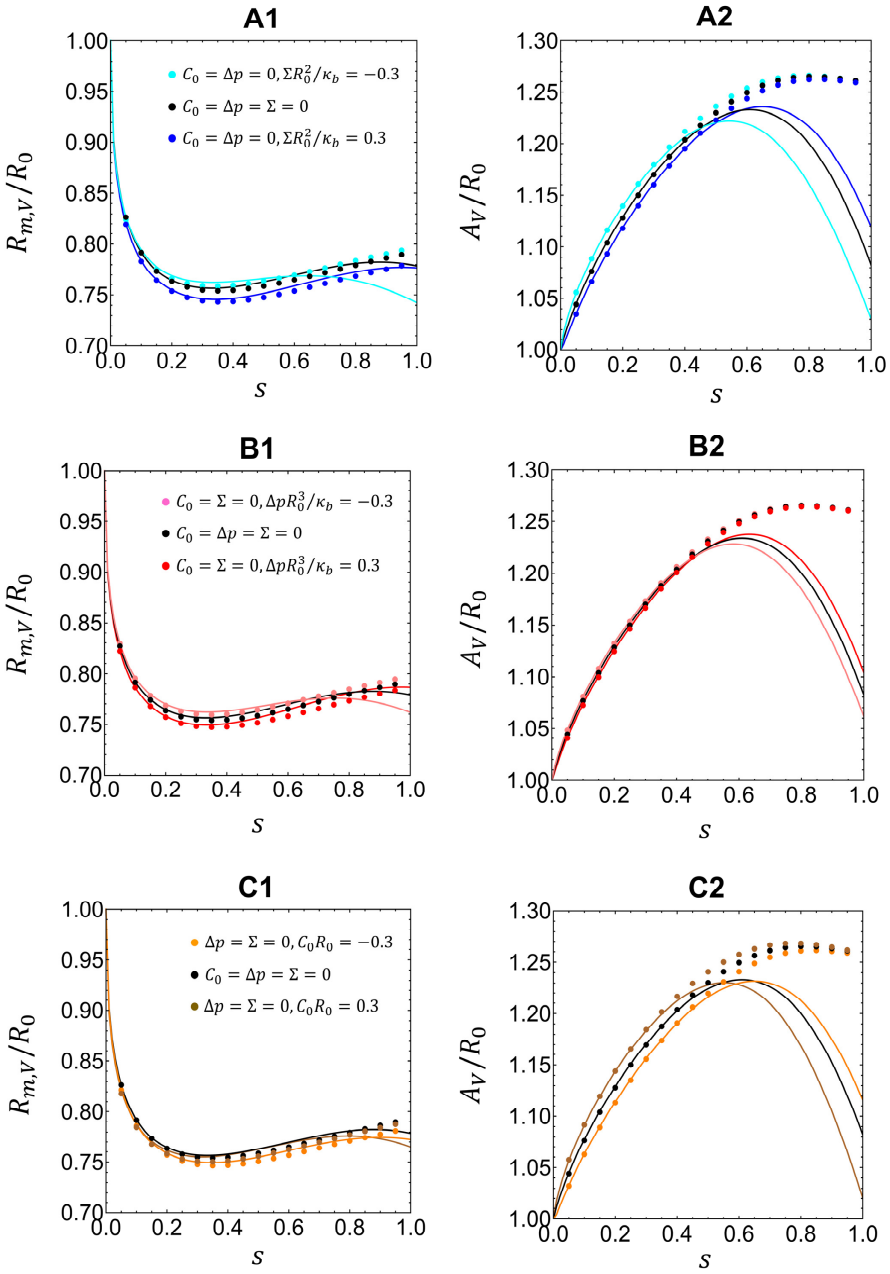

Figure A5.2. Constant volume constriction. Decrease of polar radius (left-hand column) and increase of membrane area (right-hand column) along the constriction pathway maintaining constant volume. Comparison between analytical and numerical results. (A) Influence of the surface tension Σ. (B) Influence of the osmotic pressure Δp. (C) Influence of the spontaneous curvature of the membrane C_0. Constriction process at constant volume requires a final decrease in polar radius of around 20% and an final increase in the membrane area of around 26%, independently of C_0, Σ, and Δp.

A5.4.2 Decrease of Volume at Constant Area

Constriction at constant area requires a decrease in both the polar radius $R_{m,A}$ and the volume enclosed by the vesicle V_A (see Figure A5.3). As in constant volume constriction, the analytical results reproduce the exact solution in the range of low and intermediate constrictions, but fail at higher regimes. The decrease in both polar radius and volume enclosed on the vesicle at the final constriction state is

$$\lim_{s\to 1}\frac{R_{m,A}}{R_0}=\lim_{s\to 1}\frac{V_A}{V_0}=2^{-1/2}\approx 0.71, \tag{A5.23}$$

implying that the constriction process at constant area requires a final decrease in both polar radius and volume enclosed by the vesicle of around 30% independently of C_0, Σ, and Δp, which corresponds with the numerical limit (see Figure A5.3).

Constriction at constant area may describe divided cells with low or inhibited membrane trafficking. Moreover, in constant area constriction, a greater initial area is required to have the same final volume. Heat shock has been shown to increase the area before division [200, 201] and to affect membrane trafficking molecules genes expression, but also other genes as those of signalling molecules [202].

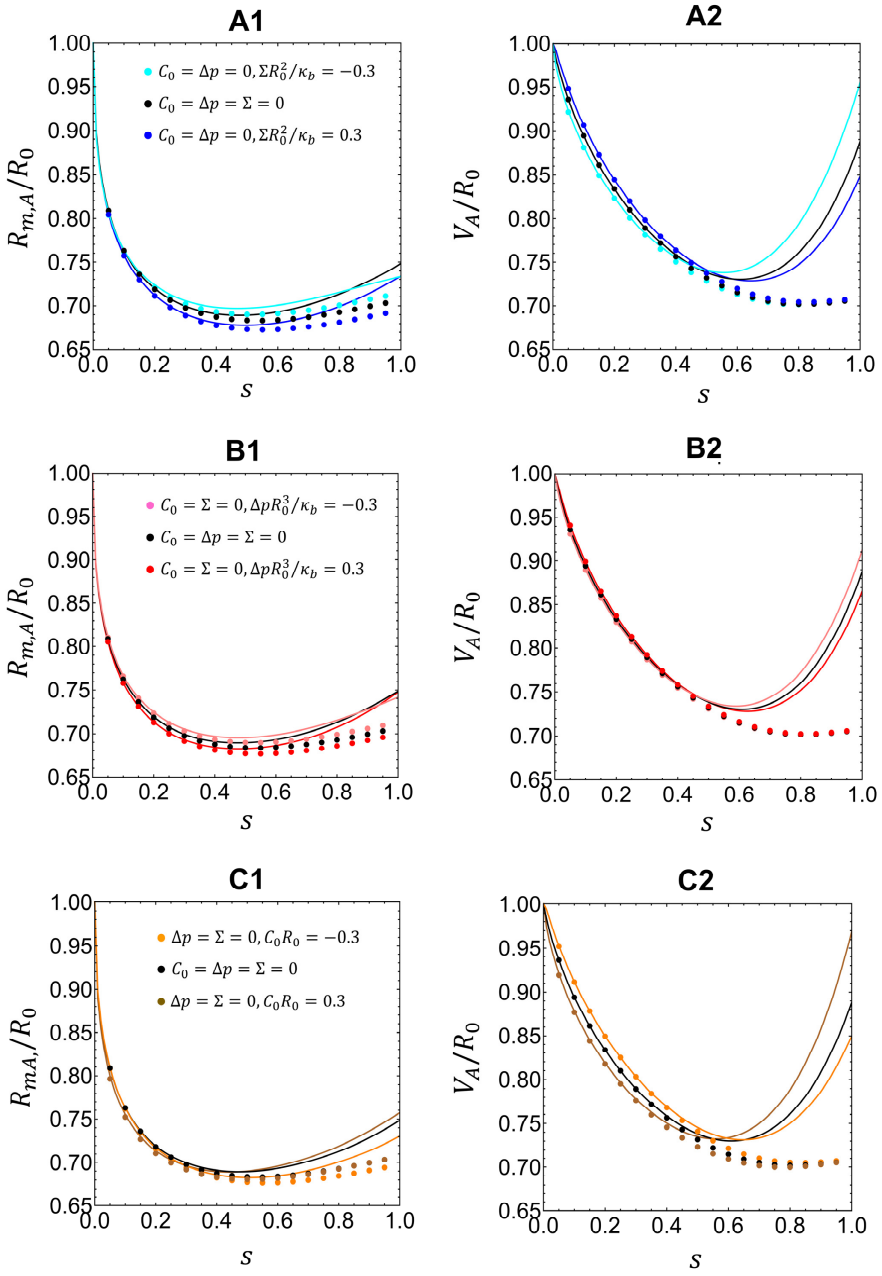

Figure A5.3. Constant area constriction. Decrease of both polar radius (left-hand column) and volume enclosed on the vesicle (right-hand column) during constant area constriction. Comparison between analytical and numerical results. (A) Influence of the surface tension Σ. (B) Influence of the osmotic pressure Δp. (C) Influence of the spontaneous curvature of the membrane C_0. Constriction process at constant area requires a final decrease in both polar radius and volume enclosed on the vesicle of around 30%, independently of C_0, Σ, and Δp.

A5.5 Stability of Symmetric Constriction: Stability Coefficients

The stability of the symmetric constriction can be addressed by introducing small changes on the symmetric shape and comparing its energy with the original one. In order to perform this computation, the constriction ring is displaced a length Δx from the middle point giving an asymmetric shape in which the right and the left lobes are not equal but one of the lobes is greater than the other (see Figure A5.4).

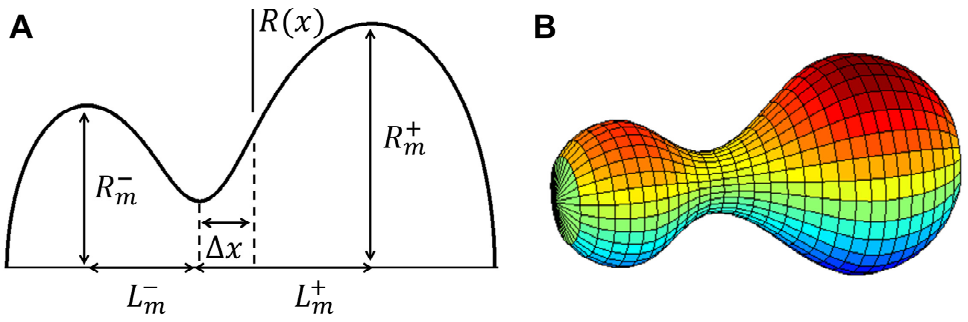

Figure A5.4. Asymmetrically constricted vesicle. (A) Asymmetric profile after displacing the constriction ring a length Δx from the middle point. (B) Surface obtained from the revolution around the x–axis.

We study here the cases in which the transition between the symmetric and the asymmetric shape takes place by keeping the volume enclosed in the vesicle or its membrane area constant. In terms of energy, this new shape can be expressed as

$$E_{\text{asym},VA} = E_{\text{sym}} + k_{VA}\left(\frac{\Delta x}{R_{m,VA}}\right)^2, \tag{A5.24}$$

where k_{VA} are the stability coefficients with units of energy (k_V for constant volume and k_A for constant area), and $R_{m,VA}$ is the polar radius. Symmetric constriction will be stable when the stability coefficients are positive, because in this case the energy of the symmetric configuration is smaller than the asymmetric one. In contrast, negative stability coefficients predict unstable symmetric shapes against longitudinal deformations. In terms of the first and second derivatives of E_T, L_T, and V (for constant volume constriction), or A (for constant area constriction) with respect R_m (see next section for a detailed deduction), k_{VA} take the form

$$k_V = \frac{R_{m,V}^2}{2(\mathrm{d}L_T/\mathrm{d}R_m)^2}\left[\frac{\mathrm{d}^2E_{T,\text{sym}}}{\mathrm{d}R_m^2} - \frac{\mathrm{d}E_{T,\text{sym}}}{\mathrm{d}R_m}\frac{\mathrm{d}^2V/\mathrm{d}R_m^2}{\mathrm{d}V/\mathrm{d}R_m}\right], \tag{A5.25}$$

$$k_A = \frac{R_{m,A}^2}{2(\mathrm{d}L_T/\mathrm{d}R_m)^2}\left[\frac{\mathrm{d}^2E_{T,\text{sym}}}{\mathrm{d}R_m^2} - \frac{\mathrm{d}E_{T,\text{sym}}}{\mathrm{d}R_m}\frac{\mathrm{d}^2A/\mathrm{d}R_m^2}{\mathrm{d}A/\mathrm{d}R_m}\right]. \tag{A5.26}$$

Replacing the expressions of E_T, L_T V, and A previously obtained by us (see Section A4.2 in Annex A4), we can determine analytical approximated solutions of the stability coefficients along the constriction pathway in terms of the spontaneous curvature of the membrane C_0, the membrane tension Σ, and the pressure difference Δp. In Refs. [74, 75]we addressed this question in vesicles with zero spontaneous curvature, $C_0 = 0$, negligible membrane tension, $\Sigma = 0$, and isotonic conditions (no pressure difference between internal and external media), $\Delta p = 0$. In

this particular case, the values of k_{VA} are negative during all process, indicating the unstable character of symmetric constriction. Here, we generalize this previous work to more realistic situations by accounting the additional effects of C_0, Σ, and Δp. This allow us to study whether it is possible to get stable symmetric constriction for appropriate combinations of these parameters.

Maintaining constant volume, the stability coefficient k_V in equation (A5.25) can be expressed as

$$k_V = -\pi^2 \kappa_b \frac{k_V^N}{k_V^D}, \tag{A5.27}$$

with the numerator and denominator given by

$$\begin{aligned} k_V^N = {} & \frac{6^{1/4}2}{9(\Gamma+29)^2\Lambda^{1/4}}[3807 + 417\Gamma + 12\Gamma^2 + 1494\Lambda + 162\Gamma\Lambda + 4\Gamma^2\Lambda - 1125\Lambda^2 - 25\Gamma\Lambda^2 \\ & -15C_0R_m - 10C_0R_m\Lambda + 25C_0R_m\Lambda^2]s^{1/2} - \frac{\pi}{288\Lambda}[30\Lambda^2 + 216\Gamma\Lambda - 144\Lambda \\ & -1446^{1/2}\Gamma\Lambda^{1/2}]s + \cdots. \end{aligned} \tag{A5.28}$$

$$\begin{aligned} k_V^D = {} & \frac{6^{3/4}\,\pi^3}{16\Lambda^{3/4}}s^{1/2} - \frac{6^{1/2}\pi^2}{3(\Gamma+29)^2\Lambda^{1/2}}[3018 + 459\Gamma + 13\Gamma^2 - 1365\Lambda - 25\Gamma\Lambda - 40C_0R_m \\ & +40C_0R_m\Lambda]s + \cdots. \end{aligned} \tag{A5.29}$$

Alternatively, if the constraint of constant area is considered, the corresponding stability coefficient k_A in equation (A5.26) takes the form

$$k_A = -\pi^2 \kappa_b \frac{k_A^N}{k_A^D}, \tag{A5.30}$$

with the numerator and denominator given by

$$\begin{aligned} k_A^N = {} & \frac{6^{1/4}4}{9(\Gamma+29)^3\Lambda^{1/4}}[110403 + 17466\Gamma + 819\Gamma^2 + 12\Gamma^3 + 35266\Lambda + 5892\Gamma\Lambda + 278\Gamma^2\Lambda \\ & +4\Gamma^3\Lambda - 25785\Lambda^2 - 1570\Gamma\Lambda^2 - 25\Gamma^2\Lambda^2 + 1220\Lambda^3 + 20\Gamma\Lambda^3 - 435C_0R_m \\ & -15C_0R_m\Gamma - 330C_0R_m\Lambda - 10C_0R_m\Gamma\Lambda + 805C_0R_m\Lambda^2 + 25C_0R_m\Gamma\Lambda^2 \\ & -40C_0R_m\Lambda^3]s^{1/2} - \frac{\pi}{288\Lambda}[1446^{1/2}\Lambda^{1/2}(\Lambda-\Gamma) + 36\Gamma\Lambda - 42\Lambda^2 - 144\Lambda]s + \cdots. \end{aligned} \tag{A5.31}$$

$$\begin{aligned} k_A^D = {} & \frac{6^{3/4}\,\pi^3}{8\Lambda^{3/4}}s^{1/2} - \frac{6^{1/2}2\pi^2}{3(\Gamma+29)^3\Lambda^{1/2}}[85507 + 16254\Gamma + 836\Gamma^2 + 13\Gamma^3 - 37875\Lambda - 2020\Gamma\Lambda \\ & -25\Gamma^2\Lambda + 305\Lambda^2 + 5\Gamma\Lambda^2 - 1170C_0R_m + 40C_0R_m\Gamma(\Lambda-1) + 1180C_0R_m\Lambda \\ & -10C_0R_m\Lambda^2]\,s + \cdots. \end{aligned} \tag{A5.32}$$

These coefficients are written in terms of Λ [Eq. (5.3) in Chapter 5] and $\Gamma = (2 - C_0R_m)^2 + 2\Sigma R_m^2/\kappa_b - 1$, as are the expressions of E_T, L_T, V, and A involved (see Chapter 4).

As stated above, in the particular case of vesicles with zero spontaneous curvature, $C_0 = 0$, negligible membrane tension, $\Sigma = 0$, and isotonic conditions, $\Delta p = 0$, the coefficients k_{VA} are negative during all the process (black line in Figure A5.6): they converge down to the asymptotic limit $\lim_{s\to 0} k_{VA} = -2.77\kappa_b \approx 28 k_B T$ for a flexible membrane ($\kappa_b \approx 10\, k_B T$), and becomes progressively less unstable with increasing constriction approaching zero in the large-constriction limit $\lim_{s\to 1} k_{VA} = 0$. This case was previously study by us in Refs. [74, 75]. In the general case studied here, when C_0, Σ, and Δp are not necessary zero, we also see that symmetric constriction becomes progressively more stable with increasing constriction. Additionally, we obtain a new and interesting result: the symmetric constriction can be stable ($k_{VA} > 0$) against lateral deformations for appropriate combinations of these parameters (see Figures A5.5 and Figures 5.3-5.4 in Chapter 5).

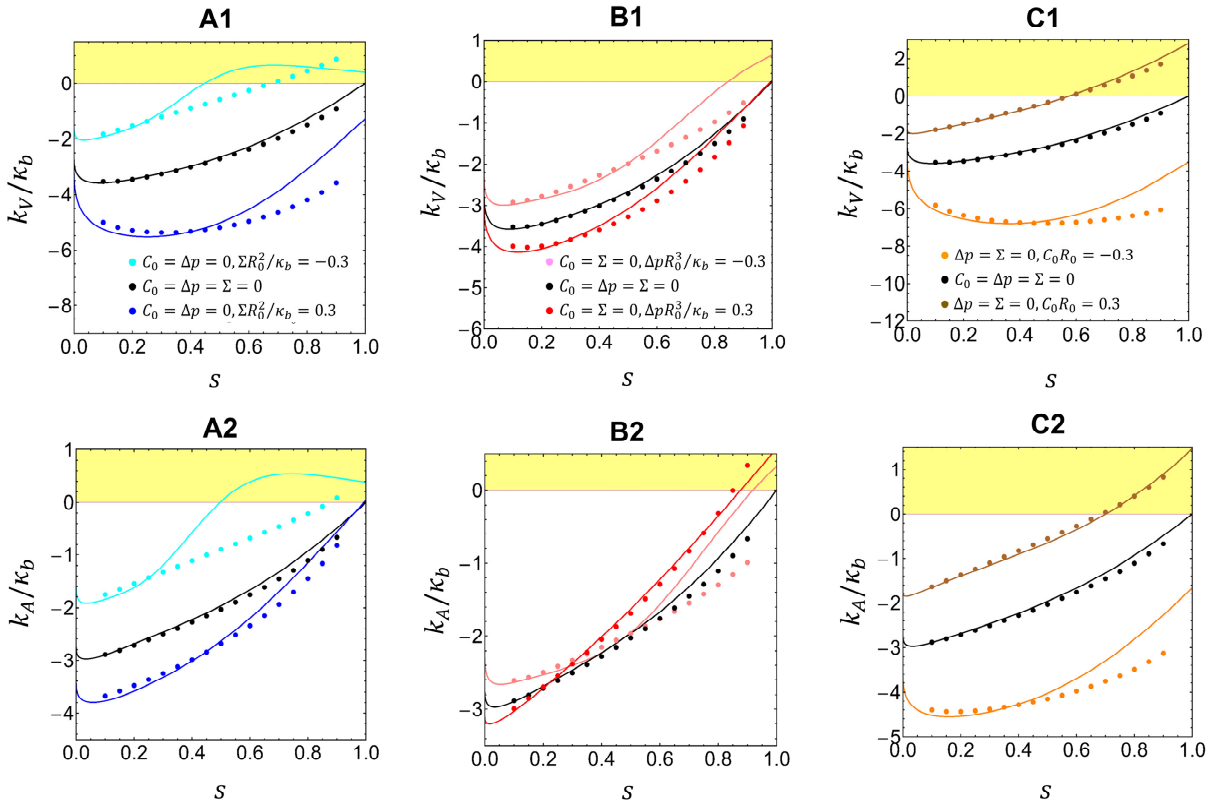

Figure A5.5. Stability coefficients for constant volume and constant area constrictions. Stability coefficients maintaining volume constant k_V/κ_b (above) and maintaining membrane area constant k_A/κ_b (below) at all stages of constriction. Comparison of the exact numerical results with the analytical approximate solutions. (A) Influence of the membrane tension Σ. (B) Influence of the external pressure Δp. (C) Influence of the spontaneous curvature of the membrane C_0. Regions with stable configurations ($k_{V,A} > 0$) are shaded in yellow.

The approximate analytical results of the stability coefficients reproduce the numerical solutions for low and intermediate constriction regimes, with better agreements for vesicles with positive membrane tensions ($\Sigma > 0$), immersed in hypertonic media ($\Delta p > 0$) and with positive spontaneous curvatures ($C_0 > 0$) (see Figure A5.5). The analytical result for the case with $\Sigma R_m^2/\kappa = -0.3$ and with $C_0 = \Delta p = 0$ (cyan triangles of Figure A5.5) differs from the exact numerical values more than the other cases. The reason is that this combination of parameters gives the closer-to-zero value of Λ and the analytical formulas of the stability coefficients [Eqs. (A5.32)-(A5.35)] diverge as Λ approaches to zero.

A5.5.1 Deduction of the Stability Coefficients

Each lobe of the asymmetric shape is characterized by a different polar radius: one of them has a greater polar radius $R_m^+ > R_m$ (the right lobe in Figure A5.4) while the other has a smaller one $R_m^- < R_m$ (the left lobe in Figure A5.4). We denote these changes as

$$\Delta R_m^{\pm} = R_m^{\pm} - R_m. \tag{A5.33}$$

Similarly, the total length L_T in each lobe changes with respect to the symmetric case in the form

$$\Delta L_T^{\pm} = L_T\left(R_m^{\pm}, R_c\right) - L_T(R_m, R_c). \tag{A5.34}$$

These parameters are clearly indicated in Figure A5.4.

Stability coefficient at constant volume

If the transition between the symmetric and the asymmetric shape occurs by keeping the volume constant, we can write

$$V(R_m, R_c) = \frac{1}{2}[V(R_m + \Delta R_m^-, R_c) + V(R_m + \Delta R_m^+, R_c)]. \tag{A5.35}$$

This equation can be solved numerically which allows us for obtaining the relation between ΔR_m^+ and ΔR_m^- that maintains constant the volume enclosed by the vesicle. However, for small departures from the symmetrical shape Δx, an analytic perturbative computation is also valid. Expanding Eq. (A5.35) up to second order, it is obtained

$$V\left(R_m + \Delta R_m^{\pm}, R_c\right) = V(R_m, R_c) + \frac{\mathrm{d}V(R_m, R_c)}{\mathrm{d}R_m}\Delta R_m^{\pm} + \frac{1}{2}\frac{\mathrm{d}^2V(R_m, R_c)}{\mathrm{d}R_m^2}\left(\Delta R_m^{\pm}\right)^2. \tag{A5.36}$$

Introducing Eq. (A5.36) into Eq. (A5.35) gives

$$0 = \frac{1}{2}(\Delta R_m^+ + \Delta R_m^-)\frac{\mathrm{d}V(R_m, R_c)}{\mathrm{d}R_m} + \frac{1}{4}[(\Delta R_m^+)^2 + (\Delta R_m^-)^2]\frac{\mathrm{d}^2V(R_m, R_c)}{\mathrm{d}R_m^2}. \tag{A5.37}$$

Solving this quadratic equation for ΔR_m^- and expanding the positive solution up to second order we have

$$\Delta R_m^- = -\Delta R_m^+ - \frac{\mathrm{d}^2V/dR_m^2}{\mathrm{d}V/dR_m}(\Delta R_m^+)^2. \tag{A5.38}$$

The displacement of the constriction ring from the middle point of the symmetric shape Δx can be related with the total lengths $L_T^{\pm}$ of the asymmetric poles as

$$\Delta x(R_m, R_c) = \frac{1}{2}[L_T(R_m + \Delta R_m^+, R_c) - L_T(R_m + \Delta R_m^-, R_c)]. \tag{A5.39}$$

Expanding these lengths in Taylor series up to second order for small asymmetries we obtain

$$L_T\left(R_m + \Delta R_m^{\pm}, R_c\right) = L_T(R_m, R_c) + \frac{\mathrm{d}L_T(R_m, R_c)}{\mathrm{d}R_m}\Delta R_m^{\pm} + \frac{1}{2}\frac{\mathrm{d}^2L_T(R_m, R_c)}{dR_m^2}\left(\Delta R_m^{\pm}\right)^2. \tag{A5.40}$$

Introducing Eqs. (A5.40) and (A5.38) into Eq. (A5.39), it is obtained

$$\Delta x(R_m, R_c) = \Delta R_m^+ \frac{\mathrm{d}L_T(R_m, R_c)}{\mathrm{d}R_m} + \frac{(\Delta R_m^+)^2}{2} \frac{\mathrm{d}^2 L_T(R_m, R_c)}{\mathrm{d}R_m^2} \frac{\mathrm{d}^2 V/dR_m^2}{\mathrm{d}V/dR_m}. \tag{A5.41}$$

Solving for ΔR_m^+

$$\Delta R_m^+ = \frac{\Delta x}{\mathrm{d}L_T/dR_m} - \frac{(\Delta x)^2}{2(\mathrm{d}L_T/dR_m)^2} \frac{\mathrm{d}^2 V/dR_m^2}{\mathrm{d}V/dR_m}. \tag{A5.42}$$

Following the same steps, we can express the energy of the asymmetric shape in terms of the energies of the asymmetric lobes as

$$E_{T,\mathrm{asym}}(R_m, R_c) = \frac{1}{2}\left[E_{T,\mathrm{sym}}(R_m + \Delta R_m^-, R_c) + E_{T,\mathrm{sym}}(R_m + \Delta R_m^+, R_c)\right]. \tag{A5.43}$$

Expanding it in power series up to second order for small asymmetries we have

$$E_{T,\mathrm{sym}}\left(R_m + \Delta R_m^\pm, R_c\right) = E_{T,\mathrm{sym}}(R_m, R_c) + \frac{\mathrm{d}E_{T,\mathrm{sym}}(R_m, R_c)}{\mathrm{d}R_m} \Delta R_m^\pm + \frac{1}{2}\frac{\mathrm{d}^2 E_{T,\mathrm{sym}}(R_m, R_c)}{\mathrm{d}R_m^2}\left(\Delta R_m^\pm\right)^2. \tag{A5.44}$$

Introducing the results of ΔR_m^- [Eq. (A5.38)] and of ΔR_m^+ [Eq. (A5.42)] into Eq. (A5.44) we obtain that the difference of energy with respect to the symmetric configuration is given by a quadratic form as

$$\Delta E_T = E_{T,\mathrm{asym}}(R_m, R_c) - E_{T,\mathrm{sym}}(R_m, R_c) = k_V \left(\frac{\Delta x}{R_{m,V}}\right)^2, \tag{A5.45}$$

with the effective harmonic constant

$$k_V = \frac{R_{m,V}^2}{2(\mathrm{d}L_T/\mathrm{d}R_m)^2}\left[\frac{\mathrm{d}^2 E_{T,\mathrm{sym}}}{\mathrm{d}R_m^2} - \frac{\mathrm{d}E_{T,\mathrm{sym}}}{\mathrm{d}R_m}\frac{\mathrm{d}^2 V/\mathrm{d}R_m^2}{\mathrm{d}V/\mathrm{d}R_m}\right]. \tag{A5.46}$$

Stability coefficient at constant area

Similarly, if in the transition between the symmetric and the asymmetric shape the area is kept constant, the difference their energies is given by the quadratic form

$$\Delta E_T = E_{T,\mathrm{asym}}(R_m, R_c) - E_{T,\mathrm{sym}}(R_m, R_c) = k_A \left(\frac{\Delta x}{R_{m,A}}\right)^2. \tag{A5.47}$$

with the effective harmonic constant

$$k_A = \frac{R_{m,A}^2}{2(\mathrm{d}L_T/\mathrm{d}R_m)^2}\left[\frac{\mathrm{d}^2 E_{T,\mathrm{sym}}}{\mathrm{d}R_m^2} - \frac{\mathrm{d}E_{T,\mathrm{sym}}}{\mathrm{d}R_m}\frac{\mathrm{d}^2 A/\mathrm{d}R_m^2}{\mathrm{d}A/\mathrm{d}R_m}\right]. \tag{A5.48}$$

A5.5.2 Useful Relations between Derivatives to Numerically Compute the Stability Coefficients

To obtain the stability coefficients of Eqs. (A5.46) and (A5.48) we have to calculate the following -first and second- derivatives with respect to R_m

$$\frac{\mathrm{d}L_m}{\mathrm{d}R_m}, \frac{\mathrm{d}E_T}{\mathrm{d}R_m}\ \frac{\mathrm{d}A}{\mathrm{d}R_m}, \frac{\mathrm{d}V}{\mathrm{d}R_m}, \frac{\mathrm{d}^2E_T}{\mathrm{d}R_m^2}\ \frac{\mathrm{d}^2A}{\mathrm{d}R_m^2}, \frac{\mathrm{d}^2V}{\mathrm{d}R_m^2}. \tag{A5.49}$$

The numerical algorithm computes E_T and the scaled quantities L_m/R_m, A/R_m^2, and V/R_m^3, which allows us to determine their -first and second- partial derivatives with respect to s, C_0R_m,ΣR_m^2, and ΔpR_m^3 , using the mean value theorem. To compute the total derivatives with respect to R_m, we can expand them into their partial derivatives as

$$\begin{aligned}\frac{\mathrm{d}}{\mathrm{d}R_m} &= \frac{\partial s}{\partial R_m}\frac{\partial}{\partial s} + \frac{\partial (C_0R_m)}{\partial R_m}\frac{\partial}{\partial (C_0R_m)} + \frac{\partial (\Sigma R_m^2)}{\partial R_m}\frac{\partial}{\partial (\Sigma R_m^2)} + \frac{\partial (\Delta pR_m^3)}{\partial R_m}\frac{\partial}{\partial (\Delta pR_m^3)} \\ &= \frac{(1-s)}{R_m}\frac{\partial}{\partial s} + \Delta,\end{aligned} \tag{A5.50}$$

$$\frac{\mathrm{d}^2}{\mathrm{d}R_m^2} = \frac{(1-s)^2}{R_m^2}\frac{\partial^2}{\partial s^2} - \frac{2(1-s)}{R_m^2}\frac{\partial}{\partial s} + \Delta^2, \tag{A5.51}$$

using that $s = 1 - R_c/R_m$ and with

$$\Delta = C_0\frac{\partial}{\partial (C_0R_m)} + 2\Sigma R_m\frac{\partial}{\partial (\Sigma R_m^2)} + 3\Delta pR_m^2\frac{\partial}{\partial (\Delta pR_m^3)}, \tag{A5.52}$$

and

$$\begin{aligned}\Delta^2 = {} & C_0^2\frac{\partial^2}{\partial (C_0R_m)^2} + 4\Sigma^2R_m^2\frac{\partial^2}{\partial (\Sigma R_m^2)^2} + 2\Sigma\frac{\partial}{\partial (\Sigma R_m^2)} + 9\Delta p^2R_m^4\frac{\partial^2}{\partial (\Delta pR_m^3)^2} \\ & + 6\Delta pR_m\frac{\partial}{\partial (\Delta pR_m^3)} + 4C_0\Sigma R_m\frac{\partial^2}{\partial (C_0R_m)\partial (\Sigma R_m^2)} \\ & + 6C_0\Delta pR_m^2\frac{\partial^2}{\partial (C_0R_m)\partial (\Delta pR_m^3)} + 12\Sigma\Delta pR_m^3\frac{\partial^2}{\partial (\Sigma R_m^2)\partial (\Delta pR_m^3)} \\ & + 2C_0\frac{(1-s)}{R_m}\frac{\partial^2}{\partial (s)\partial (C_0R_m)} + 4\Sigma(1-s)\frac{\partial^2}{\partial (s)\partial (\Sigma R_m^2)} \\ & + 6\Delta p(1-s)R_m\frac{\partial^2}{\partial (s)\partial (\Delta pR_m^3)}.\end{aligned} \tag{A5.53}$$

Now, we have to relate the partial derivatives of the scaled quantities computed numerically, L_m/R_m, A/R_m^2, and V/R_m^3, with the partial derivatives of the absolute quantities L_m, A, and V. After simple mathematical calculations, the partial derivatives with respect to s are related as

$$\frac{\partial L_T}{\partial s} = R_m\frac{\partial (L_T/R_m)}{\partial s} + \frac{L_T}{(1-s)}, \tag{A5.54}$$

$$\frac{\partial A}{\partial s} = R_m^2\frac{\partial (A/R_m^2)}{\partial s} + \frac{2A}{(1-s)}, \tag{A5.55}$$

$$\frac{\partial^2 A}{\partial s^2} = R_m^2\frac{\partial^2 (A/R_m^2)}{\partial s^2} + \frac{4}{(1-s)}\frac{\partial A}{\partial s} - \frac{2A}{(1-s)^2}, \tag{A5.56}$$

$$\frac{\partial V}{\partial s} = R_m^3\frac{\partial (V/R_m^3)}{\partial s} + \frac{3V}{(1-s)}, \tag{A5.57}$$

$$\frac{\partial^2 V}{\partial s^2} = R_m^3 \frac{\partial^2 (V/R_m^3)}{\partial s^2} + \frac{6}{(1-s)} \frac{\partial V}{\partial s} - \frac{6V}{(1-s)^2}. \tag{A5.58}$$

Note that the second derivatives of L_T are not determined since they are not involved in the Eqs. (A5.46) and (A5.48). Finally, introducing the results of Eqs. (A5.54)-(A5.58) into Eqs. (A5.50)-(A5.51), and using the mean value theorem, we obtain the expressions of the total derivatives required to numerically determine the stability coefficients.

PART III

Cardiolipin Segregation Induced by Membrane Curvature

Chapter 6

Membrane Curvature Induces Cardiolipin Sorting

Chapter based on Beltran-Heredia E*, Tsai FC*, Cao FJ, Bassereau P, & Monroy, F (2018) Membrane curvature induces cardiolipin sorting. *These authors contributed equally. *Manuscript submitted for publication.*

Cardiolipin (CL) is a cone-shaped lipid found predominantly localized in the cellular poles and the division site of bacteria and in the highly curved mitochondrial *cristae* of eukaryotes. This specific localization has been argued to be geometry-driven since the CL's conical shape relaxes the curvature frustration on these curved sites. Although previous evidence suggests a coupling between CL concentration and membrane shape *in vivo*, no precise experimental data are available for curvature-based CL-sorting *in vitro*. Here, we test this hypothesis in experiments that isolate the effects of membrane curvature by using lipid-bilayer nanotubes of controlled radii pulled from cell-sized giant unilamellar vesicles (GUVs) containing CL. CL-sorting is observed with increasing tube curvature, reaching a maximum at optimal CL-concentrations that vary with the tube radius, a fact compatible with self-associative clustering despite of entropic mixing playing against sorting. Our data are compatible with a model based on membrane elasticity and van der Waals entropy, from which an intrinsic curvature of 1.1 nm^{-1} is predicted for CL, in agreement with previous estimates based on its crystalline structure. Additionally, we find that CL molecules diffuse through the neck that connects the tube and the GUV, supporting the notion of fluidity for CL concomitant with self-clustering. The results contribute to understand the physicochemical interplay between membrane curvature and CL composition, providing key insights into mitochondrial and bacterial membrane organization and dynamics.

6.1 Introduction

As previously introduced in Section 1.4, cardiolipin (CL) is a negatively charged lipid found predominantly in the inner mitochondrial membrane of eukaryotic cells [15] and in the plasma membranes of some bacteria [58]. The CL molecule is composed of two phosphatidic acids linked together by a short glycerol bridge, which results in a conical molecular shape with a smaller cross-sectional area in the polar head relative to the hydrophobic tails. Previous estimations suggest that the intrinsic curvature of CL should be of the order of 1 nm^{-1} [12], making this lipid prone to localize in highly curved regions of the lipid membrane. Indeed, CL-enriched

domains have been observed to localize at the poles and division sites in bacterial cells [12–14, 60, 61]. These CL-rich domains appear to participate in the binding of proteins responsible for selection and recognition of the division site, which suggests a CL involvement in the process of bacterial division. In eukaryotic cells, CL is related to the maintenance of mitochondrial cristae structures with tubular-like invaginations, which stabilize different protein complexes necessary for respiration and oxidative phosphorylation [234, 235], and for the synthesis of ATP [235, 236], both processes taking place at the inner mitochondrial membrane.

The proposed mechanism to form these CL-enriched domains is customary assumed to be geometry-driven [16]; arguably, a coupling between membrane composition and CL shape would minimize the curvature frustration of the curved regions of the membrane. Different studies have shown that CL-containing bilayers have a propensity to create folds and adopt highly curved structures [17], which are favored by the presence of divalent cations or low pH [65, 66]. Experimental observations with model membranes have shown how cristae-like invaginations are induced by flowing protons to GUVs containing CL [237, 238]. The coupling between CL concentration and membrane shape is also supported by the evidence of the accumulation of CL in *E. coli* minicell membranes [18]. At a molecular level, recent simulations of the bilayer structure by molecular dynamics (MD) reveal that the CL molecule, with a high spontaneous curvature due to its four acyl chains, is expected to concentrate at curved regions of the membrane. Differently, phosphatidylethanolamine (PE), another cone-shaped lipid with only two chains, seems to have much a weaker propensity to localize in these curved regions [16]. Because CL specifically binds or interacts with many mitochondrial and bacterial proteins, and its segregation may influence the spatial distribution of these proteins, a quantitative estimation of the intrinsic curvature and sorting energy of CL molecules is biologically relevant as far it could contribute to understand whether these functional molecules can be sorted by curvature.

In order to understand how intracellular trafficking maintains the composition differences between membranes compartments of the cell, curvature-driven sorting has been extensively explored *in vitro* for typical lipid systems [9, 48, 97, 239, 240] as well as for membrane embedded proteins [52, 54, 55, 241]. Despite it had been suggested that lipid sorting could be mediated by a coupling between membrane composition and curvature [47, 98–100, 242–247], both experimental and theoretical works show that lipid sorting due to bending minimization is a very weak effect and mixing entropy tends to homogenize the lipid distribution [9, 48, 51, 192]. Bassereau and coworkers [9, 48] noticed that is very unlikely that individual lipids, unassisted by interactions with themselves or with proteins, may be enriched in curved regions simply based on their shape alone. Instead, lipid-lipid interactions or lipid-protein-interactions appear to be essential in making the membrane susceptible to curvature-driven sorting. Indeed, they observed that lipid sorting only occurs if the system is close to a phase-separation point, when lipid-lipid interactions are important, and this process is amplified when lipids are clustered upon proteins [9, 48]. These analyses have been made with different lipid species commonly found in membrane cells, but CL has not been so far examined in this context.

Here, we measure CL sorting as a function of membrane curvature in a homogeneous mixture with the natural extract of egg phosphatidylcholine (EPC) at different CL-contents. Membranes nanotubes of controlled radii are pulled out from GUVs using micromanipulation techniques (see Figure 6.1; also Refs. [9, 55, 94]). On one side, a GUV is held by a micropipette exerting a

small suction. On the other side, an optically trapped bead is used to apply the force necessary to pull a membrane nanotube. The control of the pipette aspiration sets the tube radius over a biologically relevant range. This construction allows for a quantitative validation of the curvature-induced sorting hypothesis [84]. We have also implemented a model based on membrane elasticity and van der Waals entropy including possible CL-CL interactions. Interestingly, we experimentally found that CL becomes enriched in the tubes, with a higher enrichment in the more highly curved membranes. Despite entropic randomization present in the lipid mixture, CL-sorting is observed up to relatively high CL concentrations, which is plausibly explained by the presence of cohesive CL-CL interaction. This supports the idea for CL self-association into finite-sized molecular clusters, as observed *in vivo* at membrane sites with a high curvature [12–14, 60, 61].

6.2 Results

6.2.1 Measuring Curvature-Induced Cardiolipin Sorting *in Vitro*

Membranes nanotubes of controlled radii were pulled out from GUVs made of the biomimetic mixture EPC/CL. Two fluorescent lipid probes were included to detect lipid sorting: green-labelled CL (Top-Fluor CL) and red-labelled reference (Bodipy-TR Ceramide). Since the distribution of this reference dye is approximately uniform in our system [9], the enrichment of the CL in the tube can be measured by comparing its fluorescence I_{CL} to the fluorescence of the Bodipy-TR Ceramide $I_{\mathrm{BOD\text{-}TR}}$. If CL had the same affinity for the membrane tube as Bodipy-TR Ceramide, then their fluorescence intensities would be similar and the tube would appear yellowish. If, on the contrary, the CL-to-Bodipy-TR Ceramide ratio in the curved membrane is larger/lower than in the flatter GUV membrane, then the tube would appear greenish/reddish, respectively. This relative CL enrichment can be quantified by the sorting ratio, S, defined as

$$S = \frac{(I_{\mathrm{CL}}/I_{\mathrm{BOD\text{-}TR}})_{\mathrm{tube}}}{(I_{\mathrm{CL}}/I_{\mathrm{BOD\text{-}TR}})_{\mathrm{GUV}}}. \tag{6.1}$$

According to this definition, a sorting ratio higher than unity, $S > 1$, implies that CL is enriched in the tube as compared to the GUV, while a value in the range $0 \leq S < 1$ means that CL is depleted from the tube. In the absence of driving mechanisms for sorting, the CL molecules must be homogeneously distributed throughout the membrane both in the tube and in the GUV, resulting in a sorting ratio equal to unity, $S = 1$. Dye photobleaching was not significant under our confocal illumination (see Figure A6.3), and mesoscopic phase separation was not observed (see Figure A6.1). The sorting ratio is expected to be equal to unity at large tube radii (R), when the effect of membrane curvature ($c \equiv 1/R$) is negligible and CL molecules must be homogeneously distributed throughout the whole membrane. We studied lipid tubes over a biologically relevant range of radii between 8 and 40 nm, corresponding to curvatures in the range $0.02 - 0.13$ nm^{-1}, controlled through GUV aspiration (see Figure 6.1A-B).

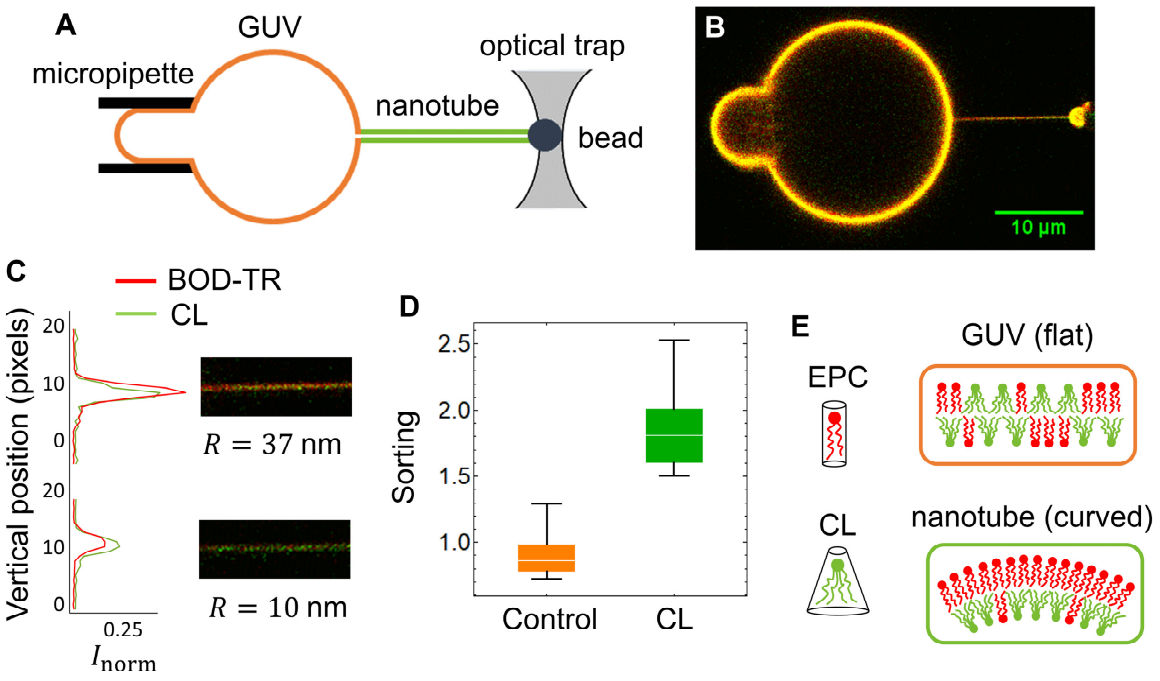

Figure 6.1. CL is enriched in curved membranes. (A) Schematic of tube assay. A bead in an optical trap is used to pull a membrane tube from a GUV held by a micropipette. The pressure in the micropipette controls the membrane tension and the resulting tube radius, whereas the concentration of the reference lipid and the CL in the tube are measured by confocal fluorescence microscopy. (B) Confocal image of a tube pulled from a GUV containing CL. The membrane (red) was marked with a fluorescent reference lipid (Bodipy TR-Ceramide), whereas the CL (green) was marked with Top-Fluor CL. Contrast has been enhanced, and green and red intensities have been scaled to match in the GUV (which is orange-yellowish). Thus, the green colour of the tube reflects CL enrichment in the tube (relative to the GUV). (C) Images and intensity profiles of tubes pulled from GUVs containing CL for large ($R \approx 37$ nm) and small ($R \approx 10$ nm) tube radii. The CL is enriched in curved membranes, obtaining more intensity in the green channel compared to the red channel in small tubes. (D) Box plots comparing the sorting ratio for curved tubes [$c = (0.10 \pm 0.03)$ nm^{-1}] pulled from GUVs containing green fluorescent lipids: control (in orange) and a CL density of (0.10 ± 0.05) molecules per nm^2 (in green). The median is represented with a line; the box represents the 25th to 75th percentiles; and the error bars show the 5th-95th percentile. CL is enriched in the tubes (average sorting ratio 1.9 ± 0.3, 10 GUVs) comparing with the lipid control (average sorting ratio 0.9 ± 0.2, 21 GUVs).

6.2.2 Curvature Induces Cardiolipin Sorting

Figure 6.1C shows confocal microscopy images of membrane tubes formed from GUVs containing CL with a density of approximately 0.04 molecules per nm^2. For the thicker tube ($R \approx 37$ nm), the Bodipy-TR-Ceramide (red) fluorescence signal is similar than that of CL (green) and the tube appears orange-yellowish with a calculated sorting ratio ($S = 0.99 \pm 0.01$). This means that the composition of the membrane tube is indistinguishable from that of the GUV at low tube curvatures, $c \equiv 1/R \approx 0.03$ nm^{-1}. In contrast, when the tube radius was reduced to $R \approx 10$ nm ($c \approx 0.1$ nm^{-1}), the CL fluorescence (green) in the tube increases with respect to the fluorescence (red) of the Bodipy-TR Ceramide, and then the tube appears greener with a significantly high value of the sorting ratio ($S = 2.19 \pm 0.01$). An additional control experiment was performed to discard possible systematic differences between the red and green lasers in this set-up. In this control, vesicles do not contain CL but a green fluorescent lipid (BODIPY-FL HPC), which was previously shown to have equal affinity for the membrane tube

that the lipid dye emitting in the red channel (Bodipy-TR Ceramide) [55]. In this control experiment, the sorting ratio is approximately equal to unity even for curved membranes ($S = 0.9 \pm 0.2$), as expected (see Figure 6.1D).

To determine whether CL sorting depends on membrane density, we prepare GUVs with different CL concentrations $\rho_{GUV,CL}$ ranging from approximately 0.004 molecules per nm^2, which corresponds to a partial area fraction $\rho_{GUV,CL} \times A_{CL}$ of about 0.5% (with the average cross-sectional area of CL, $A_{CL} = 1.3$ nm^2) up to approximately 0.25 molecules per nm^2 (which corresponds to an area fraction of ≈ 30%). Figure 6.2 shows the CL-enrichment as increasing area fraction in four ranges of tube curvature (experimental data can be found in Table A6.1 in Annex 6). We find that CL becomes enriched in the tubes, with a higher enrichment in highly curved membranes. Furthermore, our results indicate that CL is enriched in curved membranes at both low and high CL densities with greater sorting at intermediate ones (between 0.1 and 0.15 molecules per nm^2) (see Figure A6.6 in Annex 6).

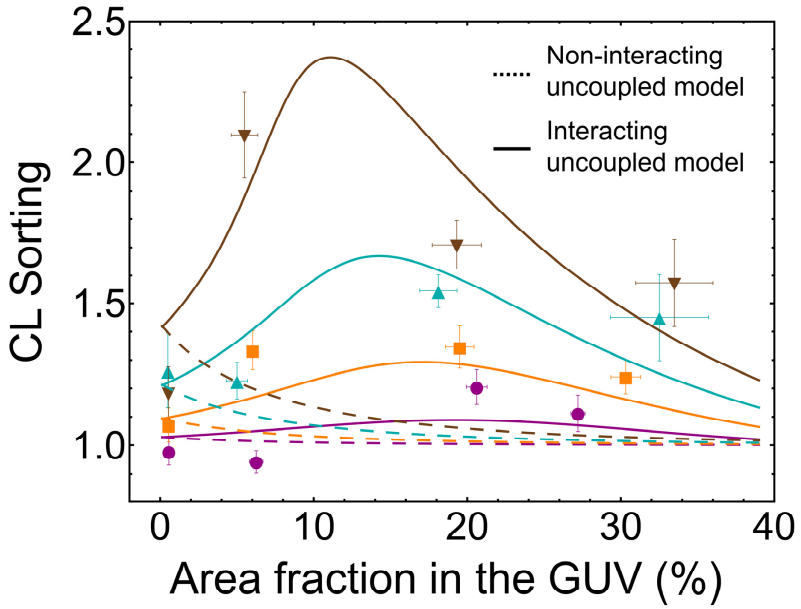

Figure 6.2. CL enrichment as a function of CL density in GUVs. CL sorting as a function of the area fraction $\rho_{GUV,CL} \times A_{CL}$ (in percent) for four ranges of tube curvature: ▼ very high (0.1287 ± 0.0012) nm^{-1} in brown; ▲ high (0.0926 ± 0.008) nm^{-1} in cyan; ■ low (0.062 ± 0.01) nm^{-1} in orange; and ● very low (0.034 ± 0.009) nm^{-1} in purple. The points are the arithmetic means of binned CL GUV densities and sorting ratios, and the error bars represent the corresponding standard deviations. Dashed lines represent the minimum square fit to the non-interacting uncoupled model (*i.e.*, in the absence of binary interactions between CL molecules, interacting parameter $a = 0$), which gives a CL intrinsic curvature of $c_{CL} = 1.12 \pm 0.4$ nm^{-1}. Solid lines represent the minimum square fit to the interacting uncoupled model (*i.e.,* assuming possible CL-CL interactions with the free interacting parameter a) is represented with solid lines and gives $c_{CL} = 1.10 \pm 0.05$ nm^{-1} and $a = -18 \pm 1\ k_BT$ nm^2. The computations are made with the following values: CL area $A_{CL} = 1.3$ nm^2 [248], bending modulus of a pure CL bilayer $\kappa_{CL} = 26\ k_BT$ [248], and bending modulus of a pure EPC bilayer $\kappa_{EPC} = 10\ k_BT$ [9].

6.2.3 Non-Interacting Model

Membrane deformations, such as the creation of nanotubes, imply an increase of membrane bending energy. In its simplest form, the bending energy per unit of membrane area can be calculated using the elastic response of a thin sheet:

$$g_{\text{bend}} = \frac{1}{2}\kappa(c - c_0)^2 \tag{6.2}$$

where κ is the bending modulus, c the membrane curvature, and c_0 the spontaneous curvature, which permits to describe membranes that are prone to bend in their equilibrium state due to the compositional inhomogeneity between the inner and the outer monolayers.

Flickering spectroscopy measurements of pure CL bilayers yield a bending modulus of approximately $\kappa_{\text{CL}} = 26\, k_B T$ [248], which is larger than that observed in pure EPC bilayers, $\kappa_{\text{EPC}} = 10\, k_B T$ [9]. Since CL molecules stiffen the membrane, if reduction of the bending energy through softening was at the origin of CL redistribution, we would expect a depletion of CL in the tube ($S < 1$) and not an enrichment ($S > 1$). Thus, the enrichment could be related to a reduction of the bending energy through the intrinsic curvature of the CL. Lipids that compose EPC globally have a nearly cylindrical shape with an intrinsic curvature close to zero (see Figure 6.1E). Additionally, the area per molecule of CL is nearly a factor of two larger than that of EPC lipids, due to its four acyl chains as compared to the two of EPC (the average cross-sectional area of EPC is around 0.69 nm^2 [249], while it extends out almost twice for CL, around $A_{\text{CL}} = 1.30$ nm^2 [248]). To implement the sorting model, CL molecules are assumed to insert homogeneously in both monolayers of the GUV with opposite orientations due to their polar heads and their hydrophobic tails. Then, CL molecules in the outer and the inner monolayers can be though as species with opposite intrinsic curvature: $c_{\text{CL}} < 0$ for the outer monolayer and $c_{\text{CL}} > 0$ for the inner one. CL molecules in the outer monolayer ($c_{\text{CL}} < 0$) contribute negatively to the membrane spontaneous curvature, so they are depleted from the tube (c and c_{CL} with opposite sign). In contrast, CL molecules in the inner monolayer ($c_{\text{CL}} > 0$) contribute positively to the membrane spontaneous curvature and then are enriched in the tube (c and c_{CL} with the same sign). These opposite effects do not cancel each other and so the total CL concentration of the tube varies with curvature, as shown in Figure 6.3. Thus, the enrichment could be related to a reduction of the bending energy through the intrinsic curvature of the CL.

At equilibrium, this reduction of bending energy must be counterbalanced with the entropic cost of distributing molecules non-uniformly, g_{ent}, which may be approximated with the van der Waals entropy (see Section A6.5.1 in Annex 6). Finally, the expected sorting is calculated by computing the tube composition that minimizes the total free energy of the tube ($g_T = g_{\text{bend}} + g_{\text{ent}}$) coupled to the nearly flat GUV (see Section A6.5.2 in Annex 6). This model neglects possible interactions among lipid species thus it will be named below as the non-interacting model.

Two different scenarios are considered: uncoupled or coupled monolayers (see Section A6.5 in Annex 6). Uncoupled monolayers (*i.e.*, free to slide past each other) behave as two independent systems, each one with its own monolayer bending energy; Eq. (6.2) being computed with the bending modulus and spontaneous curvature given for the CL abundances in the respective monolayer (see Section A6.5.1 in Annex 6 for details). In the coupled model, the two monolayers are stuck together, thus the bilayer bends as a uniform whole. Consequently, the bending energy

is computed for the whole bilayer as a single flexible sheet, with the bending modulus and spontaneous curvature given by the CL abundances in both monolayers (see Section A6.5.2 in Annex 6 for details).

CL intrinsic curvature enhances sorting at very low CL densities

At very low CL densities (for area fractions $\rho_{\mathrm{GUV,CL}} \times A_{\mathrm{CL}}$ lower than 0.02 with $A_{\mathrm{CL}} = 1.3\ \mathrm{nm}^2$, see Figure 6.2), the CL enrichment in the tube is enhanced by the CL intrinsic curvature contribution and limited by the bending modulus and entropic penalty, as predicted by the non-interacting model (see above and Section A6.5.1 in Annex 6). These effects mutually counterbalance and the resulting sorting does not exceed 1.5. Only at this very low CL densities the non-interacting model is enough to explain the observed CL sorting induced by membrane curvature.

Observed sorting at high CL densities is higher than expected in a non-interacting model

In Figure 6.2, the fit of the experimental data to non-interacting uncoupled model is represented with dashed lines. Clearly, the non-interacting model fails to reproduce the experimental data, for any values of the tube curvature c. Although the non-interacting model describes a curvature-increasing sorting at low CL-content, it largely underestimates the results at intermediate and high CL concentration. The non-interacting coupled model also fails to describe the data (see Figure A6.10).

6.2.4 Interacting Model

In general, membranes consisting of a mixture of lipids are characterized not only by elasticity and entropy but also by the short-range interactions among the different lipid species. Conclusions extracted from the previous non-interacting model are strongly altered by including an excess energy per unit of membrane area, which is associated to binary interactions between CL molecules with the form:

$$g_{\mathrm{int}} = a\rho_{\mathrm{CL}}^2, \tag{6.3}$$

where the interaction parameter a can take positive or negative values depending on whether the CL-CL interactions are repulsive or attractive, respectively. In the complete interacting theory, CL sorting between the nanotube and the vesicle is determined by the tradeoff between the bending, the entropic, and the interaction contributions to free energy ($g_T = g_{\mathrm{bend}} + g_{\mathrm{ent}} + g_{\mathrm{int}}$). It can be obtained numerically by computing the tube composition that minimizes the total free energy of the system. Note that the previous non-interacting model (in the absence of binary interactions) corresponds to a value $a = 0$ ($g_{\mathrm{int}} = 0$).

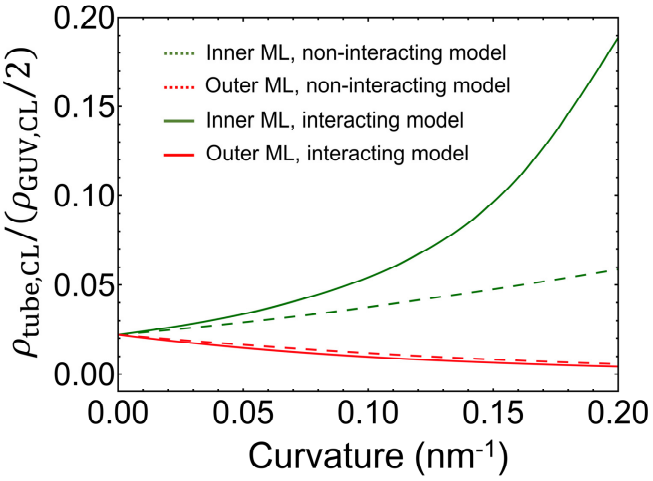

Figure 6.3. CL density in the nanotube's monolayers according to the uncoupled model. CL molecules in the inner monolayer (green lines), which bend the membrane in the direction of the imposed curvature, are enriched in the tube while CL molecules in the outer monolayer (red lines), which bend the membrane against the imposed curvature, are depleted from the tube. Unlike the non-interacting model (green dashed line), the interacting model predicts a significant CL enrichment in the inner monolayer of the nanotube (green solid line). The computations are made with the following values: CL area $A_{\mathrm{CL}} = 1.3\ \mathrm{nm}^2$ [248], bending modulus of a pure CL bilayer $\kappa_{\mathrm{CL}} = 26\ k_B T$ [248], bending modulus of a pure EPC bilayer $\kappa_{\mathrm{EPC}} = 10\ k_B T$ [9], and a CL density in the GUV of $\rho_{\mathrm{GUV,CL}} = 0.04$ molecules per nm^2, corresponding to an area fraction of about 6%, (half in each monolayer).

Observed CL sorting can be explained by the interacting model

Solid lines in Figure 6.2 are the fit of the interacting uncoupled model to the observed data. Unlike the preceding model (with $a = 0$, dashed lines), the interacting uncoupled model is successful in reproducing the experimental measurements. The intrinsic curvature of CL (c_{CL}) is obtained as an adjustable parameter of the fit, resulting in a value $|c_{\mathrm{CL}}| = 1.10 \pm 0.05\ \mathrm{nm}^{-1}$. This result is in accordance with the previous estimate based on the membrane curvature of the CL-rich curved sites in *E. coli* [12]. The interaction parameter is also obtained from the fit, resulting in a negative value of $a = -18 \pm 1\ k_B T\ \mathrm{nm}^2$, which suggests the existence of attractive CL-CL interactions.

The interacting uncoupled model predicts an increase of sorting with density (or equivalently with the area fraction $\rho_{\mathrm{GUV,CL}} \times A_{\mathrm{CL}}$) up to a maximum value from which sorting starts to decrease (see Figure 6.2). This reflects accurately the trade-off between bending, entropic and interaction contributions to free energy that explain the observed CL sorting. At very low CL densities, the interaction contribution is negligible, thereby there are not significant differences between the results of the non-interacting and the interacting models. In this regime, sorting is enhanced by the CL intrinsic curvature contribution and limited by the bending modulus and entropic penalties. As CL density increases, the interaction contribution tends to increase the relative CL enrichment in the tube while the bending and the entropic contributions tend to reduce it. Therefore, the initial increase of sorting with density showed in Figure 6.2 does exist because the cohesive CL-CL interaction offsets both the bending and the entropic penalties, causing CL accumulation in the inner (coherently curved) monolayer (see Figure 6.3). From certain onset in CL density the cohesive interaction contribution becomes lower than contributions by bending and entropy, thus sorting starts to decrease (for a detailed comparison

of these contributions to free energy, see Section A6.5.1 in Annex 6). In addition to the uncoupled sorting model, we have also performed the fit to a membrane model assuming monolayer coupling within the membrane bending energy. Although the interacting coupled model also predicts high sorting at high CL densities, it fails in reproducing the observed sorting at high curvatures (see Figure A6.10). Taken together, the theoretical analysis to our experimental data suggests the existence of short-range CL-CL attractive interactions and the uncoupled behavior of EPC/CL bilayers. This result endows both lateral packing of lipids and the additional lateral CL-CL cohesion as the dominant factors of curvature mediated CL sorting in lipid tubes.

Finally, it is important to verify whether CL molecules can exchange between the GUV and the tube. This test is essential since a diffusion impediment would mean that the CL distribution in our experiments would not be at equilibrium. To study this CL transport, the first step we did was to completely photobleach the fluorescently labelled CL in the tube by imaging it at high laser power. Next, we monitored the green fluorescence recovery in the tube after photobleaching by imaging at low laser power. Figure A6.2 shows the green fluorescence in the tube before, just right after photobleaching, and a few seconds after photobleaching. Our observations establish that CL repopulates the tube in a few seconds after bleaching, deducing that there is no detectable diffusion barrier at the neck. In a more biological wisdom, this result depicts CL as a mobile molecule, and the association clusters formed by CL-CL interactions as labile structures in dynamic equilibrium with their lipid environment.

6.3 Discussion

Despite the evidence accumulated from *in vivo* studies, and the results from MD simulations showing that CL concentrates in negatively curved regions of membranes (11), there was no *in vitro* data available so far that support the hypothesis for a curvature-based CL enrichment. Here, we have unequivocally determined that CL molecules can be sorted by curvature. This is an essential result from a biological point of view and will contribute to understand the interplay between CL composition and membrane shape. Using an *in vitro* approach with an homogenous mixture of EPC and CL, we have seen that membrane shape alone can modulate the distribution of CL without the involvement of any cellular protein machinery. We found that CL molecules accumulate in curved regions of the membrane, with a higher enrichment in highly curved membranes.

In general, the amount of lipid sorting arises from a competition between two forces: the energetic benefit of curvature matching and the cost of mixing entropy. Theoretical works [48, 192] show that the energetic gain of curvature matching for a single lipid at physiological curvatures is on the order of 1% of k_BT, which suggests that geometry alone does not significantly contribute to sorting at the cellular scale due to the overwhelming cost of mixing entropy. This conclusion is critically altered provided lipid-lipid interactions are considered forming stable finite-sized lipid clusters, which can spontaneously and independently target the lipids to curved regions of the membrane. Indeed, the energy bonus of curvature matching for a cluster of CL has been demonstrated to be sufficient to result in a sensing of membrane curvature and consequent CL positioning in bacterial poles [192, 250]. The analysis above is in accordance with our theoretical result that CL-CL attractive interactions are required to explain the observed

sorting at intermediate and high CL densities. Additionally, Sennato et al. [251] reported differences in cohesive interactions between lipids, in an experimental monolayer study indicating that CL interacts in a different way with PE and PC, the other two main lipid components of the mitochondrial inner membrane. Therefore, the predicted CL-CL interactions are expected to induce the formation of self-associating CL finite-sized clusters possibly stabilized by long-range repulsive electrostatic interactions [16]. These opposing forces should determine the CL cluster size. Model fits to our data predict an interaction parameter $a \approx -18\ k_B T$ nm^2, which corresponds to cluster size of the order of 10 molecules[1]. The CL cluster size obtained ($\approx 10\ A_{\mathrm{CL}} \approx 10 - 20$ nm^2) resembles the nanometric estimate of lipid-raft dimensions [252]. Fluorescence microscopy only detects mesosopic phase separation (domains larger than 1 μm). However, there was no visible evidence of phase separation in EPC/CL bilayers under our confocal microscope, neither in the tubes nor the mother GUVs. The absence of such a separation is consistent with the results of Nichols-Smith [17], who observed a complete miscibility for mixed EPC/CL monolayers at all the molar ratios at room temperature. Unfortunately, there are no studies that demonstrate the existence of CL nanodomains in EPC/CL membranes. Definitive evidences might be obtained from CL-containing bilayers in highly curved tubes, an experimental setting extremely difficult to be realized with AFM or other nanoscopies that allow to resolve molecular clusters. The size of the domains is limited by the high intrinsic curvature of CL, but this effect is reduced in curved regions [192]. Thus, definitive evidences might be obtained from CL-containing bilayers in highly curved tubes, an experimental setting extremely difficult to be realized with AFM or other nanoscopies that allow to resolve molecular clusters.

The fact that CL alone is able to be enriched in curved model membranes is coherent with the observation of CL-enriched domains at the poles and division sites of rod-shaped bacteria *in vivo* [12–14, 60, 61], and by the increase in the content of CL in the membranes of minicells [18]. Additionally, *in vivo*, the curvature enrichment in curved regions shown here could be further enhanced by interactions of CL with curvature sensitive proteins. The presence of CL in bacterial division sites contributes to create locally concave curvature, so contributing to reduce the constriction forces [222], thus supporting the CL involvement in the process of bacterial division. Our results can also help to understand the importance of CL in the maintenance of the highly curved structure of the mitochondrial inner membrane where it plays an essential role in mitochondrial bioenergetics. In that respect, our measurements showed that the neck joining the GUV to the tube (which resembles the geometry of mitochondrial *cristae junctions*) should not prevent CL molecules from diffusing through it. All these results reconcile with the experimental observation of Nichols-Smith [17], who showed that CL-containing membranes have a propensity to create folds.

[1] Since $A_{\mathrm{CL}} = 1.3$ nm^2 and $|c_{\mathrm{CL}}| = 1.10$ nm^{-1}, we get an estimate for the ratio of the interaction energy to the intrinsic curvature squared of $|a|/(A_{\mathrm{CL}} c_{\mathrm{CL}}^2) \approx 11\ k_B T$ nm^{-2}, which using the results of Ref. [192] gives a cluster size of the order of 10 molecules.

6.4 Material and Methods

For a fully detailed description of the experimental procedure followed, see Chapter 2.

GUVs formation

GUVs made of EPC and CL were grown by using electroformation technique [253] at room temperature, 22 ± 1 °C in 400 mOsm sucrose solution. The red fluorescent reference lipid, BODIPY-TR Ceramide, is included at 1% by mole to allow membrane visualization. The green fluorescent lipid, Top-Fluor CL, is also included at 1% by mole to allow the quantification of the CL-enrichment as a function of the membrane curvature. To allow adhesion between the membrane and the streptavidin-coated beads holding the tube in the trap, 0.2% by mole of DSPE-PEG(2000)-Biotin was added to the mixture. We made vesicles with EPC at different CL-contents, in particular at 4%, 9%, 14%, and 24% by mole (resulting in a total CL concentration of 5%, 10%, 15%, and 25% by mole, respectively). For control experiments (with no CL) and for the green fluorescence calibration (see Section A6.3 in Annex 6), we use 1% by mole of the green fluorescent lipid BODIPY-FL HPC. In no case phase separation was observed (see Figure A6.1).

Procedure for membrane nanotube extraction

The procedure is based on pulling membrane nanotubes from GUVs aspirated in a micropipette. For each experiment, a GUV is aspirated in a micropipette and a streptavidin-coated bead is trapped in an optical trap. The vesicle, which contains a very small fraction of biotinylated lipids, is then pushed against this bead so that a small patch of membrane sticks to the bead. The vesicle is then pulled away to create a membrane nanotube of 5-10 μm in length. This length is kept constant during the whole experiment. We perform successive step-variations of the membrane tension (which changes the tube radius R) by adjusting the pipette aspiration pressure. The tube radius was determined by comparing the red fluorescence intensity of the membrane tube to that of the GUV through a previous calibration with the reference lipid BODIPY-TR Ceramide (see Section A6.3 in Annex 6). Between each data point we wait for at least 45 seconds to let the system equilibrate by lipid diffusion and then we acquire one fluorescence image using a confocal microscope. All experiments were performed at room temperature, 22 ± 1 °C.

Acknowledgments

EBH sincerely thanks K. Mawoussi for his help with the experiments. All authors thank F. Joubert for providing material; J.B. Manneville, M. Velez, and E. Enciso for access to their setups; and A. Callan-Jones, M. Velez, L. Rodríguez-Arriaga, L. H. Moleiro, C. Ruiz, and S. Salinas for stimulating discussions. EBH acknowledges financial support from Ministerio de Educación, Cultura y Deporte (MECD, Spain) under FPU grant 13/02826. FM acknowledges financial support from Ministerio de Economía y Competitividad (MINECO, Spain) and European Regional Development Fund (ERDF) under grant FIS201570339-C2-1-R, and from Comunidad de Madrid (CAM, Spain) under grant S2013/MIT-2807. FJC acknowledges financial support from Ministerio de Economía y Competitividad (MINECO, Spain) and from European Regional Development Fund (ERDF) under grant FIS2015-67745-R (MINECO/FEDER).

Annex A6

Membrane Curvature Induces Cardiolipin Sorting

This chapter contains additional information related to the previous chapter, Chapter 6. In Section A6.1 we detail the reagents used for Giant Unilamellar Vesicles (GUVs) formation and a brief description of the electroformation technique. Section A6.2 contains the protocol followed for tube extraction experiments and Section A6.3 describes the image analysis. Next, in Section A6.4, we show the precise sorting data obtained and finally, in Section A6.5, we expose the theoretical aspects considered to model the experimental results.

A6.1 GUV Formation

Reagents

Egg-PC (EPC), 18:1 CL, Top-Fluor CL, and DSPE-PEG (2000)-Biotin were purchased in powder form from Avanti Polar Lipids. BODIPY-TR Ceramide (red fluorescent lipid) and BODIPY-FL HPC (green fluorescent lipid) were purchased from Molecular Probes. Streptavidin-coated polystyrene beads with diameter 3-3.4 μm were purchased from Bangs Laboratories (Carmel, IN). β-casein from bovine milk, mineral oil, and other reagents were purchased from Sigma.

Experimental procedure

Lipid mixtures composed of EPC and CL at different CL-content ,4%, 9%, 14%, and 24% by mole, were supplemented with the green fluorescent lipid Top-Fluor CL at 1% by mole to allow the quantification of the CL-enrichment as a function of the membrane curvature (resulting in a total CL concentration of 5%, 10%, 15%, and 25% by mole, respectively), with the red fluorescent reference lipid BODIPY-TR Ceramide at 1% by mole to allow membrane visualization, and with 0.2% by mole of DSPE-PEG(2000)-Biotin to allow adhesion between the membrane and the streptavidin-coated beads holding the tube in the trap. For control experiments (with no CL) and for the green fluorescence calibration (see Section A6.3 below), we use 1% by mole of the green fluorescent lipid BODIPY-FL HPC. Briefly, the procedure for preparing GUVs using the electroformation technique [253] was the following: two lipid films at 1 mg/ml are spread on two conductive ITO coated glasses and dried under high vacuum during 1 hour. The lipid films are then rehydrated in a sucrose solution 400 mM (osmolarity 400 mOsm) and grown during at least 1 hour under an AC electric field of typically 1.1 V, 10 Hz between the two ITO electrodes.

After growth, vesicles were transferred for observation and manipulation in a chamber containing 20 mM Tris pH 7.5 and 200 mM KCl (osmolarity ≈ 400 mOsm). Phase separation was not observed (even at high CL excess, see Figure A6.1) but GUVs exhibit a homogeneous fluorescence intensity. All steps were performed at room temperature, 22 ± 1 °C.

A6.2 Protocol for Tube Pulling Experiments

Tube pulling experiments were performed using a setup developed by P. Bassereau's group. It consists on a commercial Nikon TE2000 confocal microscope equipped with micromanipulators and optical trap. The details of the microscopy setup can be found in Chapter 2 and in Ref. [94]. This system allows for manipulating individual GUVs, controlling their surface tension, generating membrane nanotubes, measuring their radius and pulling force, and determining the density of membrane components between the GUV and the tube. The procedure is based on pulling membrane nanotubes from GUVs aspirated in a custom micropipette of ≈ 5 μm diameter. For each experiment, an open micromanipulation chamber was built with two clean glass coverslips (bottom: 11x32 mm, top: 9x35 mm). Before starting experiments, the micropipette and the chamber are filled with a solution containing of β-casein at 5 mg/ml during approximately 20 minutes in order to prevent the GUV from sticking to the glass. Then, the chamber is rinsed with the experimental buffer, containing 20 mM Tris pH 7.5 and 200 mM KCl and then is filled with a few μl of GUVs and streptavidin-coated beads and completed with buffer. To be able to impose a tension using the micropipette aspiration technique it is necessary to have GUVs with an initially low tension. This can be achieved by waiting for at least 30 min to slowly increase the osmolarity of the solution in the chamber by evaporation. When the tension is low enough (based on the visual observation of fluctuating vesicles), we close both edges of the chamber with mineral oil in order to maintain a constant pressure inside the chamber. Before each set of experiments on a new vesicle, it is necessary to set the zero reference pressure in the micropipette by detecting the absence of movement of a bead in the pipette. Once that is done, a GUV is aspirated in a micropipette applying a high aspiration pressure (checking the GUV "tongue" in the micropipette) and a streptavidin-coated bead is trapped in an optical trap. The vesicle, which contains a very small fraction of biotinylated lipids, is then pushed against this bead so that a small patch of membrane sticks to the bead. The vesicle is then pulled away to create a membrane nanotube of 5-10 μm in length. This length is kept constant during the whole experiment. We perform successive step-variations of the membrane tension (which varies the tube radius R over a biologically relevant range, typically between 8 and 40 nm) by adjusting the pipette aspiration pressure. Between each data point we wait for at least 45 seconds to let the system equilibrate by lipid diffusion (enough time to ensure that the system is at equilibrium, see Figure A6.2) and then we acquire one fluorescence image. All experiments were performed at room temperature, 22 ± 1 ºC.

A6.3 Image Analysis

The confocal images are acquired with the EZ-C1 software (Nikon) and then analyzed using a custom Matlab program which allows to quantify the intensity values for the two fluorophores in the tube and in the vesicle, as described previously in Chapter 2. The software works within a user-defined regions of interest. In our case, along the GUV contour and along the tube. Within these regions, pixel values are averaged along horizontal lines, converting the images into one-

dimensional data sets. After that, the maxima of the fluorescence profiles are reduced by the corresponding noise levels (average values of the background). These intensities are used to determine the CL density in GUVs, the sorting ratio, and the tube radius. The same area in the tube and in the vesicle is used for each dye.

Absence of phase separation

Under our confocal image acquisitions conditions, we observed no phase separation but GUVs exhibit a homogeneous fluorescence along their contour. Figure A6.1 shows a confocal image with a total CL concentration of 40% by mole. Even at this high CL excess, there is no visible evidence of phase separation in EPC/CL bilayers.

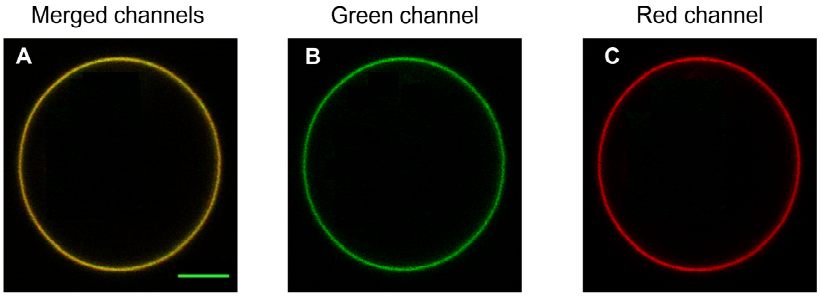

Figure A6.1. Absence of phase separation. Confocal image of a GUV with a total CL concentration of 40% by mole showing the distribution of Top-Fluor CL (green channel) and Bodipy-TR Ceramide (red channel). There is no visible evidence of phase separation in EPC/CL bilayers but GUVs exhibit a homogeneous fluorescence along their contour. Scale bar is 5 µm.

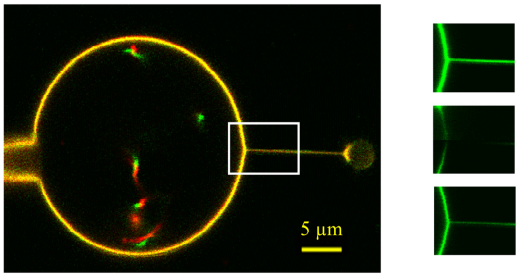

Figure A6.2. CL molecules can diffuse across the membrane nanotube. CL fluorescence recovery in the tube ($R = 25$ nm, $L = 7$ µm) after photobleaching the zone indicated by the white square. Righ: images of the tube before (top); just right after photobleaching (middle) and 6 seconds after photobleaching (bottom).

Photobleaching

Under our imaging conditions (laser intensity, pixel dwell, pinhole size and PMT gain), photobleaching is weak. Our confocal microscopy is designed to acquire sequentially the green and the red channel images in order to avoid any fluorescence bleed between both channels. We can estimate the amount of photobleaching by fitting the fluorescence decrease with the number of consecutive images (see Figure A6.2). In the vesicle, the loss of intensity per image is less than 0.2% for BODIPY-TR Ceramide (red channel) and less than 0.4% for Top-Fluor CL (green channel). The bleaching of the tube, which is larger than the vesicle due to its confined geometry, results in a loss of intensity per image less than 0.4% for BODIPY-TR Ceramide (red channel) and less than and 2% for Top-Fluor CL (green channel), respectively. To further limit bleaching, only one image per membrane tension step is acquired and no more than 8 images

are taken during one experiment on the same vesicle. The bleaching of the tube is also prevented by taking images with a time interval of 45 seconds (enough time to a re-equilibration, see Figure A6.3).

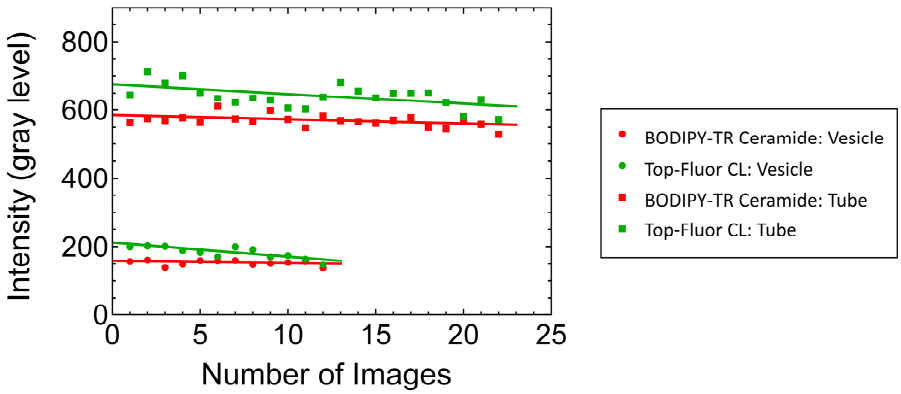

Figure A6.3. Photobleaching quantification. Evolution of fluorescence in the vesicle (red and green squares) and in the tube (red and green circles) during the acquisition of consecutive images. Frame rate around 1 Hz. Linear fit to the dataset gives for Top-Fluor CL in the vesicle, $y = 676 - 2.9x$; for Bodipy-TR Ceramide in the vesicle, $y = 585 - 1.2x$; for Top-Fluor CL in the tube, $y = 212 - 4.0x$; for Bodipy-TR Ceramide in the tube, $y = 159 - 0.66x$.

Sorting ratio

As previously introduced in Chapter 2, the CL-enrichment relative to the reference lipid (Bodipy-TR-Ceramide) is quantified by the sorting ratio S. We calculate it as the ratio of fluorescence of green and red channels in the tube normalized by the same ratio in the vesicle

$$S = \frac{(I_{\mathrm{CL}}/I_{\mathrm{BOD\text{-}TR}})_{\mathrm{tube}}}{(I_{\mathrm{CL}}/I_{\mathrm{BOD\text{-}TR}})_{\mathrm{GUV}}}. \tag{A6.1}$$

The control experiment is made with vesicles containing no CL but 1% by mole of the green fluorescent lipid BODIPY-FL HPC. Our fluorescence labelled lipids (Bodipy-TR Ceramide, Top-Fluor CL, and Bodipy FL-HPC) are not sensitive to membrane polarization and then we have not to correct for the polarization effects. We can conclude this from the measurements on membrane tubes with very low curvatures (*i.e.*, large radii), where we expect the sorting ratio to be equal to unity independently of membrane composition. As shown in Tables A6.1 and A6.2, the sorting ratio approaches 1 at very low curvatures, and then Eq. (A6.1) requires no normalization factor. For control experiments the observed sorting is approximately equal to one even for curved membranes, as expected (see Table A6.2).

Tube radius calibration

As described in Chapter 2, the radius of the nanotube can be easily obtained from the reference lipid fluorescence intensities through a previous calibration. Since the ratio of the tube lipid fluorescence $I_{\mathrm{tube,\,BOD\text{-}TR}}$ and GUV lipid fluorescence $I_{\mathrm{GUV,\,BOD\text{-}TR}}$ is proportional to the tube surface, and then to the tube radius, we can write the relationship

$$R = R_c \times \left(\frac{I_{\mathrm{tube}}}{I_{\mathrm{GUV}}}\right)_{\mathrm{BOD\text{-}TR}}, \tag{A6.2}$$

where R_c is a constant of proportionally. This constant can be determined by a linear fit of the radii values obtained from tube force and membrane tension measurements. For an ideal, elastic membrane at equilibrium, the tube force F, the membrane tension Σ, and the tube radius R are related as

$$R = \frac{F}{4\pi\Sigma}. \tag{A6.3}$$

and F and Σ are measured quantities in our system. Bassereau and co-workers previously measured the constant R_c for GUVs containing PC lipids using the same set up. They obtained: $R_c = (200 \pm 50)$ nm for DOPC with 6 independents GUVs [53], $R_c = (229 \pm 30)$ nm for mixtures of EPC:EPA 9:1 with 4 independents GUVs [55], $R_c = (203 \pm 16)$ nm for 57% EPC, 8% PIP2, 15% cholesterol, 10% DOPS and 10% DOPE with 11 independents GUVs [96]. All their measurements are consistent within their standard deviation errors. For our analysis (EPC vesicles) we have used a constant R_c of 200 nm.

Cardiolipin density in GUVs

A green fluorescence calibration allows us to obtain a relation between the green fluorescence intensity of the GUV and the surface density of labelled CL molecules in the membrane $\rho_{\text{GUV,Top-CL}}$. As described in Chapter 2, this can be done by using a controlled amount of a lipid dye emitting in the same channel as Top-Fluor CL. Here, we used the green fluorescent lipid BODIPY-FL HPC. We found that the measured fluorescent signal $I_{\text{GUV, BOD-FL}}$ from GUVs is linear with labelled molecule concentration up to 4500 molecules per μm^2 (see Figure A6.4) and then we can derive a calibration coefficient A^{gain}

$$\rho_{\text{GUV,BOD-FL}} = A^{\text{gain}} \times I^{\text{gain}}_{\text{GUV,BOD-FL}}. \tag{A6.4}$$

The proportionality constant A^{gain} depends upon both the confocal parameters (microscope objective, laser intensity, dwell time, the pinhole diameter, laser power, and PMT gain) and the BODIPY-FL HPC fluorescence efficiency. For the three gains of the confocal PMT used during experiments (100, 110, and 120) with the same excitation/acquisition conditions, we obtain: $A^{100} = (23.9 \pm 0.9)$, $A^{110} = (12.6 \pm 0.7)$, $A^{120} = (7.2 \pm 0.5)$ (see Figure A6.4A). However, Eq. (A6.4) is only valid to quantify BODIPY-FL HPC fluorescence in the membrane. Since Top-Fluor CL has a different efficiency than BODIPY-FL HPC, the calibration has to be corrected to take into account the spectral differences of the two dyes and how these spectra are affected by the microscope optics

$$\rho_{\text{GUV,Top-CL}} = \frac{\rho_{\text{GUV,BOD-FL}}}{F^{\text{gain}}} = \frac{A^{\text{gain}} \times I^{\text{gain}}_{\text{GUV,BOD-FL}}}{F^{\text{gain}}}, \tag{A6.5}$$

where $F^{\text{gain}} = I^{\text{gain}}_{\text{bulk,Top-CL}} / I^{\text{gain}}_{\text{bulk,BOD-FL}}$ quantifies the relatives fluorescence intensities of the two dyes at a given concentration. It can be deduced from the evolution of the intensity ratio measured in solution as a function of the concentration of labelled molecules in bulk. We found that both signals are linear with labelled molecule concentration (see Figure A6.4B-C) and then F^{gain} can be deduced from the ratio between the slopes of the linear fits $I^{\text{gain}}_{\text{bulk,Top-CL}}$ vs. $\rho_{\text{bulk,Top-CL}}$ (Figure A6.4C) and $I^{\text{gain}}_{\text{bulk,BOD-FL}}$ vs. $\rho_{\text{bulk,BOD-FL}}$ (Figure A6.4B). Finally, the area density of labelled

CL in the GUV membrane, in number of molecules bound per squared micron, for the three values of PMT gains used during experiments, is

$$\rho_{\mathrm{GUV,Top\text{-}CL}}(\mu\mathrm{m}^{-2}) = (21.8 \pm 1.4) \times I^{100}_{\mathrm{GUV,Top\text{-}CL}}, \tag{A6.6a}$$

$$\rho_{\mathrm{GUV,Top\text{-}CL}}(\mu\mathrm{m}^{-2}) = (9.0 \pm 0.5) \times I^{110}_{\mathrm{GUV,Top\text{-}CL}}, \tag{A6.6b}$$

$$\rho_{\mathrm{GUV,Top\text{-}CL}}(\mu\mathrm{m}^{-2}) = (5.9 \pm 0.4) \times I^{120}_{\mathrm{GUV,Top\text{-}CL}}, \tag{A6.6c}$$

GUVs are made with 1% by mole of Top-Fluor CL and with different concentrations of CL, in particular, 4%, 9%, 14%, and 24% by mole (resulting in a total CL concentration of 5%, 10%, 15%, and 25% by mole, respectively). For example, the sample with 10% of total CL contains 1% of Top-Fluor CL and 9% of CL; the sample with 25% of total CL contains 1% of Top-Fluor CL and 24% of CL. Assuming that the 1% of Top-Fluor CL represents the total CL in each sample, we can obtain an estimation of the total density of CL in the GUV membrane $\rho_{\mathrm{GUV,CL}} \equiv \rho_{\mathrm{GUV,Total\text{-}CL}}$ by multiplying the density of labelled CL by the corresponding factor 1, 5, 10, 15, or 25.

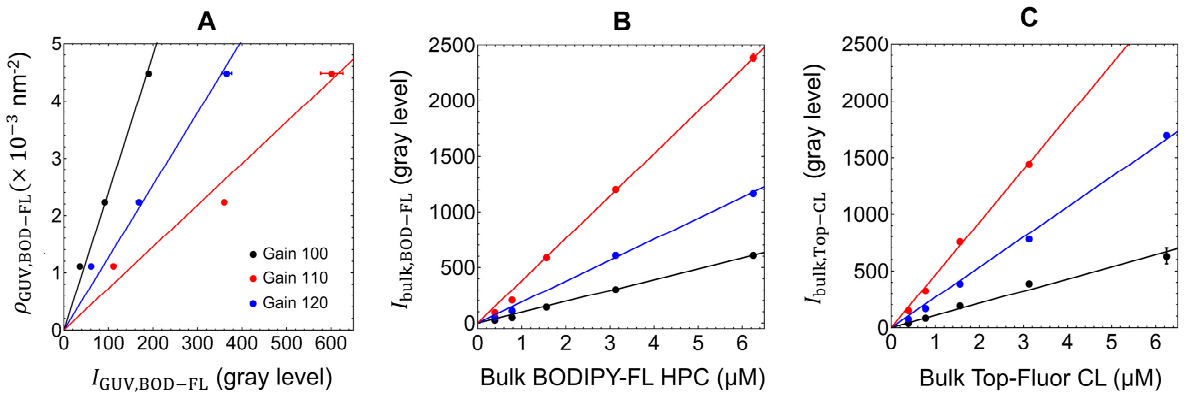

Figure A6.4. Determination of CL density in GUVs. Green fluorescence calibration for the three values of PMT gains used during experiments (100 in black, 110 in blue, and 120 in red). (A) Fluorescence measured from GUVs with increasing amount of BODIPY-FL HPC. Linear fit $\rho_{\mathrm{GUV,BOD\text{-}FL}} = A^{\mathrm{gain}} \times I^{\mathrm{gain}}_{\mathrm{GUV,BOD\text{-}FL}}$ gives the conversion constants $A^{100} = (23.9 \pm 0.9)$, $A^{110} = (12.6 \pm 0.7)$, and $A^{120} = (7.2 \pm 0.5)$. (B) Fluorescence measured in bulk as a function of the volume concentration of BODIPY-FL. (C) Fluorescence measured in bulk as a function of the volume concentration of Top-Fluor CL. The efficient ratio $F^{\mathrm{gain}} = I^{\mathrm{gain}}_{\mathrm{bulk,Top\text{-}CL}}/I^{\mathrm{gain}}_{\mathrm{bulk,BOD\text{-}FL}}$ can be deduced from the ratio between the slopes of the linear fits $I^{\mathrm{gain}}_{\mathrm{bulk,Top\text{-}CL}}$ versus $\rho_{\mathrm{bulk,Top\text{-}CL}}$ (C) and $I^{\mathrm{gain}}_{\mathrm{bulk,BOD\text{-}FL}}$ versus $\rho_{\mathrm{bulk,BOD\text{-}FL}}$ (B) obtaining $F^{100} = (1.10 \pm 0.06)$, $F^{110} = (1.41 \pm 0.04)$, and $F^{120} = (1.22 \pm 0.03)$.

A6.4 Experimental Data

To reduce the noise in the presentation of sorting data versus tube curvature and CL density in GUVs, we have binned the raw data over four range of tube curvatures and four range of CL densities (see Table A6.1). We do the same for control experiment (see Table A6.2).

Table A6.1. CL sorting as a function of tube curvature at different CL densities (related to Figure 6.2 in Chapter 6).

Very high density $\rho_{GUV,CL} = (23.3 \pm 0.6) \times 10^{-2}$ nm^{-2}

Curvature (nm^{-1})	№ of GUVs	GUV density (nm^{-2})	Sorting
0.033±0.003	10	20.9±0.4	1.11±0.06
0.063±0.003	14	23.3±0.7	1.24±0.06
0.092±0.002	6	25±2	1.45±0.15
0.129±0.006	6	25.7±1.9	1.57±0.15

High density $\rho_{GUV,CL} = (15.1 \pm 0.4) \times 10^{-2}$ nm^{-2}

Curvature (nm^{-1})	№ of GUVs	GUV density (nm^{-2})	Sorting
0.035±0.002	18	15.9±0.5	1.20±0.06
0.060±0.002	12	15.0±0.7	1.35±0.07
0.094±0.003	8	13.9±0.9	1.54±0.06
0.125±0.006	6	14.9±1.2	1.71±0.09

Low density $\rho_{GUV,CL} = (4.4 \pm 0.2) \times 10^{-2}$ nm^{-2}

Curvature (nm^{-1})	№ of GUVs	GUV density (nm^{-2})	Sorting
0.033±0.002	29	4.8±0.3	0.94±0.04
0.065±0.002	31	4.6±0.3	1.33±0.07
0.094±0.002	12	3.8±0.5	1.23±0.06
0.130±0.007	6	4.2±0.7	2.10±0.15

Very low density $\rho_{GUV,CL} = (0.43 \pm 0.02) \times 10^{-2}$ nm^{-2}

Curvature (nm^{-1})	№ of GUVs	GUV density (nm^{-2})	Sorting
0.037±0.002	23	0.43±0.03	0.98±0.05
0.060±0.003	9	0.42±0.05	1.07±0.06
0.090±0.004	5	0.39±0.06	1.26±0.13
0.130±0.006	6	0.41±0.02	1.19±0.09

Table A6.2. Control experiment. BODIPY-FL HPC sorting as a function of tube curvature.

Curvature (nm^{-1})	Nº of GUVs	Sorting
0.034±0.003	14	1.03±0.03
0.065±0.003	7	0.93±0.03
0.091±0.005	6	1.04±0.06
0.123±0.008	6	1.00±0.12

A6.5 Cardiolipin Sorting Theory

There exist numerous theoretical works studying the coupling between membrane shape and composition [51, 55, 97–101]. In this section we implement a thermodynamic model for curvature-dependent CL sorting in a homogeneous binary lipid mixture EPC/CL basing on the model proposed by Aimon et al. [55]. The model determines the membrane tube composition that minimizes the total free energy of the curved membrane in which bending is modelled as a thin elastic sheet and mixing entropy is approximated by the van der Waals equation of state that includes possible CL-CL interactions.

In our experiments, GUVs are made of homogeneous lipid mixtures of EPC and CL. As expected from the molecular dimensions of CL, the absolute value of its intrinsic curvature should be of the order of 1 nm^{-1}, a value compatible with the smaller cross-sectional area of its head group relative to its hydrophobic domain [12]. Conversely, EPC lipids have a nearly cylindrical shape with an intrinsic curvature close to zero. Additionally, the area per molecule of a CL molecule is nearly a factor of two larger than that of a EPC lipid, due to its four acyl chains as compared to the two of EPC (the average cross-sectional area of EPC is around 0.67 nm^2 [254], while it extends out almost twice for CL, around 1.30 nm^2 [248]). Therefore, membrane curvature should have less effect on EPC than on CL. In order to implement the model, CL molecules are assumed to insert homogeneously in both monolayers of the GUV membrane with opposite orientations due to their polar heads and their apolar tails. CL molecules of the inner monolayer, which bend the membrane in the direction of the imposed curvature, are expected to be enriched in the tube while CL molecules in the outer monolayer, which bend the membrane against the imposed curvature, are expected to be depleted from the tube (see Figure A6.5). In the following, the inner monolayer of the membrane is denoted with + and the outer monolayer of the membrane is denoted with $-$. CL molecules of the inner and outer monolayers can be thought as species with opposite intrinsic curvature (c_{CL}^{+} and $c_{CL}^{-} = -c_{CL}^{+}$). The total CL concentration in the membrane can be then described in terms of the surface densities ρ_{CL}^{+} and ρ_{CL}^{-}.

A6.5.1 Membrane with Uncoupled Monolayers

In principle, we assume that membrane monolayers are uncoupled (free to slide past each other), and then they are treated as two independent systems with their corresponding bending energies. At the end of this annex, in Section A6.5.2, we will also address an analysis when a monolayer coupling in bending energy is considered. If a CL molecule occupies an area A_{CL}, the

presence of a CL density ρ_{CL}^{i} in the monolayer i lowers the EPC concentration of that monolayer by an amount

$$\frac{\rho_{\mathrm{EPC}}^{i}}{\rho_{\mathrm{EPC},\rho_{\mathrm{CL}}^{i}=0}^{i}} = 1 - A_{\mathrm{CL}}\rho_{\mathrm{CL}}^{i}, \qquad i = +,-, \tag{A6.7}$$

and so the CL concentration and experimentally measured sorting ratio S are related by the expression

$$S = \left(\frac{\rho_{\mathrm{CL}}^{+} + \rho_{\mathrm{CL}}^{-}}{\rho_{\mathrm{EPC}}^{+} + \rho_{\mathrm{EPC}}^{-}}\right)_{\mathrm{tube}} \Big/ \left(\frac{\rho_{\mathrm{CL}}^{+} + \rho_{\mathrm{CL}}^{-}}{\rho_{\mathrm{EPC}}^{+} + \rho_{\mathrm{EPC}}^{-}}\right)_{\mathrm{GUV}} = \frac{(\rho_{\mathrm{tube,CL}}^{+} + \rho_{\mathrm{tube,CL}}^{-})(2 - A_{\mathrm{CL}}\rho_{\mathrm{GUV,CL}})}{[2 - A_{\mathrm{CL}}(\rho_{\mathrm{tube,CL}}^{+} + \rho_{\mathrm{tube,CL}}^{-})]\rho_{\mathrm{GUV,CL}}}, \tag{A6.8}$$

where we have assumed that $\rho_{\mathrm{GUV,CL}}^{+} = \rho_{\mathrm{GUV,CL}}^{-} = \rho_{\mathrm{GUV,CL}}/2$ (equal amount of each orientation).

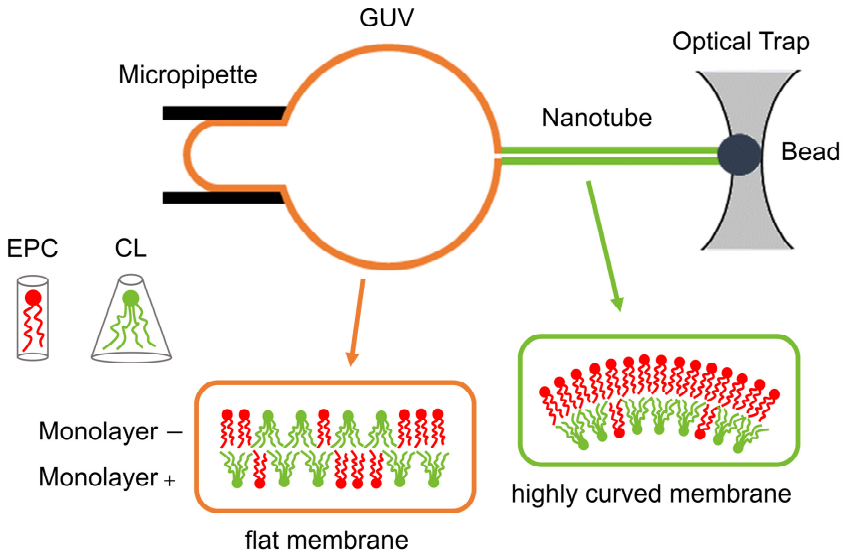

Figure A6.5. Cartoon illustrating the proposed mechanism of CL sorting. A coupling between membrane composition and shape could minimize the curvature frustration of the curved regions of the membrane. CL molecules bending the membrane in the direction of the imposed curvature will drive CL enrichment while CL molecules bending the membrane against the imposed curvature will cause CL depletion.

Membrane free energy

As noted by Aimon et al. [55], for these experiments it is sufficient to consider just the total curvature of the membrane c because the Gaussian curvature K is zero for both the GUV (approximately flat) and the membrane tube (approximately cylindrical). Then, the membrane free energy per unit area for a curved monolayer can be written as

$$g^{i}(c) = g_{\mathrm{mix}}^{i} + g_{\mathrm{bend}}^{i}(c), \qquad i = +,-, \tag{A6.9}$$

where g_{mix}^{i} is the free energy of mixing in a flat monolayer and $g_{\mathrm{bend}}^{i}(c)$ is the energy required to bend the membrane monolayer i into a cylinder with total curvature $c = 1/R$. The total free energy per unit area of the bilayer $g^{\mathrm{b}}(c)$ is the sum of the free energies of each monolayer, *i.e.*, $g^{\mathrm{b}}(c) = g^{+}(c) + g^{-}(c)$. The free energy of mixing can be approximated using the van der Waals equation of state

$$g^i_{\text{mix}} = g^i_{\text{ent}} + g^i_{\text{int}} = k_B T \rho^i_{\text{CL}} \log\left(\frac{\rho^i_{\text{CL}} A_{\text{ref}}}{1 - \rho^i_{\text{CL}} A_{\text{CL}}}\right) + a\left(\rho^i_{\text{CL}}\right)^2, \qquad i = +, -, \tag{A6.10}$$

where k_B is Boltzmann's constant, T is the temperature, and a is an interaction term that describes the interactions among CL molecules. Note we are assuming neither interaction between EPC lipids nor between EPC and CL molecules. We are also neglecting the interactions between monolayers and the transbilayer (flip-flop) lipid motion (slow process compared to sorting). The mixing energy of the bilayer $g^{\text{b}}_{\text{mix}}$ is the sum of the mixing energies of each monolayer, *i.e.,* $g^{\text{b}}_{\text{mix}} = g^{+}_{\text{mix}} + g^{-}_{\text{mix}}$. The values of a should be reflected in the phase behavior of the system. In fluorescence microscopy images, the CL distribution in the GUVs appear uniform even at high CL excess (see Figure A6.1), therefore CL-CL interactions could only induce the formation of short-range CL clusters (below the optical limit of our confocal microscopy) possibly stabilized by long-range repulsive electrostatic interactions [16].

The energy required to bend the membrane into a curved shape can be estimated using the elastic response a thin, cylindrical fluid sheet. For small deflections, the monolayer bending energy per unit area is

$$g^i_{\text{bend}}(c) = \frac{\kappa^i}{2}\left(c - c^i_0\right)^2, \qquad i = +, -, \tag{A6.11}$$

where κ^i and c^i_0 are, respectively, the bending modulus and the spontaneous curvature of the monolayer i. The bending energy of the bilayer $g^{\text{b}}_{\text{bend}}(c)$ is the sum of the bending energies of each monolayer, *i.e.,* $g^{+}_{\text{bend}}(c) + g^{-}_{\text{bend}}(c)$ (recall that we are not considering any coupling between monolayers).

CL molecules can alter the bending energy by changing either the monolayer rigidity κ^i or the curvature of the monolayer in its unstressed state c^i_0. On one side, the effect of the CL molecules on the monolayer resting shape can be calculated assuming that the individual components deflect like a set of (torsional) spring in series [55]

$$c^i_0 = A_{\text{CL}} c^i_{\text{CL}} \rho^i_{\text{CL}}, \qquad i = +, -, \tag{A6.12}$$

where c^i_{CL} is the intrinsic curvature of CL. CL molecules bending the membrane in the direction of the imposed curvature (c and c^{+}_{CL} with the same sign, inner monolayer) will drive CL enrichment while CL molecules bending the membrane against the imposed curvature (c and c^{-}_{CL} with opposite sign, outer monolayer) will cause CL depletion.

On other side, the effect of the CL molecules on the membrane bending modulus is given by [55]

$$\frac{1}{\kappa^i} = \frac{1 - A_{\text{CL}} \rho^i_{\text{CL}}}{\kappa^{\text{m}}_{\text{EPC}}} + \frac{A_{\text{CL}} \rho^i_{\text{CL}}}{\kappa^{\text{m}}_{\text{CL}}}, \qquad i = +, -, \tag{A6.13}$$

so

$$\kappa^i = \frac{\kappa^{\text{m}}_{\text{EPC}} \kappa^{\text{m}}_{\text{CL}}}{\kappa^{\text{m}}_{\text{CL}} + \left(\kappa^{\text{m}}_{\text{EPC}} - \kappa^{\text{m}}_{\text{CL}}\right) A_{\text{CL}} \rho^i_{\text{CL}}}, \qquad i = +, -, \tag{A6.14}$$

where $\kappa^{\text{m}}_{\text{EPC}}$ is the bending modulus of a pure EPC monolayer. The bending moduli $\kappa^{\text{m}}_{\text{EPC}}$ and $\kappa^{\text{m}}_{\text{CL}}$

are the same in both monolayers because the stiffness is independent of the lipid orientation. According to Eq. (A6.14), the bending modulus drives enrichment if CL molecules soften the membrane and depletion if CL molecules stiffen the membrane. Thus, CL molecules must have a strong spontaneous curvature and/or significantly soften the membrane to lead to a bending contribution to sorting, as previously explained when we introduced the lipid sorting mechanisms in Section 1.4 of Chapter 1.

Equilibrium composition of a curved membrane

The total free energy of a membrane tube with total curvature c, area A_{tube}, and composition $\rho^{+}_{\text{tube,CL}} + \rho^{-}_{\text{tube,CL}}$, coupled to a flat GUV reservoir with area A_{GUV} and composition $\rho^{+}_{\text{GUV,CL}} + \rho^{-}_{\text{GUV,CL}}$, is

$$G = [g^{+}(c) + g^{-}(c)]_{\text{tube}} A_{\text{tube}} + [g^{+}(0) + g^{-}(0)]_{\text{GUV}} A_{\text{GUV}}. \tag{A6.15}$$

Transferring $\mathrm{d}N^{i}_{\text{CL}}$ CL molecules into the tube will change the composition of both the tube and GUV by

$$\mathrm{d}N^{i}_{\text{CL}} = \mathrm{d}\rho^{i}_{\text{tube,CL}} A_{\text{tube}} = -\mathrm{d}\rho^{i}_{\text{GUV,CL}} A_{\text{GUV}}, \qquad i = +, -. \tag{A6.16}$$

The corresponding change in free energy is then

$$\begin{aligned} \mathrm{d}G &= \left[\frac{\partial g^{+}(c)}{\partial \rho^{+}_{\text{CL}}}\mathrm{d}\rho^{+}_{\text{CL}} + \frac{\partial g^{-}(c)}{\partial \rho^{-}_{\text{CL}}}\mathrm{d}\rho^{-}_{\text{CL}}\right]_{\text{tube}} A_{\text{tube}} + \left[\frac{\partial g^{+}(0)}{\partial \rho^{+}_{\text{CL}}}\mathrm{d}\rho^{+}_{\text{CL}} + \frac{\partial g^{-}(0)}{\partial \rho^{-}_{\text{CL}}}\mathrm{d}\rho^{-}_{\text{CL}}\right]_{\text{GUV}} A_{\text{GUV}} \\ &= \left[\frac{\partial g^{+}_{\text{tube}}(c)}{\partial \rho^{+}_{\text{tube,CL}}} - \frac{\partial g^{+}_{\text{GUV}}(0)}{\partial \rho^{+}_{\text{GUV,CL}}}\right]\mathrm{d}N^{+}_{\text{CL}} + \left[\frac{\partial g^{-}_{\text{tube}}(c)}{\partial \rho^{-}_{\text{tube,CL}}} - \frac{\partial g^{-}_{\text{GUV}}(0)}{\partial \rho^{-}_{\text{GUV,CL}}}\right]\mathrm{d}N^{-}_{\text{CL}}, \end{aligned} \tag{A6.17}$$

where

$$\begin{aligned} \frac{\partial g^{i}(c)}{\partial \rho^{i}_{\text{CL}}} = {} & -\kappa^{i}\left(c - c^{i}_{0}\right) A_{\text{CL}} c^{i}_{\text{CL}} + \frac{\left(\kappa^{i}\right)^{2}\left(c - c^{i}_{0}\right)^{2}}{2\kappa^{\text{m}}_{\text{EPC}}}\left(1 - \frac{\kappa^{\text{m}}_{\text{EPC}}}{\kappa^{\text{m}}_{\text{CL}}}\right) A_{\text{CL}} \\ & + k_{B}T\left[\log\left(\frac{\rho^{i}_{\text{CL}} A_{\text{ref}}}{1 - \rho^{i}_{\text{CL}} A_{\text{CL}}}\right) + 1 + \frac{\rho^{i}_{\text{CL}} A_{\text{CL}}}{1 - \rho^{i}_{\text{CL}} A_{CL}}\right] + a\rho^{i}_{\text{CL}}, \qquad i = +, -, \end{aligned} \tag{A6.18}$$

where κ^{i} is given by Eq. (A6.14). At equilibrium

$$\left[\frac{\partial g(c)}{\partial \rho_{\text{CL}}}\right]^{i}_{\text{tube}} = \left[\frac{\partial g(0)}{\partial \rho_{\text{CL}}}\right]^{i}_{\text{GUV}}, \qquad i = +, -. \tag{A6.19}$$

We have to solve the Eq. (A6.19) for both monolayers (+ and −) to obtain $\rho^{+}_{\text{tube,CL}}$ and $\rho^{-}_{\text{tube,CL}}$, and then replace them in Eq. (A6.8) to determine sorting. There is no simple analytical solution for this equation but numerical solutions can be obtained. Due to the three orders of magnitude difference in area between the GUV and the tube, the change in GUV composition can be neglected and can be considered as a chemiostat (reservoir) for the tube. The, the CL densities in the GUV can be assumed to remain approximately constant and equal to $\rho^{+}_{\text{GUV,CL}} = \rho^{-}_{\text{GUV,CL}} = \rho_{\text{GUV,CL}}/2$ (equal amount of each orientation).

Estimation of the monolayer bending modulus

The uncoupled model requires to know the bending moduli of EPC and CL monolayers. However, the easily measured quantity is the bilayer bending modulus, but not so much the monolayer one, and no data are available about the bending modulus of pure CL monolayers. In order to estimate these parameters, we write the bending energy of the bilayer $g^{\mathrm{b}}_{\mathrm{bend}}$ as the sum of the bending energies of the monolayers + and − (uncoupled case)

$$g^{\mathrm{b}}_{\mathrm{bend}} = \frac{1}{2}\kappa^{\mathrm{b}}\left(c - c^{\mathrm{b}}_0\right)^2 = g^{+}_{\mathrm{bend}} + g^{-}_{\mathrm{bend}} = \frac{1}{2}\kappa^{+}(c - c^{+}_0)^2 + \frac{1}{2}\kappa^{-}(c - c^{-}_0)^2, \tag{A6.20}$$

where κ^{b} is the bilayer bending modulus and c^{b}_0 is the spontaneous curvature of the bilayer corresponding to its un-stressed, resting shape. In a simple approach, the spontaneous curvature of the bilayer can be written as the sum of the spontaneous curvatures of both monolayers [9]

$$c^{\mathrm{b}}_0 = c^{+}_0 + c^{-}_0. \tag{A6.21}$$

For a bilayer in which CL inserts homogeneously with both orientations we have $\kappa^{\mathrm{m}} \equiv \kappa^{+} = \kappa^{-}$ and $|c^{\mathrm{m}}_0| \equiv c^{+}_0 = -c^{-}_0$. Therefore, according to Eq. (A6.21), $c^{\mathrm{b}}_0 = 0$ and then

$$g^{\mathrm{b}}_{\mathrm{bend}} = \frac{1}{2}\kappa^{\mathrm{b}}c^2 = \kappa^{\mathrm{m}}(c^2 + |c^{\mathrm{m}}_0|)^2 = \kappa^{\mathrm{m}}c^2 + \text{constant}, \tag{A6.22}$$

where the constant term is just a change in the energy origin. Therefore, the bending modulus of an uncoupled monolayer can be approximated by half the bending modulus of a bilayer with the same composition

$$\kappa^{\mathrm{m}} = \kappa^{\mathrm{b}}/2\,. \tag{A6.23}$$

Note that Eq. (A6.23) is not true when monolayers are coupled since in this case the membrane bending energy cannot be written as the sum of the bending energies of the monolayers [Eq. (A6.20)].

Experimental values from literature

Implementing the theoretical model requires to introduce the following parameters: area of a CL molecule A_{CL}, bending modulus of a pure EPC monolayer $\kappa^{\mathrm{m}}_{\mathrm{EPC}}$, bending modulus of a pure CL monolayer $\kappa^{\mathrm{m}}_{\mathrm{CL}}$, intrinsic curvature of CL c_{CL}, and CL-CL interaction term a. Except for the interaction term, there exist previous experimental measurements of these parameters. On one side, scattering analysis gave a CL area of approximately 1.3 nm^2 [248], which is nearly a factor of two larger than that of a EPC lipid (around 0.67 nm^2 [254]), due to its four acyl chains as compared to the two of EPC. On other side, flickering spectroscopy measurements of CL bilayers yield a bending modulus $\kappa^{\mathrm{b}}_{\mathrm{CL}} = 1.06 \times 10^{-19}$ J $\approx 26\ k_BT$ at $T = 298\ K$ [248], which is larger than that observed in EPC bilayers $\kappa^{\mathrm{b}}_{\mathrm{EPC}} = 10 \pm 1\ k_BT$ at $T = 298\ K$ [9]. According to Eq. (A6.23), the bending modulus of an uncoupled monolayer can be estimated as $\kappa^{\mathrm{m}} = \kappa^{\mathrm{b}}/2$, and then $\kappa^{\mathrm{m}}_{\mathrm{EPC}} = 5\ k_BT$ and $\kappa^{\mathrm{m}}_{\mathrm{CL}} = 13\ k_BT$ at $T = 298\ K$. The fit to the observed data using the previous experimental values will provide the expected CL curvature and the range of CL clusters. The CL intrinsic curvature obtained from the fit can be then compared with previous estimations, which suggest that it should be of the order of 1 nm^{-1} [12] due to the smaller cross-sectional area of its head group relative to its hydrophobic domain.

Sorting as a function of tube curvature

Figure A6.2 in Chapter 6 shows the CL enrichment as a function of the area fraction $\rho_{GUV,CL} \times A_{CL}$ (which corresponds to the fraction of the GUV surface covered with CL molecules) for four ranges of tube curvature (see Table A6.1). The minimum square fit to the observed data in the absence of binary interactions between CL molecules (*i.e.*, interacting parameter $a = 0$) gives $c_{CL} = 1.12 \pm 0.4$ nm^{-1} (dashed lines) and assuming possible CL-CL interactions gives $c_{CL} = 1.10 \pm 0.05$ nm^{-1} and $a = -18 \pm 1\ k_BT$ nm^2 (solid lines). Clearly, the non-interacting uncoupled model fails to reproduce the experimental data, for any values of the tube curvature (c). Although the non-interacting uncoupled model describes a curvature-increasing sorting at low CL-content, it largely underestimates the results at intermediate and high CL concentration. In contrast, interacting uncoupled model is successful in reproducing the experimental measurements. This conclusion can be also extracted from Figure A6.6, where it is represented the CL enrichment as a function of the tube curvature for four ranges of the area fraction.

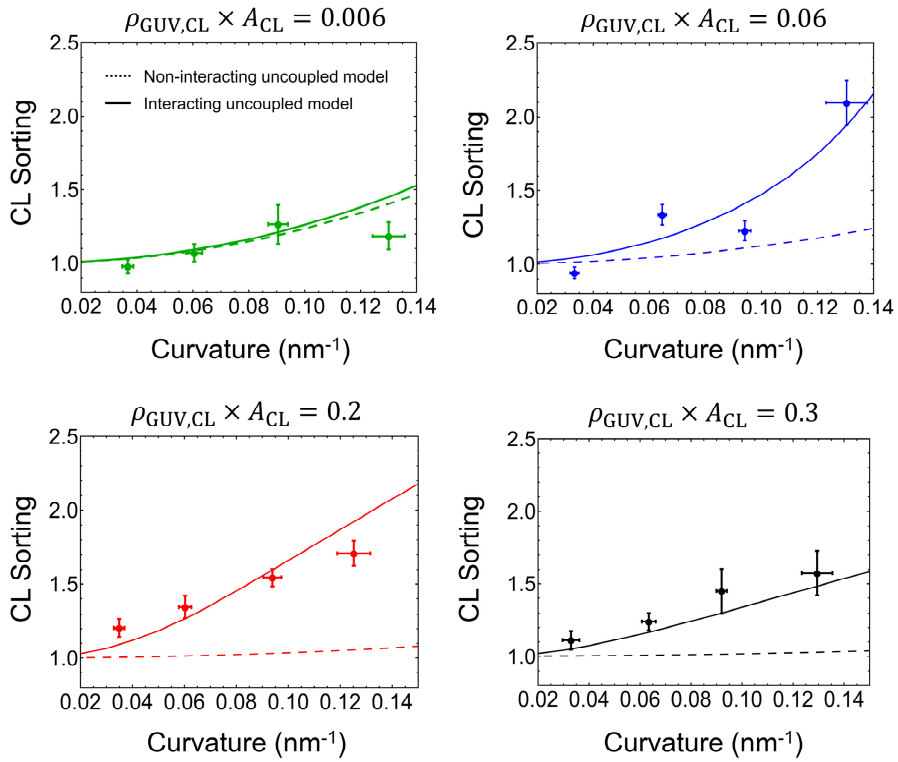

Figure A6.6. CL enrichment as a function of tube curvature. CL sorting as a function of the tube curvature for four ranges of the area fraction $\rho_{GUV,CL} \times A_{CL}$: — very low (0.0056 ± 0.0003); — low (0.057 ± 0.003); — high (0.196 ± 0.005); and — very high (0.303 ± 0.008). Points are the mean of binned tube curvatures and sorting ratios and the error bars represent the corresponding standard deviations. The minimum square fit of the theoretical uncoupled model (*i.e.,* in the absence of binary interactions between CL molecules, $a = 0$) is represented with dashed lines and gives an intrinsic curvature of CL of $c_{CL} = 1.12 \pm 0.4$ nm^{-1}. The minimum square fit of the interacting uncoupled model (*i.e.,* assuming possible CL-CL interactions, with free interacting parameter a) is represented with solid lines and gives $c_{CL} = 1.10 \pm 0.05$ nm^{-1} and $a = -18 \pm 1\ k_BT$ nm^2. It is clear that the non-interacting uncoupled model does not reproduces our data. In contrast, CL-CL attractive interactions can explain the observed sorting. The computations are made with the following values: CL area $A_{CL} = 1.3$ nm^2 [248], bending modulus of a pure CL bilayer $\kappa_{CL}^{b} = 26\ k_BT$ [248], and bending modulus of a pure EPC bilayer $\kappa_{EPC}^{b} = 10\ k_BT$ [9].

Tube spontaneous curvature and bending modulus

GUV membrane is assumed to contain CL molecules with both orientations: $c_{CL}^{+} = 1.10$ nm^{-1} in the inner monolayer and $c_{CL}^{-} = -1.10$ nm^{-1} in the outer monolayer. The model predicts CL molecules in the inner monolayer, which bend the membrane in the direction of the imposed curvature (c and c_{CL}^{+} with the same sign), are enriched in the tube while CL molecules in the outer monolayer, which bend the membrane against the imposed curvature (c and c_{CL}^{-} with opposite sign), are depleted from the tube (see Figure 6.3 in Chapter 6). These opposite effects of curvature on the two monolayers do not cancel each other and so the total CL concentration of the bilayer increases with curvature. The spontaneous curvature in the tube [Eq. (A6.12)] is positive in the inner monolayer and negative in the outer one (Figure A6.7A). It increases with tube curvature in both monolayers due to the enrichment of positively curved CL molecules and the depletion of negatively curved CL molecules. Because CL stiffens the membrane, the bending modulus of the tube [Eq. (A6.14)] increase with curvature in the inner monolayer while decrease in the outer one (Figure A6.7B).

Since the GUV can be considered a reservoir for the tube, its CL densities can be assumed to remain approximately constant and equal to $\rho_{GUV,CL}^{+} = \rho_{GUV,CL}^{-} = \rho_{GUV,CL}/2$ (equal amount of each orientation). As a result, the spontaneous curvature of the GUV is zero [Eq. (A6.12)] and the bending modulus of the GUV is equal in both monolayers and depends on $\rho_{GUV,CL}$ according to Eq. (A6.14).

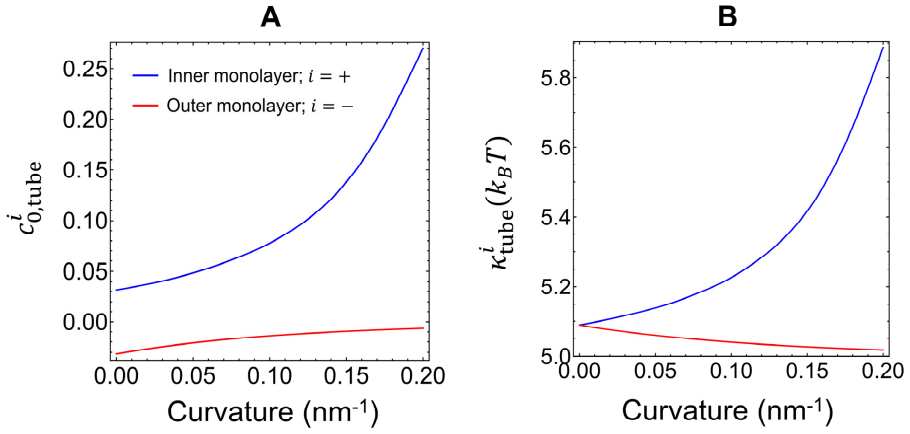

Figure A6.7. Spontaneous curvature and bending modulus in the membrane nanotube according to the interacting uncoupled model. (A) The spontaneous curvature in the tube is positive in the inner monolayer and negative in the outer one. It increases with tube curvature in both monolayers due to the enrichment of positively curved CL molecules and the depletion of negatively curved CL molecules. (B) Because CL stiffens the membrane, the bending modulus of the tube increase with curvature in the inner monolayer while decrease in the outer one. The computations are made with the following values: CL area $A_{CL} = 1.3$ nm^2 [248], bending modulus of a pure CL bilayer $\kappa_{CL}^{b} = 26\ k_BT$ [248], bending modulus of a pure EPC bilayer $\kappa_{EPC}^{b} = 10\ k_BT$ [9], and a CL density in the GUV of $\rho_{GUV,CL} = 0.04$ molecules per nm^2, corresponding to an area fraction $\rho_{GUV,CL} \times A_{CL}$ of about 6% (half in each monolayer). Quantities referred to the inner/outer monolayer of the tube are represented with blue/red lines.

Analysis of the bending, entropic, and interaction contributions to sorting

In this section, we address a deeper analysis of the bending, entropic, and interaction contributions to sorting and study how they are affected by CL density. To do that, we recall the

expression of the chemical potential $\mu^i(c) \equiv \partial g^i(c)/\partial \rho^i$, defined as the rate of change of the total free energy of a system with respect to the change in the number of molecules that are added to it. From Eq. (A6.18) we have

$$\mu^i(c) \equiv \frac{\partial g^i(c)}{\partial \rho^i_{\mathrm{CL}}} = -\kappa^i\left(c - c_0^i\right)A_{\mathrm{CL}}c^i_{\mathrm{CL}} + \frac{\left(\kappa^i\right)^2\left(c - c_0^i\right)^2}{2\kappa^{\mathrm{m}}_{\mathrm{EPC}}}\left(1 - \frac{\kappa^{\mathrm{m}}_{\mathrm{EPC}}}{\kappa^{\mathrm{m}}_{\mathrm{CL}}}\right)A_{\mathrm{CL}} + k_BT\left[\log\left(\frac{\rho^i_{\mathrm{CL}}A_{\mathrm{ref}}}{1-\rho^i_{\mathrm{CL}}A_{\mathrm{CL}}}\right) + 1 + \frac{\rho^i_{\mathrm{CL}}A_{\mathrm{CL}}}{1-\rho^i_{\mathrm{CL}}A_{\mathrm{CL}}}\right] + a\rho^i_{\mathrm{CL}}, \qquad i = +,- \tag{A6.24}$$

where the bending, entropic and interaction terms are written in blue, red, and green, respectively. The equilibrium condition in our system is given by [Eq. (A6.19)]

$$0 = \Delta\mu^i = \mu^i_{\mathrm{tube}} - \mu^i_{\mathrm{GUV}} = \left[\kappa^i_{\mathrm{tube}}\left(c - c^i_{0,\mathrm{tube}}\right) - \kappa^i_{\mathrm{GUV}}c^i_{0,\mathrm{GUV}}\right]A_{\mathrm{CL}}C^i_{\mathrm{CL}} + \left[\frac{\left(\kappa^i\right)^2\left(c - c^i_{0,\mathrm{tube}}\right)^2}{2\kappa^{\mathrm{m}}_{\mathrm{EPC}}} - \frac{\left(\kappa^i_{\mathrm{GUV}}\right)^2\left(c^i_{0,\mathrm{GUV}}\right)^2}{2\kappa^{\mathrm{m}}_{\mathrm{EPC}}}\right]\left(1 - \frac{\kappa^{\mathrm{m}}_{\mathrm{EPC}}}{\kappa^{\mathrm{m}}_{\mathrm{CL}}}\right)A_{\mathrm{CL}} + k_BT\left\{\log\left[\frac{\rho^i_{\mathrm{tube,CL}}\left(1-\rho^i_{\mathrm{GUV,CL}}A_{\mathrm{CL}}\right)}{\left(1-\rho^i_{\mathrm{tube,CL}}A_{\mathrm{CL}}\right)\rho^i_{\mathrm{GUV,CL}}}\right] + \frac{\rho^i_{\mathrm{tube,CL}}A_{\mathrm{CL}}}{1-\rho^i_{\mathrm{tube,CL}}A_{\mathrm{CL}}} - \frac{\rho^i_{\mathrm{GUV,CL}}A_{\mathrm{CL}}}{1-\rho^i_{\mathrm{GUV,CL}}A_{\mathrm{CL}}}\right\} + a\left(\rho^i_{\mathrm{tube,CL}} - \rho^i_{\mathrm{GUV,CL}}\right), \qquad i = +,-. \tag{A6.25}$$

A positive difference in Eq. (A6.25) ($\Delta\mu^i > 0$) implies a net flux of CL molecules from the tube to the GUV, decreasing sorting, while a negative difference ($\Delta\mu^i < 0$) implies a net flux of CL molecules from the GUV to the tube, increasing sorting. As we can see in Figure A6.5, CL molecules in the inner monolayer $i = +$, which bend the membrane in the direction of the imposed curvature, are enriched in the tube, while CL molecules in the outer monolayer $i = -$, which bend the membrane against the imposed curvature, are depleted from the tube. Then, we can write

$\Delta\mu^- > 0$ (outer monolayer) → net flux of CL from the tube to the GUV → sorting decrease. (A6.26a)

$\Delta\mu^+ < 0$ (inner monolayer) → net flux of CL from the GUV to the tube → sorting increase. (A6.26b)

Once the system is at equilibrium the net flux of both monolayers is zero. We can determine how bending, entropic, and interactive terms alter sorting by analyzing the sign of their corresponding chemical potential differences. Since the CL density in the outer monolayer of the tube $\rho^-_{\mathrm{tube,CL}}$ is much lower than that in inner monolayer $\rho^+_{\mathrm{tube,CL}}$ (see Figure 6.3 in Chapter 6), it is sufficient to evaluate these terms in the inner monolayer Eq. (A6.26b). Thus, we have to calculate the following expressions

$$\Delta\mu^+_{\mathrm{bend}} = \Delta\mu^+_{\mathrm{bend},c_0} + \Delta\mu^+_{\mathrm{bend},\kappa} = -\left[\kappa^+_{\mathrm{tube}}\left(c - c^+_{0,\mathrm{tube}}\right) + \kappa^+_{\mathrm{GUV}}c^+_{0,\mathrm{GUV}}\right]A_{\mathrm{CL}}c^+_{\mathrm{CL}} + \frac{(\kappa^+_{\mathrm{tube}})^2\left(c - c^+_{0,\mathrm{tube}}\right)^2 - (\kappa^+_{\mathrm{GUV}})^2\left(c^+_{0,\mathrm{GUV}}\right)^2}{2\kappa^{\mathrm{m}}_{\mathrm{EPC}}}\left(1 - \frac{\kappa^{\mathrm{m}}_{\mathrm{EPC}}}{\kappa^{\mathrm{m}}_{\mathrm{CL}}}\right)A_{\mathrm{CL}}, \tag{A6.27}$$

$$\Delta\mu^+_{\mathrm{ent}} = k_BT\left[\log\left[\frac{\rho^+_{\mathrm{tube,CL}}\left(1-\rho^+_{\mathrm{GUV,CL}}A_{\mathrm{CL}}\right)}{\left(1-\rho^+_{\mathrm{tube,CL}}A_{\mathrm{CL}}\right)\rho^+_{\mathrm{GUV,CL}}}\right] + \frac{\rho^+_{\mathrm{tube,CL}}A_{\mathrm{CL}}}{1-\rho^+_{\mathrm{tube,CL}}A_{\mathrm{CL}}} - \frac{\rho^+_{\mathrm{tube,CL}}A_{\mathrm{CL}}}{1-\rho^+_{\mathrm{GUV,CL}}A_{\mathrm{CL}}}\right], \tag{A6.28}$$

$$\Delta\mu^+_{\mathrm{int}} = a\left(\rho^+_{\mathrm{tube,CL}} - \rho^+_{\mathrm{GUV,CL}}\right), \tag{A6.29}$$

where the bending contribution to sorting has been separated into the spontaneous curvature contribution (written above in purple)

$$\Delta\mu^{+}_{\mathrm{bend},c_0} = \frac{\partial g^{+}_{\mathrm{bend}}}{\partial c_0^{+}} \frac{\partial c_0^{+}}{\partial \rho^{+}_{\mathrm{CL}}}, \tag{A6.30}$$

and the bending modulus contribution (written above in cyan)

$$\Delta\mu^{+}_{\mathrm{bend},\kappa} = \frac{\partial g^{+}_{\mathrm{bend}}}{\partial \kappa^{+}} \frac{\partial \kappa^{+}}{\partial \rho^{+}_{\mathrm{CL}}}. \tag{A6.31}$$

The chemical potential differences of these individual contributions as a function of CL density for a tube curvature of 0.1 $\mathrm{nm^{-1}}$ are shown in Figure A6.8. Curves fitting to the interacting uncouple model ($c_{\mathrm{CL}} = 1.10\ \mathrm{nm^{-1}}$ and $a = -18\ k_B T\ \mathrm{nm^2}$) are represented with solid lines while curves fitting to the non-interacting uncoupled model ($c_{\mathrm{CL}} = 1.12\ \mathrm{nm^{-1}}$ and $a = 0$) are represented with dashed lines. In both cases sorting is limited by the entropic term since $\Delta\mu^{+}_{\mathrm{ent}} > 0$ (red lines in Figure A6.8A). This is something expected since mixing entropy tends to homogenize the lipid distribution. The bending contribution to sorting is, however, quite different between the interacting and the non-interacting uncoupled models: when non-CL interaction is assumed, the bending term (blue dashed line in Figure A6.8A) contributes slightly to sorting ($\Delta\mu^{+}_{\mathrm{bend}} \lessapprox 0$) and this contribution diminishes as CL density increases. In contrast, when CL-CL attractive interactions are considered, the bending term enhances CL enrichment just for very low CL densities (up to the product $\rho_{\mathrm{GUV,CL}} \times A_{\mathrm{CL}}$ is approximately 0.1 in Figure A6.8A). Above this value, the bending term drives CL depletion. High CL accumulation in the tube minimizes its curvature frustration but increases its bending modulus ($\kappa_{\mathrm{CL}} > \kappa_{\mathrm{EPC}}$). The resulting CL enrichment is then enhanced by the spontaneous curvature term ($\Delta\mu^{+}_{\mathrm{bend},c_0} < 0$, purple line in Figure A6.8B) but limited by the stiffness penalty ($\Delta\mu^{+}_{\mathrm{bend},\kappa} > 0$, cyan line in Figure A6.8B). The interaction term (green solid line in Figure A6.8A) contributes to a strong CL enrichment ($\Delta\mu^{+}_{\mathrm{int}} < 0$) and then it is required to explain the observed data at high densities. Finally, $\Delta\mu^{+}_{\mathrm{total}} = 0$ (black line) since the calculations are made when the system is at equilibrium.

Additionally, Figure A6.9 shows the influence of the bending, entropic and interacting contributions to sorting as a function of tube curvature for very low (Figure A6.9A) and very high (Figure A6.9B) CL densities. At low CL densities, the influence of CL interaction (green solid line) is negligible, thereby there are no significant differences between the results of the non-interacting (dashed lines) and the interacting (solid lines) uncoupled models. Entropy drives CL depletion ($\Delta\mu^{+}_{\mathrm{ent}} > 0$) and bending contributes slightly to sorting ($\Delta\mu^{+}_{\mathrm{bend}} < 0$). In contrast, at high densities, there exist quite differences between the interacting and the non-interacting uncoupled models and CL-CL attractive interactions are essential to explain the observed data.

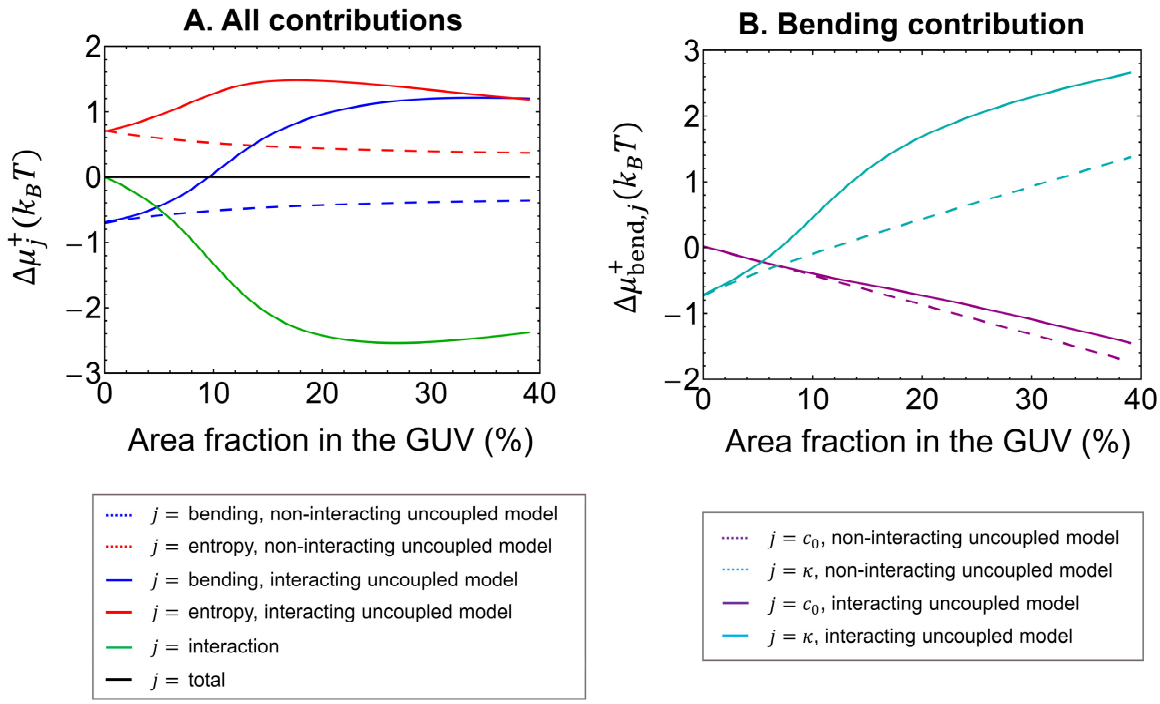

Figure A6.8. Bending, entropic, and interaction contributions to sorting as a function of area fraction in the GUV (in percent). In both interacting (solid lines) and non-interacting (dashed lines) uncoupled models, sorting is limited by the entropic term ($\Delta\mu_{\mathrm{ent}}^+ > 0$, red lines). The bending contribution to sorting is, however, quite different between the interacting and the non-interacting uncoupled models: when non-CL interaction is assumed, the bending term (blue dashed line) contributes slightly to sorting ($\Delta\mu_{\mathrm{bend}}^+ \lessapprox 0$) and this contribution diminishes as CL density increases. In contrast, when CL-CL interactions are considered, the bending term enhances CL enrichment just for very low CL densities (blue solid line). Above this value, the bending term drives CL depletion ($\Delta\mu_{\mathrm{bend}}^+ > 0$). The resulting bending contribution to sorting is enhanced by the spontaneous curvature term ($\Delta\mu_{\mathrm{bend},c_0}^+ < 0$, purple lines) but limited by the stiffness penalty ($\Delta\mu_{\mathrm{bend},\kappa}^+ > 0$, cyan lines). The interaction term (green solid line) drive strong CL enrichment ($\Delta\mu_{\mathrm{int}}^+ < 0$) and then it is required to explain the observed data at high densities. Finally, $\Delta\mu_{\mathrm{total}}^+ = 0$ (black line) since the system is at equilibrium. The computations are made with the following values: CL area $A_{\mathrm{CL}} = 1.3\ \mathrm{nm}^2$ [248], bending modulus of a pure CL bilayer $\kappa_{\mathrm{CL}}^{\mathrm{b}} = 26\ k_BT$ [248], bending modulus of a pure EPC bilayer $\kappa_{\mathrm{EPC}}^{\mathrm{b}} = 10\ k_BT$ [9], and tube curvature $c = 0.1\ \mathrm{nm}^{-1}$.

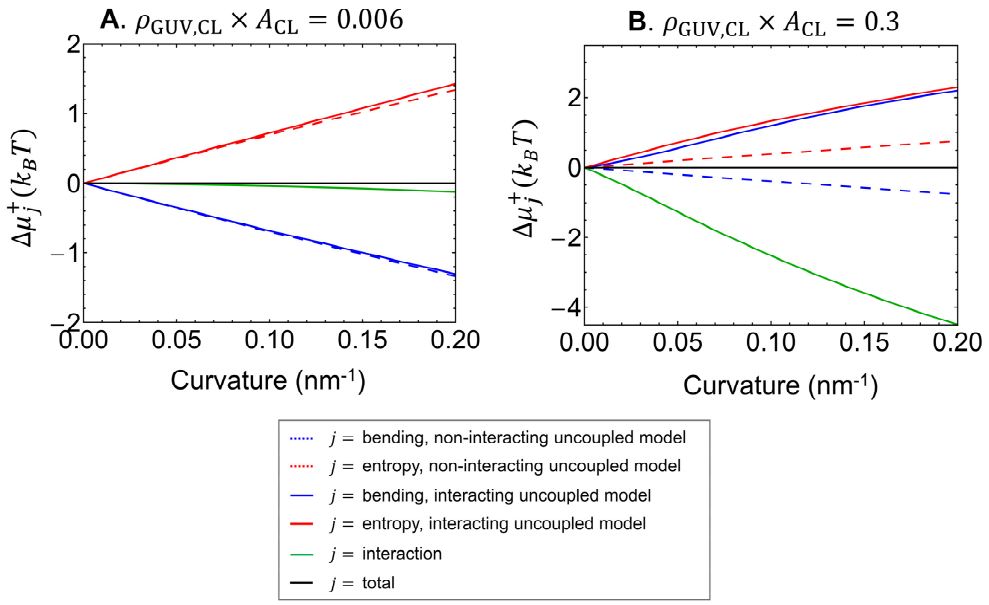

Figure A6.9. Bending, entropic, and interacting contributions to sorting as a function of curvature. At low CL densities (A) the influence of CL interaction (green solid line) is negligible, thereby there are no significant differences between the results of the non-interacting (dashed lines) and the interacting (solid lines) models. Entropy drives CL depletion ($\Delta\mu^+_{\text{ent}} > 0$) and bending contributes slightly to sorting ($\Delta\mu^+_{\text{bend}} < 0$). In contrast, at high densities (B), there exist quite differences between the interacting and the non-interacting uncoupled models and CL-CL attractive interactions are essential to explain the observed data. The computations are made with the following values: CL area $A_{\text{CL}} = 1.3$ nm^2 [248], EPC lipid area $A_{\text{EPC}} = 0.675$ nm^2 [254], bending modulus of a pure CL bilayer $\kappa^{\text{b}}_{\text{CL}} = 26\ k_BT$ [248], bending modulus of a pure EPC bilayer $\kappa^{\text{b}}_{\text{EPC}} = 10\ k_BT$ [9].

A6.5.2 Membrane with Coupled Monolayers

Previous sections analyze the sorting model when both membrane monolayers are assumed to be uncoupled and therefore the bending energy of the bilayer can be written as the sum of the bending energies of the monolayers [Eq. (A6.20)]. In order to get insight about the coupled/uncoupled behavior of the membrane, we have also performed the fit to a membrane model with monolayer coupling in the bending energy, specifically, in the bending modulus. In this case, the bending energy of the bilayer is

$$g^{\text{b}}_{\text{bend}}(c) = \frac{1}{2}\kappa^{\text{b}}\left(c - c^{\text{b}}_0\right)^2. \tag{A6.32}$$

As in the uncoupled case, the bilayer spontaneous curvature is, in a simple approach, proportional to the differences in the CL content in the two monolayers [9]

$$c^{\text{b}}_0 = A_{\text{CL}}(c^+_{\text{CL}}\rho^+_{\text{CL}} + c^-_{\text{CL}}\rho^-_{\text{CL}}) = A_{\text{CL}}|c_{\text{CL}}|(\rho^+_{\text{CL}} - \rho^-_{\text{CL}}). \tag{A6.33}$$

However, unlike the uncoupled case, the bending modulus of a coupled membrane can be obtained as

$$\kappa^{\text{b}} = \frac{\kappa^{\text{b}}_{\text{EPC}}}{1 - \left(1 - \kappa^{\text{b}}_{\text{EPC}}/\kappa^{\text{b}}_{\text{CL}}\right)A_{\text{CL}}\left(\rho^+_{\text{CL}} - \rho^-_{\text{CL}}\right)}. \tag{A6.34}$$

The mixing energy of the bilayer [Eq. (A6.10)] is the same in both uncoupled and coupled model since we are neglecting the transbilayer CL motion and the interaction between monolayers. In other words, we are considering that CL molecules can only mix and interact within their monolayer. The rest of equations written in Section A6.2.1 for the uncoupled model are also valid here replacing the monolayer spontaneous curvature [Eq. (A6.12)] and the monolayer bending modulus [Eq. (A6.14)] by the bilayer ones [Eqs. (A6.33) and (A6.34), respectively]. Now, instead of having two independent equations [Eq. (A6.19)] ($i = +$ which gives $\rho^{+}_{\text{tube,CL}}$ and $i = -$ which gives $\rho^{-}_{\text{tube,CL}}$) we have two coupled equations with two parameters $\rho^{+}_{\text{tube,CL}}$ and $\rho^{-}_{\text{tube,CL}}$.

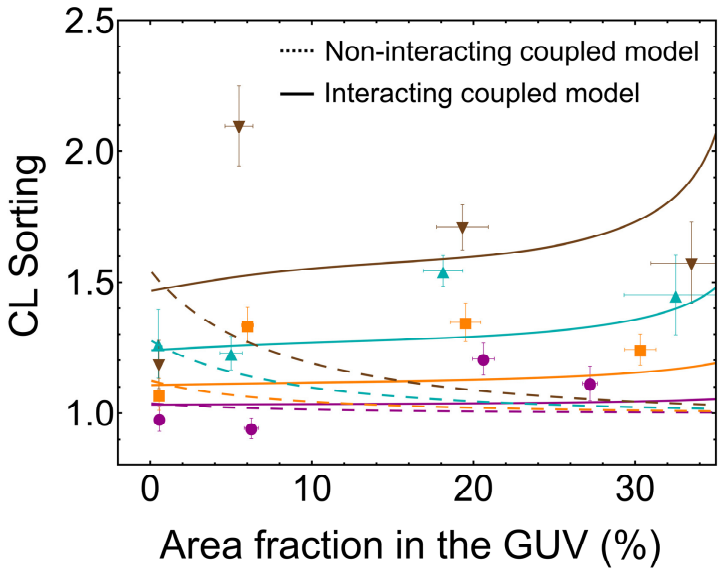

Figure A6.10. CL enrichment as a function of CL density in GUVs according to the coupled model. CL sorting as a function of the area fraction $\rho_{\text{GUV,CL}} \times A_{\text{CL}}$ (in percent) for four ranges of tube curvature: ▼ very high (0.1287 ± 0.0012) nm^{-1} in brown; ▲ high (0.0926 ± 0.008) nm^{-1} in cyan; ■ low (0.062 ± 0.01) nm^{-1} in orange; and ● very low (0.034 ± 0.009) nm^{-1} in purple. The points are the arithmetic means of binned CL GUV densities and sorting ratios, and the error bars represent the corresponding standard deviations. Dashed lines represent the minimum square fit to the non-interacting coupled model (*i.e.*, in the absence of binary interactions between CL molecules, interacting parameter $a = 0$), which gives a CL intrinsic curvature of $c_{\text{CL}} = 0.7 \pm 0.2$ nm^{-1}. Solid lines represent the minimum square fit to the interacting coupled model (*i.e.,* assuming possible CL-CL interactions with the free interacting parameter a) is represented with solid lines and gives $c_{\text{CL}} = 0.6 \pm 0.1$ nm^{-1} and $a = -9.4 \pm 0.4\ k_BT$ nm^2. The computations are made with the following values: CL area $A_{\text{CL}} = 1.3$ nm^2 [248], bending modulus of a pure CL bilayer $\kappa_{\text{CL}} = 26\ k_BT$ [248], and bending modulus of a pure EPC bilayer $\kappa_{\text{EPC}} = 10\ k_BT$ [9].

Although the coupled model also predicts high sorting at high CL densities when we assume CL-CL interactions (solid lines of Figure A6.10), it does not reproduce our experimental data at high curvatures (brown solid line of Figure A6.10). The minimum square fit to the coupled model in the absence of binary interactions between CL molecules (*i.e.,* interacting parameter $a = 0$) is represented in Figure A6.10 with dashed lines and gives an intrinsic curvature of CL of $c_{\text{CL}} = 0.7 \pm 0.2$ nm^{-1}. The minimum square fit to the coupled model possible CL-CL interactions is represented in Figure A6.6 with solid lines and gives $c_{\text{CL}} = 0.6 \pm 0.1$ nm^{-1} and $a = -9.4 \pm 0.4\ k_BT$ nm^2. By comparing the uncoupled (Figure 6.2 in Chapter 6) and coupled results, it appears that the EPC/CL bilayers do not have significant coupling in bending modulus, thereby

both monolayers can be treated as independent systems, like occurs in other lipid bilayers in the absence of significantly flip-flopping lipids [255].

PART IV

Phytoplankton Size Scaling

Chapter 7

Phytoplankton Size Scaling with Nutrient Concentration

Chapter based on Beltran-Heredia E, Aksnes DL, & Cao FJ (2017) Phytoplankton size scaling with nutrient concentration. *Mar Ecol Prog Ser* 571: 59-64.

Phytoplankton, the autotrophic component of the plankton community, is a key factor in oceanic ecosystems and in biogeochemical cycling. Over much of the ocean, phytoplankton growth is limited by nitrogen uptake (as nitrate), which is commonly described in ecosystem modelling by the Michaelis-Menten equation: $V = V_{max}S/(K + S)$. Previous phytoplankton data compilations have shown that the maximum uptake rate, V_{max}, and the half-saturation constant, K, increase with organism size. Independent studies have also reported that K increases with nitrate concentration, S. In this chapter, we assume that this K increase with S is due to an increase in the dominant organism size in the phytoplankton community with increasing nutrient concentration. Previous studies support this assumption, showing that nitrate abundance is the main factor determining dominant organism size. Based on this assumption and on previously published experimental observations for K, we show that phytoplankton dominant size, r, scales approximately with $S^{0.85}$. This increase in dominant size can also entail size-related changes in traits (such as the number of porters) that impact K and V_{max}. Furthermore, by combining a trait-based uptake model with the experimental results of K and V_{max}, we derive scaling relations for the number of porters and the handling time in terms of r. Our results indicate that handling time decreases approximately with $r^{-0.90}$ while porter number increases approximately with $r^{1.56}$. These results may be useful in characterizing size dependent nutrient uptake in marine ecosystems and biogeochemical cycling models.

7.1 Introduction

As we introduced in Chapter 3, the Michaelis-Menten (MM) model remains the dominant paradigm for describing uptake rate V, as a function of the environmental nutrient concentration S, in experiments and modelling [117, 127]. This model is expressed as $V = V_{max}\, S/(K + S)$, where V_{max} is the maximal uptake rate and K the half-saturation constant, which corresponds to the concentration when the uptake rate is $V_{max}/2$. The MM model is simple, and measurements of the two coefficients are widely available in the literature. However, it is commonly used as a pure empirical description that provides no theoretical predictions on how

the kinetic parameters scale with inherent microbial traits (cell size, number of transporters [or porters], handling time and porter size) and environmental variables (temperature and nutrient concentration with its diffusion coefficient). Such relations are commonly required in ecological modeling. Theoretical trait-based models [104, 106, 109, 111] do provide such scaling relations. A challenge to the verification of these theoretical models is that they contain traits that are not commonly measured. These traits include the number of porters, a key property of models where nutrient molecules are assumed to be actively transported through porters at the cell membrane [106, 109, 111], and handling time, which corresponds to the time period during which a porter is occupied because it is handling an encountered nutrient molecule. However, a convenient property of these theoretical models is that measured variables like V_{max} and K can be expressed as functions of the unmeasured microbial traits, which facilitates indirect estimation of these parameters. It has been shown experimentally that the maximum uptake rate and half-saturation coefficient increase with phytoplankton size [107, 110, 117, 256], see Figure 3.7A-B in Chapter 3. The half-saturation coefficient has also been shown to increase with the ambient nutrient concentration of nitrate [118–120, 127], see Figure 3.7C in Chapter 3. In this chapter, we combine these experimental data from the literature to obtain the scaling relationship of the dominant organism size with nutrient concentration. Additionally, using the theoretical model of Aksnes and Cao described in Section 3.2.2 of Chapter 3, we extract several empirical relationships that determine how microbial traits (such as number of porters and handling time) are expected to vary with organism size and nutrient supply regime. Our results provide simple parameterizations that might be useful in biogeochemical models, but are also likely to encourage future direct measurements of inherent traits, such as the number of nutrient uptake porters and their handling times.

7.2 Methods

7.2.1 Use of Experimental Observations from Previous Studies

Here, we have used results and observations reported in Refs. [117, 127]. Edwards et al. [117] compiled trait data from published studies and estimated the scaling relations between the parameters of the MM model and phytoplankton volume measured for nitrate and phosphate in both freshwater and marine species. They used studies in which temperature was at or near 20°C and light was not severely limiting. In order to quantify the scaling relations between the nutrient traits and phytoplankton volume, they applied standardized major axis (SMA) regression. The results for marine species with nitrate as the limiting nutrient [117] are (see Figure 3.7 in Chapter 3):

$$K(\log_{10}\,\mu\text{m l}^{-1}) = 0.33\ (0.24,0.45) \times \text{Vol}(\log_{10}\,\mu\text{m}^3) - 0.84\ (0.44,1.20), \tag{7.1}$$

and

$$V_{max}(\log_{10}\,\mu\text{mol day}^{-1}) = 0.82\ (0.65,1.00) \times \text{Vol}(\log_{10}\,\mu\text{m}^3) - 8.1\ (7.5,8.8), \tag{7.2}$$

where K and V_{max} are, respectively, the half-saturation constant and the maximal uptake rate at which the dominant organism's volume is Vol. The values in parentheses represent the 95% confidence intervals of each parameter. The above scalings are also compatible with the data of Lomas et al. [107] (their Figure 2); our SMA fit to their data gives slopes of 0.34 (0.18, 0.51) and 1.09 (0.56, 1.61) for K and V_{max}, respectively. Litchman et al [256] also reported compatible slope

values of 0.27 (0.20, 0.36) and 0.67 (0.53, 0.84) for K and V_{max}, respectively. Written as power laws in terms of the dominant organism radius r in the units we use, Eqs. (7.1) and (7.2) become

$$K(\text{molecules } \mu m^{-3}) = 140\, r^{0.99}, \tag{7.3}$$

and

$$V_{max}(\text{molecules } s^{-1}) = 1.79 \times 10^{5}\, r^{2.46}, \tag{7.4}$$

where the conversion factors $\text{Vol} = 4\pi r^3/3$, 1 µm l^{-1} = 602 molecules μm^{-3} and 1 µmol day^{-1} = 6.97×10^{12} molecules s^{-1} were used. Smith et al. [127] collected K values that were measured for natural communities in various shipboard incubation studies from a wide variety of ocean regions [118–120]. These data are shown in Figure 3.7C in Chapter 3. They showed that incorporation of a physiological trade-off between maximum uptake rate and affinity [103, 257] into the model of Aksnes and Cao [106] might explain the increasing trend of the half-saturation constant with ambient nitrate concentration and its range of variation for typical phytoplankton sizes in the ocean. Fitting the collected with SMA (Standardized Major Axis) regression, the following scaling relation is obtained (see Figure 7.1):

$$K(\log_{10} \mu m\ l^{-1}) = 0.84 \times S\ (\log_{10} \mu m\ l^{-1}) + 0.27. \tag{7.5}$$

Written as power law in the units applied in our study, it becomes:

$$K(\text{molecules } \mu m^{-3}) = 5.18\, S^{0.84}\ (\text{molecules } \mu m^{-3}), \tag{7.6}$$

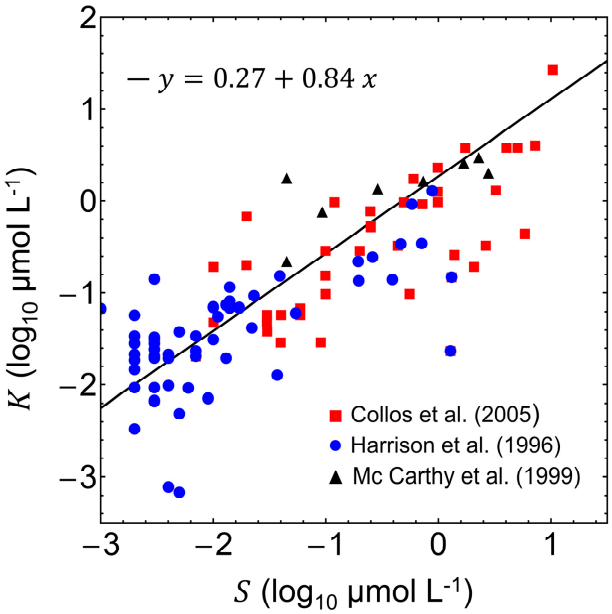

Figure 7.1. Compilation of half-saturation values K as a function of nutrient concentration S (adapted from Figure 2B in Ref. [127]) observed for natural communities from a wide variety of marine environments [118–120] and our fit using Standardized Major Axis (SMA) regression.

Small phytoplankton species tend to dominate in low-nutrient regions of the ocean, whereas large species tend to thrive in nutrient-rich waters [121–125, 127]. In addition, Acevedo-Trejos et al. [126] showed that nutrient concentration is the main factor determining phytoplankton community size structure. The relationship in Eq. (7.6) is then expected to be affected by this correlation between dominant organism size and nutrient supply regime. In the present study,

we have assumed that the observed increase of K with nutrient concentration is due to the larger sizes of phytoplankton present at higher nutrient concentrations (this larger phytoplankton size may also entail the change of other traits that affect K and $V_{\max}$.) Thus, we combined the empirical relations for the half saturation as a function of size and nutrient concentration [Eqs. (7.3) and (7.6)] in order to express phytoplankton dominant size as a function of the ambient nitrate concentration in the ocean.

7.2.2 Trait Model of an Individual Organism

As previously described in Section 3.2.2, the trait-based model proposed by Aksnes and Cao [106] gives the nutrient uptake rate of an idealized spherical and non-swimming organism as

$$V = \frac{b}{2a}\left(1 - \sqrt{1 - \frac{4a}{b^2}}\right), \tag{7.7}$$

with

$$a = \frac{h}{4\pi DrSn}\left(1 - \frac{\pi rp}{ns}\right), \qquad b = \frac{1}{\alpha S} + \frac{h}{n}, \qquad \alpha = 4\pi Dr\frac{ns}{ns + \pi r(1-p)},$$

and $p = ns^2/4r^2$, and where the handling time, h, is the time interval required to process one nutrient by one porter; during this time interval the porter is blocked and unable to absorb additional nutrients. D is the diffusivity of nutrient particles in the extracellular medium, S is the bulk nutrient particle concentration, r is the radius of the individual organism, s is the effective porter radius, n is the number of uptake porters in the surface, α is the uptake affinity (*i.e.,* $\alpha = \lim_{S\to 0} V/S$) and p is the porter density (*i.e.,* the fraction of the sphere's surface covered by porters). This model is not of MM type but it can be written as an approximated MM functional form (see also Ref. [109]), with

$$V_{\max} = \lim_{S\to\infty} V = \frac{n}{h}, \qquad K = \frac{\pi r(2-p) + ns}{8h\pi Drs}. \tag{7.8}$$

The error of this MM approximation diminishes for low porter densities, *i.e.,* when $ns^2 \ll 4r^2$, and particularly when the stronger condition $ns \ll \pi r$ holds [106]. This individual trait-based model gives $V_{\max}$ and K for an organism of radius r, with n porters and handling time h. Organisms may, in principle, present any combination of these three traits. However, the fitness of an organism in a given nutrient concentration determines its optimal size, together with the optimal number of porters and optimal handling time for this size. Thus, the dominant organism at a given nutrient concentration would be expected to present optimal trait values for that nutrient concentration. The optimal radius at a given nutrient concentration defines the dominant organism radius r at this concentration. Hereafter nutrient concentration S is specifically nitrate concentration.

7.3 Results

7.3.1 Relationship between Cell Size and Ambient Nutrient Concentration

Previous phytoplankton data compilations have shown that K increases with both dominant radius, r, and nitrate concentration, S. Previous studies [122, 126] have shown that the distribution of phytoplankton community size structure is mainly influenced by S, especially in eutrophic regimes (in oligotrophic conditions the temperature has also a structuring impact). Consequently, we here assume that the increase in K with S is mainly due to an increase in r (of the phytoplankton community) with increasing nutrient concentration. This allows us to combine the empirical Eqs. (7.3) and (7.6), obtaining that r scales approximately with S, as

$$r(\mu\text{m}) = 8.20\, S^{0.85}(\mu\text{mol l}^{-1}), \tag{7.9}$$

or, equivalently, $r(\mu\text{m}) = 0.036\, S^{0.85}(\text{molecules } \mu\text{m}^{-3})$. This equation gives the expected dominant phytoplankton size for a given S (see Figure 7.2). This increase in the dominant size entails size-related changes in other traits (such as n and h) that impact K and $V_{\max}$. If we invert Eq. (7.9), we obtain the nutrient concentration S, at which the dominant size is r

$$S(\mu\text{mol l}^{-1}) = 0.082\, r^{1.18}(\mu\text{m}), \tag{7.10}$$

or, equivalently, $S(\text{molecules } \mu\text{m}^{-3}) = 50\, r^{1.18}(\mu\text{m})$.

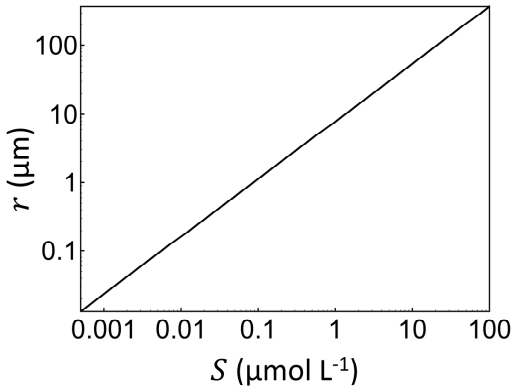

Figure 7.2. Dominant phytoplankton size r as a function of nutrient concentration, S [see Eq. (7.9)].

7.3.2 Estimates of Scaling Relationships of Handling Time and Porter Number as a Function of Dominant Size

Previous Eq. (7.8) relates h and n (inherent traits) on the one hand with $V_{\max}$ and, on the other hand, with K (apparent traits). The observed scaling of $V_{\max}(r)$ and $K(r)$, with the dominant size r, is given by Eqs. (7.3) and (7.4). Therefore, by inverting Eq. (7.8) we can estimate the relationship between handling time h (or porter number n) and r by

$$h = \frac{8\pi r^2}{s(32\pi D r^2 K - 4 r V_{\max} + \pi s V_{\max})}, \tag{7.11}$$

and

$$n = V_{\max} h \tag{7.12}$$

From these equations, we get $h(r)$ and $n(r)$ by insertion of the empirical relations from Edwards et al. [117] for $K(r)$ and $V_{\max}(r)$ [Eqs. (7.3) and (7.4)], a nutrient diffusion coefficient of $D = 1000$ μm²s⁻¹ [258] and $s = 0.01$ μm [112]. For these values we see that the denominator of Eq. (7.11) can be approximated by $32\pi sDr^2K$, and then

$$h \approx \frac{1}{4sDK}, \qquad n \approx \frac{V_{\max}}{4sDK}. \tag{7.13}$$

These formulas lead to the approximate scalings

$$h(\mathrm{s}^{-1}) \approx 1.78 \times 10^{-3} r^{-0.99} (\mu\mathrm{m}), \tag{7.14}$$

and

$$n \approx 320\, r^{1.47} (\mu\mathrm{m}). \tag{7.15}$$

Alternatively, we can fit power laws to the exact formulas [Eqs. (7.11) and (7.12)], obtaining

$$h(\mathrm{s}^{-1}) = 1.90 \times 10^{-3} r^{-0.90} (\mu\mathrm{m}), \tag{7.16}$$

and

$$n = 338\, r^{1.56} (\mu\mathrm{m}). \tag{7.17}$$

These relations indicate that h decreases while n increases with r (Figure 7.3). Replacing in Eq. (7.17) the scaling behavior $r(S)$ given by Eq. (7.9) provides an estimate of the average porter number for different ambient nitrate concentrations as

$$n = 1.89\, S^{1.32} (\text{molecules } \mu\mathrm{m}^{-3}). \tag{7.17}$$

Eq. (7.17) implies $p = ns^2/4r^2 \sim r^{-0.44}$. This result, obtained from the experimental data compilation in Refs. [117, 127], is consistent with Lindemann et al. [259], who report a downward trend in p with r when all data points in their analysis were included (their Figure 3).

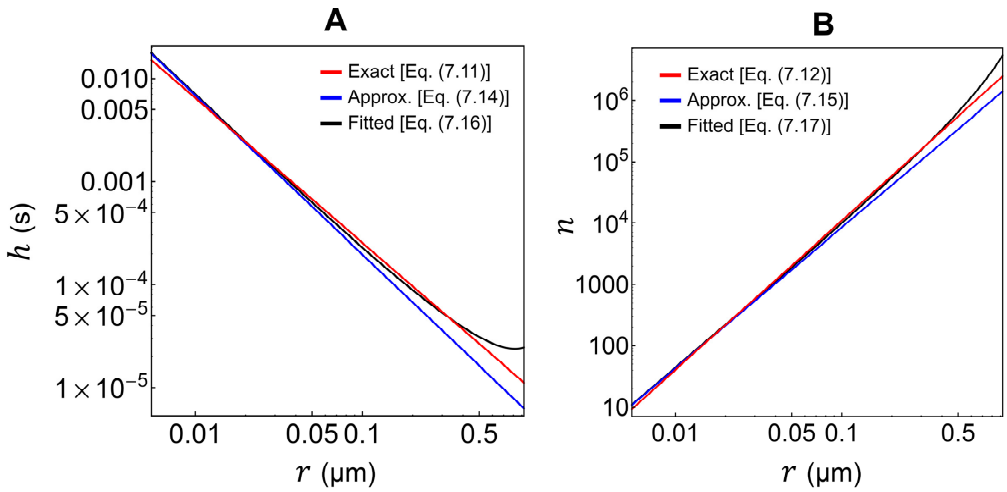

Figure 7.3. (A) Handling time, h, and (B) porter number, n, as a function of dominant phytoplankton size r obtained by combining the empirical scaling of the half-saturation constant, K [Eq. (7.3)] and the maximal uptake rate, $V_{\max}$ [Eq. (7.4)] with the trait-based model proposed by Aksnes and Cao [106] [Eq. (7.7)]. Black lines: exact results from Eqs. (7.11) and (7.12), respectively for h and n; blue lines: approximated results from Eq. (7.13) giving, respectively for h and n, the Eqs. (7.14) and (7.15); red: approximated power law fits of Eqs. (7.16) and (7.17), respectively for h and n.

7.4 Discussion

The experimental datasets from different oceanic regions measured by Collos et al. [120], Harrison et al. [118] and McCarthy et al. [119], and collected by Smith et al. [103, 127], show an increase in half saturation constant K with an increase in ambient S. Additionally, as pointed out by Smith et al. [127], previous studies have indicated that natural assemblages tend to have larger (smaller) cell sizes at higher (lower) ambient S [121–126]. They also indicate that larger cells tend to have greater K [117, 127, 256]. Acevedo-Trejos et al. [126] showed that S is the main factor de termining the size structure of phytoplankton community in the ocean while temperature only has an impact under low-nutrient conditions (within the range of conditions present in the ocean) [122]. Based on these observations, it might be assumed that the observed relationship between K and S would emerge from the scaling between phytoplankton size and nutrient supply regime. Under this assumption, using the scaling relation of K versus r we have obtained a relationship that predicts r as a function of S [Eq. (7.9)]. It is important to note that this does not mean that size is the only relevant trait, as other traits (such as p) may change with size. The r predicted by Eq. (7.9) as a function of S is in agreement with experimental observations [126, 260]. For example, S at around 0.1 μmol l^{-1}, as in low-nutrient regions of the ocean, indicate smaller phytoplankton with r of the order of 1 μm. S ranging from 1 to 10 μmol l^{-1}, as in the medium and nutrient-rich regions in the ocean, suggest r of the range 8 to 60 μm. Future experimental observations of r versus S in the ocean would be useful to further tests of the predicted relationship between r and S.

We also derived the dominant size dependence of two traits (p and h for the dominant organisms) in the Aksnes and Cao model [106]. We estimated the scaling of h with r from the experimental data of Refs. [117, 127]. The handling time is predicted to decrease with size according to $h \sim r^{-0.90}$, implying that larger organisms have shorter h. This result is approximately consistent with the size dependency of the h, *i.e.,* $h \sim r^{-1}$, assumed by Smith et al. [127] to give a good fit to experimental data. Smith et al. [127] showed that incorporation of a physiological trade-off between V_{max} and affinity [127, 257] into the model of Aksnes and Cao [106] might explain the increasing trend of K for nitrate uptake with ambient S and its range of variation as measured by shipboard experiments in the ocean. Smith et al. [127] also assumed that n increased with the square of the phytoplankton dominant size, $n \sim r^2$, which implies a constant p with increasing r. As shown above, our results imply a decreasing p, *i.e.,* $p = ns^2/4r^2 \sim r^{-0.44}$, which is consistent with Lindemann et al. [259]. It should be noted that our results for $n(r)$ and $h(r)$ are not assumptions. They are derived from observed V_{max} and K scaling with r from the observations reported in Refs. [117, 127].

It should be noted that the dependences of K and V_{max} on r are led by indirect contributions through dependences of n and h on r. From Eq. (7.8), we see that organism size modifies V_{max} only indirectly, through the changes it implies in n and h. In Eq. (7.8), we see that size changes both directly and indirectly the value of K. In addition, using in Eq. (7.8) the size scaling of n obtained in Eq. (7.17), it can be shown that, for medium and large phytoplankton sizes, the contribution of the size dependence on n in the numerator is of the same order or greater than the direct contribution of r. This is consistent with the hypothesis, suggested by Collos et al.[120], that increasing n could be a mechanism to increase K in high ambient S. It is intriguing that, according to our analysis, phytoplankton h decreases approximately proportional to the

inverse of the organism radius, *i.e.,* $h \sim r^{-1}$. It might be hypothesized that the arrival of an enzyme is the rate-limiting process of the reset of the porter after capture of a nutrient. In that case, h is inversely proportional to the enzyme collision rate, and it seems reasonable to assume that the collision rate of the enzymes with the porter is proportional to the enzyme density. Thus, enzyme density, ρ_e, will be proportional to the inverse of the handling time, $\rho_e \sim 1/h \sim r$ (*i.e.,* enzyme density will grow proportionally to phytoplankton size $\sim r$). If the enzyme and porter encounter is mainly a surface process, the relevant enzyme density would be a surface density $\rho_e = N_e/r^2$, implying a growth of the number of enzymes $N_e \sim r^3$ (*i.e.,* proportional to the organism volume). Whereas if enzyme and porter encounter is a volume rather than a surface process, the relevant enzyme density would be a volume density $\rho_e = N_e/r^2$, implying an increase in the number of enzymes proportional to r^4 (*i.e.,* faster than the organism volume increase).

By using nutrient uptake theory in combination with MM experimental results, our study aimed at increasing understanding of how empirical scaling relations in phytoplankton nutrient uptake connect with inherent phytoplankton traits. Although classical MM uptake experiments are useful, further insight into the role of porter dynamics in phytoplankton nutrient uptake and growth will require actual experimental measurements of the p, their h, and processes involved in h. The results presented here and the experimental measurements proposed could be used to improve current biogeochemical models, which specifically account for atmospheric carbon dioxide abundance and fixation.

Acknowledgments

We acknowledge S. Lan Smith and John L. Nevins for providing us with the experimental data included in Figure 7.1, which they published in Smith et al. [127] and McCarthy et al. [119]. We also acknowledge A. Martiny for providing us with the experimental data published in Lomas et al. [107] and included in their Figure 2D. We thank Emilio Marañon for comments on dominant phytoplankton size at different nutrient concentrations. D.L.A., E.B.-H., and F.J.C. acknowledge EEA grant 005-ABEL-CM-2014A, which provided the main funding for this collaboration. Additionally, E.B.-H. acknowledges financial support from FPU grant 13/02826 (Ministerio de Educación, Cultura y Deporte, Spain) and F.J.C. acknowledges financial support from grants GR35/14-920911 (Banco Santander and Universidad Complutense de Madrid, Spain), and FIS2010-17440 and FIS2015-67745-R (Ministerio de Economía y Competitividad, Spain).

PART V

Discussion, Conclusions, and Future Work

Discussion, Conclusions, and Future Work

Cell membranes are highly curved during key cellular processes, such as cytokinesis, membrane trafficking, or cell motion. The importance of curvature as a structural feature of biological membranes has been recognized for many years and has fascinated scientists from a wide range of different backgrounds. Changes in membrane morphology are involved in a large amount of phenomena involving the plasma membrane of eukaryotic cells, including cell division, endo- and exocytosis, and phagocytosis. Furthermore, a multitude of intracellular processes at the level of organelles rely on generation, modulation, and maintenance of membrane curvature to maintain the organelle shape and functionality. In this thesis, we have addressed the study of two cellular processes in which the effect of membrane curvature plays a crucial role. On the one hand, we have developed a theoretical approach to the mechanics of cell constriction during division that combines analytical and numerical methods and a discussion of their implications (see Part II). On the other hand, we have studied, both experimental and theoretically, an open problem on lipid sorting: whether cardiolipin molecules are sorted (or not) by the effect of the membrane curvature (see Part III).

Cells of a given type usually maintain a characteristic dominant "convenient" size that is suited for their ecological or organismic context. Because cells are the primary unit of life, understanding mechanisms controlling their growth and proliferation is relevant across multiple scales and levels of organization. In this thesis, we have analyzed the effect of the dominant cell size on phytoplankton traits and how this size depends on the nutrient concentration in the ocean (see Part IV).

Our works help clarify central processes in biology and contribute to a better understanding of the physical mechanisms by which cells duplicate, organize, and growth. We have successfully achieved the objectives described in the introduction and summarized at the beginning of the thesis. An integrative discussion of the results is presented below. After that, we expose the main conclusions of the thesis concluding with some open questions and possible future work.

Discussion

The primary goal about the physics of cell division was to study the mechanical problem of a membrane vesicle stressed under equatorial constriction in the frame of the Canham-Helfrich Hamiltonian. This is a crucial problem of bioenergetics, whose solution should inform us about the amount of mechanical energy necessary to duplicate cell contents in a stable way. Independently of the details of the constriction engine, the membrane components respond against deformation by minimizing the elastic energy at every constriction state following a pathway still unknown. In Chapters 3 and 4 of Part II we have developed a procedure to find the

optimal cell shapes along the constriction pathway as well as approximate analytical expressions for the more relevant properties involved in the constriction process of a vesicle (or simplified cell) in terms of the cell size, the spontaneous curvature of the membrane, the membrane tension, and the pressure difference between external and internal environments. These properties include the energy of the vesicle, its membrane area, its volume enclosed, and the constriction and stabilization forces along the constriction pathway. Our results have shown that cell constriction is, in general, a non-spontaneous process that requires to be initiated by a constriction apparatus that stresses a radial force at the site of division. As expected from a dimensional argument, constriction forces with an amplitude of the order of κ_b/R_m are predicted, where κ_b is the membrane bending modulus and R_m the radius of the cell (≈ 10 μm). The constriction force scales inversely proportional to R_m, *i.e.*, smaller cells are harder to constrict. Cells with flexible membranes ($\kappa_b \approx 10 - 20\ k_BT$) require an initial force in the range $0.1 - 1$ pN, which is the range of forces practicable by molecular motors. The instability of symmetrical constriction is shown and quantified with a characteristic coefficient of the order of $-k_BT$ at the beginning of constriction, thus evidencing that cells need an external mechanism to stabilize constriction at midcell. We have found that the stabilization force scales inversely proportional to R_m^2, *i.e.*, smaller cells are more unstable against lateral displacements of the constriction ring. The stabilization forces required are also in the range of the picoNewton. Our results have shown that the spontaneous curvature of the membrane C_0 has an important effect on the force required for constriction and cells whose membranes tend to build up in a convex prolate configuration (*e.g.*, cylinderlike bacteria) are the most easily constricted. The more interesting results of this part are those corresponding to the conditions under which division becomes spontaneous and stable against lateral asymmetries. Amazingly, once the symmetric constriction is initiated, it is shown to progress spontaneously for spontaneous curvatures above a threshold determined by the cell size.

The constriction pathway proposed in this thesis constitutes a minimal model of symmetrical division of a homogeneous membrane vesicle (or simplified cell). Thus, it is expected to represent the simple mechanism of cell division in primordial protocells to undergo spontaneous division without a specific cytokinetic machinery. Despite the inherent simplicity, our analysis is very useful to understand the physical paths of divisional constriction in living cells and to guide the design of artificial divisomes in self-actuated microsystems. Other biological processes involving membrane bending (such as exocytosis and endocytosis) can also benefit from the insight provided by these results and this method.

The theory for the mechanics of cell division developed in this thesis could also be applied to other axisymmetric shapes observed experimentally, such as stomatocytes, pearlikes, dummbells, discocytes, ... For cell division inside a cell tissue, cell geometries away from spheroids are found, and one must consider the interacting forces between neighboring cells and how these forces change the cell shapes. This study can also be generalized to non-axisymmetric shapes, as well as for multicomponent membrane composition (for a review of useful methods to extend the study see Ref. [71]). Although our model assumes a homogeneous spontaneous curvature, recall that, in general, C_0 is not uniform over the membrane of a real cell. This homogeneous scenario could be greatly improved in vesicles (or cells) with asymmetric membranes. Since the constriction site is saddle-shaped, an accumulation of conical lipids in the constriction region would contribute to minimize the local bending energy of the membrane

(see Figure 4.9). There is experimental evidence about the possible mechanical role of negative curvature lipids (such as phosphatidylethanolamine and cardiolipin) during late constriction [12, 15, 167, 172–174]. Therefore, any realistic model of cell division should consider local negative values of the spontaneous curvature in the constriction site of the cell membrane.

Previous paragraph describes how lipid distribution can shape the membrane. It has been proposed that the reverse is also true, *i.e.*, that membrane shape can influence its lipid distribution. Because the bending energy depends on the membrane properties, such as spontaneous curvature and bending rigidity, and because these properties depend on membrane composition, a coupling between lipid composition and curvature might reduce the bending energy. In other words, when a uniformly mixed membrane is subject to inhomogeneous curvature, the bending energy could be reduced provided by an inhomogeneous lipid distribution. This phenomenon was also addressed in this thesis with cardiolipin (CL), a cone-shaped lipid observed at high concentration in specific membrane sites with high curvature (poles and constriction site of dividing bacteria and folds of the inner mitochondrial membrane). Despite a few evidences in the literature suggesting that CL concentrates in negatively curved regions of those membranes *in vivo*, no definitive evidence of curvature induced CL-sorting is available from controlled experiments performed *in vitro*. In this thesis, we have explored the curvature-based CL sorting using the experimental set-up of P. Bassereau (Paris, France). The procedure was based on pulling membrane nanotubes from Giant Unilamellar Vesicles (GUVs) aspirated in a micropipette following the technique deeply described in Chapter 2 of this thesis. We used GUVs made of the homogeneous mixture EPC/CL at different CL contents. Our *in vitro* measurements confirm that CL molecules are prone to accumulate in curved zones of the membrane based on their shape alone, with a higher enrichment in highly curved membranes. This provides experimental evidence for the initial hypothesis that the CL spatial preference is a consequence of geometric and physical constraints of the membrane. Our data are compatible with a model based on membrane elasticity and non-ideal solution theory, from which an intrinsic curvature of 1.10 nm^{-1} is predicted for CL, in agreement with previous estimates [12]. These results show the crucial interplay between membrane curvature and CL local content, a key feature of mitochondrial and bacterial membrane organization and dynamics. For instance, our data can help elucidate the importance of CL in the maintenance of the highly curved structure of the mitochondrial inner membrane, where it plays an essential role in membrane bioenergetics. They can also help better understand the observed CL-enriched domains in bacterial poles and divisions sites.

The results of this thesis are completed with Part IV, where we studied the phytoplankton size scaling with nutrient concentration. Phytoplankton are the plant-like components of plankton and represent a key factor in oceanic ecosystems as well as in biogeochemical cycling. Phytoplankton incorporate nutrients from the environment across the cell membrane. Over much of the ocean, phytoplankton growth is limited by nitrogen uptake (as nitrate). In this thesis, we have combined experimental observations of marine species of phytoplankton with a trait-based uptake model to determine how phytoplankton dominant size is predicted to scale with ambient nitrate concentration and how phytoplankton traits (handling time h and number of porters n) depend on cell size. Our results indicate that phytoplankton dominant size r should scale approximately with $S^{0.85}$, where S represents the ambient nitrate concentration. We have found that the handling time decreases with size according to $h \sim r^{-0.90}$, implying that larger

organisms have shorter h. Moreover, the number of porters in the cell is predicted to increase according to $n \sim r^{1.56}$, which implies a decrease of porter density with r. Although these scaling relations remain hypothetical today since they are still untested experimentally, they may be very useful in characterizing size-dependent nutrient uptake in marine ecosystems and biogeochemical cycling models, which specifically account for atmospheric carbon dioxide abundance and fixation.

Conclusions

According to the results obtained and presented here, we can establish the following conclusions for each of the thesis objectives.

Mechanics of constriction during cell division

1. Cell constriction requires to be initiated by a constriction apparatus that exerts a linear tension at the site of division, which is the way in which cells undergo the cytokinesis. Additionally, a mechanism that generates a stabilization potential is initially required to stabilize symmetric constriction. For vesicles (or cells) of micro size with flexible membranes ($\kappa_b \approx 10 - 20\ k_B T$), constriction and stabilization forces are in the order of the picoNewton. This is the range of forces practicable not only by natural divisomes, but also by other biomolecular motors (see Chapters 4 and 5).

2. Surface tension reduction, for example due to membrane-targeted lipid biogenesis or directed cortical flows, increases the stability and spontaneity of cellular constriction. A reduction on external pressure has similar effects. This implies that prolate-shaped cells (cylinders) favored by low values of pressure and surface tension require, in general, lower constriction and stabilization forces to undergo division than oblate shaped cells (discocytes) (see Chapters 4 and 5).

3. Our analytical expressions provide a good approximation to the exact values of the main physical magnitudes during constriction, as we show through comparison with numerical results. Therefore, they represent an easy and compact way to predict the requirement for successful symmetrical constriction (see Chapters 4 and 5).

4. In Chapter 4, our model was deeply analyzed for constant radius condition, which can be a simplified description of cytokinesis of rod-shaped cells, like bacteria, in which the radius is maintained by the cell wall. Under this condition, our model predicts unchanged poles during all the constriction process, which is consistent with the approximately constant shape of the poles in the rod-shaped cells. Other conditions such as constant area and volume were additionally addressed. We have seen in Chapter 5 (see Figure 5.2) that constriction at constant volume requires a nearly 26% increase in area, which may describe divided cells with intense membrane trafficking, which is known to play an important role in cytokinesis. On the other hand, if constriction takes place at constant area, the volume must be reduced approximately in 30%. This may be an idealization of cases where membrane trafficking is inhibited, for example, through heat shocks.

5. Once the symmetric constriction is initiated, we have seen in Chapter 5 that it can progress till final division without intervention of the external forces. This answers another important question of this thesis, namely, the conditions under which symmetrical constriction becomes spontaneous and stable against lateral asymmetries. Our analysis has demonstrated that the spontaneous curvature C_0 has an important effect on the forces required for constriction. In particular, for vesicles whose membranes have $C_0 > 0$ (*i.e.*, whose membranes are prone to adopt convex configurations) constriction becomes stable at the final stages of the process (see Figure 5.4B). When the stronger condition $C_0 > 1/R_m$ holds (*i.e.*, when membranes have a spontaneous curvature higher than the characteristic inverse cell size) constriction also becomes spontaneous in a broad range of values of membrane tensions and external pressures (see Figure 5.3). Conversely, for negative values of C_0, which favors global concave shapes, constriction is unstable and non-spontaneous during the whole process, thus requiring positive, high-strength, constriction and stabilization forces (see Figures 5.3 and 5.4A). Finally, we have also evidenced that the stability and spontaneity of symmetric constriction increase as constriction progresses (see Figure 5.4).

Cardiolipin segregation induced by membrane-curvature

6. Our experimental measurements on membrane nanotubes pulled from GUVs demonstrate that CL molecules accumulate in curved membranes based on their shape alone, without the involvement of any cellular protein machinery. Additionally, our results show that this accumulation is higher in more highly curved membranes, reaching a maximum at optimal CL concentrations (see Figure 6.2).

7. A theoretical model based on membrane elasticity and van der Waals entropy reproduces our sorting data and gives an intrinsic curvature of CL of 1.10 nm^{-1}, in agreement with previous estimates [12]. Model fits to our data predict a negative value of the interaction parameter ($a = -18\ k_BT\ nm^2$), which suggests the existence of attractive CL-CL interactions. The model also predicts that CL molecules are enriched in the inner monolayer of the nanotube and depleted from the outer one.

8. Despite the apparent self-clustering, our observations establish that CL repopulates the tube within seconds (see Figure A6.2), deducing that there is no detectable diffusion barrier at the neck (which resemble the geometry of the mitochondrial inner membrane). In a more biological wisdom, this result depicts CL as a mobile molecule, and the association clusters formed by CL-CL attractive interactions as labile structures in dynamic equilibrium with their lipid environment.

9. According to the model fits, EPC/CL bilayers are expected to not have significant coupling in membrane bending energy, thereby both monolayers can be dealt as independent systems, like occurs in other lipid bilayers in the absence of significantly rapid flip-flopping lipids [255].

Phytoplankton size scaling

10. The dominant size of marine species of phytoplankton r scales approximately with $S^{0.85}$, where S is the nitrate concentration in the ocean. This increase in dominant size can also

entail size-related changes in phytoplankton traits (such as the handling time and the number of membrane porters).

11. Our results indicate that the handling time, which corresponds to the time period during which a porter is occupied because it is handling an encountered nutrient molecule, decreases approximately with $r^{-0.90}$, while the number of porters in the membrane increases approximately with $r^{1.56}$. These relations are consistent with previous estimates [127, 259].

Future Work

The constriction model for cell division proposed in the Part II of this thesis is sufficiently general and powerful to accommodate additional elements present in real cells that participate actively to drive cytokinesis such as the viscoelasticity of the cytoplasm, the cell nucleus, and the organelle structures. As previously mentioned in the Discussion section, real cells accumulate negatively curved lipids in the constriction furrow and positively curved lipids in the lateral lobes, which contributes to reduce the constriction force necessary for cell division. This is experimentally observed in both eukaryotes [167] and bacteria [12]. In this sense, our model can be easily extended to a three-domain vesicle which will require lower forces to constrict in a stable way. Other improvement will entail the inclusion of the cell wall dynamics in prokaryotes and plant cells. Another additional effect not included in our model is the anisotropic contraction ring nucleation, which can lead to a non-concentric ring and break the axial symmetry [261]. Although all this complexity might be included on an extended, more realistic, model of cell division, the physical problem exceeds the limits of the present work, which can be however considered as a good starting point to construct a general minimal model of cell constriction. The big question, which remains still to be addressed in a comprehensive way, is to know how much of the division of real cells can be understood in terms of a simplified physical model integrating the passive mechanics of the membrane with the active actuation of the cytokinetic engine. In other words, try to know whether additional elements are or not required to account for the main ingredients of the cell division mechanics (as for example, anisotropic composition and mechanical properties of the cell membrane).

Our experimental measurements of CL-sorting induced by membrane curvature (see Part III) can be only explained theoretically by a sorting model that includes CL-clustering via attractive CL-CL self-interactions. Although the required existence of CL clusters might also explain why the CL-localization at bacterial poles requires a minimum concentration threshold [60], they need additional direct evidences that we hope will be achieved shortly. The CL cluster size obtained from the fit to the sorting model ($\approx 10 - 20$ nm^2, in the order of 10 CL molecules) is similar to some estimates of lipid-raft dimensions and recent developments in experimental techniques might allow for the detection of these clusters. An interesting test could be to make AFM (Atomic Force Microscopy) experiments on supported lipid bilayers containing CL. This technique forms an image of the three-dimensional shape (topography) of the sample surface at a high resolution providing information of its domain structure and perhaps allowing the visualization of these CL clusters. The size of the domains is limited by the high intrinsic curvature of CL, but this effect is reduced in curved regions [192]. Thus, definitive evidences might be obtained from CL-containing bilayers in highly curved tubes, an experimental setting

possibly more difficult to be realized with AFM or other nanoscopies that allow to resolve molecular clusters.

Our experimental measurements show that CL molecules can exchange between the GUV and the nanotube, however, further experiments must be done in order to accurately determine the CL diffusion coefficient through membrane nanotubes. Some techniques that can be used for this purpose are FRAP (Fluorescence Recovery After Photobleaching) or SPT (Single Particle Tracking).

Another pending task is to measure the bending modulus of membrane bilayers at different CL-contents, instead using a theoretical estimation [Eq. (A6.13)]. This can be done, for example, with flickering spectrometry experiments.

The theoretical sorting model predicts a CL enrichment in the inner monolayer of the nanotube while a CL depletion in the outer one. Therefore, it would be also interesting to verify experimentally this asymmetrical sorting between both monolayers. A possible way to detect if CL prefers the inner monolayer of a curved bilayer would be to use a specific dye for CL and to encapsulate it inside small vesicles (< 30 nm in diameter). The negative control would be adding the dye outside these vesicles. Then, we will detect and compare the fluorescence intensities of the dye in both situations. In this way, although the geometry of these small vesicles is not the same as the nanotubes, we could still address, indirectly, at high curvature, CL prefer to be in the inner monolayer of a bilayer. Another possible experiment is to measure the zeta potential of eggPC small vesicles (as a control), that quantifies the magnitude of the electrical charge on the outer monolayer. Thereafter, we can do the same for vesicles of eggPC + CL. Since CL is a negatively charged lipid, if the zeta potential does not change, we could say that the CL is in the inner monolayer of the membrane.

More generally, this work could also apply to other lipid types that can cluster and have a conical shape, such as some glycolipids.

In this thesis we have shown that curvature contributes to CL sorting *in vitro*, but an important question remains: is it operating in cells? Performing similar experiments inside cells represent an open challenge for the future. For example, one can imagine an experiment in which the mitochondria lipids were labeled with two dyes like in our *in vitro* experiments. It would be exciting to pull tubes from the inner mitochondrial membrane and check if these tubes are enriched in CL. Similar experiments would be interesting in bacteria to investigate whether CL molecules spontaneously flow to the cell poles and constriction sites. A first step towards providing an answer would be to study native membranes (pure biological membranes previously extracted from cells) *in vitro*.

The empirical relations for phytoplankton traits derived in Part IV of this thesis constitute phenomenological predictions in the sense that they are consistent with the uptake models, but they are not directly derived from them. Further experimental observations would be very helpful to validate these phenomenological predictions. Collaborations between cell biologists and ecologists to design experiments with concurrent measurements of phytoplankton traits and nutrient uptake rates would be really interesting.

Another remaining challenge is to understand the trade-offs in phytoplankton communities. A trade-off arises when a trait is beneficial for one function but gives a disadvantage for another function. For example, it is clear that the more uptake porters the organism have, the more nutrients they can acquire at the same time. However, there is a maintenance cost of porters, which can be an important factor in determining the optimal uptake porter density. Viral infection through uptake porters could be an additional adaptive reason to limit their density. We are currently working on an optimal uptake model in which we assume there is an optimal number of porters in the cell that balances their uptake advantage with their maintenance cost. Another thing to consider is that both the handling time and the number of uptake porters may be quite flexible and vary as a function of environmental conditions. In this sense, the results presented here can be extended to incorporate such plasticity once the microbial trade-offs become clearer.

All these results contribute to a deeper quantitative understanding of the physical mechanisms underlying different cellular processes and bring new and exciting challenges for the future. The implications of these results are insightful in cell biology and span across different integrative areas of biology as eventually involve physical chemistry, mechanics, biophysics, and ecology. In this context, we hope that this work encourages the cooperation between scientifics from different disciplines to conduct multidisciplinary and integrated research about the cell and the cellular processes.

Discusión, conclusiones y trabajo futuro

Las membranas celulares están altamente curvadas durante procesos celulares clave, como son la citocinesis, el tráfico de lípidos de membrana o el movimiento celular. La importancia de la curvatura como característica estructural de las membranas biológicas ha sido reconocida durante muchos años y ha fascinado a científicos de diferentes campos. Cambios en la morfología de la membrana están presentes en una gran cantidad de fenómenos que afectan a la membrana plasmática de las células eucariotas, incluidos la división celular, la endo y exocitosis y la fagocitosis. Además, una multitud de procesos intracelulares a nivel de orgánulos se basan en la generación, la modulación y el mantenimiento de la curvatura de la membrana para conservar la forma y la funcionalidad del orgánulo. En esta tesis, hemos abordado el estudio de dos procesos celulares en los que el efecto de la curvatura de la membrana es crucial. Por un lado, hemos desarrollado un modelo teórico de la mecánica de la constricción celular durante la división que combina métodos analíticos y numéricos y una discusión de sus implicaciones (ver Parte II). Por otro lado, hemos estudiado, tanto experimental como teóricamente, un problema abierto en la segregación de lípidos: si las moléculas de cardiolipina se segregan (o no) por el efecto de la curvatura de la membrana (ver Parte III).

Las células de un determinado tipo usualmente mantienen un tamaño característico dominante ("conveniente") que es el adecuado para su contexto ecológico. Dado que las células son la unidad primaria de la vida, comprender los mecanismos que controlan su crecimiento y su proliferación es relevante en múltiples escalas y niveles de organización. En esta tesis, hemos analizado el efecto del tamaño dominante del fitoplancton sobre sus características y cómo este tamaño depende de la concentración de nutrientes en el océano (ver Parte IV).

Nuestros trabajos ayudan a clarificar procesos centrales en biología y contribuyen a una mejor comprensión de los mecanismos físicos por los cuales las células se duplican, se organizan y crecen. Hemos logrado con éxito los objetivos descritos en la introducción y resumidos al comienzo de esta tesis. A continuación, se presenta una discusión integradora de los resultados. Después, exponemos las principales conclusiones de la tesis concluyendo con algunas preguntas abiertas y posible trabajo futuro.

Discusión

El principal objetivo relacionado con la física de la división celular era estudiar el problema mecánico de una vesícula de membrana constreñida ecuatorialmente en el marco del Hamiltoniano de Canham-Helfrich. Este es un problema crucial de la bioenergética, cuya solución debería informarnos sobre la cantidad de energía mecánica necesaria para duplicar los contenidos celulares de una forma estable. Independientemente de los detalles de la maquinaria

citocinética, la membrana celular responde contra la deformación minimizando la energía elástica siguiendo un camino aún desconocido. En los Capítulos 3 y 4 de la Parte II hemos desarrollado un método para encontrar expresiones analíticas aproximadas de las propiedades más relevantes involucradas en el proceso de constricción de una vesícula (o célula simplificada) en términos del tamaño celular, de la curvatura espontánea de la membrana, la tensión de la membrana y de la diferencia de presión entre el medio externo e interno. Estas propiedades incluyen la energía de la vesícula, el área de su membrana, su volumen y las fuerzas de constricción y estabilización a lo largo del proceso de constricción. Nuestros resultados han demostrado que la constricción celular es, en general, un proceso no espontáneo que requiere ser iniciado mediante un aparato de constricción que ejerza una tensión de línea en el sitio de división. Como es predecible desde un punto de vista dimensional, se han obtenido fuerzas de constricción con una amplitud del orden de κ_b/R_m, donde κ_b es el módulo de flexión de la membrana y R_m el radio de la célula (≈ 10 μm). La fuerza de constricción escala inversamente proporcional a R_m, es decir, células más pequeñas son más difíciles de constreñir. Células con membranas flexibles ($\kappa_b \approx 10 - 20\ k_BT$) requieren una fuerza de constricción inicial en el rango de $0.1 - 1$ pN, que es el rango de fuerzas practicables por los motores moleculares. Hemos cuantificado la estabilidad de la constricción simétrica, obteniendo un coeficiente característico del orden de $-k_BT$ al comienzo de la constricción, lo que demuestra que las células necesitan un mecanismo externo para estabilizar la constricción en el centro de la célula. La fuerza de estabilización escala inversamente proporcional a R_m^2, es decir, células más pequeñas son más inestables frente a desplazamientos laterales del anillo de constricción. Las fuerzas de estabilización requeridas también están en el rango de picoNewton. Nuestros resultados han demostrado que la curvatura espontánea de la membrana C_0 tiene un efecto importante sobre la fuerza requerida para la constricción y las células c cuyas membranas son propensas a adoptar configuraciones convexas (por ejemplo, bacterias con forma cilíndrica) son las que se constriñen más fácilmente. Los resultados más interesantes de esta parte son los correspondientes a las condiciones bajo las cuales la división se vuelve espontánea y estable frente a asimetrías laterales. Sorprendentemente, hemos visto que una vez que se ha iniciado la constricción simétrica, ésta progresa espontáneamente hasta la división final para curvatura espontáneas por encima de un umbral determinado por el tamaño de la célula.

El proceso de constricción propuesto en esta tesis constituye un modelo mínimo para la división simétrica de una vesícula de membrana homogénea (o célula simplificada). Por lo tanto, se espera que represente el mecanismo simple de la división celular en protocélulas primitivas, las cuales se dividían espontáneamente sin una maquinaria citocinética específica. A pesar de la simplicidad inherente, nuestro análisis es muy útil para comprender la física del mecanismo de constricción celular durante la división en células vivas y para guiar el diseño de divisomas artificiales en microsistemas auto-actuados. El método propuesto puede servir también para obtener información sobre otros procesos biológicos que involucran curvatura de membrana, como exocitosis y endocitosis.

La teoría de la mecánica de la división celular desarrollada en esta tesis también podría aplicarse a otras formas axisimétricas observadas experimentalmente, como estomatocitos, formas de pera, dummbells, discocitos, ... Para divisiones celulares dentro de un tejido celular, se encuentran geometrías celulares alejadas de los esferoides, y uno debe considerar las fuerzas interactivas entre las células vecinas y cómo estas fuerzas cambian las formas de las células. Este

estudio también puede generalizarse a formas no axisimétricas, así como para membranas multicomponentes (para una revisión de métodos útiles para ampliar el estudio, ver Ref. [71]). Aunque nuestro modelo asume una curvatura espontánea homogénea, hay que recordar que, en general, C_0 no es uniforme a lo largo la membrana de una célula real. El escenario homogéneo anterior podría mejorarse enormemente en vesículas (o células) con membranas asimétricas. Dado que el sitio de constricción tiene forma de silla de montar, una acumulación de lípidos cónicos en la región de constricción puede contribuir a minimizar la energía local de curvatura de la membrana (ver Figura 4.9). Existen evidencias experimentales sobre el posible papel mecánico de los lípidos de curvatura negativa (como fosfatidiletanolamina y cardiolipina) durante las fases finales de la constricción [12, 15, 167, 172–174]. Por lo tanto, cualquier modelo realista de división celular debe considerar valores negativos de curvatura espontánea en el sitio de constricción de la membrana celular.

El párrafo anterior describe cómo una distribución asimétrica de lípidos puede dar forma a la membrana. Se ha propuesto que lo contrario también es cierto, es decir, que la forma de la membrana puede influir en la distribución lipídica. Debido a que la energía de curvatura depende de las propiedades de la membrana, como son la curvatura espontánea y el módulo de curvatura, y debido a que estas propiedades dependen de la composición de la membrana, un acoplamiento entre la composición lipídica y la curvatura puede reducir esta energía. En otras palabras, cuando una membrana uniformemente mezclada está sometida a una curvatura no homogénea, la energía de curvatura podría reducirse con una distribución de lípidos no homogénea. Este fenómeno también ha sido estudiado en esta tesis con cardiolipina (CL), un lípido con forma de cono observado a alta concentración en regiones específicas de membrana con alta curvatura (polos y sitio de división bacteriana y pliegues de la membrana mitocondrial interna). A pesar de que hay bastantes evidencias *in vivo* en la literatura que sugieren que la CL se concentra en regiones de membrana curvadas negativamente, no existen experimentos *in vitro* que muestren la segregación de CL basada en curvatura. En esta tesis hemos estudiado la separación del contenido en CL inducida por la curvatura de la membrana utilizando el sistema experimental desarrollado por P. Bassereau (París, Francia). El procedimiento llevado a cabo se basa en extraer nanotubos de membrana de vesículas unilamelares gigantes aspiradas en una micropipeta siguiendo la técnica descrita detalladamente en el Capítulo 2 de esta tesis. Hemos utilizado vesículas hechas de la mezcla homogénea EPC/CL con diferentes contenidos de CL. Nuestras medidas *in vitro* confirman que las moléculas de CL se acumulan en las zonas curvadas de la membrana debido a su forma, con una mayor acumulación en membranas más curvadas. Esto proporciona evidencia experimental de la hipótesis de partida: la preferencia espacial CL es una consecuencia de las limitaciones geométricas y físicas de la membrana. Nuestros datos son compatibles con un modelo basado en la elasticidad de las membranas biológicas y la teoría de fluidos no ideales, a partir del cual se predice una curvatura intrínseca de 1.10 nm^{-1} para la molécula de CL, que coincide con estimaciones previas [12]. Este trabajo muestra la interacción crucial entre la curvatura de la membrana y el contenido local de CL, un hecho clave en la organización y la dinámica mitocondrial y bacteriana. Por ejemplo, nuestros datos pueden ayudar a dilucidar la importancia de la CL en el mantenimiento de la estructura altamente curvada de la membrana mitocondrial interna, donde la CL desempeña un papel esencial en la bioenergética de la membrana. También pueden ayudar a comprender mejor la existencia de dominios enriquecidos en CL en los polos y zona de división bacteriana.

Los resultados de esta tesis se han completado con la Parte IV, donde hemos estudiado el escalado del tamaño del fitoplancton con la concentración de nutrientes. El fitoplancton es el componente tipo planta del plancton y es un factor clave para los ecosistemas oceánicos y para el ciclo biogeoquímico. El fitoplancton incorpora nutrientes del medio ambiente a través de su membrana celular. En gran parte del océano el crecimiento del fitoplancton está limitado por la absorción de nitrógeno (como nitrato). En esta tesis hemos combinado observaciones experimentales de especies marinas de fitoplancton con un modelo de absorción de nutrientes basado en las características para determinar cómo el tamaño dominante del fitoplancton debe escalar con la concentración de nitrato ambiental y cómo las características del fitoplancton (tiempo de absorción de nutrientes h y número de portadores de la membrana n) dependen del tamaño de la célula. Nuestros resultados indican que el tamaño dominante del fitoplancton r debe escalar aproximadamente con $S^{0.85}$, donde S representa la concentración de nitrato ambiental. Hemos determinado que el tiempo de absorción de nutrientes disminuye con el tamaño celular de acuerdo con $h{\sim}r^{-0.90}$, lo que implica que los organismos más grandes tienen un tiempo de absorción h más corto. Además, nuestros resultados predicen que el número de portadores de la membrana aumenta de acuerdo con $n{\sim}r^{1.56}$, lo que implica una disminución de la densidad de portadores con r. Aunque nuestras relaciones de escalado siguen siendo hipotéticas actualmente, ya que aún no se han probado experimentalmente, pueden ser útiles para caracterizar la dependencia de la absorción de nutrientes con el tamaño de los microrganismos en ecosistemas marinos y en modelos de ciclo biogeoquímico, que explican abundancia y la fijación del dióxido de carbono en la atmósfera.

Conclusiones

De acuerdo con los resultados obtenidos y presentados aquí, podemos establecer las siguientes conclusiones para cada uno de los objetivos de la tesis.

Mecánica de la constricción durante la división celular

1. Para que la constricción comience se necesita un aparato de constricción que ejerza una tensión de línea en el sitio de división, que es la forma en que las células experimentan la citocinesis. Además, inicialmente se requiere un mecanismo que genere un potencial de estabilización para estabilizar la constricción simétrica. Para las vesículas (o células) de tamaño microscópico con membranas flexibles ($\kappa_b \approx 10 - 20\ k_B T$), las fuerzas de constricción y estabilización están en el orden de los picoNewtons. Este es el rango de fuerzas ejercidas no solo por divisomas naturales, sino también por otros motores moleculares (ver los Capítulos 4 y 5).

2. Una reducción de la tensión superficial, debida, por ejemplo, a la biogénesis lipídica dirigida a la membrana o a los flujos corticales dirigidos, aumenta la estabilidad y la espontaneidad de la constricción celular. Una reducción en la presión externa tiene efectos similares. Esto implica que las células con forma prolata (cilíndrica), que son favorecidas por bajas presiones y bajas tensiones, requieren, en general, menores fuerzas de constricción y estabilización para dividirse que células con forma oblata (discocitos) (ver los Capítulos 4 y 5).

3. Nuestras expresiones analíticas proporcionan una buena aproximación a los valores exactos de las principales magnitudes físicas durante la constricción, como se ha demostrado a través de la comparación con los resultados numéricos. Por lo tanto, estas fórmulas representan una manera fácil y compacta de predecir los requisitos de una constricción simétrica eficaz (véanse los Capítulos 4 y 5).

4. En el Capítulo 4 nuestro modelo fue analizado en profundidad para la condición de radio polar constante, que puede ser una descripción simplificada de la citocinesis de células con forma de barra, como las bacterias, en las cuales la pared celular mantiene el radio de la célula aproximadamente constante. También han sido estudiadas otras condiciones, como son las constricciones a área y a volumen constante. Hemos visto en el Capítulo 5 (ver Figura 5.2) que la constricción a volumen constante requiere un aumento del área de la membrana de casi el 26%, situación que puede describir a células con intenso tráfico de membrana, que se sabe que desempeña un papel importante en la citocinesis. Por otro lado, si la constricción tiene lugar a área constante, el volumen de la célula debe reducirse en un 30% aproximadamente. Esto puede ser una idealización de casos en los que el tráfico de membranas se inhibe, por ejemplo, a través de choques de calor.

5. Hemos visto en el Capítulo 5 que una vez que se inicia la constricción simétrica, ésta puede progresar hasta la división final sin intervención de fuerzas externas. Esto responde a otra pregunta importante de esta tesis, a saber, las condiciones bajo las cuales la constricción simétrica se vuelve espontánea y estable frente a asimetrías laterales. Nuestro análisis ha demostrado que la curvatura espontánea tiene un efecto importante en las fuerzas necesarias para la constricción. En particular, para vesículas cuyas membranas tienen $C_0 > 0$ (es decir, cuyas membranas son propensas a adoptar configuraciones convexas) la constricción se vuelve estable al final del proceso (ver Figura 5.4B). Cuando se cumple la condición más fuerte $C_0 > 1/R_m$ (es decir, cuando las membranas tienen una curvatura espontánea mayor que el inverso del tamaño característico de la célula), la constricción también se vuelve espontánea para un amplio rango de valores de tensión y presión (ver Figura 5.3). Por el contrario, para valores negativos de C_0, que favorecen formas globalmente cóncavas, la constricción es inestable y no espontánea durante todo el proceso, requiriendo altas fuerzas de constricción y estabilización (ver Figuras 5.3 y 5.4A). Finalmente, también hemos visto que la estabilidad y la espontaneidad de la constricción simétrica aumentan a medida que progresa la constricción (ver Figura 5.4).

Segregación de cardiolipina basada en la curvatura de la membrana

6. Nuestras medidas experimentales en nanotubos de membrana extraídos de vesículas gigantes demuestran que las moléculas de CL se acumulan en membranas curvadas debido a su forma, sin la participación de ninguna maquinaria de proteínas celulares. Además, nuestros resultados muestran que esta acumulación es mayor cuanto más curvadas son las membranas, alcanzando un máximo a concentraciones óptimas de CL (ver Figura 6.2).

7. Un modelo teórico basado en la elasticidad de membrana y en la entropía de van der Waals reproduce nuestros datos y da una curvatura intrínseca de la CL de 1.10 nm^{-1}, que está de acuerdo con estimaciones previas [12]. Los ajustes del modelo predicen un valor negativo del parámetro de interacción ($a = -18\, k_B T\ \mathrm{nm}^2$), lo que sugiere la existencia de interacciones atractivas CL-CL. El modelo también predice que las moléculas de CL se concentran en la monocapa interior del tubo mientras que se reducen en la externa.

8. A pesar de la aparente existencia de estas agrupaciones de CL, nuestras observaciones establecen que la CL repuebla el nanotubo en pocos segundos (ver Figura A6.2), deduciendo que el cuello que conecta la vesícula con el nanotubo (que se asemeja a la geometría de los pliegues mitocondriales) no es una barrera para la difusión de CL. Desde un punto de visto más biológico, este resultado muestra a la CL como una molécula móvil, y a las agrupaciones formadas por interacciones atractivas CL-CL como estructuras lábiles en equilibrio dinámico con su entorno lipídico.

9. Según los ajustes al modelo, se espera que las bicapas EPC/CL no tengan un acoplamiento significativo en la energía de curvatura de la membrana, por lo que ambas monocapas pueden tratarse como sistemas independientes, al igual que ocurre en otras bicapas lipídicas en ausencia de lípidos con rápido movimiento de flip-flop [255].

Escalado del tamaño del fitoplancton

10. El tamaño dominante de las especies marinas del fitoplancton r escala aproximadamente con $S^{0.85}$, donde S representa la concentración de nitrato en el océano. Este aumento en el tamaño dominante también puede implicar otros cambios en las características del fitoplancton que dependen del tamaño (como el tiempo de absorción de nutrientes y el número de portadores de la membrana).

11. Nuestros resultados indican que el tiempo de absorción de nutrientes, que se corresponde con el período de tiempo durante el cual un portador de la membrana se encuentra ocupado digiriendo una molécula de nutriente, decrece aproximadamente con $r^{-0.90}$, mientras que el número de portadores de la membrana aumenta aproximadamente con $r^{1.56}$. Estas relaciones son consistentes con estimaciones previas [127, 259].

Trabajo futuro

El método de constricción propuesto en la Parte II de esta tesis es suficientemente general y potente para acomodar elementos adicionales presentes en células reales que participan activamente en la citocinesis, como son la viscoelasticidad del citoplasma, el núcleo celular, y las estructuras de los orgánulos. Como se mencionó anteriormente en la sección Discusión, las células reales acumulan lípidos curvados negativamente en el surco de constricción y lípidos curvados positivamente en los lóbulos laterales, lo que contribuye a reducir la fuerza de constricción necesaria para la división celular. Esto se observa experimentalmente tanto en eucariotas [167]como en bacterias [12]. En este sentido, nuestro modelo se puede extender fácilmente a una vesícula de tres dominios que requerirá fuerzas más bajas para contraerse de una manera estable. Otras mejoras implicarían la inclusión de la dinámica de la pared celular en

procariotas y células vegetales. Otro efecto adicional no incluido en nuestro modelo es la nucleación anisotrópica del anillo de contracción, que puede dar lugar a un anillo no concéntrico y romper la simetría axial [261]. Aunque toda esta complejidad podría incluirse en un modelo extendido, más realista, de división celular, el problema físico excede los límites del presente trabajo, que sin embargo puede considerarse como un buen punto de partida para construir un modelo general mínimo de constricción celular. La gran pregunta, que aún no se ha abordado de manera exhaustiva, es saber cuánto de la división de células reales se puede entender en términos de un modelo físico simplificado que integra la mecánica pasiva de la membrana con la actuación activa del motor citocinético. En otras palabras, tratar de saber si se requieren o no elementos adicionales para explicar los principales aspectos de la mecánica de división celular (como, por ejemplo, composición y propiedades mecánicas anisotrópicas de la membrana celular)

Nuestras medidas experimentales de la segregación de CL inducida por la curvatura de la membrana (ver Parte III) solo pueden explicarse teóricamente con un modelo que incluye agrupaciones de CL formadas por interacciones atractivas CL-CL. Aunque la existencia requerida de estas agrupaciones de CL también podría explicar por qué la localización de CL en los polos bacterianos requiere un umbral de concentración mínimo [60], se necesitan evidencias directas que esperamos que se logren en breve. El tamaño de las agrupaciones obtenido del ajuste al modelo teórico ($\approx 10-20$ nm^2, del orden de 10 moléculas de CL) es similar a algunas estimaciones de las dimensiones de balsas lipídicas y los avances recientes en técnicas experimentales podrían permitir su detección. Una posibilidad podría ser realizar experimentos de AFM (Microscopía de Fuerza Atómica) en bicapas lipídicas que contengan CL. Esta técnica forma una imagen tridimensional (topografía) de la muestra a alta resolución, proporcionando información de su estructura y quizás permitiendo la visualización de estas agrupaciones CL. El tamaño de los dominios está limitado por la alta curvatura intrínseca de CL, pero este efecto se reduce en regiones curvadas [192]. Por lo tanto, podrían obtenerse evidencias definitivas en bicapas de CL de tubos altamente curvados, un sistema experimental posiblemente más difícil de realizar con AFM u otras nanoscopías que permiten resolver agrupaciones moleculares.

Nuestras medidas muestran que las moléculas de CL se intercambian entre la vesícula y el nanotubo en pocos segundos, sin embargo, se deben realizar más experimentos para determinar con precisión el coeficiente de difusión de la CL a través de nanotubos de membrana. Algunas de las técnicas que se pueden usar para este propósito son FRAP (Recuperación de Fluorescencia Después del Fotoblanqueo) o SPT (Seguimiento de Partículas Individuales).

Otra tarea pendiente es medir el módulo de curvatura en bicapas lipídicas con diferentes concentraciones de CL, en lugar de utilizar una estimación teórica [Eq. (A6.13)]. Esto se puede hacer, por ejemplo, con experimentos de espectrometría.

El modelo teórico de segregación predice un enriquecimiento de CL en la monocapa interior del nanotubo mientras que una reducción de CL en la monocapa exterior. Por lo tanto, también sería interesante contrastar experimentalmente esta segregación asimétrica entre ambas monocapas. Una posible forma de detectar si la CL realmente prefiere la monocapa interior de una bicapa curvada sería utilizar un marcador específico de CL y encapsularlo dentro de vesículas pequeñas (< 30 nm de diámetro). El control negativo de este experimento sería agregar el marcador fuera de estas vesículas. A continuación, detectaríamos y compararíamos las

intensidades de fluorescencia del marcador en ambas situaciones. De esta manera, aunque la geometría de estas pequeñas vesículas no es la misma que la de los nanotubos, podríamos decir, de forma indirecta, que la CL preferiría estar en la monocapa interior de una bicapa altamente curvada. Otro experimento posible puede ser medir el potencial zeta de vesículas pequeñas de eggPC (como control), cuantificando así la magnitud de la carga eléctrica en la monocapa externa. Después podemos hacer lo mismo para las vesículas de eggPC + CL. Como la CL es un lípido cargado negativamente, si el potencial zeta no cambia, podríamos decir que el CL se concentra preferentemente en la monocapa interna de la membrana.

En términos más generales, este trabajo también podría aplicarse a otros tipos de lípidos que forman agrupaciones y tienen forma cónica, como algunos glucolípidos.

En esta tesis hemos demostrado que la curvatura contribuye a la segregación de CL *in vitro*, pero una pregunta importante sigue siendo: ¿esto ocurre en células reales? Realizar experimentos similares dentro de las células representa un importante reto para el futuro. Por ejemplo, se puede imaginar un experimento en el cual los lípidos de la mitocondria fuesen marcados con dos fluorescentes como en nuestros experimentos *in vitro*. Sería interesante extraer nanotubos de la membrana mitocondrial interna y comprobar si estos tubos están enriquecidos en CL. Experimentos similares podrían realizarse en bacterias para investigar si las moléculas de CL se dirigen espontáneamente a las regiones curvadas de la membrana. Un primer paso para dar una respuesta sería estudiar membranas nativas (membranas biológicas puras previamente extraídas de las células) *in vitro*.

Las relaciones de escalado de las características del fitoplancton presentadas en la Parte IV de esta tesis constituyen predicciones fenomenológicas, en el sentido de que son consistentes con los modelos de absorción de nutrientes, pero no derivan directamente de ellos. Observaciones experimentales adicionales serían muy útiles para contrastarlas. En este sentido, serían necesarias colaboraciones entre biólogos celulares y ecologistas para diseñar experimentos que proporcionen medidas simultáneas de las características del fitoplancton y la velocidad de absorción de nutrientes.

Otro reto pendiente es comprender los *tradeoffs* en las comunidades fitoplanctónicas. Un *tradeoff* se produce cuando una característica del microorganismo es beneficiosa para una función, pero perjudicial para otra. Por ejemplo, está claro que cuantos más portadores de absorción tenga el microorganismo, más nutrientes podrán adquirir en el mismo tiempo. Sin embargo, existen costes de mantenimiento de los portadores de membrana, que pueden ser un factor importante para determinar la densidad óptima de portadores. La infección viral a través de estos portadores podría ser una razón adaptativa adicional para limitar su densidad. Actualmente estamos trabajando en un modelo de absorción de nutrientes óptimo en el que suponemos que hay un número óptimo de portadores de membrana en la célula que equilibra la ventaja de absorción de nutrientes con su coste de mantenimiento. Otra cuestión a considerar es que tanto el tiempo de absorción de nutrientes como el número de portadores pueden ser bastante flexibles y variar en función de las condiciones ambientales. A este respecto, los resultados presentados aquí pueden ampliarse para incorporar dicha plasticidad una vez que los *tradeoffs* microbianos estén más claros.

Todos estos resultados contribuyen a una comprensión cuantitativa más profunda de los mecanismos físicos que subyacen a diferentes procesos celulares y brindan nuevos y emocionantes retos para el futuro. Las implicaciones de estos resultados son esclarecedoras para la biología celular y se extienden a diferentes áreas de la biología, que eventualmente involucran la química física, la mecánica, la biofísica y la ecología. En este sentido, esperamos que este trabajo aliente la cooperación entre científicos de diferentes disciplinas para llevar a cabo investigaciones multidisciplinarias e integradas sobre la célula y los procesos celulares.

References

1. Hooke R, Allestry J, & Martyn J (1665) *Micrographia. Some physiological descriptions of minute bodies made by magnifying glasses with observations and inquiries thereupon*. Eds. Martyn J & Allestry J. (Royal Society, London).

2. Porter KR (1945) A study of tissue culture cells by electron microscopy: methods and preliminay observations. *J Exp Med* 81(3):233–246.

3. Falconer H & Lents N (2003) Discovery and structure of cells. *Visionlearning Vol BIO-1*. Available at: https://www.visionlearning.com/en/library/Biology/2/Discovery-and-Structure-of-Cells/64 [Accessed August 23, 2018].

4. Barton NH (2007) *Evolution*. (Cold Spring Harbor Laboratory Press, Huntington).

5. Marston AL & Amon A (2004) Meiosis: cell-cycle controls shuffle and deal. *Nat Rev Mol Cell Biol* 5(12):983–997.

6. Brügger B, et al. (2000) Evidence for segregation of sphingomyelin and cholesterol during formation of COPI-coated vesicles. *J Cell Biol* 151(3):507–18.

7. Klemm RW, et al. (2009) Segregation of sphingolipids and sterols during formation of secretory vesicles at the trans-Golgi network. *J Cell Biol* 185(4):601–612.

8. Sprong H, van der Sluijs P, & van Meer G (2001) How proteins move lipids and lipids move proteins. *Nat Rev Mol Cell Biol* 2(7):504–513.

9. Sorre B, et al. (2009) Curvature-driven lipid sorting needs proximity to a demixing point and is aided by proteins. *Proc Natl Acad Sci U S A* 106(14):5622–5626.

10. Lingwood D, Ries J, Schwille P, & Simons K (2008) Plasma membranes are poised for activation of raft phase coalescence at physiological temperature. *Proc Natl Acad Sci* 105(29):10005–10010.

11. Tejpal D (2018) Microbial physiology and metabolism-I: nutrient uptake and transport. Available at: http://vle.du.ac.in/mod/book/view.php?id=12689&chapterid=26839 [Accessed August 23, 2018].

12. Renner LD & Weibel DB (2011) Cardiolipin microdomains localize to negatively curved regions of Escherichia coli membranes. *Proc Natl Acad Sci* 108(15):6264–6269.

13. Mileykovskaya E & Dowhan W (2000) Visualization of phospholipid domains in Escherichia coli by using the cardiolipin-specific fluorescent dye 10-N-nonyl acridine orange. *J Bacteriol* 182(4):1172–5.

14. Kawai F, et al. (2004) Cardiolipin domains in Bacillus subtilis marburg membranes. *J Bacteriol* 186(5):1475–83.

15. van Meer G, Voelker DR, & Feigenson GW (2008) Membrane lipids: where they are and how they

behave. *Nat Rev Mol Cell Biol* 9(2):112–124.

16. Boyd KJ, Alder NN, & May ER (2017) Buckling under pressure: curvature-based lipid segregation and stability modulation in cardiolipin-containing bilayers. *Langmuir* 33(27):6937–6946.

17. Nichols-Smith S, Teh S-Y, & Kuhl TL (2004) Thermodynamic and mechanical properties of model mitochondrial membranes. *Biochim Biophys Acta* 1663(1–2):82–88.

18. Koppelman C-M, Den Blaauwen T, Duursma MC, Heeren RMA, & Nanninga N (2001) Escherichia coli minicell membranes are enriched in cardiolipin. *J Bacteriol* 183(20):6144–6147.

19. Dahlberg M & Maliniak A (2008) Molecular dynamics simulations of cardiolipin bilayers. *J Phys Chem B* 112(37):11655–11663.

20. Overton CE (1895) Über die osmotischen Eigenschaften der Lebenden Pflanzen-und Tierzelle. *Vierteljahresschr D Naturforsch Ges Zürich* 40:159–201.

21. Overton CE (1899) Über die allgemeinen osmotischen Eigenschaften der Zelle, ihre vermutlichen Ursachen und ihre Bedeutung für die Physiologie. *Vierteljahresschr D Naturforsch Ges Zürich* 64:87–136.

22. Langmuir I (1917) The constitution and fundamental properties of solids and liquids . *J Am Chem Soc* 39(9):1848–1906.

23. Gorter E & Grendel F (1925) On biomolecular layers of lipoids on the chromocytes of the blood. *J Exp Med* 41(4):439–443.

24. Danielli JF & Davson H (1935) A contribution to the theory of permeability of thin films. *J Cell Comp Physiol* 5(4):495–508.

25. Singer SJ & Nicolson GL (1972) The fluid mosaic model of the structure of cell membranes. *Science* 175(4023):720–731.

26. Unwin PN & Henderson R (1975) Molecular structure determination by electron microscopy of unstained crystalline specimens. *J Mol Biol* 94(3):425–440.

27. Robertson JD (1981) Membrane structure. *J Cell Biol* 91(3):189–204.

28. Phillips R, Theriot J, Kondev J, & Garcia H (2012) *Physical biology of the cell*. Eds. Phillips R, Kondev J, & Garcia HG. (Garland Science, New York). 2nd Ed.

29. Kuhl TL, Leckband DE, Lasic DD, & Israelachvili JN (1994) Modulation of interaction forces between bilayers exposing short-chained ethylene oxide headgroups. *Biophys J* 66(5):1479–1488.

30. Israelachvili JN (2011) *Intermolecular and surface forces*. (Elsevier, Ámsterdam). 3rd Ed.

31. Girard P (2012) *Membranes hors d'équilibre: échanges et transport actif (PhD)*. (Université Paris 7 - Denis Diderot, Paris).

32. Walde P, Cosentino K, Engel H, & Stano P (2010) Giant vesicles: preparations and applications. *ChemBioChem* 11(7):848–865.

33. Canham PB (1970) The minimum energy of bending as a possible explanation of the biconcave shape of the human red blood cell. *J Theor Biol* 26(1):61–81.

34. Helfrich W (1973) Elastic properties of lipid bilayers: theory and possible experiments. *Zeitschrift fur Naturforsch C* 28(11–12):693–703.

35. Boal DH (2002) *Mechanics of the cell*. (Cambridge University Press, Cambridge).

36. Rawicz W, Olbrich KC, McIntosh T, Needham D, & Evans E (2000) Effect of chain length and unsaturation on elasticity of lipid bilayers. *Biophys J* 79(1):328–339.

37. Evans E, Heinrich V, Ludwig F, & Rawicz W (2003) Dynamic tension spectroscopy and strength of biomembranes. *Biophys J* 85(4):2342–2350.

38. Brochard F & Lennon JF (1975) Frequency sprectrum of the flicker phenomenon. *J Phys* 36(11):1035–1047.

39. Helfrich W & Servuss R-M (1984) Undulations, steric interaction and cohesion of fluid membranes. *Nuovo Cim D* 3(1):137–151.

40. Aimon S (2011) *Study of a voltage-gated potassium channel in giant unilamellar vesicles (PhD)*. (Universite Paris VI, Paris).

41. Marsh D (2006) Elastic curvature constants of lipid monolayers and bilayers. *Chem Phys Lipids* 144(2):146–159.

42. Martínez–Balbuena L, Maldonado-Arce A, & Hernández-Zapata E (2010) Elasticidad de membranas biológicas. *Rev Mex física E* 56(1):107–122.

43. Baumgart T, Hess ST, & Webb WW (2003) Imaging coexisting fluid domains in biomembrane models coupling curvature and line tension. *Nature* 425(6960):821–824.

44. van Meer G (1989) Lipid traffic in animal cells. *Annu Rev Cell Biol* 5(1):247–275.

45. Pagano RE (1990) Lipid traffic in eukaryotic cells: mechanisms for intracellular transport and organelle-specific enrichment of lipids. *Curr Opin Cell Biol* 2(4):652–663.

46. Sorre B (2010) *Role of membrane curvature in intracellular trafficking (PhD)*. (Université Paris 7 - Denis Diderot, Paris).

47. van Meer G & Lisman Q (2002) Sphingolipid transport: rafts and translocators. *J Biol Chem* 277(29):25855–25858.

48. Callan-Jones A, Sorre B, & Bassereau P (2011) Curvature-driven lipid sorting in biomembranes. *Cold Spring Harb Perspect Biol* 3(2):a004648.

49. Tian A & Baumgart T (2009) Sorting of lipids and proteins in membrane curvature gradients. *Biophys J* 96(7):2676–2688.

50. Kamal MM, Mills D, Grzybek M, & Howard J (2009) Measurement of the membrane curvature preference of phospholipids reveals only weak coupling between lipid shape and leaflet curvature. *Proc Natl Acad Sci* 106(52):22245–22250.

51. Derganc J (2007) Curvature-driven lateral segregation of membrane constituents in Golgi cisternae. *Phys Biol* 4(4):317–324.

52. Parton DL, Klingelhoefer JW, & Sansom MSP (2011) Aggregation of model membrane proteins, modulated by hydrophobic mismatch, membrane curvature, and protein class. *Biophys J* 101(3):691–699.

53. Sorre B, et al. (2012) Nature of curvature coupling of amphiphysin with membranes depends on its bound density. *Proc Natl Acad Sci* 109(1):173–178.

54. Wu Q-Y & Liang Q (2014) Interplay between curvature and lateral organization of lipids and peptides/proteins in model membranes. *Langmuir* 30(4):1116–1122.

55. Aimon S, et al. (2014) Membrane shape modulates transmembrane protein distribution. *Dev Cell*

28(2):212–218.

56. Safouane M, et al. (2010) Lipid cosorting mediated by shiga toxin induced tubulation. *Traffic* 11(12):1519–1529.

57. Römer W, et al. (2007) Shiga toxin induces tubular membrane invaginations for its uptake into cells. *Nature* 450(7170):670–675.

58. Lewis RNAH & McElhaney RN (2009) The physicochemical properties of cardiolipin bilayers and cardiolipin-containing lipid membranes. *Biochim Biophys Acta - Biomembr* 1788(10):2069–2079.

59. Schlame M, Rua D, & Greenberg ML (2000) The biosynthesis and functional role of cardiolipin. *Prog Lipid Res* 39(3):257–288.

60. Romantsov T, et al. (2007) Cardiolipin promotes polar localization of osmosensory transporter ProP in Escherichia coli. *Mol Microbiol* 64(6):1455–1465.

61. Mileykovskaya E (2007) Subcellular localization of Escherichia coli osmosensory transporter ProP: focus on cardiolipin membrane domains. *Mol Microbiol* 64(6):1419–1422.

62. Rand RP & Sengupta S (1972) Cardiolipin forms hexagonal structures with divalent cations. *Biochim Biophys Acta* 255(2):484–92.

63. Vail WJ & Stollery JG (1979) Phase changes of cardiolipin vesicles mediated by divalent cations. *Biochim Biophys Acta* 551(1):74–84.

64. Cullis PR, Verkleij AJ, & Ververgaert PHJT (1978) Polymorphic phase behaviour of cardiolipin as detected by31P NMR and freeze-fracture techniques. Effects of calcium, dibucaine and chlorpromazine. *Acta - Biomembr* 513(1):11–20.

65. Arslan P, Beltrame M, & Muscatello U (1980) Ultrastructural characterization of cardiolipin liquid-crystalline structures in the absence and the presence of divalent cations. *Micron (1969)* 11(2):115–125.

66. De Kruijff B, et al. (1982) Further aspects of the Ca2+-dependent polymorphism of bovine heart cardiolipin. *Biochim Biophys Acta* 693(1):1–12.

67. Seddon JM, Kaye RD, & Marsh D (1983) Induction of the lamellar-inverted hexagonal phase transition in cardiolipin by protons and monovalent cations. *Biochim Biophys Acta - Biomembr* 734(2):347–352.

68. Killian JA, et al. (1994) Effect of divalent cations on lipid organization of cardiolipin isolated from Escherichia coli strain AH930. *Biochim Biophys Acta* 1189(2):225–32.

69. Ortiz A, Killian JA, Verkleij AJ, & Wilschut J (1999) Membrane fusion and the lamellar-to-inverted-hexagonal phase transition in cardiolipin vesicle systems induced by divalent cations. *Biophys J* 77(4):2003–2014.

70. Slonczewski J & Foster JW (2013) *Microbiology: an evolving science*. (W.W. Norton & Company, New York). 3er Ed.

71. Seifert U & Lipowsky R (1995) Chapter 8. Morphology of vesicles. *Handbook of Biological Physics*, Eds. Lipowsky R & Sackmann E (Elsevier Science, Ámsterdam), pp 403–463.

72. Jülicher F & Lipowsky R (1996) Shape transformations of vesicles with intramembrane domains. *Phys Rev E* 53(3):2670–2683.

73. Hörger I, Campelo F, Hernández-Machado A, & Tarazona P (2010) Constricting force of filamentary protein rings evaluated from experimental results. *Phys Rev E* 81(3):031922.

74. Almendro-Vedia VG, Monroy F, & Cao FJ (2015) Analytical results for cell constriction dominated by bending energy. *Phys Rev E* 91(1):12713.

75. Almendro-Vedia VG, Monroy F, & Cao FJ (2013) Mechanics of constriction during cell division: a variational approach. *PLoS One* 8(8):e69750.

76. Seifert U, Berndl K, & Lipowsky R (1991) Shape transformations of vesicles: phase diagram for spontaneous- curvature and bilayer-coupling models. *Phys Rev A* 44(2):1182–1202.

77. Sheetz MP & Singer SJ (1974) Biological membranes as bilayer couples. A molecular mechanism of drug-erythrocyte interactions. *Proc Natl Acad Sci* 71(11):4457–4461.

78. Evans E (1974) Bending resistance and chemically induced moments in membrane bilayers. *Biophys J* 14(12):923–31.

79. Svetina S & Zeks B (1989) Membrane bending energy and shape determination of phospholipid vesicles and red blood cells. *Eur Biophys J* 17(2):101–11.

80. Berndl K, Käs J, Lipowsky R, Sackmann E, & Seifert U (1990) Shape transformations of giant vesicles: extreme sensitivity to bilayer asymmetry. *Europhys Lett* 13(7):659–664.

81. Svetina S, Brumen M, & Zeks B (1985) Lipid bilayer elasticity and the bilayer couple interpretation of red cell shape transformations and lysis. *Stud Biophys* 110:177–184.

82. Miao L, Seifert U, Wortis M, & Döbereiner H-G (1994) Budding transitions of fluid-bilayer vesicles: the effect of area-difference elasticity. *Phys Rev E* 49(6):5389–5407.

83. Robinson DN, Cavet G, Warrick HM, & Spudich JA (2002) Quantitation of the distribution and flux of myosin-II during cytokinesis. *BMC Cell Biol* 3:4.

84. Sens P, Johannes L, & Bassereau P (2008) Biophysical approaches to protein-induced membrane deformations in trafficking. *Curr Opin Cell Biol* 20(4):476–482.

85. Ashkin A (1970) Acceleration and trapping of particles by radiation pressure. *Phys Rev Lett* 24(4):156–159.

86. Morin JA, et al. (2017) DNA synthesis determines the binding mode of the human mitochondrial single-stranded DNA-binding protein. *Nucleic Acids Res* 45(12):7237–7248.

87. Lumicks Optical tweezers: an introductory explanation of the logic behind optical trapping experiments. Available at: https://lumicks.com/optical-tweezers-working-principle/ [Accessed August 23, 2018].

88. Dholakia K, Reece P, & Gu M (2008) Optical micromanipulation. *Chem Soc Rev* 37(1):42–55.

89. Neuman KC & Block SM (2004) Optical trapping. *Rev Sci Instrum* 75(9):2787–2809.

90. Almaas E & Brevik I (1995) Radiation forces on a micrometer-sized sphere in an evanescent field. *J Opt Soc Am B* 12(12):2429.

91. Barton JP, Alexander DR, & Schaub SA (1988) Internal and near-surface electromagnetic fields for a spherical particle irradiated by a focused laser beam. *J Appl Phys* 64(4):1632–1639.

92. Zemánek P, Jonáš A, & Liška M (2002) Simplified description of optical forces acting on a nanoparticle in the Gaussian standing wave. *J Opt Soc Am A* 19(5):1025.

93. Ren KF, Gréha G, & Gouesbet G (1994) Radiation pressure forces exerted on a particle arbitrarily located in a Gaussian beam by using the generalized Lorenz-Mie theory, and associated resonance effects. *Opt Commun* 108(4–6):343–354.

94. Prévost C, Tsai F-C, Bassereau P, & Simunovic M (2017) Pulling membrane nanotubes from giant unilamellar vesicles. *J Vis Exp* (130):e56086.

95. Schmid EM, Richmond DL, & Fletcher DA (2015) Reconstitution of proteins on electroformed giant unilamellar vesicles. *Methods Cell Biol* 128:319–338.

96. Prévost C, et al. (2015) IRSp53 senses negative membrane curvature and phase separates along membrane tubules. *Nat Commun* 6(1):8529.

97. Cooke IR & Deserno M (2006) Coupling between lipid shape and membrane curvature. *Biophys J* 91(2):487–495.

98. Leibler S (1986) Curvature instability in membranes. *J Phys* 47(3):507–516.

99. Markin VS (1981) Lateral organization of membranes and cell shapes. *Biophys J* 36(1):1–19.

100. Seifert U (1993) Curvature-induced lateral phase segregation in two-component vesicles. *Phys Rev Lett* 70(9):1335–1338.

101. Singh P, Mahata P, Baumgart T, & Das SL (2012) Curvature sorting of proteins on a cylindrical lipid membrane tether connected to a reservoir. *Phys Rev E* 85(5):051906.

102. Michaelis L & Menten M (1913) Die Kinetik der Invertinwirkung. *Biochem Z* 49:333–369.

103. Smith S, Yamanaka Y, Pahlow M, & Oschlies A (2009) Optimal uptake kinetics: physiological acclimation explains the pattern of nitrate uptake by phytoplankton in the ocean. *Mar Ecol Prog Ser* 384:1–12.

104. Bonachela JA, Raghib M, & Levin SA (2011) Dynamic model of flexible phytoplankton nutrient uptake. *Proc Natl Acad Sci U S A* 108(51):20633–20638.

105. Harrison P, Parslow J, & Conway H (1989) Determination of nutrient uptake kinetic parameters: a comparison of methods. *Mar Ecol Prog Ser* 52:301–312.

106. Aksnes D & Cao F (2011) Inherent and apparent traits in microbial nutrient uptake. *Mar Ecol Prog Ser* 440:41–51.

107. Lomas MW, Bonachela JA, Levin SA, & Martiny AC (2014) Impact of ocean phytoplankton diversity on phosphate uptake. *Proc Natl Acad Sci U S A* 111(49):17540–17545.

108. Pasciak WJ & Gavis J (1974) Transport limitation of nutrient uptake in phytoplankton1. *Limnol Oceanogr* 19(6):881–888.

109. Armstrong RA (2008) Nutrient uptake rate as a function of cell size and surface transporter density: a Michaelis-like approximation to the model of Pasciak and Gavis. *Deep Sea Res Part I Oceanogr Res Pap* 55(10):1311–1317.

110. Fiksen Ø, Follows MJ, & Aksnes DL (2013) Trait-based models of nutrient uptake in microbes extend the Michaelis-Menten framework. *Limnol Oceanogr* 58(1):193–202.

111. Aksnes DL & Egge JK (1991) A theoretical model for nutrient uptake. *Mar Ecol Prog Ser* 70(1):65–72.

112. Berg HC & Purcell EM (1977) Physics of chemoreception. *Biophys J* 20(2):193–219.

113. Northrup SH (1988) Diffusion-controlled ligand binding to multiple competing cell-bound receptors. *J Phys Chem* 92(20):5847–5850.

114. Zwanzig R (1990) Diffusion-controlled ligand binding to spheres partially covered by receptors: an effective medium treatment. *Proc Natl Acad Sci U S A* 87(15):5856–5857.

115. Beltran-Heredia E (2015) Model of microbial nutrient uptake. Available at: http://demonstrations.wolfram.com/ModelOfMicrobialNutrientUptake/ [Accessed August 23, 2018].

116. Earth Nasa Observatory. What are phytoplankton? Available at: https://earthobservatory.nasa.gov/ [Accessed August 23, 2018].

117. Edwards KF, Thomas MK, Klausmeier CA, & Litchman E (2012) Allometric scaling and taxonomic variation in nutrient utilization traits and maximum growth rate of phytoplankton. *Limnol Oceanogr* 57(2):554–566.

118. Harrison AWG, et al. (2012) The kinetics of nitrogen utilization in the oceanic mixed layer. Nitrate and ammonium interactions at nanomolar concentrations. *Limnol Ocean* 41(1):16–32.

119. McCarthy JJ, Garside C, & Nevins JL (1999) Nitrogen dynamics during the Arabian Sea Northeast Monsoon. *Deep Sea Res Part II Top Stud Oceanogr* 46(8–9):1623–1664.

120. Collos Y, Vaquer A, & Souchu P (2005) Acclimation of nitrate uptake by phytoplankton to high substrate levels. *J Phycol* 41(3):466–478.

121. Chisholm S (1992) Phytoplankton size. *Primary Productivity and Biogeochemical Cycles in the Sea.*, Eds. Falkowski PG & Woodhead AD (Springer Science & Business Media), pp 213–237.

122. Marañón E (2015) Cell size as a key determinant of phytoplankton metabolism and community structure. *Ann Rev Mar Sci* 7(1):241–264.

123. Marañón E, et al. (2001) Patterns of phytoplankton size structure and productivity in contrasting open-ocean environments. *Mar Ecol Prog Ser* 216:43–56.

124. Li WKW (2002) Macroecological patterns of phytoplankton in the northwestern North Atlantic Ocean. *Nature* 419(6903):154–157.

125. Kostadinov TS, Siegel DA, & Maritorena S (2010) Global variability of phytoplankton functional types from space: assessment via the particle size distribution. *Biogeosciences* 7(10):3239–3257.

126. Acevedo-Trejos E, Brandt G, Merico A, & Smith SL (2013) Biogeographical patterns of phytoplankton community size structure in the oceans. *Glob Ecol Biogeogr* 22(9):1060–1070.

127. Smith S, Merico A, Hohn S, & Brandt G (2014) Sizing-up nutrient uptake kinetics: combining a physiological trade-off with size-scaling of phytoplankton traits. *Mar Ecol Prog Ser* 511:33–39.

128. Carlson BM (2007) *Principles of regenerative biology*. (Elsevier, Ámsterdam).

129. Blom T, Somerharju P, & Ikonen E (2011) Synthesis and biosynthetic trafficking of membrane lipids. *Cold Spring Harb Perspect Biol* 3(8):1–16.

130. Lan G, Wolgemuth CW, & Sun SX (2007) Z-ring force and cell shape during division in rod-like bacteria. *Proc Natl Acad Sci* 104(41):16110–16115.

131. Bi E & Lutkenhaus J (1991) FtsZ ring structure associated with division in Escherichia coli. *Nature* 354(6349):161–164.

132. Dajkovic A & Lutkenhaus J (2006) Z ring as executor of bacterial cell division. *J Mol Microbiol Biotechnol* 11(3–5):140–151.

133. Romberg L & Levin PA (2003) Assembly dynamics of the bacterial cell division protein FtsZ: poised at the edge of stability. *Annu Rev Microbiol* 57(1):125–154.

134. Lecuit T & Lenne P-F (2007) Cell surface mechanics and the control of cell shape, tissue patterns

and morphogenesis. *Nat Rev Mol Cell Biol* 8(8):633–644.

135. Rappaport R (1996) *Cytokinesis in animal cells*. (Cambridge University Press, Cambridge).

136. Cao LG (1990) Mechanism of the formation of contractile ring in dividing cultured animal cells. I. Recruitment of preexisting actin filaments into the cleavage furrow. *J Cell Biol* 110(4):1089–1095.

137. Alberts B, et al. (2002) *Molecular biology of the cell*. (Garland Science, New York).

138. Weiss P (1961) Chapter 1. From cell to molecule. *The Molecular Control of Cellular Activity*, Ed. Allen J (McGraw-Hill, New York), pp 1–72.

139. Koch AL, Higgins ML, & Doyle RJ (1981) Surface tension-like forces determine bacterial shapes: Streptococcus faecium. *Microbiology* 123(1):151–161.

140. Huang KC, Mukhopadhyay R, Wen B, Gitai Z, & Wingreen NS (2008) Cell shape and cell-wall organization in Gram-negative bacteria. *Proc Natl Acad Sci* 105(49):19282–19287.

141. Bisson-Filho AW, et al. (2017) Treadmilling by FtsZ filaments drives peptidoglycan synthesis and bacterial cell division. *Science* 355(6326):739–743.

142. Manning ML, Foty RA, Steinberg MS, & Schoetz E-M (2010) Coaction of intercellular adhesion and cortical tension specifies tissue surface tension. *Proc Natl Acad Sci* 107(28):12517–12522.

143. Stewart MP, et al. (2011) Hydrostatic pressure and the actomyosin cortex drive mitotic cell rounding. *Nature* 469(7329):226–230.

144. Sens P & Turner MS (2006) Budded membrane microdomains as tension regulators. *Phys Rev E* 73(3):031918.

145. Lipowsky R (1991) The conformation of membranes. *Nature* 349(6309):475–481.

146. Chen IA (2009) Cell division: breaking up is easy to do. *Curr Biol* 19(8):R327–R328.

147. Budin I & Szostak JW (2011) Physical effects underlying the transition from primitive to modern cell membranes. *Proc Natl Acad Sci* 108(13):5249–5254.

148. Morre DJ (1975) Membrane biogenesis. *Annu Rev Plant Physiol* 26(1):441–481.

149. Nohturfft A & Zhang SC (2009) Coordination of lipid metabolism in membrane biogenesis. *Annu Rev Cell Dev Biol* 25(1):539–566.

150. Jackowski S (1996) Cell cycle regulation of membrane phospholipid metabolism. *J Biol Chem* 271(34):20219–20222.

151. McCusker D & Kellogg DR (2012) Plasma membrane growth during the cell cycle: unsolved mysteries and recent progress. *Curr Opin Cell Biol* 24(6):845–851.

152. Sanchez-Alvarez M, Zhang Q, Finger F, Wakelam MJO, & Bakal C (2015) Cell cycle progression is an essential regulatory component of phospholipid metabolism and membrane homeostasis. *Open Biol* 5(9):150093.

153. Dobbelaere J (2004) Spatial coordination of cytokinetic events by compartmentalization of the cell cortex. *Science* 305(5682):393–396.

154. Albertson R, Riggs B, & Sullivan W (2005) Membrane traffic: a driving force in cytokinesis. *Trends Cell Biol* 15(2):92–101.

155. Boucrot E & Kirchhausen T (2007) Endosomal recycling controls plasma membrane area during mitosis. *Proc Natl Acad Sci* 104(19):7939–7944.

156. Booth IR, Edwards MD, Black S, Schumann U, & Miller S (2007) Mechanosensitive channels in bacteria: signs of closure? *Nat Rev Microbiol* 5(6):431–440.

157. Nagle JF (2013) Introductory lecture: basic quantities in model biomembranes. *Faraday Discuss* 161:11–29.

158. Rodríguez-García R, et al. (2009) Bimodal spectrum for the curvature fluctuations of bilayer vesicles: pure bending plus hybrid curvature-dilation modes. *Phys Rev Lett* 102(12):128101.

159. Siegel DP & Kozlov MM (2004) The gaussian curvature elastic modulus of N-monomethylated dioleoylphosphatidylethanolamine: relevance to membrane fusion and lipid phase behavior. *Biophys J* 87(1):366–374.

160. Hu M, Briguglio JJ, & Deserno M (2012) Determining the gaussian curvature modulus of lipid membranes in simulations. *Biophys J* 102(6):1403–1410.

161. Zheng W-M & Liu J (1993) Helfrich shape equation for axisymmetric vesicles as a first integral. *Phys Rev E* 48(4):2856–2860.

162. Masters TA, Pontes B, Viasnoff V, Li Y, & Gauthier NC (2013) Plasma membrane tension orchestrates membrane trafficking, cytoskeletal remodeling, and biochemical signaling during phagocytosis. *Proc Natl Acad Sci* 110(29):11875–11880.

163. Solon J, et al. (2006) Negative tension induced by lipid uptake. *Phys Rev Lett* 97(9):98103.

164. Claessens MMAE, Leermakers FAM, Hoekstra FA, & Stuart MAC (2008) Osmotic shrinkage and reswelling of giant vesicles composed of dioleoylphosphatidylglycerol and cholesterol. *Biochim Biophys Acta - Biomembr* 1778(4):890–895.

165. Oglęcka K, Sanborn J, Parikh AN, & Kraut RS (2012) Osmotic gradients induce bio-reminiscent morphological transformations in giant unilamellar vesicles. *Front Physiol* 3(120):1–11.

166. Käs J & Sackmann E (1991) Shape transitions and shape stability of giant phospholipid vesicles in pure water induced by area-to-volume changes. *Biophys J* 60(4):825–844.

167. Emoto K, Inadome H, Kanaho Y, Narumiya S, & Umeda M (2005) Local change in phospholipid composition at the cleavage furrow is essential for completion of cytokinesis. *J Biol Chem* 280(45):37901–37907.

168. Bretscher MS (1973) Membrane structure: some general principles. *Science* 181(4100):622–629.

169. Ritacco H, López-Montero I, Monroy F, Ortega F, & Rubio R (2010) Monolayers and multilayers: equilibrium and mechanical properties. *Nanoscience: Colloidal and Interfacial Aspects*, Ed. Starov V (CRC Press, Boca Raton, Florida), pp 649–695.

170. Munder PG, Modolell M, Andreesen R, Weltzien HU, & Westphal O (1979) Lysophosphatidylcholine (lysolecithin) and its synthetic analogues. Immunemodulating and other biologic effects. *Springer Semin Immunopathol* 2(2):187–203.

171. Martens S & McMahon HT (2008) Mechanisms of membrane fusion: disparate players and common principles. *Nat Rev Mol Cell Biol* 9(7):543–556.

172. Heberle FA & Feigenson GW (2011) Phase separation in lipid membranes. *Cold Spring Harb Perspect Biol* 3(4):1–13.

173. Donaldson JG (2009) Phospholipase D in endocytosis and endosomal recycling pathways. *Biochim Biophys Acta* 1791(9):845–849.

174. Litvak V, Dahan N, Ramachandran S, Sabanay H, & Lev S (2005) Maintenance of the diacylglycerol

level in the Golgi apparatus by the Nir2 protein is critical for Golgi secretory function. *Nat Cell Biol* 7(3):225–234.

175. Schekman R & Orci L (1996) Coat proteins and vesicle budding. *Science* 271(5255):1526–1533.

176. Lipowsky R (1992) Budding of membranes induced by intramembrane domains. *J Phys II* 2(10):1825–1840.

177. Bashkirov PV, et al. (2008) GTPase cycle of dynamin Is coupled to membrane squeeze and release, leading to spontaneous fission. *Cell* 135(7):1276–1286.

178. Boucrot E, et al. (2012) Membrane fission is promoted by insertion of amphipathic helices and is restricted by crescent BAR domains. *Cell* 149(1):124–136.

179. Miao L, Fourcade B, Rao M, Wortis M, & Zia RKP (1991) Equilibrium budding and vesiculation in the curvature model of fluid lipid vesicles. *Phys Rev A* 43(12):6843–6856.

180. Döbereiner HG, Käs J, Noppl D, Sprenger I, & Sackmann E (1993) Budding and fission of vesicles. *Biophys J* 65(4):1396–1403.

181. Kohyama T, Kroll DM, & Gompper G (2003) Budding of crystalline domains in fluid membranes. *Phys Rev E* 68(6):061905.

182. Sens P (2004) Dynamics of nonequilibrium membrane bud formation. *Phys Rev Lett* 93(10):108103.

183. Erickson HP & Osawa M (2010) Cell division without FtsZ - a variety of redundant mechanisms. *Mol Microbiol* 78(2):267–270.

184. De Camilli P, Emr SD, McPherson PS, & Novick P (1996) Phosphoinositides as regulators in membrane traffic. *Science* 271(5255):1533–1539.

185. Schuck S & Simons K (2004) Polarized sorting in epithelial cells: raft clustering and the biogenesis of the apical membrane. *J Cell Sci* 117(25):5955–5964.

186. Zurzolo C, van't Hof W, van Meer G, & Rodriguez-Boulan E (1994) VIP21/caveolin, glycosphingolipid clusters and the sorting of glycosylphosphatidylinositol-anchored proteins in epithelial cells. *EMBO J* 13(1):42–53.

187. Brown DA & Rose JK (1992) Sorting of GPI-anchored proteins to glycolipid-enriched membrane subdomains during transport to the apical cell surface. *Cell* 68(3):533–544.

188. Lipowsky R (1993) Domain-induced budding of fluid membranes. *Biophys J* 64(4):1133–1138.

189. Lipowsky R & Dimova R (2003) Domains in membranes and vesicles. *J Phys Condens Matter* 15(1):S31–S45.

190. Baumgart T, Das S, Webb WW, & Jenkins JT (2005) Membrane elasticity in giant vesicles with fluid phase coexistence. *Biophys J* 89(2):1067–1080.

191. Wang X & Du Q (2007) Modelling and simulations of multi-component lipid membranes and open membranes via diffuse interface approaches. *J Math Biol* 56(3):347–371.

192. Huang KC, Mukhopadhyay R, & Wingreen NS (2006) A curvature-mediated mechanism for localization of lipids to bacterial poles. *PLoS Comput Biol* 2(11):e151.

193. Sackmann E, Bausch A, & Vonna L (2002) Physics of composite cell membrane and actin based cytoskeleton. *Physics of Bio-Molecules and Cells*, Eds. Flyvbjerg F, Jülicher F, Ormos P, & David F (Springer, Berlin).

194. Leaver M, Domínguez-Cuevas P, Coxhead JM, Daniel RA, & Errington J (2009) Life without a wall or division machine in Bacillus subtilis. *Nature* 457(7231):849–853.

195. de Lozanne A & Spudich J (1987) Disruption of the Dictyostelium myosin heavy chain gene by homologous recombination. *Science* 236(4805):1086–1091.

196. Knecht D & Loomis W (1987) Antisense RNA inactivation of myosin heavy chain gene expression in Dictyostelium discoideum. *Science* 236(4805):1081–1086.

197. Cabeen MT & Jacobs-Wagner C (2005) Bacterial cell shape. *Nat Rev Microbiol* 3(8):601–610.

198. Reshes G, Vanounou S, Fishov I, & Feingold M (2008) Cell shape dynamics in Escherichia coli. *Biophys J* 94(1):251–264.

199. Field C, Li R, & Oegema K (1999) Cytokinesis in eukaryotes: a mechanistic comparison. *Curr Opin Cell Biol* 11(1):68–80.

200. Niven GW, Morton JS, Fuks T, & Mackey BM (2008) Influence of environmental stress on distributions of times to first division in Escherichia coli populations, as determined by digital-image analysis of individual cells. *Appl Environ Microbiol* 74(12):3757–3763.

201. Kutalik Z, Razaz M, Elfwing A, Ballagi A, & Baranyi J (2005) Stochastic modelling of individual cell growth using flow chamber microscopy images. *Int J Food Microbiol* 105(2):177–190.

202. Kim H-J, et al. (2011) Systemic analysis of heat shock response Induced by heat shock and a proteasome inhibitor MG132. *PLoS One* 6(6):e20252.

203. Edelman GM & Gally JA (2001) Degeneracy and complexity in biological systems. *Proc Natl Acad Sci* 98(24):13763–13768.

204. Campbell NA, et al. (2008) *Biology*. (Benjamin Cummings/Pearson, San Francisco). 11th Ed.

205. Morgan DO (2007) *The cell cycle: principles of control*. (New Science Press, London).

206. Nasmyth K (1996) Viewpoint: putting the cell cycle in order. *Science* 274:1643–1645.

207. Barr FA & Gruneberg U (2007) Cytokinesis: placing and making the final cut. *Cell* 131(5):847–860.

208. Rappaport R (1986) Establishment of the mechanism of cytokinesis in animal cells. *Int Rev Cytol* 105:245–281.

209. Nurse P (1992) Eukaryotic cell-cycle control. *Biochem Soc Trans* 20(2):239–242.

210. Daniel RA & Errington J (2003) Control of cell morphogenesis in bacteria: two distinct ways to make a rod-shaped cell. *Cell* 113(6):767–776.

211. van den Ent F, Amos LA, & Löwe J (2001) Prokaryotic origin of the actin cytoskeleton. *Nature* 413(6851):39–44.

212. Miller AL (2011) The contractile ring. *Curr Biol* 21(24):R976–R978.

213. Ghuysen JM & Hakenbeck R (1994) *Bacterial cell wall*. Eds. Ghuysen JM & Hakenbeck R. (Elsevier Science, Ámsterdam).

214. Ayala JA, Garrido T, de Pedro MA, & Vicente M (1994) Chapter 5. Molecular biology of bacterial septation. *New Compr Biochem* 27:73–101.

215. de Pedro MA, Donachie WD, Holtje J-V, & Schwarz H (2001) Constitutive septal murein synthesis in Escherichia coli with impaired activity of the morphogenetic proteins RodA and penicillin-binding protein 2. *J Bacteriol* 183(14):4115–4126.

216. Adams DW & Errington J (2009) Bacterial cell division: assembly, maintenance and disassembly of the Z ring. *Nat Rev Microbiol* 7(9):642–653.

217. Xiao J & Goley ED (2016) Redefining the roles of the FtsZ-ring in bacterial cytokinesis. *Curr Opin Microbiol* 34:90–96.

218. Fletcher DA & Mullins RD (2010) Cell mechanics and the cytoskeleton. *Nature* 463(7280):485–492.

219. Steigmann DJ (2018) *The role of mechanics in the study of lipid bilayers*. Ed. Steigmann DJ. (Springer International Publishing, Switzerland).

220. McMahon HT & Gallop JL (2005) Membrane curvature and mechanisms of dynamic cell membrane remodelling. *Nature* 438(7068):590–596.

221. Seifert U (1997) Configurations of fluid membranes and vesicles. *Adv Phys* 46(1):13–137.

222. Beltrán-Heredia E, Almendro-Vedia VG, Monroy F, & Cao FJ (2017) Modeling the mechanics of cell division: influence of spontaneous membrane curvature, surface tension, and osmotic pressure. *Front Physiol* 8:312.

223. Deserno M (2015) Fluid lipid membranes: from differential geometry to curvature stresses. *Chem Phys Lipids* 185:11–45.

224. Tinevez J-Y, et al. (2009) Role of cortical tension in bleb growth. *Proc Natl Acad Sci* 106(44):18581–18586.

225. Turlier H, Audoly B, Prost J, & Joanny J-F (2014) Furrow constriction in animal cell cytokinesis. *Biophys J* 106(1):114–123.

226. Mohan K, Iglesias PA, & Robinson DN (2012) Separation anxiety: stress, tension and cytokinesis. *Exp Cell Res* 318(12):1428–1434.

227. Gerald N, Dai J, Ting-Beall HP, & de Lozanne A (1998) A role for Dictyostelium racE in cortical tension and cleavage furrow progression. *J Cell Biol* 141(2):483–492.

228. Green RA, Paluch E, & Oegema K (2012) Cytokinesis in animal cells. *Annu Rev Cell Dev Biol* 28(1):29–58.

229. Balasubramanian MK, Bi E, & Glotzer M (2004) Comparative analysis of cytokinesis in budding yeast, fission yeast and animal cells. *Curr Biol* 14(18):R806–R818.

230. Rappaport R (1967) Cell division: direct measurement of maximum tension exerted by furrow of echinoderm eggs. *Science* 156(3779):1241–1243.

231. Sweeney HL & Houdusse A (2010) Structural and functional insights into the myosin motor mechanism. *Annu Rev Biophys* 39(1):539–557.

232. Zhong-can O-Y & Helfrich W (1987) Instability and deformation of a spherical vesicle by pressure. *Phys Rev Lett* 59(21):2486–2488.

233. Zhong-can O-Y & Helfrich W (1989) Bending energy of vesicle membranes: general expressions for the first, second, and third variation of the shape energy and applications to spheres and cylinders. *Phys Rev A* 39(10):5280–5288.

234. Vogel F, Bornhövd C, Neupert W, & Reichert AS (2006) Dynamic subcompartmentalization of the mitochondrial inner membrane. *J Cell Biol* 175(2):237–247.

235. Mitchell P (1961) Coupling of phosphorylation to electron and hydrogen transfer by a chemi-

osmotic type of mechanism. *Nature* 191(4784):144–148.

236. Almendro-Vedia VG, et al. (2017) Nonequilibrium fluctuations of lipid membranes by the rotating motor protein F1F0-ATP synthase. *Proc Natl Acad Sci U S A* 114(43):11291–11296.

237. Khalifat N, Fournier J-B, Angelova MI, & Puff N (2011) Lipid packing variations induced by pH in cardiolipin-containing bilayers: the driving force for the cristae-like shape instability. *Biochim Biophys Acta - Biomembr* 1808(11):2724–2733.

238. Khalifat N, Puff N, Bonneau S, Fournier J-B, & Angelova MI (2008) Membrane deformation under local pH gradient: mimicking mitochondrial cristae dynamics. *Biophys J* 95(10):4924–4933.

239. Parthasarathy R, Yu C, & Groves JT (2006) Curvature-modulated phase separation in lipid bilayer membranes. *Langmuir* 22(11):5095–5099.

240. Liang Q & Ma Y (2009) Curvature-induced lateral organization in mixed lipid bilayers supported on a corrugated substrate. *J Phys Chem B* 113(23):8049–8055.

241. Reynwar BJ, et al. (2007) Aggregation and vesiculation of membrane proteins by curvature-mediated interactions. *Nature* 447(7143):461–464.

242. Mukherjee S, Soe TT, & Maxfield FR (1999) Endocytic sorting of lipid analogues differing solely in the chemistry of their hydrophobic tails. *J Cell Biol* 144(6):1271–1284.

243. Mukherjee S & Maxfield FR (2000) Role of membrane organization and membrane domains in endocytic lipid trafficking. *Traffic* 1(3):203–211.

244. van Meer G & Sprong H (2004) Membrane lipids and vesicular traffic. *Curr Opin Cell Biol* 16(4):373–378.

245. Chen C-M, Higgs PG, & MacKintosh FC (1997) Theory of fission for two-component lipid vesicles. *Phys Rev Lett* 79(8):1579–1582.

246. Derényi I, et al. (2007) Membrane nanotubes. *Controlled Nanoscale Motion: Nobel Symposium 131 (Lecture Notes in Physics)*, Eds. Linke H & Mansson A (Springer-Verlag, Berlin), pp 141–159.

247. Jiang H & Powers TR (2008) Curvature-driven lipid sorting in a membrane tubule. *Phys Rev Lett* 101(1):018103.

248. Pan J, et al. (2015) Structural and mechanical properties of cardiolipin lipid bilayers determined using neutron spin echo, small angle neutron and X-ray scattering, and molecular dynamics simulations. *Soft Matter* 11(1):130–138.

249. Kučěrka N, Tristram-Nagle S, & Nagle JF (2005) Structure of fully hydrated fluid phase lipid bilayers with monounsaturated chains. *J Membr Biol* 208(3):193–202.

250. Huang KC & Ramamurthi KS (2010) Macromolecules that prefer their membranes curvy. *Mol Microbiol* 76(4):822–832.

251. Sennato S, et al. (2005) Evidence of domain formation in cardiolipin−glycerophospholipid mixed monolayers. A thermodynamic and AFM study. *J Phys Chem B* 109(33):15950–15957.

252. Eggeling C, et al. (2009) Direct observation of the nanoscale dynamics of membrane lipids in a living cell. *Nature* 457(7233):1159–1162.

253. Angelova MI, Soléau S, Méléard P, Faucon F, & Bothorel P (1992) Preparation of giant vesicles by external AC electric fields. Kinetics and applications. *Trends in Colloid and Interface Science VI*, Eds. Helm C, Lösche M, & Möhwald H (Steinkopff, Darmstadt), pp 127–131.

254. Hénin J, Shinoda W, & Klein ML (2009) Models for phosphatidylglycerol lipids put to a structural test. *J Phys Chem B* 113(19):6958–6963.

255. Arriaga LR, et al. (2017) Dissipative dynamics of fluid lipid membranes enriched in cholesterol. *Adv Colloid Interface Sci* 247:514–520.

256. Litchman E, Klausmeier CA, Schofield OM, & Falkowski PG (2007) The role of functional traits and trade-offs in structuring phytoplankton communities: scaling from cellular to ecosystem level. *Ecol Lett* 10(12):1170–1181.

257. Pahlow M (2005) Linking chlorophyll-nutrient dynamics to the RedÞeld N:C ratio with a model of optimal phytoplankton growth. *Mar Ecol Prog Ser* 287:33–43.

258. Tambi H, et al. (2009) Relationship between phosphate affinities and cell size and shape in various bacteria and phytoplankton. *Aquat Microb Ecol* 57(3):311–320.

259. Lindemann C, Fiksen Ø, Andersen KH, & Aksnes DL (2016) Scaling laws in phytoplankton nutrient uptake affinity. *Front Mar Sci* 3:26–32.

260. Brewin RJW, et al. (2010) A three-component model of phytoplankton size class for the Atlantic Ocean. *Ecol Modell* 221(11):1472–1483.

261. Maddox AS, Lewellyn L, Desai A, & Oegema K (2007) Anillin and the septins promote asymmetric ingression of the cytokinetic furrow. *Dev Cell* 12(5):827–35.